Sources of variability in short-lived climate pollutants and their effect on climate

Matthew James Rowlinson

Submitted in accordance with the requirements for the degree of Doctor of Philosophy

The University of Leeds

School of Earth and Environment

September 2019

Declaration of authorship

The candidate confirms that the work submitted is his own, except where work which has formed part of jointly authored publications has been included. The contribution of the candidate and the other authors to this work has been explicitly indicated below. The candidate confirms that appropriate credit has been given within the thesis where reference has been made to the work of others.

The work in Chapter 4 has been submitted for publication as follows:

Rowlinson, M. J., Rap, A., Hamilton, D. S., Pope, R. J., Hantson, S., Arnold, S. R., Kaplan, J. O., Arneth, A., Chipperfield, M. P., Forster, P., Nieradzik, L., (2019). Tropospheric ozone radiative forcing uncertainty due to pre-industrial natural emissions. Submitted to *Atmospheric Chemistry and Physics*.

The manuscript was written by the candidate with comments from co-authors. The candidate conceptualised the study along with A. Rap and D. Hamilton. Emission inventories were produced by S. Hantson, J. Kaplan, A. Arneth and L. Nieradzik, and processed for use in TOMCAT-GLOMAP by R. Pope and D. Hamilton. All model runs and analysis was performed by the candidate with guidance from supervisors A. Rap and S. Arnold.

The work in Chapter 5 has appeared in publication as follows:

Rowlinson, M. J., Rap, A., Arnold, S. R., Pope, R. J., Chipperfield, M. P., McNorton, J., Forster, P., Gordon, G., Pringle, K. J., Feng, W., Kerridge, B. J., Latter, B. L., Siddans, R. (2019), Impact of El Niño–Southern Oscillation on the interannual variability of methane and tropospheric ozone, *Atmos. Chem. Phys.*, *19*(13), 8669-8686.

The manuscript was written by the candidate with comments from co-authors. The candidate conceptualised the study along with A. Rap and S. Arnold. The model development was completed by M. Chipperfield, K. Pringle, W. Feng and H. Gordon with help from the candidate. The satellite-model comparison was

conducted by R. Pope. All other model-observation evaluation was performed by the candidate. All model runs and analysis was performed by the candidate, with guidance from A. Rap and S. Arnold.

Abstract

Targeting short-lived climate pollutants (SLCPs) such as methane (CH_4), tropospheric ozone (O_3) and atmospheric aerosols has been proposed as an effective method of reducing the rate of near-term warming, due to their considerable contribution to climate change and relatively short atmospheric lifetimes. Many SLCPs are also air pollutants, presenting the opportunity to simultaneously tackle both climate change and air quality. The aim of this thesis is to improve understanding of factors controlling SLCPs and their role in global climate. Model simulations using the TOMCAT chemical transport model and the SOCRATES radiative transfer model are used to explore sources of uncertainty and variability of SLCPs, as well as potential as mitigation strategies.

Recent evidence from proxy-records indicates that fire and biogenic emissions were likely larger in the pre-industrial era than in the present-day. Greater emissions of O_3 precursors CO and NO_x in revised pre-industrial emissions inventories result in increases in simulated pre-industrial tropospheric O_3 concentrations, decreasing the pre-industrial to present-day radiative forcing (RF) of tropospheric O_3 by up to 35%.

The variability of CH_4 and tropospheric O_3 during El Niño is largely driven by changes in fire emissions. During the 1997 El Niño, enhanced fire emissions of CO suppressed oxidant availability and extended CH_4 lifetime, causing a 7.5 ppb yr^{-1} increase in simulated global CH_4 growth rate in 1998. Increased fire emissions also lead to an increase in O_3 RF of 0.03 Wm^{-2}, while meteorological effects decrease O_3, reducing tropospheric O_3 RF by 0.03 Wm^{-2}, thus resulting in a small net change to tropospheric O_3.

The potential of targeting SLCPs as a mitigation strategy is also assessed by investigating the climate and air pollution impacts of various emission reduction measures. It is found that maximum technically feasible reductions of anthropogenic emissions reduce global air pollution, however the removal of cooling aerosol results in an accelerated rate of warming, surpassing 2°C by 2050. Targeted measures which decrease emissions of only warming components enables mitigation of global mean temperature change of up to 0.3°C by 2050, but does not combat the growing problem of air pollution.

Acknowledgements

Firstly, I would like to thank my primary supervisor Alex for his constant support and guidance over the last four years. I would also like to thank Steve and Piers for all their valuable feedback and encouragement. I am extremely grateful to have had the best team of supervisors I could have hoped for.

I'd like to thank Richard and Joey for their help with TOMCAT, emission inventories and generally helping out right through my PhD. I'd also like to thank Hamish, Martyn, Kirsty and all the TOMCAT-GLOMAP group for all their help and patience. Thanks also go to Chris Smith for his help with SOCRATES, FaIR and Python.

I am very grateful to all co-authors who have provided insightful feedback, and also want to thank all the members of my three research groups (Biosphere-Atmosphere Group, Physical Climate Change and the Aerosol modellers group) for making me feel welcome right from the start. A big thank you to everyone who I've played football and squash with down the years, and the regular attendees of ICAS coffee and pub Thursdays. I also want to thank the rest of my PhD cohort, with a special mention for Josh and Charlie for the many evenings with pizza and football ignoring our PhD woes.

I would like to thank my family for their unwavering support throughout this process. A special thanks to my Mum and Dad and my sisters Claire and Lauren, without whom I wouldn't be where I am, Finally, I would like to thank Krystie for her incredible support and endless optimism, for always keeping me positive and always believing I would get there in the end.

Table of Contents

List of Figures

List of Tables

Abbreviations

ACCMIP	**A**tmospheric **C**hemistry and **C**limate **M**odel **I**ntercomparison **P**roject
AR4	IPCC **F**ourth **A**ssessment **R**eport
AR5	IPCC **F**ifth **A**ssessment **R**eport
BC	**B**lack **C**arbon
BVOC	**B**iogenic **V**olatile **O**rganic **C**ompound
CCMI	**C**hemistry-**C**limate **M**odel **I**nitiative
CCN	**C**loud **C**ondensation **N**uclei
CDN	**C**loud **D**roplet **N**umber
CLE	**C**urrent **Le**gislation scenario
CMIP	**C**oupled **M**odel **I**ntercomparison **P**roject
CTM	**C**hemical **T**ransport **M**odel
ECLIPSE	**E**valuating the **CL**imate and Air Quality **I**mpacts of Short-Lived **P**ollutant**S**
ECMWF	**E**uropean **C**entre for **M**edium-range **W**eather **F**orecasts
EDGAR	**E**mission **D**atabase for **G**lobal **A**tmospheric **R**esearch
ERF	**E**ffective **R**adiative **F**orcing
ENSO	**E**l **N**ino-**S**outhern **O**scillation
FaIR	**F**inite **A**mplified **I**mpulse **R**esponse
FAR	IPCC **F**irst **A**ssessment **R**eport
FINN	**F**ire **IN**ventory from **N**CAR

GBD	**G**lobal **B**urden of **D**iseases, Injuries and Risk Factors
GFED	**G**lobal **F**ire **E**missions **D**atabase
GLOMAP	**GLO**bal **M**odel of **A**erosol **P**rocesses
GTP	**G**lobal **T**emperature **P**otential
GWP	**G**lobal **W**arming **P**otential
HFC	**H**ydro**F**luoro**C**arbon
IAV	**I**nter**A**nnual **V**ariability
IPCC	**I**ntergovernmental **P**anel on **C**limate **C**hange
ISCCP	**I**nternational **S**atellite **C**loud **C**limatology **P**roject
JULES	**J**oint **U**K **L**and **E**nvironment **S**imulator
MACCity	**M**onitoring **A**tmospheric **C**omposition and **C**limate
MEGAN	**M**odel of **E**missions of **G**ases and **A**erosols from **N**ature
MEI	**M**ultivariate **E**NSO **I**ndex
MTFR	**M**aximum **T**echnically **F**easible **R**eductions
NMB	**N**ormalised **M**ean **B**ias
NMVOC	**N**on-**M**ethane **V**olatile **O**rganic **C**ompound
OEI	**O**zone **E**NSO **I**ndex
OMI	**O**zone **M**onitoring **I**nstrument
PAN	**P**eroxy**A**cetyl **N**itrate
PD	**P**resent-**D**ay
PI	**P**re-**I**ndustrial

RCP	**R**epresentative **C**oncentration **P**athway
RF	**R**adiative **F**orcing
SAR	IPCC **S**econd **A**ssessment **R**eport
SLCP	**S**hort-**L**ived **C**limate **P**ollutant
SLCPMIT	**SLCP MIT**igation scenario
SOCRATES	**S**uite **O**f **C**ommunity **RA**diative **T**ransfer codes based on **E**dwards and **S**lingo
SST	**S**ea **S**urface **T**emperature
TAR	IPCC **T**hird **A**ssessment **R**eport
TOA	**T**op **O**f **A**tmosphere
TOMCAT	**T**oulouse **O**ff-line **M**odel of **C**hemistry **A**nd **T**ransport
UNEP	**U**nited **N**ations **E**nvironment **P**rogramme
VOC	**V**olatile **O**rganic **C**ompound
WMGHG	**W**ell-**M**ixed Green**H**ouse **G**ases
WHO	**W**orld **H**ealth **O**rganisation
WMO	**W**orld **M**eteorological **O**rganisation
2deg	**2-deg**ree climate scenario

1. Introduction

1.1. Motivation

Anthropogenic emissions of trace gases since the industrial revolution have changed the composition of the Earth's atmosphere. Greenhouse gases such as carbon dioxide (CO_2) and methane (CH_4) are released during combustion of fossil fuels, increasing atmospheric concentrations and altering the atmospheric radiative balance. Greenhouse gases absorb outgoing longwave radiation, leading to an increase in tropospheric temperatures. Observed global mean surface temperatures have increased more than 1°C since the second half of the nineteenth century (Haustein et al., 2017), leading to an increase in extreme weather events, loss of biodiversity and sea level rise.

Understanding the processes involved in climate change is essential when designing strategies to effectively mitigate future change. Accurately attributing observed warming to specific forcers improves understanding of the primary drivers of historic anthropogenic climate change, allowing projection of future change and its consequences. While satellite and in-situ observations provide valuable data on historic trends, emissions and the current atmospheric state, computer models are needed to understand processes and feedbacks occurring in the atmosphere and estimate global sources and sinks. Models allow the simulation of changes to atmospheric composition and radiative fluxes since the pre-industrial era (PI), enabling projection of future changes.

It is now well-established that man-made emissions of CO_2 are the most important driver of anthropogenic climate change. The Fifth Assessment Report

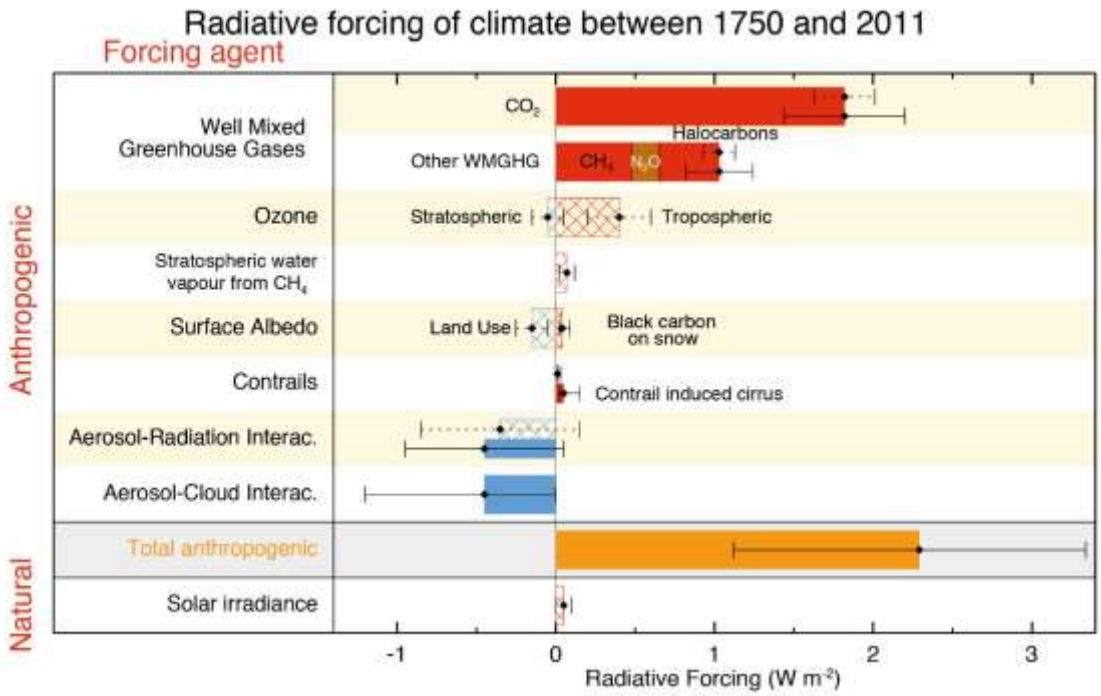

Figure 1.1 IPCC AR5 estimates of radiative forcing (hatched) and effective radiative forcing (solid) for the period 1750–2011, for various climate forcers and processes (From Myhre et al. 2013a, Figure 8.17).

(AR5) from the Intergovernmental Panel on Climate Change (IPCC) highlights the dominance of the CO_2 contribution to radiative forcing (RF) since the PI (Figure 1.1) (Myhre et al., 2013b). Although the efficiency of CO_2 as a greenhouse gas is small relative to other gases such as CH_4 or nitrous oxide (N_2O) (Forster et al., 2007), the abundance and long lifetime of CO_2 results in a large impact on climate. The exact atmospheric lifetime of CO_2 is variable, but the effect of CO_2 emitted from fossil fuel combustion can last for millennia (Archer et al., 2009). As well as the importance of CO_2, Figure 1.1 also illustrates the array of man-made forcers which influence climate. While decreasing atmospheric CO_2 concentrations must be the principal factor in mitigating future climate change, it is important to fully understand the role other climate forcers play in order to mitigate future change as effectively and efficiently as possible.

1.2. Short-lived climate pollutants

In the most recent report from the United Nation's Intergovernmental Panel on Climate Change (IPCC) (Myhre et al., 2013b), a positive RF of 1.82 Wm^{-2} over the industrial era (defined as 1750-present day) was attributed to CO_2, roughly 64% of the combined RF from all well-mixed greenhouse gases (WMGHG). Though the climate effect of CO_2 dominates, a considerable fraction of the estimated total RF is driven by non-CO_2 species. Of the non-CO_2 drivers, several of the most important have much shorter atmospheric lifetimes than CO_2. These are known as short-lived climate pollutants (SLCPs) or near-term climate forcers (NTCF).

SLCPs are gases or aerosols with an anthropogenic source, which affect climate and have an atmospheric lifetime of around a decade or less (UNEP and WMO, 2011). The short lifetime means that the benefits of decreasing emissions would be realised faster than following equivalent action on CO_2 emissions, as atmospheric concentrations and associated RF would decrease as emissions fell. As CO_2 has a very long atmospheric lifetime, reductions in emissions would only slowly reduce atmospheric concentrations of CO_2, so the effect on climate will persist for many decades. Concentrations of short-lived species on the other hand will respond to changes in emission sources much faster, consequently decreasing their impact on climate. For this reason, it has been suggested that these species may provide an opportunity for near-term mitigation. The SLCPs

Table 1.1 Estimated radiative forcing (RF) and approximate atmospheric lifetime of major anthropogenic climate forcers (from IPCC AR5 report (Myhre et al., 2013b) and Etminan et al. (2016)).

	RF (Wm^{-2})	**Lifetime**
CO_2	1.83	5-200 years
N_2O	0.17	131 years
CH_4	0.61	9-12 years
Tropospheric Ozone	0.4 (0.2 to 0.6)	~3 weeks
CFCs	0.273	45-100 years
Aerosols	-1.05 (-2.68 to -0.15)	Minutes to weeks

with the largest warming effect on climate are CH_4, tropospheric ozone (O_3), black carbon (BC) aerosol and some short-lived hydrofluorocarbons (HFCs) (UNEP, 2011; Shoemaker et al., 2013). With the exception of HFCs these species are also, either directly or indirectly, responsible for degrading air quality. Thus, decreasing emissions of SLCPs and their precursors has the potential to mitigate anthropogenic climate change whilst also tackling global air pollution.

Although it is now well-established that anthropogenic activities are responsible for the current trend in global climate, there remains substantial uncertainty regarding the contribution from individual climate forcers, particularly from SLCPs. Measuring the impact of anthropogenic emissions on climate requires knowledge of not only how a forcing agent affects climate, but also of how the composition of the atmosphere has changed over time. While networks of observatories and satellite information mean that the present-day concentration and distribution of climate forcers is relatively well-constrained, the composition of the atmosphere in the past environment is much less certain. As anthropogenic activities began affecting global land-use and releasing emissions on a large scale during the Industrial Revolution, the impact of humans on climate is typically estimated relative to the pre-industrial era, with 1750 commonly used as the baseline. Pre-industrial estimates rely on a smaller and less certain network of measurements combined with proxy records and modelling estimates, meaning there can be large uncertainty in precisely how atmospheric concentrations have changed. Furthermore, natural processes play an important role in climate which can be difficult to quantify accurately. Cycles of global variability such as the El Niño-Southern Oscillation (ENSO) drive large-scale changes in meteorology and natural emissions, altering atmospheric composition and the climate impact of SLCPs. Understanding the mechanisms and magnitude of natural variability is therefore important when trying to fully understand the role of anthropogenic activity on climate. In addition, numerous modelling studies have indicated that the occurrence of ENSO events will change substantially in a warming climate (Timmermann et al., 1999; Collins, 2000; van Oldenborgh et al., 2005; Müller and Roeckner, 2008; Cai et al., 2015). In order to be able to estimate the likely impact of these future changes, it is

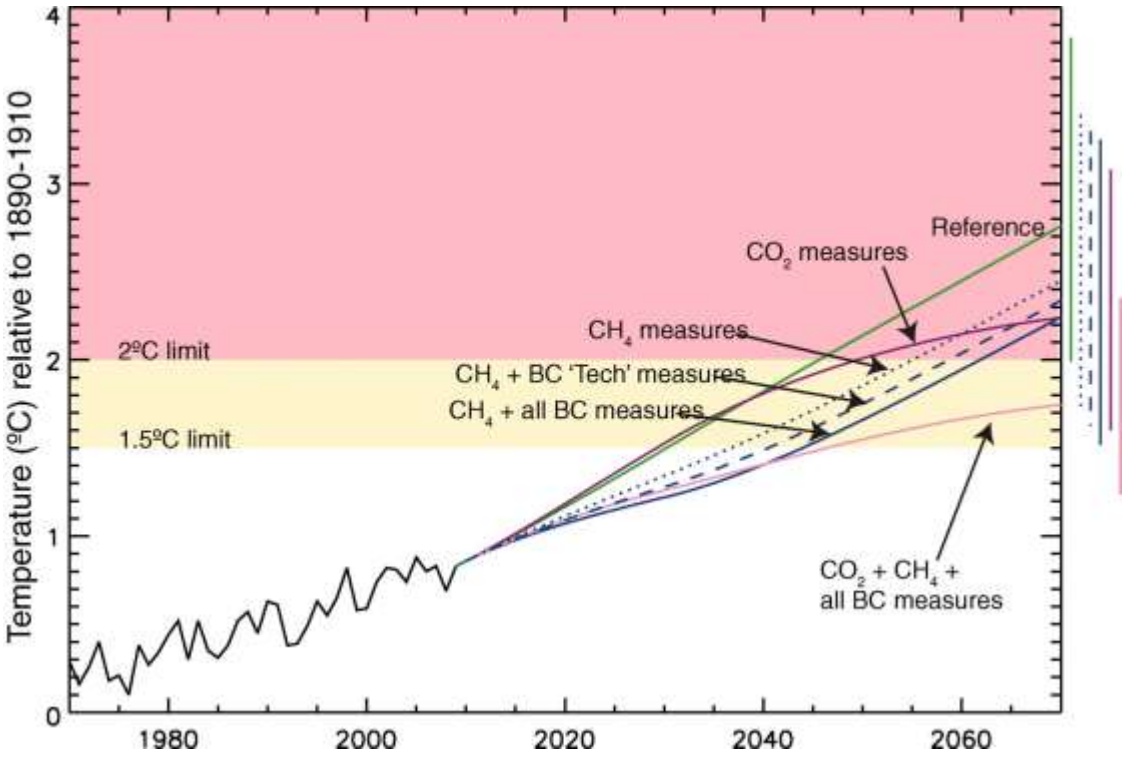

Figure 1.2 Observed temperatures through 2009 and projected temperatures thereafter under various scenarios, all relative to the 1890–1910 mean (From Shindell et al. 2012, Figure 1).

necessary to understand the precise mechanisms affecting SLCP variability in past and present-day ENSO events.

It has been proposed that action to decrease SLCP emissions offers an opportunity to limit global mean surface temperature increase since the PI to below 2°C (Hansen et al., 2007; Molina et al., 2009; UNEP and WMO, 2011), a target commonly touted as a threshold for “dangerous” climate change (Ramanathan and Xu, 2010) and agreed as the long-term goal at the 2015 Paris climate conference. Tackling BC and tropospheric O_3 precursors, in particular CH_4, is likely the most effective form of SLCP mitigation as these species contribute significantly to RF (Figure 1.1). Several studies propose such measures as the most productive strategy for decreasing the rate of near-term warming (UNEP and WMO, 2011; Shindell et al., 2012). Projections in Shindell et al. (2012) estimated that although CO_2 mitigation remains vital in the long-term, BC and CH_4 measures are more effective at slowing the rate of near-term warming (Figure 1.2). CO_2-only measures do not impact the rate of temperature

change until around 2040, whereas BC and CH_4 measures lead to an almost immediate change in temperature. Figure 1.2 emphasises the importance of a combination of CO_2 and SLCP measures for effective, long-term climate mitigation. A thorough understanding of the impact of changes to emissions of SLCPs and their precursors on the rate of climate change improves the likelihood of developing an effective and efficient mitigation strategy, which may alleviate the near-term consequences of climate change.

Understanding the role of SLCPs in the past and present-day atmosphere is essential to accurately assess their role in historic climate change and potential for future mitigation of climate change. Therefore, it is necessary to have a good knowledge of the processes affecting SLCPs in the atmosphere, their variability and extent to which they affect the radiative balance of the Earth's atmosphere.

1.3. Thesis aims

The overall aim of this thesis is to improve understanding of the climate effect of short-lived climate pollutants over the industrial era, with a view to assess their potential to mitigate anthropogenic climate change in the near-future. Several aspects of variability are investigated using a chemical transport model, in particular the response of simulated SLCPs to variations or modifications to emissions, together with the associated impact on climate via change in RF. One of the key aspects addressed here is the role of natural processes in causing trends and variations in concentrations of key SLCP species. The specific research aims undertaken in this thesis are:

1. **Investigate the effect of uncertainty in pre-industrial natural emissions on tropospheric ozone radiative forcing.** Revised inventories of pre-industrial emissions from wildfires and vegetation are used to simulate the uncertainty in pre-industrial tropospheric O_3 concentrations. The revised estimates of pre-industrial atmospheric composition are used to calculate new estimates of tropospheric O_3 RF, accounting for uncertainty in natural emissions.

2. **Evaluate the effect of the El Niño Southern Oscillation on the interannual variability of methane and tropospheric ozone.** The role of meteorology and fire emissions in driving interannual variability of important

SLCPs is quantified, particularly in response to large El Niño events such as the 1997-1998 El Niño. Specific mechanisms are identified and evaluated, and the impact of variability on climate from each driver is calculated for CH_4 and tropospheric O_3.

3. **Assess the influence of various future emissions scenarios on climate change and air quality in 2050.** Future emissions scenarios from the ECLIPSE project are used to simulate atmospheric concentrations of SLCPs in 2050, which are then evaluated for global and regional climate and air quality effects. The impact of individual emissions sectors is also evaluated to inform which specific mitigation techniques are the most beneficial, with calculations of global temperature change under each emission scenarios.

1.4. Thesis layout

This thesis consists of 7 chapters in total. Chapter 2 provides a background and literature review of the topics discussed throughout this thesis. Chapter 3 introduces the models used to conduct this study, detailing recent developments and evaluation against observational datasets. In Chapter 4, the effect of uncertainty of PI natural emissions on tropospheric O_3 RF is investigated, using revised PI fire and biogenic emission inventories. Chapter 5 explores the drivers of variability of CH_4 and tropospheric O_3, particularly during large El Niño events. Chapter 6 evaluates various future emissions scenarios for their effect on both climate and air quality, with particular attention to identifying important sectors and regions. In Chapter 7, the results from the thesis as a whole are summarised and discussed in terms of broader research goals and existing literature. The main results are then put into the context of the original thesis aims and suggestions are made for directions of future research.

2. Background

This chapter summarises background information on the major SLCPs discussed in this thesis, namely methane (CH_4), tropospheric ozone (O_3) and aerosols. A comprehensive understanding of the process controlling atmospheric concentrations of SLCPs, their role in atmospheric chemistry and anthropogenic climate change is essential in order to understand observed trends and fluctuations, and evaluate their potential for mitigation strategies.

2.1. Methane

Methane (CH_4) is a greenhouse gas with a global annual mean surface concentration estimated at 1858 ppb in 2018 (Dlugokencky, 2019). Atmospheric concentrations of CH_4 have more than doubled from 722 ppb in the PI, contributing an estimated radiative forcing (RF) of 0.48 ± 0.05 Wm^{-2} (Etheridge et al., 1998; Myhre et al., 2013b). RF is a measure of the effect on climate of a particular forcer, defined as the 1750 to present-day (PD) change in radiative flux at the tropopause after allowing for stratospheric temperature adjustment (Forster et al., 2007). The RF of CH_4 over the industrial era is the second largest greenhouse gas RF behind CO_2, accounting for approximately 17% of the RF from well-mixed greenhouse gases (WMGHG) (Myhre et al., 2013b). The PD CH_4 RF estimate of 0.48 Wm^{-2} has been consistent since the third IPCC assessment report (TAR). Etminan et al. (2016) calculated a RF due to CH_4 of 0.61 W^{-2}, a 25% increase compared to Myhre et al. (2013b). The increase is

Table 2.1 Estimated CH_4 radiative forcing, 20-year GWP and 100-year GWP in successive IPCC assessment reports.

	FAR (1990)	SAR (1995)	TAR (2001)	AR4 (2007)	AR5 (2013)
RF (Wm^{-2})	-	0.47	0.48	0.48 ± 0.05	0.48 ± 0.05
GWP20	63	56	62	74	84
GWP100	21	21	23	25	28

caused by the inclusion of the shortwave forcing due to CH_4 which is estimated at 0.1 Wm^{-2}.

On a molecule for molecule basis, CH_4 is a considerably more effective greenhouse gas than CO_2, however the greater abundance and longer lifetime of CO_2 means it is responsible for a much larger climate effect. The comparatively short atmospheric lifetime of CH_4 (i.e. 9.1 ± 0.9 years (Prather et al., 2012)), means that CH_4 has a relatively large impact over shorter time-periods. Global warming potential (GWP) is a calculation of the integrated warming effect of an emitted species over a given time period, relative to that of CO_2 (IPCC, 1990). Estimates of the 20-year GWP (GWP_{20}) of CH_4 have varied significantly since estimated at 63 in the IPCC First Assessment Report (FAR), rising to 84 by AR5 (Table 2.1). This means that per kilogram of emissions, the warming effect of CH_4 is 84 times greater than that of CO_2 over a 20-year period. The 100-year global warming potential (GWP_{100}) of CH_4 in the IPCC AR5 report was estimated at 28, however studies accounting for direct and indirect aerosol responses indicate this could rise to as much as 33 (Shindell et al., 2009; Myhre et al., 2013b).

The effect of CH_4 on climate is even larger when considered from an emission-based approach, due to its effect on tropospheric O_3, oxidation chemistry and stratospheric water vapour. When accounting for all these effects, CH_4 RF rises to 0.8—0.9 Wm^{-2}, up to 61% of the contribution due to CO_2 (Shindell et al., 2005; Shindell et al., 2009; Kirschke et al., 2013; Myhre et al., 2013b). The largest additional forcing in this estimates is due to the role of CH_4 in tropospheric O_3 production, another important anthropogenic greenhouse gas (see Section 2.2).

The large climate effect of CH_4, coupled with its relatively short atmospheric lifetime and the fact it is approximately homogeneously mixed in the troposphere, means CH_4 mitigation offers an important opportunity for near-term climate change mitigation. Studies indicate that implementation of measures to tackle CH_4 emissions could decrease warming by 0.28 ± 0.10°C by 2050, making it the most climatically important of the SLCPs (Fiore et al., 2012; Shindell et al., 2012). CH_4 mitigation also largely avoids the complicated and counteracting issue of co-emitted species which is often associated with SLCPs. Many short-lived climate forcers such as black carbon aerosols are frequently co-emitted with negative forcers such as sulphur and nitrate aerosols, which introduce an offset to the net benefit when emissions are cut (Fiore et al., 2012; Unger, 2012). CH_4 mitigation avoids this issue as emission sources generally do not have significant simultaneous aerosol emissions (Shindell et al., 2012; Stohl et al., 2015).

2.1.1. Sources and sinks

Atmospheric CH_4 has large anthropogenic and natural sources (Table 2.2). Global emissions estimates, particularly from natural sources, remain uncertain, with bottom-up and top-down estimates varying by as much as 200 Tg yr^{-1} (Saunois et al., 2016). The magnitude of natural emission sources is more uncertain than anthropogenic sources, with wetland emissions in particular poorly constrained. Despite the large uncertainties, anthropogenic emissions since the pre-industrial era lead to an imbalance in the atmospheric CH_4 budget, resulting in a net increase in CH_4. As a result the global CH_4 burden is estimated to be increasing by 6-14 Tg yr^{-1} on average (Saunois et al., 2016). The large uncertainty makes attribution of trends to particular source or sink changes especially difficult. Improved satellite retrievals and continuous surface monitoring is required to reduce uncertainty in emission estimates (Van Amstel, 2012). While the rise in global mean CH_4 concentrations since the PI has been driven by increasing anthropogenic emissions, particularly from fossil fuel burning and agriculture, natural emission sources play the dominant role in regulating the interannual variability of atmospheric CH_4 concentrations (Ciais et al., 2013).

Table 2.2 Sources and sinks of global atmospheric methane, 2010-2015. Adapted from Saunois et al. (2016), using estimates from Kirschke et al. (2013), Hossaini et al. (2016), McNorton et al. (2016) and Maasakkers et al. (2019).

Natural sources	**Source (Tg CH_4 yr^{-1})**	**Range**
Wetlands	185	153-227
Fresh water	122	60-180
Geological	40	30-56
Oceanic (including hydrates)	14	5-25
Wild animals	10	5-15
Termites	9	3-15
Wildfires	3	1-5
Permafrost	1	0-1
Total natural source	**384**	**257-524**
Anthropogenic sources	**Source (Tg CH_4 yr^{-1})**	**Range**
Fossil fuels	121	114-133
Agriculture	106	97-111
Landfills and waste	59	52-63
Rice cultivation	36	24-36
Biomass burning	18	15-21
Biofuel burning	12	10-14
Total anthropogenic source	**352**	**340-360**
Sinks	**Sink (Tg CH_4 yr^{-1})**	**Range**
Reaction with OH	475	454-617
Reaction with Cl	25	12-37
Stratospheric loss	51	16-84
Soil	32	9-47
Total sink	**570**	**491-785**

The largest natural source of CH_4 emissions is from terrestrial wetlands (Table 2.2). In anaerobic environments, microorganisms known as methanogens consume H_2 and CO_2 to release CH_4, in a process called methanogenesis (Le Mer and Roger, 2001). The largest permanent wetlands are found in the Amazon basin and Pantanal in South America, the Congo and Zambezi river basins in sub-Saharan Africa and in South-East Asia (Nisbet et al., 2019). As the largest single CH_4 source, albeit with a large uncertainty and sensitivity to climate variables including temperature and precipitation (Le Mer and Roger, 2001), natural wetlands emissions are the dominant source of CH_4 interannual variability (Bousquet et al., 2006; Hodson et al., 2011; McNorton et al., 2016b). Fire emissions are also thought to play a role (Bousquet et al., 2006), despite being a relatively minor source of atmospheric CH_4. Although the amount of CH_4 emitted per unit area burned varies greatly between fire types - with peat fires emitting around 10 times more CH_4 per unit biomass burned than savanna fires (van der Werf et al., 2010) – wildfires emit a relatively very small amount of CH_4 compared to species such CO or CO_2 (Table 2.2). As a result, the influence of fires on background CH_4 variability is thought to be small relative to the effect of wetlands. Infrequent events such as volcanic eruptions and the El Niño-Southern Oscillation can occasionally cause large changes to atmospheric composition, affecting CH_4 variability, although the exact mechanism and magnitude remains uncertain (Hodson et al., 2011; Bândă et al., 2016). Increased understanding of what causes interannual variations in CH_4 will

Table 2.3 Global mean annual fire emission estimates (in Tg) for carbon dioxide (CO_2), carbon monoxide (CO), methane (CH_4), nitrogen oxides (NO_x), organic carbon (OC), black carbon (BC) and total particulate matter (TPM) from GFEDv3, FINNv1 and GFAS. Adapted from Voulgarakis and Field (2015).

	CO_2	CO	CH_4	NO_x	OC	BC	TPM
GFEDv3 (2003–2011)	6508	329	17	9	18	2.0	44
FINNv1 (2005–2010)	7323	373	18	13	23	2.2	59
GFAS (2003–2008)	6907	352	19	10	18	2.0	45

improve future projection of CH_4 concentrations and the effect on climate. This is investigated in greater detail in Chapter 5.

The primary sink of CH_4 is via its reaction with the hydroxyl radical (OH) (reaction (2.1), which is responsible for ~90% of atmospheric CH_4 lost and therefore is the primary determining factor in calculations of CH_4 atmospheric lifetime. The OH radical is highly reactive, being responsible for the oxidation and removal of many atmospheric pollutants. Relatively minor changes to global OH concentrations can substantially affect CH_4 variability, and may explain observed trends in recent decades (McNorton et al., 2016a; Dlugokencky, 2019).

$$CH_4 + OH \xrightarrow{k_{OH}} CH_3 + H_2O \quad (2.1)$$

2.1.2. Effect on air quality

Due to the contribution of CH_4 to the formation of the greenhouse gas tropospheric O_3 (see Section 2.2.1), CH_4 emissions also indirectly affect the climate while also playing an important role in global air quality. Tropospheric O_3 has a positive RF of 0.4 Wm^{-2} (Myhre et al., 2013b), and is also a pollutant which is damaging to both human health and vegetation (UNEP, 2011; see Section 2.2). Action to decrease CH_4 emissions will also decrease tropospheric O_3 concentrations, indirectly decreasing the impact of tropospheric O_3 on both climate and human health (Anenberg et al., 2012; Shindell et al., 2012; West et al., 2013). The lifetime of CH_4, though short relative to other GHGs, is long relative to other precursors of tropospheric O_3, and long enough that CH_4 concentrations can be broadly considered globally homogeneous. Thus, mitigation of CH_4 emissions will decrease global tropospheric O_3 production on a timescale of around one decade, offering a “unique opportunity to improve air quality globally” (West et al., 2013).

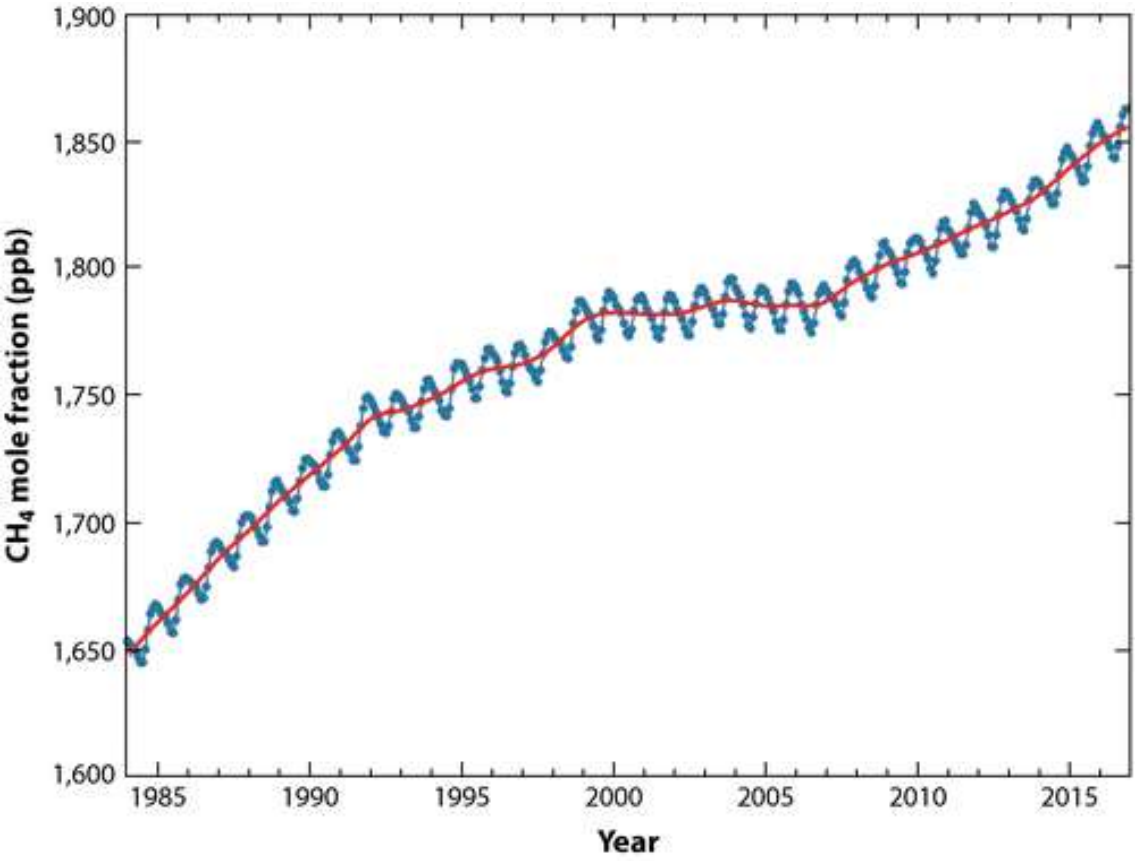

Figure 2.1 Globally averaged methane (CH_4) mole fraction in the atmosphere from 1984 to 2016. The red line is the deseasonalised monthly mean mole fraction. The blue dots and line depict the monthly averages. From Reay et al. (2018), Figure 2.

2.1.3. Recent trends in atmospheric methane

Atmospheric CH_4 concentrations have increased considerably over the industrial era due to anthropogenic emissions, however the growth rate has not been stable. In recent decades, changes in atmospheric CH_4 has been characterised by rapid growth in the late 20th century, followed by a period of stagnation from 1999-2006, before renewed growth from 2007-2019 (Rigby et al., 2008) (Figure 2.1). Due to the uncertainty in emissions and their variability, the exact cause of observed trends is not fully understood (Turner et al., 2019). During the 1998-2006 slowdown in CH_4 growth rate, Dlugokencky et al. (2003) suggested that the observed slow-down could be a result of the CH_4 budget reaching a steady-state. However, increased growth rates from 2007 onwards

indicate that this was not the case, but the result of CH_4 sink or source fluctuations.

Various mechanisms have been suggested as the cause of the irregular growth in atmospheric CH_4. Anthropogenic emissions have been shown to have increased year-on-year even during periods of slow growth (Olivier et al., 2005), indicating that natural emissions are the more likely driver. Decreases in wetland CH_4 emissions between 1999 and 2006 are thought to be a contributor to the stagnating growth rates (Bousquet et al., 2011). Pison et al. (2013) however, found large uncertainty in the role of wetland emissions, while Poulter et al. (2017) found that fluctuations in wetlands emissions could not explain the observed trends. Variations in OH concentrations, the dominant atmospheric sink of CH_4, are also very likely to play a key role. McNorton et al. (2016a) and Turner et al. (2017) found that increased OH concentrations were the largest component in decreasing CH_4 growth rate, with additional contribution from atmospheric transport changes.

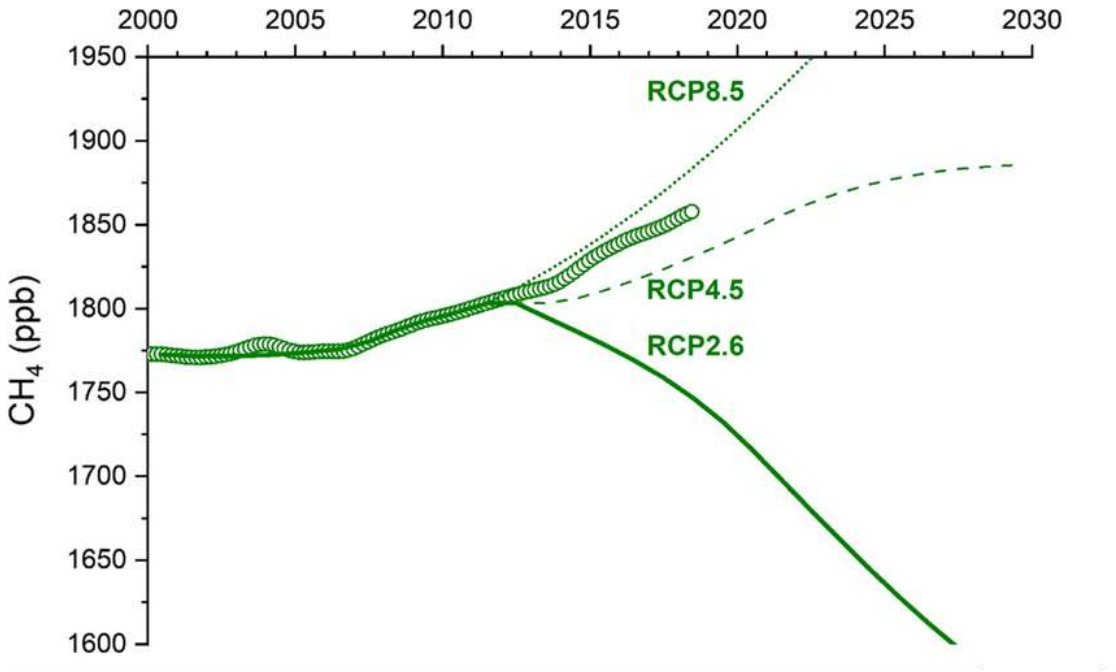

Figure 2.2 Observed global average CH_4 (green circles) at 3-monthly intervals from 2000 to 2018 (NOAA) compared to CH_4 in RCPs used in climate models (green lines). From Nisbet et al. (2019), Figure 6.

Following the 1999-2006 slow-down in the global atmospheric CH_4 growth rate, accelerated growth has been observed in the past decade (Nisbet et al., 2019). This increase conflicts with optimistic future emissions scenarios such as the Representative Concentrations Pathway 2.6 (RCP2.6). Such stringent emissions scenarios may have been capable of meeting 1.5 or 2°C targets outlined in accords such as the 2015 Paris Agreement, however RCP2.6 requires decreasing global CH_4 burden from 2010 onwards (Meinshausen et al., 2011). By 2018, global mean atmospheric CH_4 concentrations were more than 100ppb larger than the RCP2.6 projection, closer to the less desirable RCP8.5 scenario (Figure 2.2) (Nisbet et al., 2019).

The recent growth rate increase has coincided with a decline in the $^{12}C/^{13}C$ isotopic ratio. This indicates either an increase in emissions from microbial sources (Schaefer et al., 2016; Nisbet et al., 2019), large increases in natural gas and oil emissions (Hausmann et al., 2016), a decrease in the oxidation capacity of the atmosphere (Turner et al., 2017; Nisbet et al., 2019), or some combination of these effects. An observed change in the atmospheric ethane/CH_4 ratio, may point to increases in fossil fuel emissions of CH_4 as the primary driver of recent increases in CH_4 concentrations (Helmig et al., 2016; Worden et al., 2017). Worden et al. (2017) re-evaluated fossil fuel and biogenic CH_4 emissions since 2007, estimating lower biomass burning emissions than in

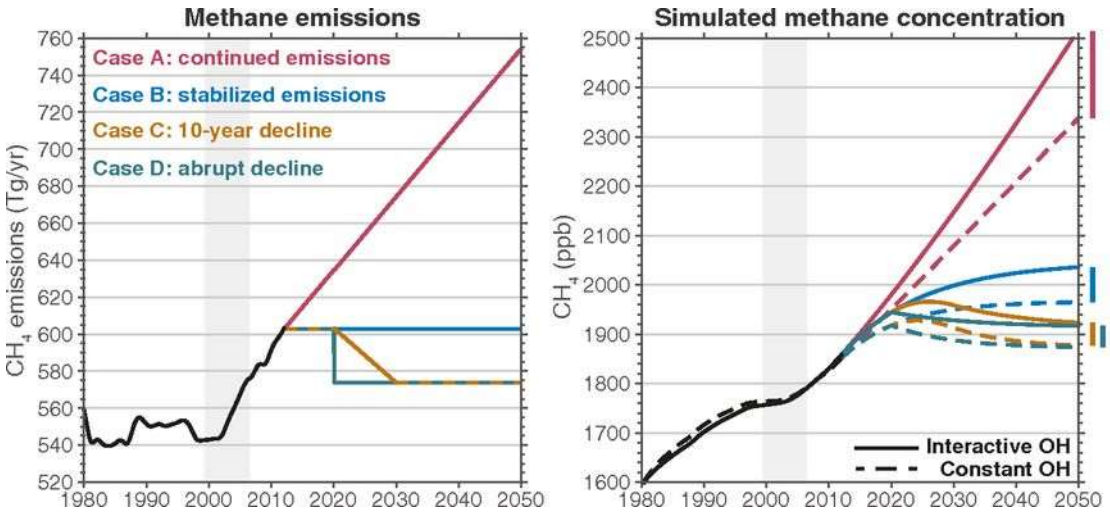

Figure 2.3 Projections of CH_4 emissions (left) and atmospheric CH_4 concentrations (right) under four different emission scenarios. From Turner et al. (2019), Figure 3 .

previous studies, and concluding that increases in fossil fuel emissions were needed to explain the observed changes to concentrations and isotopic composition. Increases in anthropogenic CH_4 emissions have been observed from China and India (Maasakkers et al., 2019), although Rigby et al. (2017) suggest that OH changes are also likely causes of the increase in growth rate. The current observational network is insufficient to fully quantify the various drivers of CH_4 growth rate change.

While it is clear that decreasing anthropogenic emissions of CH_4 will lead to decreasing global CH_4 concentrations, it is important to note that due to the approximately decadal lifetime of CH_4, it would be several decades before such measures substantially reduce CH_4 concentrations (Figure 2.3) (Turner et al., 2019). The lag time associated with CH_4 is larger than other SLCP species, moderating the benefit of CH_4 emission changes for several decades following implementation.

2.2. Tropospheric ozone

Ozone (O_3) is a greenhouse gas formed from photochemical reactions in the atmosphere (see Section 2.2.1). O_3 is present in high concentrations in the stratosphere, forming an O_3 layer which prevents dangerous, high-energy ultra-violet (UV) radiation from reaching the surface where it can cause skin cancer (Diffey, 2003) and damage vegetation (Tevini and Teramura, 1989). However O_3 is also present as a trace gas in the troposphere, where it is an air pollutant and contributes to anthropogenic climate change. Although O_3 is not directly emitted by anthropogenic activity, many of its precursors have important anthropogenic sources. Anthropogenic emissions have increased tropospheric O_3 burden by approximately 40% since 1850 (Yeung et al., 2019), therefore it is classified as an anthropogenic greenhouse gas. Stevenson et al. (2013) estimate that the increase in tropospheric O_3 concentrations since the PI was primarily caused by emissions of CH_4 (44 ± 12%) and NO_x (31 ± 9%), with smaller contributions from CO (15 ± 3%) and non-methane volatile organic compounds (NMVOCs) (9 ± 2%). Stratospheric O_3 however has decreased as

a result of anthropogenic activity, resulting in a cooling effect on climate (Figure 2.4).

Tropospheric O_3 is the 3rd most important anthropogenic greenhouse gas behind CO_2 and CH_4, with an estimated RF of 0.4 (0.2-0.6) Wm^{-2} (Myhre et al., 2013b; Stevenson et al., 2013). Despite a number of dedicated studies, the estimated PI to PD O_3 RF and uncertainty range in IPCC reports has remained unchanged since the second assessment report (SAR). The uncertainty is due in large part to a lack of understanding of PI tropospheric O_3. O_3 is not stable in ice or snow so proxy records are not available, and the accuracy and coverage of early measurements is limited (Volz and Kley, 1988; Cooper et al., 2014). PI O_3 uncertainty and its effect on O_3 RF estimates is the subject of investigation in Chapter 4.

The RF due to O_3 is more spatially variable than other important greenhouse gases due its short atmospheric lifetime of a few hours in polluted regions, to

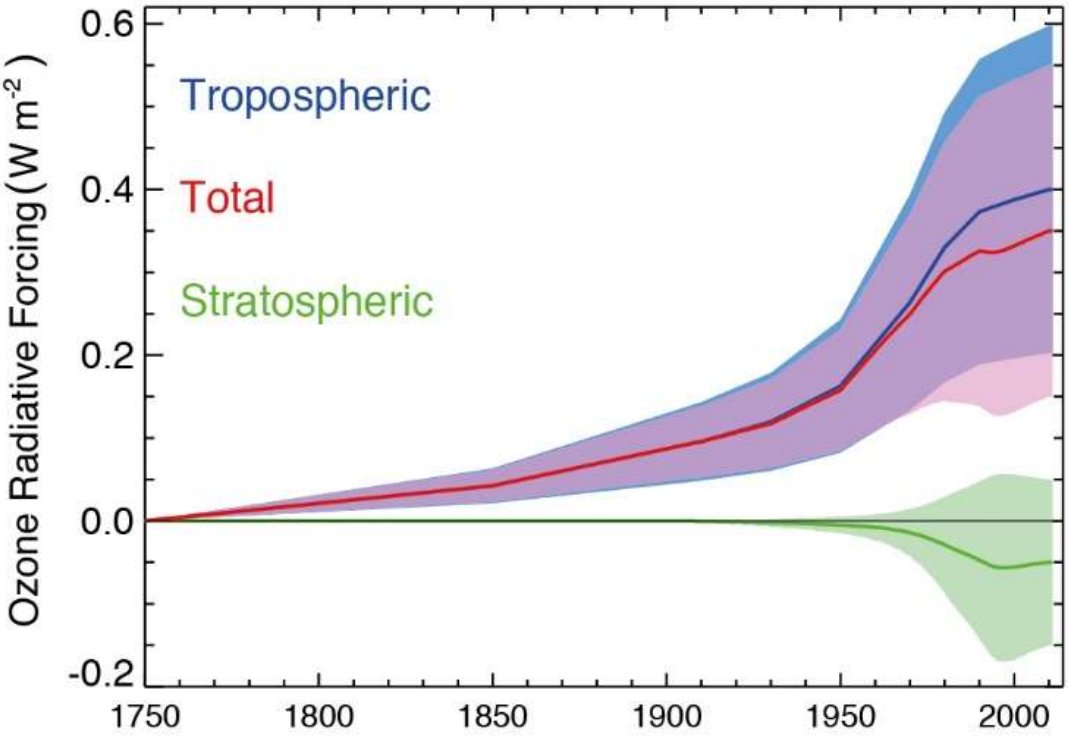

Figure 2.4 Time evolution of the radiative forcing from tropospheric and stratospheric ozone from 1750 to 2010. Tropospheric ozone data are from Stevenson et al. (2013) scaled to give 0.40 Wm^{-2} at 2010. From Myhre et al. (2013b), Figure 8.7.

several weeks in the free troposphere (Young et al., 2013; Monks et al., 2015). Despite its short lifetime, tropospheric O_3 contributes substantially to the total anthropogenic RF (Myhre et al., 2013b), therefore action to decrease tropospheric O_3 concentrations would be beneficial for near-term climate mitigation (UNEP, 2011; UNEP and WMO, 2011). The long lifetime of CH_4 relative to other O_3 precursors means it is the dominant influence on global background concentrations of tropospheric O_3 (West et al., 2006). Therefore if the primary strategy for lowering O_3 concentrations is through tackling CH_4 emissions, mitigation would take approximately a decade in line with the lifetime of CH_4 (West et al., 2006).

2.2.1. Formation

O_3 is present in the troposphere through transport from the stratosphere and through in-situ photochemical production by photolysis of NO_2:

$$NO_2 + h\nu \rightarrow NO + O \qquad (\lambda < 420\ nm) \tag{2.2}$$

$$O + O_2 + M \rightarrow O_3 + M \tag{2.3}$$

Tropospheric O_3 can then be rapidly removed through reaction with NO, creating a null cycle with net zero O_3 production.

$$O_3 + NO \rightarrow NO_2 + O_2 \tag{2.4}$$

For tropospheric O_3 to be formed an alternative source of NO_2 is required. An additional source of NO_2 can form from peroxy radicals, which may be produced by the oxidation of CH_4:

$$CH_4 + OH \rightarrow CH_3 + H_2O \tag{2.5}$$

$$CH_3 + O_2 + M \rightarrow CH_3O_2 + M \tag{2.6}$$

$$CH_3O_2 + NO \rightarrow CH_3O + NO_2 \tag{2.7}$$

And through the oxidation of carbon monoxide (CO):

$$CO + OH \rightarrow H + CO_2 \quad (2.8)$$

$$H + O_2 + M \rightarrow HO_2 + M \quad (2.9)$$

$$HO_2 + NO \rightarrow OH + NO_2 \quad (2.10)$$

Reactions (2.5) - (2.10) show the primary ways in which peroxy radicals are formed from anthropogenically emitted species. Other volatile organic compounds (VOCs) produce peroxy radicals through similar reactions to that shown for CH_4. In highly NO_x polluted urban environments the loss of O_3 by reaction (2.4) dominates and depletes tropospheric O_3, a process known as O_3 titration (Figure 2.5) (Sillman et al., 1990). As a result, decreases in NO_x emissions in a NO_x-saturated regime may actually increase tropospheric O_3 concentrations by reducing the O_3 titration effect (Jin and Holloway, 2015).

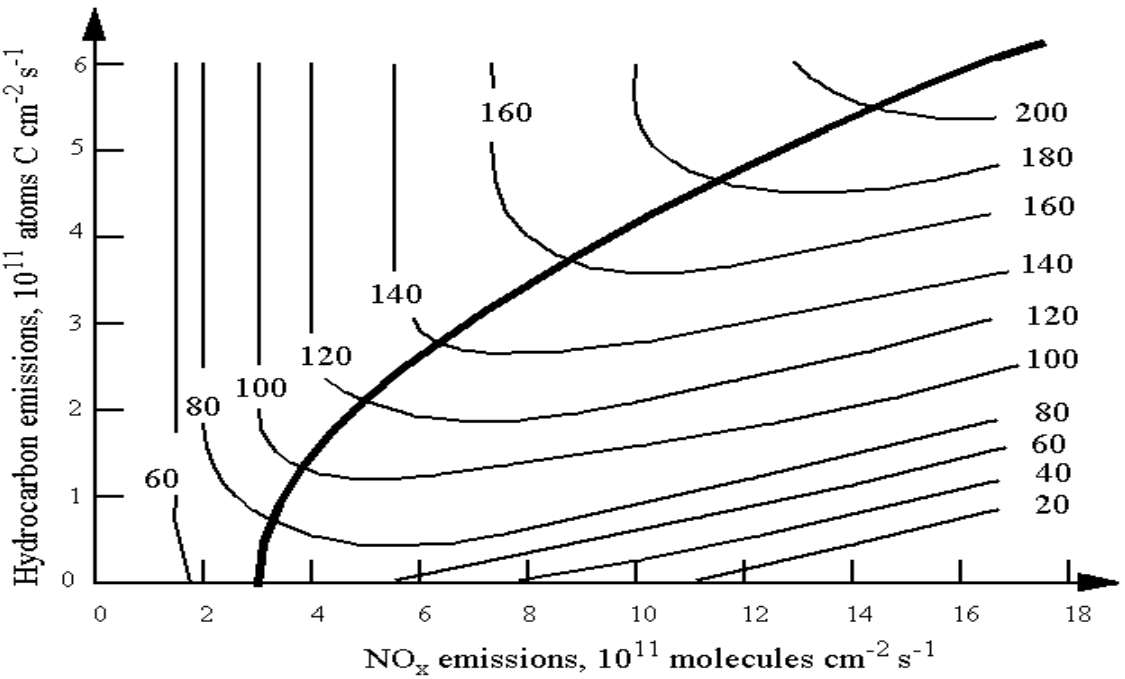

Figure 2.5 O_3 concentrations (ppbv) simulated by a regional photochemical model as a function of NO_x and hydrocarbon emissions. The thick line separates the NO_x-limited (top left) and hydrocarbon-limited (bottom right) regimes. Adapted from Sillman et al. (1990).

Due to the availability of precursor species, the production of tropospheric O_3 is greatest in the lower troposphere. However, deep convention can transport NO_x into the upper troposphere where O_3 production efficiency is up to 20 times higher than at the surface, enhancing in-situ production (Wild and Akimoto, 2001). This process is particularly important for climate as the radiative efficiency of O_3 is up to 10 times higher in the upper troposphere than elsewhere in the troposphere (Rap et al., 2015).

In a non-polluted environment, the formation of tropospheric O_3 is limited by NO_x availability, as the short atmospheric lifetimes of NO and NO_2 result in low concentrations away from emissions sources. However, the formation of peroxyacetylnitrate (PAN) ($CH_3CO_3NO_2$) can allow transport of reactive nitrogen to remote regions, enabling tropospheric O_3 formation. PAN can be formed from oxidation of non-methane hydrocarbons:

$$Hydrocarbons + O_2 + NO_2 + hv \rightarrow CH_3CO_3NO_2 \quad (2.11)$$

The atmospheric lifetime of PAN is just a few hours at the surface, but extends to several months in the upper troposphere (Tereszchuk et al., 2013). In areas of deep convection PAN can be lifted into the free troposphere where it is stable due to the low temperatures and can be transported large distances, making it a reservoir species for NO_x (Moxim et al., 1996). At sufficiently high temperatures PAN decomposes to release NO_2 back into the atmosphere, allowing O_3 formation to occur in-situ in non-polluted regions (Wild, 2007).

Like CH_4, CO and VOCs have both natural and anthropogenic sources, creating concentrations well above background levels in polluted areas, often coinciding with NO_x emissions, allowing net production of tropospheric O_3. Hence, the production of tropospheric O_3 is controlled by anthropogenically emitted precursors, making tropospheric O_3 an anthropogenic greenhouse gas (UNEP, 2011).

2.2.2. Sources and sinks

Due to the abundance of O_3 in the stratosphere, it was long believed that the majority of tropospheric O_3 originated in the stratosphere (Junge, 1962), until Chameides and Walker (1973) proposed photochemical oxidation of CH_4 as a large in-situ source. PD estimates indicate that approximately 90% of tropospheric O_3 is produced through oxidation of CO and hydrocarbons in the presence of NO_x, compared to <10% from stratospheric transport (Hu et al., 2017). Figure 2.6 shows the major sources and sinks of tropospheric O_3 and its precursors. The presence of NO_x is vital for the net production of tropospheric O_3. Atmospheric NO_x has numerous anthropogenic and natural emission sources. The anthropogenic source, primarily from burning of fossil fuels in transport and energy production (Table 2.4), is the largest component, responsible for an estimated 75% of total global NO_x emissions (Monks et al., 2017). Anthropogenic NO_x emissions increased rapidly in the second half of the 20th century, as shown in Figure 2.8 (Hoesly et al., 2018), almost doubling from approximately 68 Tg in 1970 to 122 in 2012 (Crippa et al., 2018). Although global NO_x emissions have been increasing since the PI, more economically developed

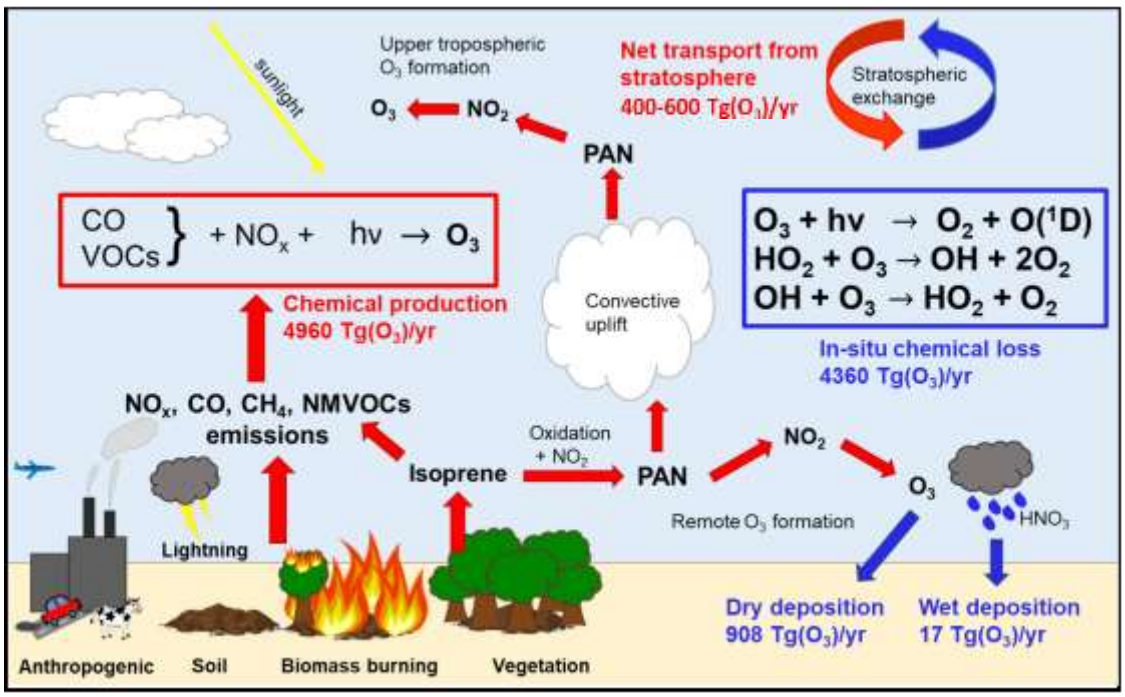

Figure 2.6 Summary schematic showing the sources, sinks and budget (in Tg ozone yr^{-1}) of tropospheric ozone. Stratosphere-tropospheric exchange range is from Yang et al. (2016). All other O_3 budget values are from Hu et al. (2017).

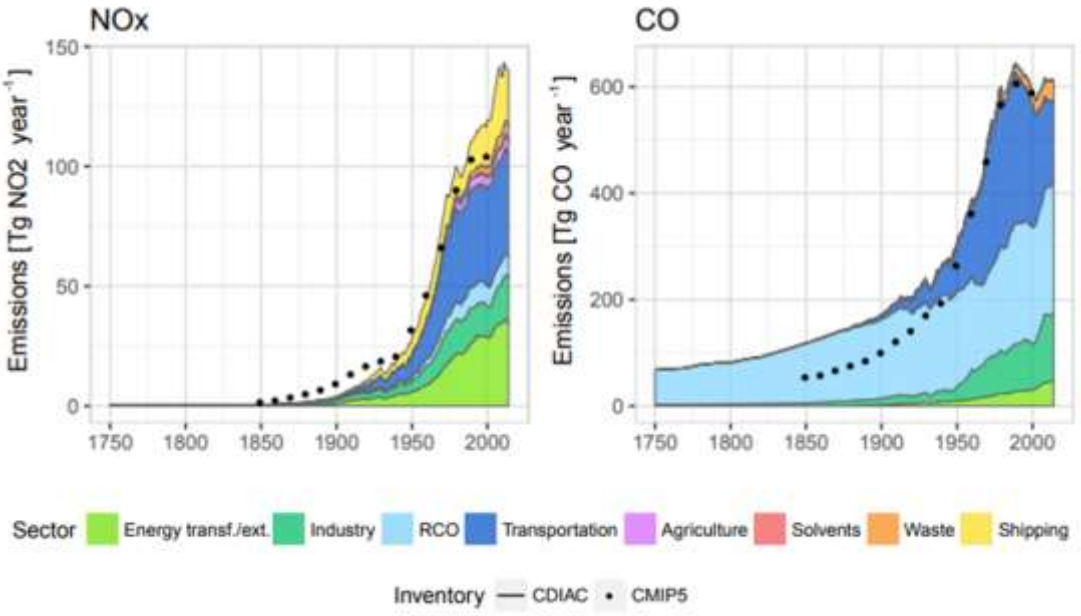

Figure 2.7 Time series of global anthropogenic NO_x (left) and CO (right) emissions by aggregate sector. Data from Community Emissions Data System (CEDS), compared with CMIP5 (Lamarque et al. (2010) (dots) and Carbon Dioxide Information Analysis Center (CDIAC) (line). Figure adapted from Hoesly et al. (2018).

regions such as North America and Europe have seen decreasing NO_x emissions since the 1990's (Figure 2.8) (Crippa et al., 2018). The growth in total emissions in recent decades is largely due to substantial increases in emissions from India and China in the early 21st century, which has resulted in enhanced tropospheric O_3 concentrations (Verstraeten et al., 2015; Silver et al., 2018). However, recent evidence from satellite observations indicates that total global NO_x emissions have been stable since 2005 (Miyazaki et al., 2017).

NO_x is also emitted from natural sources. Bacteria in soils emit NO_x through denitrification. This was previously thought to be a relatively minor source of NO_x, estimated at 5 Tg in Yienger and Levy (1995). More recent studies estimate much larger annual soil NO_x emission, i.e. Vinken et al. (2014) calculated a 9-16.8 Tg source, while Hudman et al. (2012) estimate a source of 10.7 Tg NO_x. Wildfires and biomass burning also emit NO_x into the troposphere, a source estimated at 9-13 Tg NO_x yr^{-1} in various global fire inventories (Table 2.3) (Voulgarakis and Field, 2015). The high temperatures associated with a lightning strike cause the reaction of N_2 with O_2, forming NO_x. The size of this source is

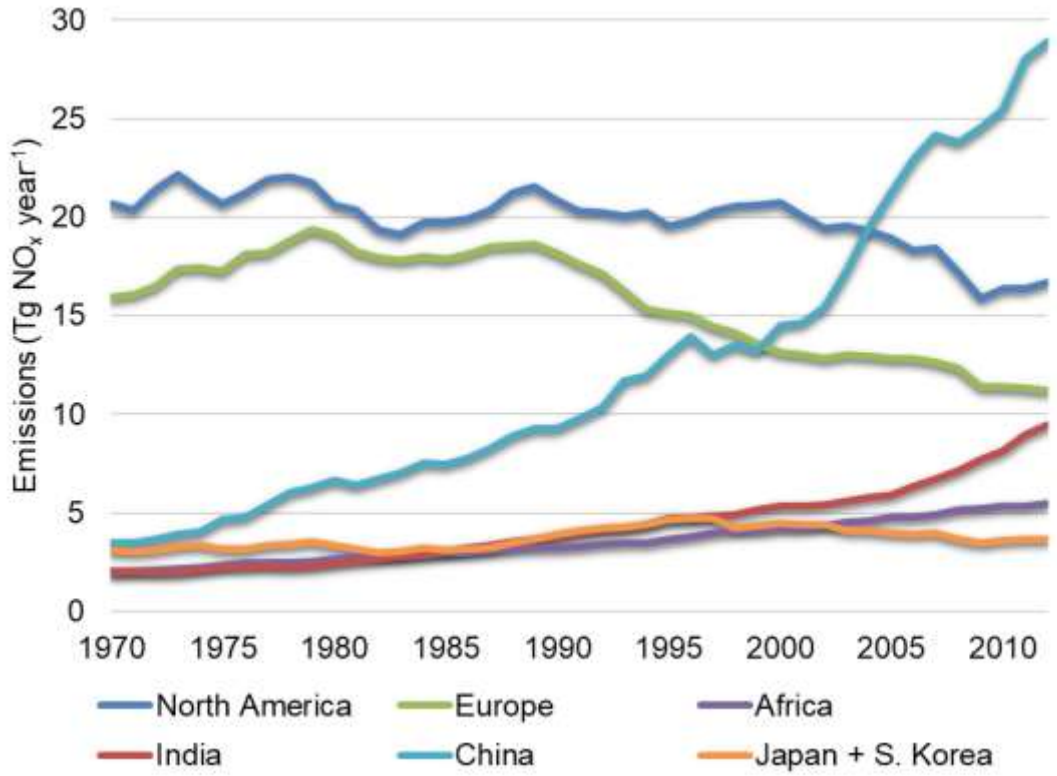

Figure 2.8 Time-series of anthropogenic NO_x emissions from key emission regions, 1970-2012. Data from EDGAR v4.3.2 (Crippa et al., 2018).

one of the largest uncertainties in the atmospheric NO_x budget, adding 2-8 Tg NO_x per year (Schumann and Huntrieser, 2007). A study by Finney et al. (2018) suggests that in a future climate lighting is likely to decrease, reducing the NO_x source. Lightning is thought to be a particularly significant source in the upper troposphere as only a fraction of NO_x emitted at the surface reaches the higher altitudes (WMO, 1999; Finney et al., 2016).

Table 2.4 shows the global atmospheric CO budget and uncertainty ranges estimated from recent studies. Like NO_x, CO has a range of natural and anthropogenic sources, with the anthropogenic source thought to be the largest component (Zhong et al., 2017). In terms of direct emissions, transport-related fossil fuel burning, residential biofuel use and agricultural burning are the largest contributors (Olivier et al., 1999). However the largest source of CO is oxidation of CH_4 by OH, accounting for ~30-40% of the total global source.

Volatile organic compounds (VOCs) are reactive compounds emitted to the atmosphere which can influence the production of tropospheric O_3. CH_4 is often

excluded when considering the role of VOCs in the atmosphere due to its abundance and importance for climate – here, CH_4 is discussed in detail in

Section 2.1. NMVOCs are emitted from anthropogenic activity, fires, oceans and vegetation Table 2.5. The largest VOCs in terms of anthropogenic contribution are aromatics such as toluene (C_7H_8) and benzene (C_6H_6) (Huang et al., 2017). Formaldehyde (HCHO) is an important NMVOC which affects the oxidising capacity of the atmosphere (Lelieveld and Crutzen, 1990), although has relatively small surface emissions as it is largely formed through CH_4 or isoprene (C_5H_8) oxidation (Stavrakou et al., 2009). Biogenic emissions also contribute to the source of NMVOCs which act as tropospheric O_3 precursors. The total annual global emission of biogenic volatile organic compounds (BVOCs) is uncertain, with estimates generally ranging from 450-650 Tg (Sindelarova et al.,

Table 2.4 Global atmospheric CO budget, 2000–2017. Best estimates are taken from Yin et al. (2015) unless indicated otherwise, ranges are taken from upper and lower limits across various studies (Olivier et al., 1999; Ehhalt et al., 2001; Zhong et al., 2017; Crippa et al., 2018).

Direct emission sources	**Source (Tg CO yr^{-1})**	**Range**
Anthropogenic	588	530-700
Biomass burning	327	300-700
Oceanic	20[a]	20-54
Biogenic	90[b]	82-97
Total direct emission source	1025	932-1551
In-situ oxidation sources		**Range**
CH_4 oxidation	885	778-900
NMVOC oxidation	335	175-430
Total oxidation source	1220	953-1330
Total source	**2245**	**1885-2881**
Sinks	**Sink (Tg CO yr^{-1})**	**Range**
Reaction with OH	2197	1920-2600
Surface deposition	190[c]	190-294
Total sink	**2387**	**2110-2894**

[a] Ocean CO emission estimate from **Duncan et al. (2007a)**.
[b] Biogenic CO emission estimate from Sindelarova et al. (2014).
[c] Surface deposition CO sink estimates from Hauglustaine et al. (1998).

2014; Messina et al., 2016). The most abundant biogenically emitted volatile organic compound (BVOC) is isoprene, making up ~70% of all global BVOC emissions, with monoterpenes accounting for ~11% and methanol ~6% (Sindelarova et al., 2014). Isoprene and monoterpenes also have the highest photochemical O_3 creation potential (POCP) of all VOCs (Huang et al., 2017).

2.2.3. Effect on air quality

Tropospheric O_3 at the Earth's surface is an air pollutant, detrimental to human health and vegetation. Air pollutant exposure increases the risk of developing health problems, which, although do not lead directly to fatalities, may lead to premature deaths. Such health conditions can have multiple causes and individuals may have varying susceptibility, making it extremely difficult to attribute individual deaths to specific causes. As a result, the global mortality rate from pollutants such as tropospheric O_3 is difficult to estimate (Lelieveld et al., 2015; Stewart and Hursthouse, 2018). Health functions have been developed from numerous cohort studies which are able to identify a causal link between pollution and health, and can subsequently be used to estimate the expected premature mortality from a known exposure to pollution (Glass et al., 2013; Zigler and Dominici, 2014). The Global Burden of Diseases, Injuries and

Table 2.5 Annual global MVOC emissions by source, as used in the TOMCAT chemical transport model. Adapted from Monks et al. (2017).

Species	Anthropogenic	Fires	Biogenic	Oceans	Total
Ethene	6.81	2.84	16.70	1.40	27.75
Ethane	6.34	1.67	0.14	0.98	9.14
Propene	3.04	1.57	6.10	1.52	12.23
Propane	5.68	0.38	0.02	1.30	7.37
Toluene	25.34	10.66	0.26	-	36.26
Butane	12.38	0.60	-	-	12.98
Formaldehyde	2.99	4.13	4.03	-	11.15
Acetone	0.54	1.86	28.58	-	30.98
Acetaldehyde	2.00	4.55	11.20	-	17.75

Risk Factors study (GBD) estimated that tropospheric O_3 exposure was responsible for 233,638 premature deaths due to chronic obstructive pulmonary disease (COPD) in 2016 (Gakidou et al., 2017). Other estimates put the number of respiratory mortalities due to O_3 at 700,000 ± 300,000 (Anenberg et al., 2010). As well as respiratory diseases, O_3 exposure has also been associated with circulatory and cardiovascular mortality, reproductive and developmental effects, and central nervous system effects (Jerrett et al., 2009; Atkinson et al., 2016; Turner et al., 2016). The risk estimates used in the GBD study were updated by Turner et al. (2016), leading to mortality estimates 200% higher than the GBD estimates over India (Conibear et al., 2018). Recent studies estimate that 39% of the global mortality due to long-term O_3 exposure occurs in India (Gakidou et al., 2017).

In addition to human health impacts, O_3 pollution also damages vegetation by reducing photosynthesis assimilation, decreasing gross primary productivity (GPP) (Krupa and Manning, 1988). The uptake of O_3 by stomata varies depending on O_3 concentrations, vegetation type and meteorological conditions (Ashmore, 2005). Once exposed to O_3, vegetation damage and decreasing plant productivity occurs through five primary processes: membrane damage, lower photosynthesis due to reduced rubisco enzyme, reduced distribution of carbohydrates, disruption of signalling pathways, and elevated senescence occurrence (Fuhrer and Booker, 2003). Ambient O_3 levels in the PD are estimated to decrease total biomass of trees by 7% compared to PI conditions (Wittig et al., 2009). Studies over Europe estimate that O_3 pollution decreases gross primary production (GPP) by 22-30% (Anav et al., 2011; Proietti et al., 2016). This effect on productivity inhibits the global land-carbon sink by decreasing uptake of CO_2 by vegetation, allowing more CO_2 accumulation and adding an additional indirect RF due to tropospheric O_3. The RF due to the indirect effect of O_3 decreasing GPP is estimated to be between 0.62 Wm^{-2} and 1.09 Wm^{-2} by 2100 (Sitch et al., 2007). The global cost of tropospheric O_3 damage to crops was estimated by Avnery et al. (2011a) to be $11-18 billion, expected to rise to $17-35 billion by 2050 (Avnery et al., 2011b). When including the impact of health costs, it is estimated that the cost of O_3 pollution will reach $580 billion by 2050 (Selin et al., 2009).

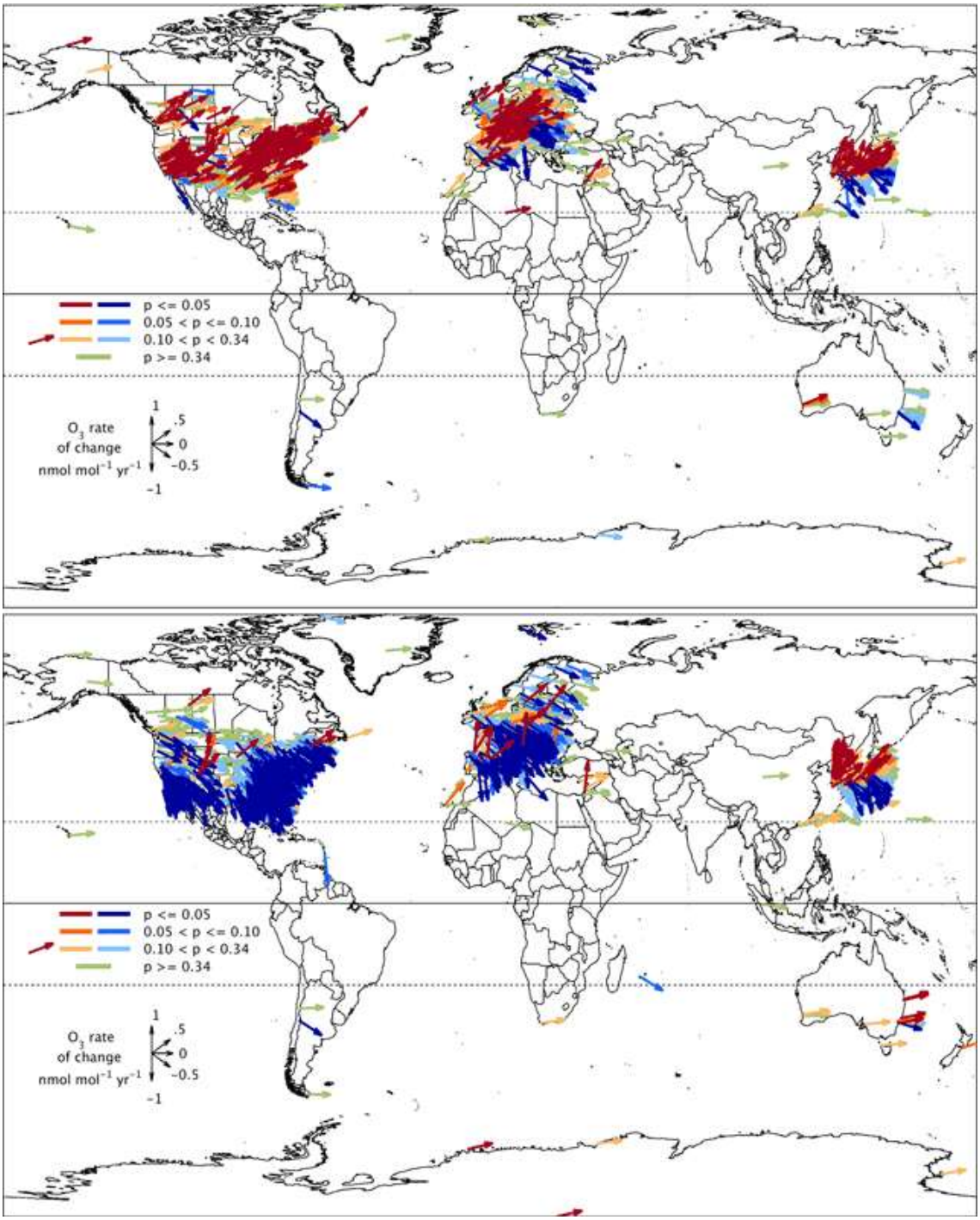

Figure 2.9 2000–2014 trends of daytime average O_3 (nmol mol^{-1} yr^{-1}) at 1375 non-urban sites in December–January–February (top) and 1784 non-urban sites in June–July–August (bottom). The number of available sites is greater in June–July–August because many US sites only operate in the warm season. Vector colours indicate the p-values on the linear trend for each site: blues indicate negative trends, oranges indicate positive trends and green indicates weak or no trend; lower p-values have greater colour saturation. From Gaudel et al. (2018), Figure 13.

2.2.4. Recent trends in tropospheric ozone

The uncertainty in PI O_3 concentrations makes the long-term trend in concentrations difficult to estimate (Cooper et al., 2014; Young et al., 2018). Since the 1970s however, monitoring of global tropospheric O_3 has been made possible through satellite measurements and an improving network of global monitoring stations (Schultz et al., 2017). In general, global tropospheric O_3 concentrations increased between 1970 and 2000, although from the 1990's regional emissions in the USA and Europe stabilised or began to decline (Cooper et al., 2014). In the 21st century, North America and European concentrations of O_3 have largely plateaued, although there is evidence of increasing concentrations in winter (Figure 2.9), and in upper tropospheric O_3 (Gaudel et al., 2018). In developing nations, particularly India and China, there have been large increases in surface O_3 concentrations in recent years, driven by increased anthropogenic emissions of VOCs (Sun et al., 2016; Silver et al., 2018).

2.3. Aerosols

Aerosols are defined as solid or liquid particles suspended in the atmosphere, usually with a diameter of 2 nm to 10 µm (McNeill, 2017). Aerosols have anthropogenic and natural sources and influence the Earth's climate in a number of ways. The net RF of aerosols remains one of the largest uncertainties in the global energy budget (Boucher et al., 2013). The total aerosol effective RF (a development of RF which accounts for rapid adjustments – see Section 3.6.1) is estimated at -0.9 Wm^{-2}, with an uncertainty range of -0.1 to -1.9 Wm^{-2} (Figure 1.1) (Myhre et al., 2013b). Although a smaller, 'likely' uncertainty range is also estimated by the IPCC (-0.4 to -1.5 Wm^{-2}), the uncertainty of aerosol RF is very large (Myhre et al., 2013b). The estimated uncertainty has not improved significantly in recent IPCC reports, and is largely due to differences in modelled RF (Myhre et al., 2013b). Uncertainty in natural emissions also contributes substantially, with a poor understanding of PI conditions limiting recent attempts to reduce uncertainty in RF (Carslaw et al., 2013). Even with stringent

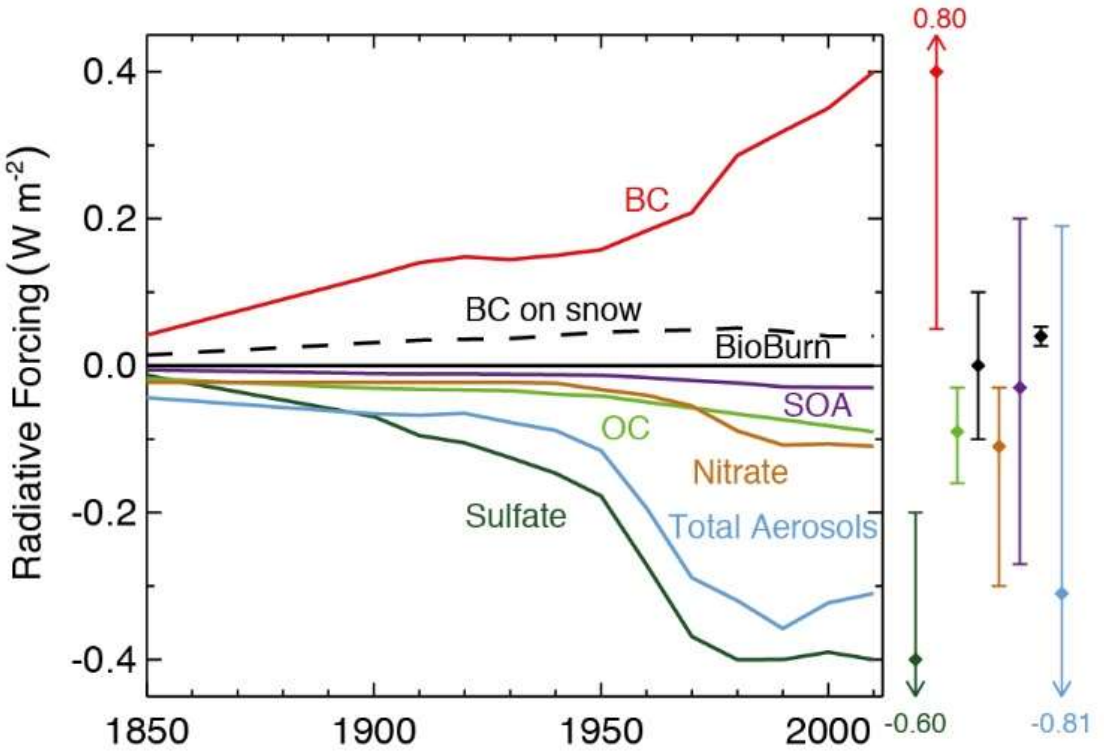

Figure 2.10 Time evolution of RF due to aerosol–radiation interaction and BC on snow and ice, with uncertainty ranges (right vertical). From Myhre et al. (2013b), Figure 8.8.

observational constraints placed on aerosol models, a large spread is found in the calculated aerosol RF due to equifinality in aerosol models giving a false impression of robustness (Lee et al., 2016).

Aerosols typically have a very short atmospheric lifetime in the troposphere, ranging from a few minutes to approximately a week, largely dependent on particle size. The composition of aerosols varies depending on the source of the particle and secondary processes occurring in the atmosphere. Although particles of different compositions are colloquially grouped as aerosols, they can have very different effects on climate, through variable interactions with radiation, atmospheric chemistry and clouds.

2.3.1. Aerosol-radiation interactions

Aerosol-radiation interaction, also known as the direct aerosol effects, is caused by scattering and absorption of radiation by aerosols in the atmosphere. The current best estimate for the direct aerosol RF in the latest IPCC report is -0.35 (-0.85 to +0.15) Wm^{-2} (Myhre et al., 2013b). The net effect is the result of positive and negative terms from individual aerosol components (Figure 2.10). The largest term is a cooling from sulphate aerosol, with a RF of -0.4 (-0.6 to -0.2). Estimates of sulphate aerosol RF have been consistent at -0.4 Wm^{-2} since the SAR in 1990. However, the uncertainty range remains large and has not been improved upon since the fourth IPCC assessment report (AR4) in 2007, due in part to the large natural contribution from volcanic emissions of SO_2. The large net cooling effect of aerosol on climate is almost certain to have masked some of the warming effect of greenhouse gases over the industrial era, however the large uncertainty of aerosol forcing means the understanding of the extent of this effect and the implications for climate sensitivity are uncertain.

The only aerosol component with an estimated positive direct forcing, and therefore of particular interest when contemplating climate change mitigation, is black carbon (BC) (also known as soot or carbonaceous aerosol). BC is strongly absorbing in the visible spectrum and has an estimated RF equal but opposite to that of sulphate aerosol at 0.4 Wm^{-2}, but with a large uncertainty range of 0.05 – 0.8 Wm^{-2} (Myhre et al., 2013b). It has been suggested that BC may be the largest warming climate forcer and have the greatest impact on global climate after CO_2 (Ramanathan and Carmichael, 2008). Annual global emissions of BC are highly uncertain, with estimates ranging from 2-29 Tg yr^{-1} (Bond et al., 2013). Due to the short lifetime and substantial warming effect of BC, it is often identified as a target species of short-term climate mitigation (Shindell et al., 2012; Bond et al., 2013). The major obstacle to mitigation via BC is whether BC emissions can be decreased without simultaneous decreases in emissions of cooling aerosol, which would counteract the mitigation attempt and possibly result in a net warming effect.

2.3.2. Aerosol-cloud interactions

Aerosols also affect the Earth's energy balance by changing the reflective properties of clouds, a process known as the aerosol first indirect effect or Twomey effect. Twomey (1977) first described the mechanism by which atmospheric aerosol could affect cloud microphysics. Increased availability of cloud and ice condensation nuclei results in increased cloud droplet concentrations and decreased droplet size, effectively brightening clouds; this increases the reflection of incident radiation and decreases shortwave radiation at the surface. The RF due to this effect is estimated at between -1.33 and -0.6Wm^{-2}, with a low confidence level (Stocker et al., 2013). Much of the uncertainty (45%) is attributed to the influence of natural aerosols (Carslaw et al., 2013). Furthermore, the poor understanding of the importance of aerosols in the PI environment currently limits the extent to which the uncertainty range can be reduced (Carslaw et al., 2013). Climate models cannot resolve processes at the cloud and aerosols scale, therefore parameterisations of cloud processes are necessary, which introduces large uncertainties (Boucher et al., 2013).

The cloud lifetime effect (second indirect aerosol effect) occurs as a result of the smaller cloud droplet formed by increased CCN, causing fewer collisions, affecting the cloud-water content and longevity of clouds and inducing an additional cooling (Albrecht, 1989; Storelvmo, 2017). However, the anthropogenic RF due to this effect was recently shown to be substantially smaller than previously thought (Toll et al., 2019), and Malavelle et al. (2017) found that cloud liquid water path was unchanged by increased aerosol concentrations following a volcanic eruption.

Aerosols can also influence climate through rapid adjustments, including through a process known as the semi-indirect effect (Boucher et al., 2013). In-situ heating due to absorbing aerosols (principally BC aerosol) increases air temperature and decreases relative humidity (Hansen et al., 1997; Johnson et al., 2004). This effect may inhibit cloud formation and decrease cloud lifetime, leading to a positive RF although the magnitude of the global effect is very uncertain.

The indirect aerosol forcing is further complicated by the presence of feedbacks which affect the net climate forcing and control natural emissions sources (Rap et al., 2018; Scott et al., 2018). In this thesis, only the aerosol first indirect effect is considered in detail and calculated in Chapter 7, due to the capabilities of the modelling tools used.

2.3.3. Effect on air quality

Aerosols near the surface degrade air quality and are damaging to human health. When considering air quality atmospheric aerosol mass is often referred to as particulate matter (PM). Particles with a diameter less than 2.5 μm are classified as $PM_{2.5}$, and under 10 μm as PM_{10}. PM2.5 has been found to be the most robust indicator of health effect from PM exposure (HEI, 2018). The cost of ambient PM pollution on human mortality is uncertain, with best estimates ranging from 2.9-4.2 million premature deaths per annum, and 95% confidence ranges from 1.61-4.81 million (Anenberg et al., 2010; Lelieveld et al., 2015; WHO, 2016; Gakidou et al., 2017). Regardless of the large uncertainty, this represents a hugely significant human and economic cost, with the WHO ranking ambient air pollution as the greatest environmental risk to health. PM2.5 exposure has been proven to increase the risk of acute lower respiratory, chronic obstructive pulmonary disease, stroke, ischaemic heart disease and lung cancer, with an estimated 9 out of 10 people worldwide exposed to polluted air every day (OECD, 2016; WHO, 2016).

2.3.4. Aerosol sources

Like other SLCPs, atmospheric aerosol and its precursors have a range of natural and anthropogenic sources. Natural aerosol sources are highly uncertain but thought to dominate the global aerosol source, responsible for 87-95% of the total mass of emissions (Hinds, 1999; Dentener et al., 2006). The largest natural aerosol sources are of dust and sea salt, with estimated annual fluxes of 1678 Tg yr^{-1} and 7925 Tg yr^{-1}, respectively (Dentener et al., 2006).

Sulphate aerosol forms in the atmosphere through oxidation of SO_2 and dimethyl sulphide (DMS) by reaction with OH (Pham et al., 1995). Approximately 98% of DMS emissions are oceanic in origin (Gondwe et al., 2003), with 30 – 67 Tg emitted annually (Woodhouse et al., 2010; Granier et al., 2019), accounting for roughly half of natural sulphate aerosol formation (Kettle and Andreae, 2000; Dentener et al., 2006), and 18-42% of all global sulphate aerosol (Woodhouse et al., 2010). Volcanic emissions and a small contribution from fires (~3 Tg yr-1 (Lamarque et al., 2010)) account for the remainder of the natural sulphate aerosol source, with an estimated mean emission of 12.6 Tg yr^{-1}, albeit with large interannual variability (Dentener et al., 2006). Anthropogenic activities also emit precursors of sulphate aerosol, approximately 92 Tg SO_2 in 2000 (Lamarque et al., 2010), predominantly through energy production and industry (Hoesly et al., 2018), in particular, from coal burning power stations (Rap et al., 2018).

Like sulphate, nitrate aerosols are formed in the atmosphere through homogeneous and heterogeneous reactions of primary precursors ammonia (NH_3) and nitric acid (HNO_3) (Orel and Seinfeld, 1977). Nitric acid is produced from the reaction of NO_2 with OH (Rodhe et al., 1981). Sources of NO_x are discussed in Section 2.2.2. Anthropogenic agricultural emissions are the primary source of ammonia emissions, as livestock manure and synthetic fertilisers account for 17.6-40.8 Tg NH_3 yr^{-1}, estimated to be 80-90% of total NH_3 emissions (Bouwman et al., 1997; Zhang et al., 2010; Kang et al., 2016). Emissions from Southern Asia make up 50% of total global emissions since 1980 (Xu et al., 2019). Biomass burning emits an estimated 8.7 (3.7-9.4) Tg NH_3 yr^{-1} (Bouwman et al., 1997; Lamarque et al., 2010), while a recent study indicates a 3 Tg yr^{-1} contribution from oceans (Paulot et al., 2015), smaller than the previously suggested value of 10 Tg yr^{-1} (Bouwman et al., 1997).

Black carbon (BC) is a directly emitted aerosol species, with a current estimated anthropogenic source of between 4 Tg yr^{-1} and ~8 Tg yr^{-1} (Lamarque et al., 2010; Crippa et al., 2018; Hoesly et al., 2018). The largest anthropogenic contribution is through burning fossil fuels, predominantly residential or commercial use (Hoesly et al., 2018), but also from biofuel use (Dentener et al., 2006). The major

natural source of BC aerosol is through biomass burning emissions, accounting for 2-3 Tg BC yr^{-1} (Lamarque et al., 2010; Bond et al., 2013; Giglio et al., 2013b; Voulgarakis and Field, 2015). Fossil fuels and biomass burning each contribute ~40% to total BC emissions, with 20% from biofuel burning (Bond et al., 2004). Organic carbon is also directly emitted, with similar emissions as BC. For OC however, biomass burning accounts for ~74% of global emissions, with 7% and 19% from fossil fuels and biofuels, respectively (Bond et al., 2004). The relative contributions may have changed in recent years, with recent studies estimating a larger contribution from anthropogenic sources (Crippa et al., 2018). Estimated global emissions are 10-20 Tg yr^{-1} from anthropogenic activities (Lamarque et al., 2010; Crippa et al., 2018; Hoesly et al., 2018) and 16-23 Tg yr^{-1} from biomass burning (Giglio et al., 2013a; Voulgarakis and Field, 2015; Hoesly et al., 2018).

2.3.5. Recent trends in atmospheric aerosols

Observational studies indicate that aerosol emissions increased through much of the 20th century, but the increasing trend has slowed or stopped in recent decades. This trend was driven largely by decreasing emissions over the USA and Europe, while emissions increased over eastern and southern Asia (Hartmann et al., 2013). This trend is perhaps most clear for sulphate aerosol, as emissions of SO_2 peaked in the 1980s and have been in decline globally ever since (Hoesly et al., 2018; Aas et al., 2019). This was initially triggered in part by the collapse of the Soviet Union, but also a growing awareness of the impact on the environment and human health. Concentrations of nitrate aerosol have been observed to be increasing in the past decade (Kang et al., 2016; Warner et al., 2016), driven in part by increasing ammonia emissions. Nitrate aerosol is expected to become more important in future as SO_2 emission reductions lead to decreases in ammonium sulphate formation, increasing ammonium nitrate concentrations (Bauer et al., 2007; Shindell et al., 2009). Trends in emissions of other aerosols are less clear, due in part to the substantial contribution of natural aerosol. Anthropogenic emissions of BC and OC have continued to increase in the 21st century, driven by increases in China and Africa. It is expected that

anthropogenic emissions of BC, OC and SO_2 will decrease in the coming decades, as legislation to improve air quality takes effect.

2.4. Summary

Numerous studies have investigated the role of SLCPs in the atmosphere, meaning that their PD atmospheric concentrations are relatively well understood, as is their effect on the planet's radiative balance. However, there remain substantial uncertainties in our understanding of how SLCPs such as tropospheric O_3 have changed since the PI era, which substantially limits confidence in estimates of its total RF for PI to PD. Accurate estimates of how human activity has affected atmospheric concentrations of key climate forcers is necessary to understand how SLCPs have contributed to observed climate change and accurately predict their impact in the future. There are also uncertainties in the atmospheric budgets of several species and the causes of observed variations and trends in atmospheric concentrations. This is due in large part to the range of natural sources of SLCP emissions, which are very difficult to monitor at a global scale. Understanding the role of natural variations improves our capability to project future SLCPs concentrations in a changing climate, and their resulting impact.

The benefits of SLCP mitigation for climate and air quality mitigation have been studied extensively, particularly in the last decade. The magnitude of the mitigating effect on climate is still uncertain, with current best estimates calculating an avoided warming of ~0.5C by 2050. The net climate effect of simultaneous reductions of warming greenhouse gases and cooling aerosols is particularly uncertain. The positive outcomes for air quality following SLCP emission reductions are much more certain, but the extent to which such measures would negate climate mitigation is unclear. It is important to understand how future policies targeting emissions of SLCPs and their precursors will change near-term climate change, and whether co-benefits with air quality can be achieved while still decreasing the rate of warming. This improved understanding will contribute to policy decisions, enabling mitigation of climate change in the most efficient and effective manner.

3. Model Description and evaluation

3.1. Introduction

Chemical Transport Models (CTM) are numerical models which simulate atmospheric chemistry and transport. CTMs have been used since the late 20th century to study processes occurring in the troposphere and stratosphere. In a CTM, the chemical processes are driven by meteorological variables from past analyses (i.e. performed offline), as opposed to in a Global Climate Model (GCM) which calculates its own meteorology (online). As a result, the computational cost of a CTM is significantly less than that of a GCM, and the use of meteorological analyses allows comparison with observations to improve understanding of chemical and dynamic processes. In addition, CTMs can also be coupled to other specific schemes to resolve more complex chemical or physical processes, such as aerosol chemistry or dispersion.

In this thesis, the TOMCAT CTM is used, coupled to the aerosol microphysics model GLOMAP in order to simulate the abundance, distribution and variability of global SLCP species. In this chapter, the TOMCAT and GLOMAP models are described, including details on several updates to the models. A comprehensive evaluation of the latest version of the model against various observational datasets is included in Section 3.5.

An offline radiative transfer model (SOCRATES) is employed throughout this thesis to estimate radiative effects of changes to SLCPs, described in Section 3.6. An emissions based climate model (FaIR) is also used to estimate global

mean changes to effective RF and temperature in Chapter 6. FaIR is described in detail in Section 0.

3.2. TOMCAT chemical transport model

The Toulouse Off-line Model of Chemistry And Transport (TOMCAT) was originally developed to study lower stratospheric trace gases in the Arctic (Chipperfield et al., 1993). Through various updates and modifications, the TOMCAT CTM was gradually developed into a tropospheric CTM (Chipperfield, 2006), and later coupled to the GLOMAP aerosol microphysics model (Section 3.3). TOMCAT is a three-dimensional global Eulerian CTM, driven by 6-hourly ERA-Interim reanalyses from the European Centre for Medium-range Weather Forecasts (ECMWF). The model as used here is run at 2.8° × 2.8° horizontal resolution with 31 vertical levels from the surface to 10 hPa. The planetary boundary layer (PBL) scheme is based on Holtslag and Boville (1993), with vertical diffusion up to 3 km in the absence of convection and explicitly determined PBL height. The moist convection scheme is based on Tiedtke (1989) and sea surface temperatures are from ECMWF reanalyses. Dry deposition rates are calculated based on the deposition velocity of a particular species. Wet deposition is calculated from model-derived large-scale and convective precipitation, and is based on the removal rate and concentrations of the relevant species.

The TOMCAT tropospheric chemistry scheme was detailed in Arnold et al. (2005) and updated in Monks et al. (2017). TOMCAT includes O_x-HO_x-NO_x-CO-CH_4 chemistry and detailed hydrocarbon chemistry (Monks et al., 2017), with ethene, propene, butane and toluene chemistry based on Folberth et al. (2006). Isoprene oxidation is based on the Mainz Isoprene Mechanism scheme (Pöschl et al., 2000), and heterogeneous reaction of N_2O_5 is included based on Evans and Jacob (2005).

In the updated version of the model used throughout this thesis, model cloud fields are provided from ECMWF reanalyses (Dee et al., 2011). This replaces the climatological cloud fields used previously from the International Satellite

Cloud Climatology Project (ISCCP) (Rossow and Schiffer, 1999). The cloud scheme now also varies annually, improving the model representation of interannual variability and photolysis rates, which influences atmospheric concentrations of OH and O_3. The effect of the change on simulated global OH concentrations is evaluated in Section 3.5. Emissions inventories for natural and anthropogenic sources of SLCP have been updated since Monks et al. (2017) and are now annually varying (see Section 3.4).

3.3. GLOMAP aerosol microphysical model

The Global Model of Aerosol Processes (GLOMAP) is an aerosol microphysical model, developed as an extension to the TOMCAT CTM to resolve aerosol chemistry and microphysics (Spracklen et al., 2005; Mann et al., 2010). GLOMAP is run here in the GLOMAP-mode version (Mann et al., 2010), with four aerosol components (sulphate, sea-salt, BC, OC) and five aerosol size distributions or modes (nucleation soluble, Aitken soluble, accumulation soluble, coarse soluble and Aitken insoluble). Aerosol processes simulated by GLOMAP include primary emissions, dry deposition, sedimentation, scavenging, ageing, hygroscopic growth, nucleation, coagulation, condensation and cloud-processing (Spracklen et al., 2005).

The new version employed throughout this thesis also includes the new particle formation (NPF) scheme developed from CLOUD-chamber experiments (Gordon et al., 2017), replacing the Merikanto et al. (2009) primary particle emissions scheme. It was found that NP, from molecules colliding in the atmosphere produced 54% of cloud condensation nuclei in the PD at 0.2% saturation. The Mårtensson sea salt parameterisation is also now included (Mårtensson et al., 2003), which includes ultrafine sea salt and substantially increases the concentrations of aerosol particles in the Southern Ocean (Gordon et al., 2017). Anthropogenic and biomass burning aerosol emissions inventories have also been updated (see Section 3.4).

3.4. TOMCAT-GLOMAP emissions

Throughout this thesis the emission inventories used in TOMCAT-GLOMAP simulations have been modified or replaced in order to answer specific research questions. Fire and biogenic emissions are modified substantially as part of the study in Chapter 4 (Section 4.2). Modifications were made to the fire emissions inventory for simulations in Chapter 5 (Section 0), while new anthropogenic emissions inventories from the ECLIPSE project were applied to TOMCAT-GLOMAP in Chapter 6 (Section 6.2). Described here are emission inventories in the control version of TOMCAT-GLOMAP. All emissions are emitted at the lowest model level, on a 1° × 1° grid before being regridded within the model to the TOMCAT resolution.

NO_x lightning emissions are calculated in the model, coupled to convective activity (Stockwell et al., 1999). Biomass burning emissions have been updated to the Global Fire Emissions Database version 4 (GFEDv4) (Randerson et al., 2017), with emissions varying by month and year. Biogenic emissions of isoprene and monoterpenes are from the Model of Emissions of Gases and Aerosols from Nature (MEGAN), developed in support of the Chemistry-Climate Model Initiative (CCMI)[1] and Monitoring Atmospheric Composition and Climate project (MACC)[2] (Sindelarova et al., 2014). The CH_4 emissions inventory was produced by (McNorton et al., 2016b), with wetland emissions derived from the Joint UK Land Environment Simulator (JULES) and biomass burning emissions from GFEDv4 (Randerson et al., 2017). These are then combined with anthropogenic emissions from EDGAR version 3.2, paddy field emissions from Yan et al. (2009) and termite, wild animal, mud volcano, hydrate and ocean emissions from Matthews and Fung (1987) (McNorton et al., 2016b). The global mean surface CH_4 mixing ratio is scaled in TOMCAT to a best estimate based on observed global surface mean concentration (McNorton et al., 2016a).

Anthropogenic and shipping emissions in the standard TOMCAT-GLOMAP setup are now annually varying from the Monitoring Atmospheric Composition

[1] http://www.met.reading.ac.uk/ccmi/
[2] http://www.gmes-atmosphere.eu

and Climate (MACCity) emissions inventories (Lamarque et al., 2010). TOMCAT-GLOMAP can be using with anthropogenic aerosol emissions from the MACCity or Aerocom inventories (Dentener et al., 2006).

3.5. TOMCAT-GLOMAP evaluation

Previous versions of the TOMCAT-GLOMAP coupled model have been extensively evaluated (Mann et al., 2010; Monks et al., 2017). Given the substantial changes to the version employed in this thesis, most notably the change in model cloud representation, a comprehensive evaluation of the model against observed datasets was required before the model could be used scientifically. Here, TOMCAT-GLOMAP model output is compared with a range of observational datasets of gas-phase and aerosol species, evaluating the capability of the model to simulate observed concentrations, distributions and trends of a range of tropospheric species.

3.5.1. Comparison with satellite retrievals

The Measurement of Pollution in the Troposphere (MOPITT) satellite retrievals (Emmons et al., 2004) have been used to evaluate CO at 800 and 500 hPa and are shown in Figure 3.1 and Figure 3.2, respectively. The MOPITT instrument is on-board NASA's EOS Terra satellite, launched in March 2000 and is nadir viewing. MOPITT has ~14 orbits per day with equator overpass at approximately 10:30 and 22:30 local time (LT) and a swath footprint of 22 km x 22 km. It has eight channels measuring radiances: four in the thermal infrared (IR) near 4.7 μm and four in near IR using reflected solar radiation near 2.3 μm (Emmons et al., 2004).

For direct comparison between TOMCAT and MOPITT CO, the satellite averaging kernels (AKs) need to be applied to the model fields. This accounts for the vertical sensitivity of the instrument when retrieving CO profiles. The AK is applied to the model as:

$$\boldsymbol{y} = \mathbf{10}.\mathbf{0}^{\boldsymbol{A}(\log_{10} x - \log_{10} x_a) - \log_{10} x_a}\ , \tag{3.1}$$

where, $\boldsymbol{y}$ is the modified model profile, $\boldsymbol{A}$ is the AK, $\boldsymbol{x}$ is the model profile interpolated onto the satellite vertical pressure grid and $\boldsymbol{x_a}$ is the satellite profile a priori. Here, satellite CO retrievals are only used where the degrees of freedom signal (DOF) is larger than 1.0, indicating acceptable satellite sensitivity (Monks et al., 2017).

TOMCAT performs similarly here as in Monks et al. (2017), competently reproducing seasonal variations in CO and locates peak CO accurately over East Asia and Central Africa. However TOMCAT underestimates CO concentrations in the Northern Hemisphere (NH) while overestimating peak

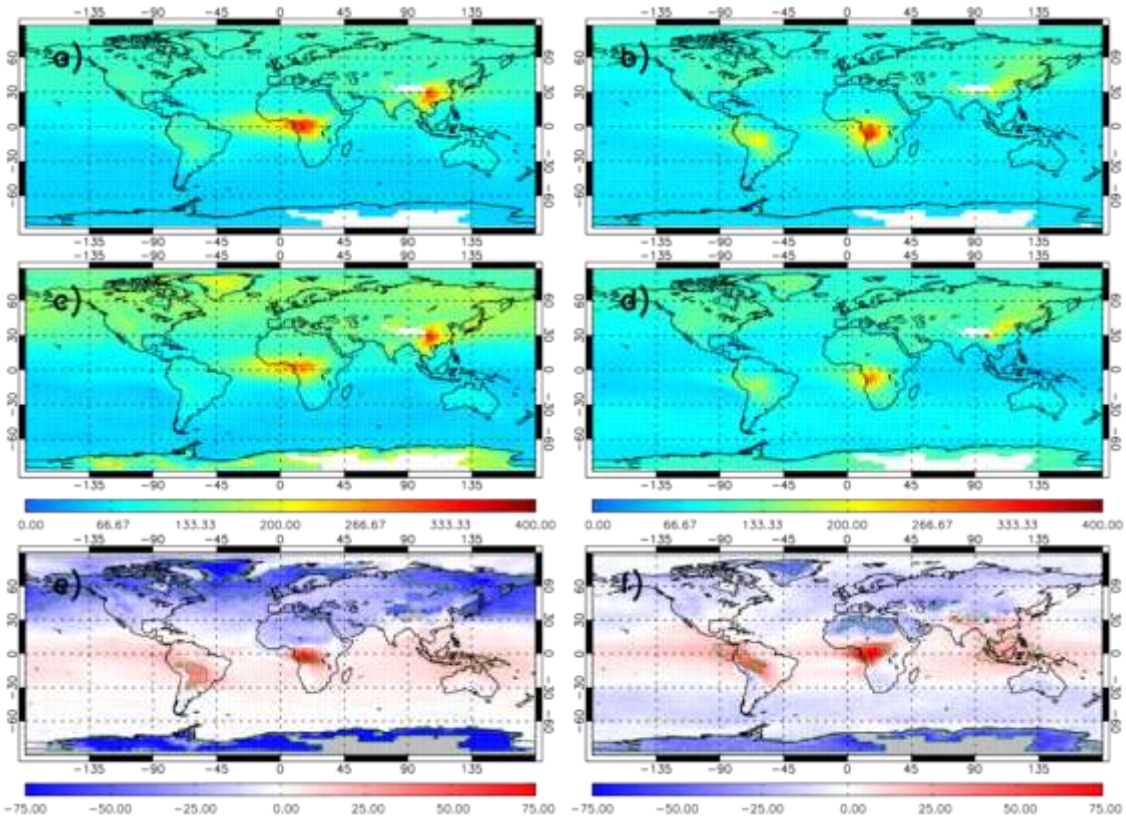

Figure 3.1 Carbon monoxide (CO) at 800 hPa seasonal averages for 2007-2008 in ppb. a) TOMCAT (December-January-February, DJF), b) TOMCAT (June-July-August, JJA), c) MOPITT DJF, d) MOPITT JJA, e) TOMCAT – MOPITT mean bias DJF and f) TOMCAT – MOPITT mean bias JJA. Green polygons in panels e-f show regions where the absolute model-satellite mean bias is greater than the satellite uncertainty. Plot created by Dr R. Pope[3].

[3] University of Leeds, UK

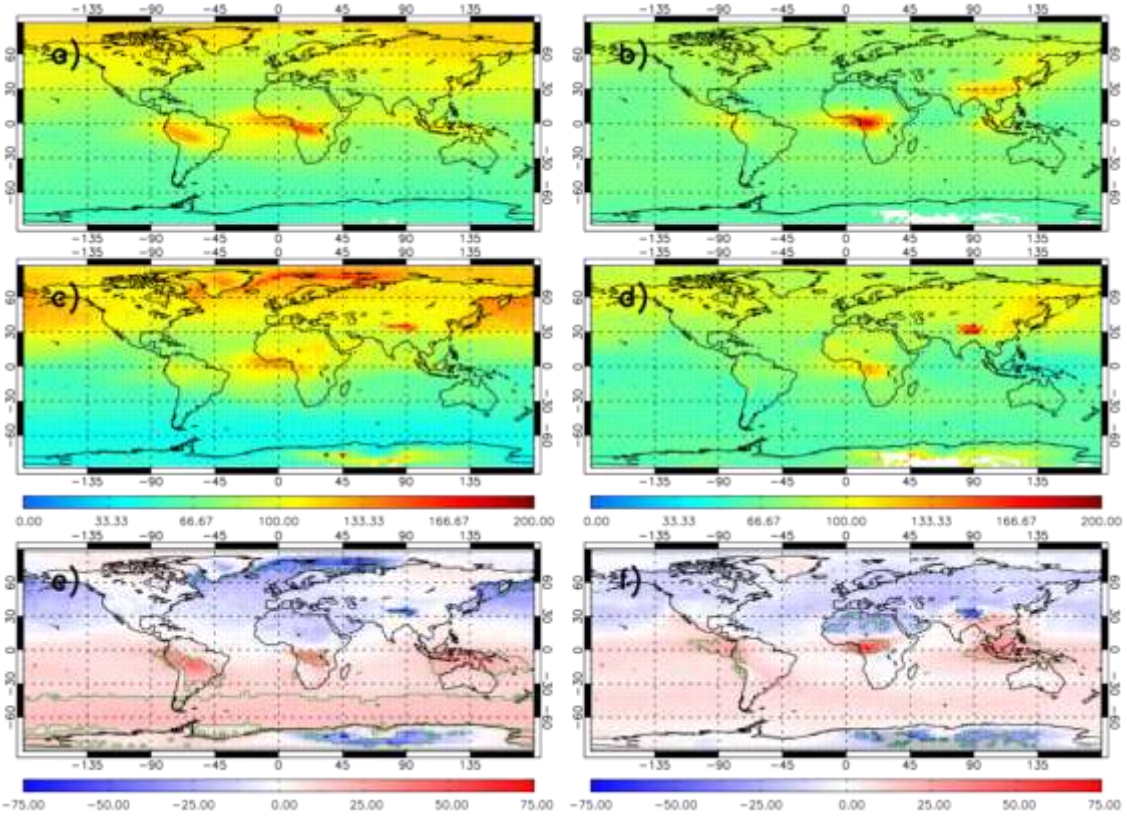

Figure 3.2 Carbon monoxide (CO) at 500 hPa seasonal averages for 2007-2008 in ppb. a) TOMCAT (December-January-February, DJF), b) TOMCAT (June-July-August, JJA), c) MOPITT DJF, d) MOPITT JJA, e) TOMCAT – MOPITT mean bias DJF and f) TOMCAT – MOPITT mean bias JJA. Green polygons in panels e-f show regions where the absolute model-satellite mean bias is greater than the satellite uncertainty. Plot created by Dr R. Pope.

concentrations in biomass burning regions, with a maximum difference of ~ 75 ppb (Figure 3.1 and Figure 3.2).

Simulated O_3 concentrations from TOMCAT were also compared with satellite observations of lower tropospheric (0–6 km) O_3 from the Ozone Monitoring Instrument (OMI). The Ozone Monitoring Instrument (OMI) is on-board NASA's EOS-Aura satellite and has an overpass time of approximately 13:30 LT. The data has been screened for geometric cloud fraction of under 0.2, good data flags and where the solar zenith angle is greater than 80°. O_3 data has also been corrected for the OMI row anomaly; a dynamic anomaly likely caused by an internal obstruction (Torres et al., 2018). The sub-column O_3 is based on an optimal estimation algorithm utilised by Miles et al. (2015).

The OMI sub-column O_3 AK is applied as:

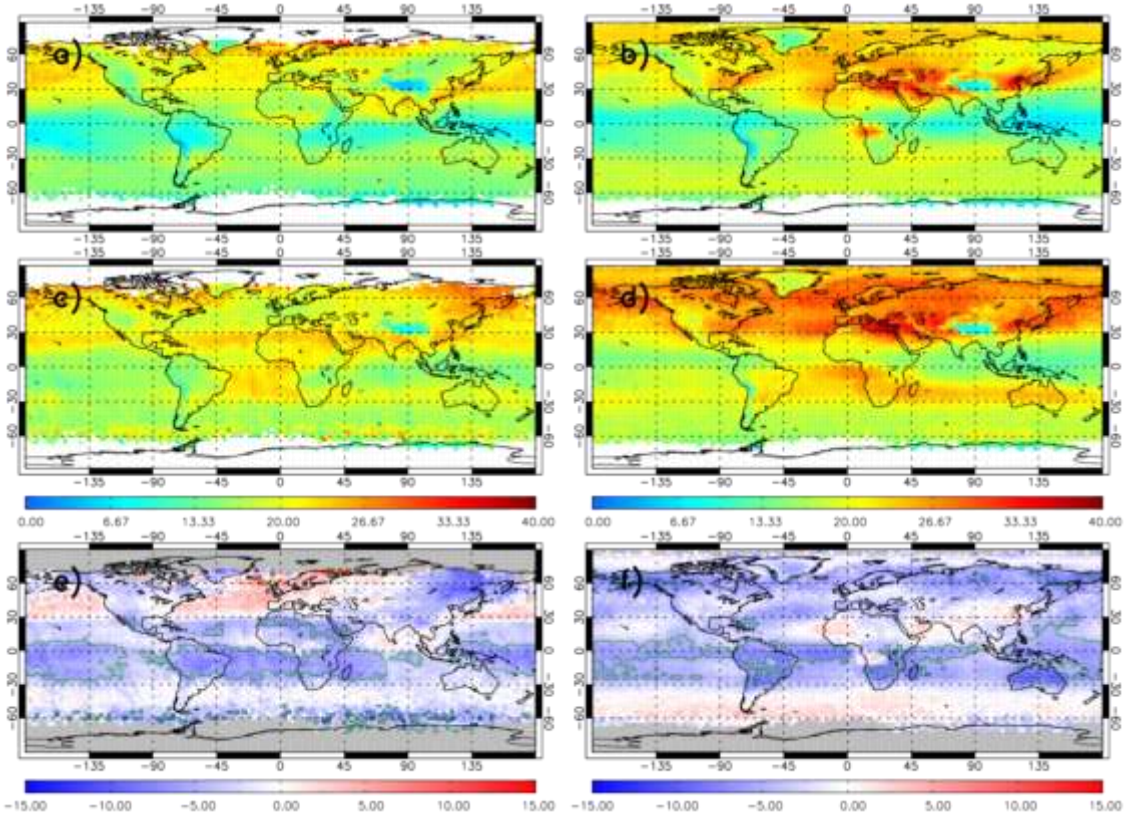

Figure 3.3 Sub-column (0-6 km) O_3 seasonal averages for 2007-2008 in Dobson units (DU). a) TOMCAT (December-January-February, DJF), b) TOMCAT (June-July-August, JJA), c) OMI DJF, d) OMI JJA, e) TOMCAT – OMI mean bias DJF and f) TOMCAT – OMI mean bias JJA. Green polygons in panels e-f show regions where the absolute model-satellite mean bias is greater than the satellite uncertainty. Plot created by Dr R. Pope.

$$\boldsymbol{y} = \boldsymbol{A}.\boldsymbol{x} + \boldsymbol{x_a} \ , \tag{3.2}$$

where, $\boldsymbol{A}$ is the AK, $\boldsymbol{x}$ is the model profile interpolated onto the satellite pressure grid and $\boldsymbol{x_a}$ is the satellite profile a priori.

These data were obtained by the Rutherford Appleton Laboratory (RAL; data version fv0214) and use an optimal estimation retrieval scheme, which resolves O_3 in the 0–6 km layer by exploiting information in the Hartley and Huggins UV bands. The scheme derives from the one discussed by Miles et al. (2015) for another UV sounder GOME-2.

TOMCAT representation of O_3 concentrations between 0 and 6 km in NH winter is slightly improved on the Monks et al. (2017) version, particularly over Central

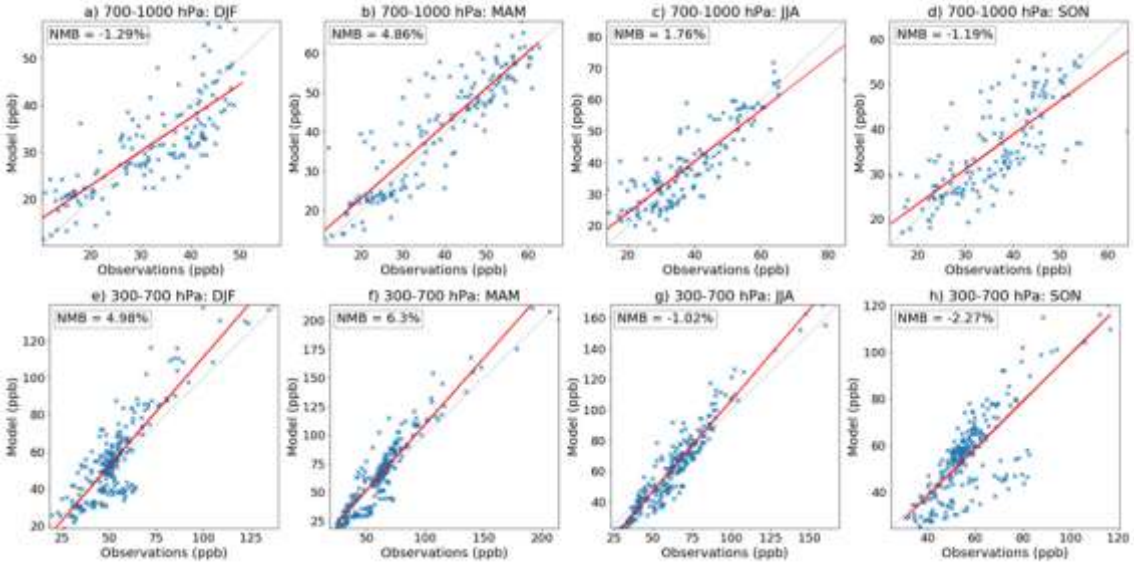

Figure 3.4 Comparison of seasonal mean simulated O_3 concentrations (ppb) against mean ozonesonde observations from Tilmes et al. (2012), for the period 1995-2011. Panels a-d show mean concentrations at 700-1000 hPa across all sites, while panels e-h show mean concentrations at 300-700 hPa. Values in each panel are seasonal means, from left to right, December-February (DJF), March-May (MAM), June-August (JJA) and September-November (SON). The red line represents the linear regression. Normalised mean bias (NMB) values between model and observations are also shown.

Africa and South East Asia where there had previously been a low bias of approximately 10 DU. However, there remains a general low bias in global O_3 of up to 10 Dobson Units (DU) in winter in regions such as the Southern Atlantic Ocean (Figure 3.3).

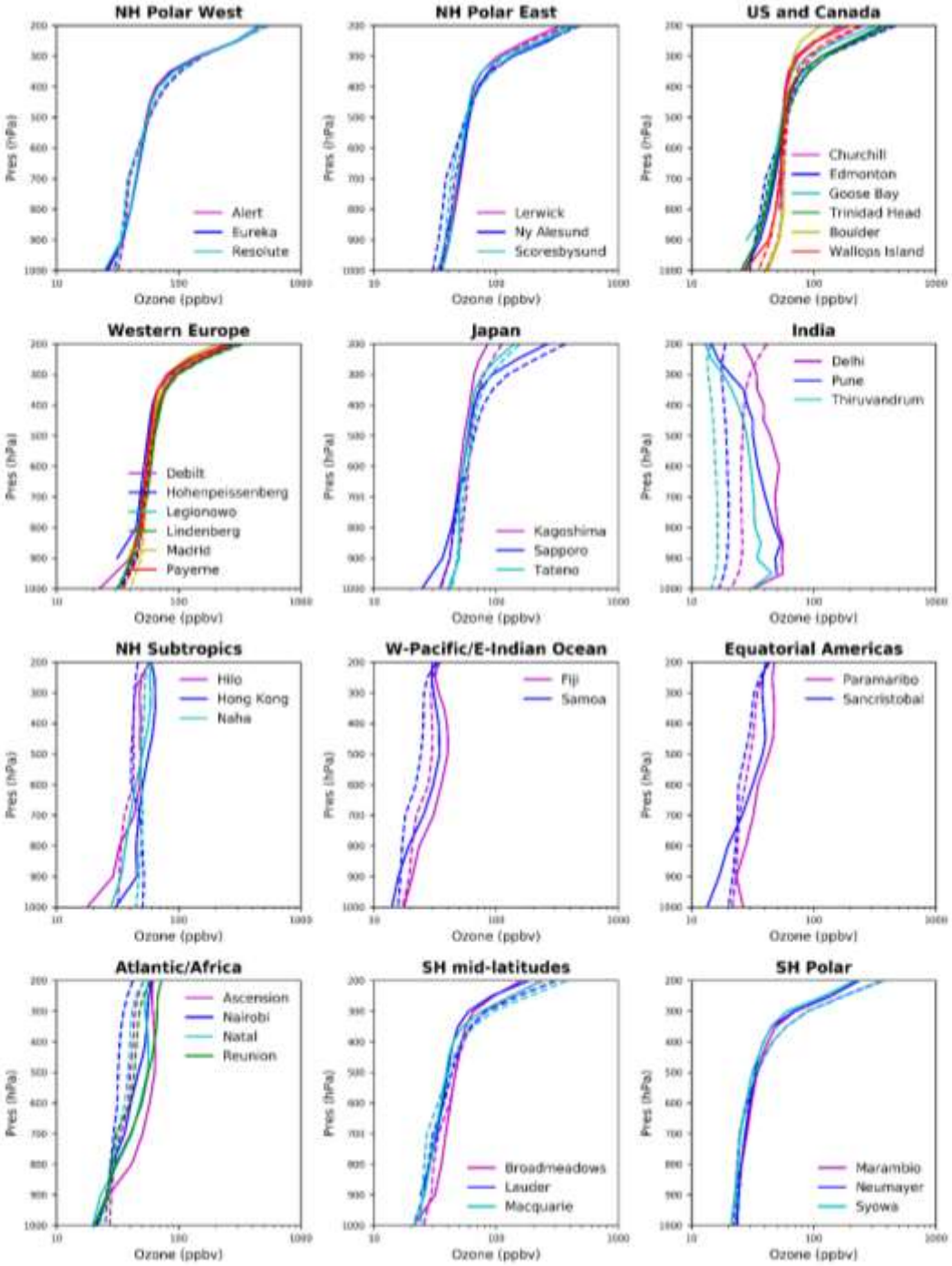
NH Polar West
Alert
Eureka
Resolute
NH Polar East
Lerwick
Ny Alesund
Scoresbysund
US and Canada
Churchill
Edmonton
Goose Bay
Trinidad Head
Boulder
Wallops Island
Western Europe
Debilt
Hohenpeissenberg
Legionowo
Lindenberg
Madrid
Payerne
Japan
Kagoshima
Sapporo
Tateno
India
Delhi
Pune
Thiruvandrum
NH Subtropics
Hilo
Hong Kong
Naha
W-Pacific/E-Indian Ocean
Fiji
Samoa
Equatorial Americas
Paramaribo
Sancristobal
Atlantic/Africa
Ascension
Nairobi
Natal
Reunion
SH mid-latitudes
Broadmeadows
Lauder
Macquarie
SH Polar
Marambio
Neumayer
Syowa
Pres (hPa)
Ozone (ppbv)

3.5.2. Comparison with ozonesondes

TOMCAT O_3 has also been evaluated using sonde observations (Figure 3.4) (Tilmes et al., 2012). Normalised mean bias (NMB) values have been calculated between the model and observations (Figure 3.5), using the following formula:

$$NMB = \left[\sum (x_n - y_n) / \sum x_n\right] \times 100\ \% \qquad (3.3)$$

where n = number of data points

x = Observational data

y = TOMCAT simulated values

The model generally simulates the vertical profiles, seasonal variation and absolute concentrations of O_3 very well, with a NMB of 1.1% across all sites at 700–1000 hPa and 2.1% at 300–700 hPa. The model capably simulates the seasonality of tropospheric O_3 (Figure 3.4), with a maximum seasonal bias of 6.3% at 300–700 hPa in March– May. There is no apparent regional or latitudinal bias, although simulated concentrations are overestimated in India (Figure 3.5). In addition, the TOMCAT-simulated global tropospheric burden of O_3 in 2000 is 342 Tg, which falls within the range of published values (Table 3.1).

3.5.3. Comparison with aircraft campaigns

Annual mean simulated gas-phase species for model year 1999 are compared with a climatological dataset of aircraft observations from 16 campaigns, conducted with a broad spatial and temporal range from 1992 to 2001 (Emmons et al., 2010). While the comparison of observational data from intermittent aircraft campaigns does not offer a perfect comparison with the model simulated long-term mean concentrations, it allows evaluation of broad characteristics of a number of species over vertical profiles in many global regions. Figure 3.6 shows the comparison of simulated annual mean global concentrations of CO,

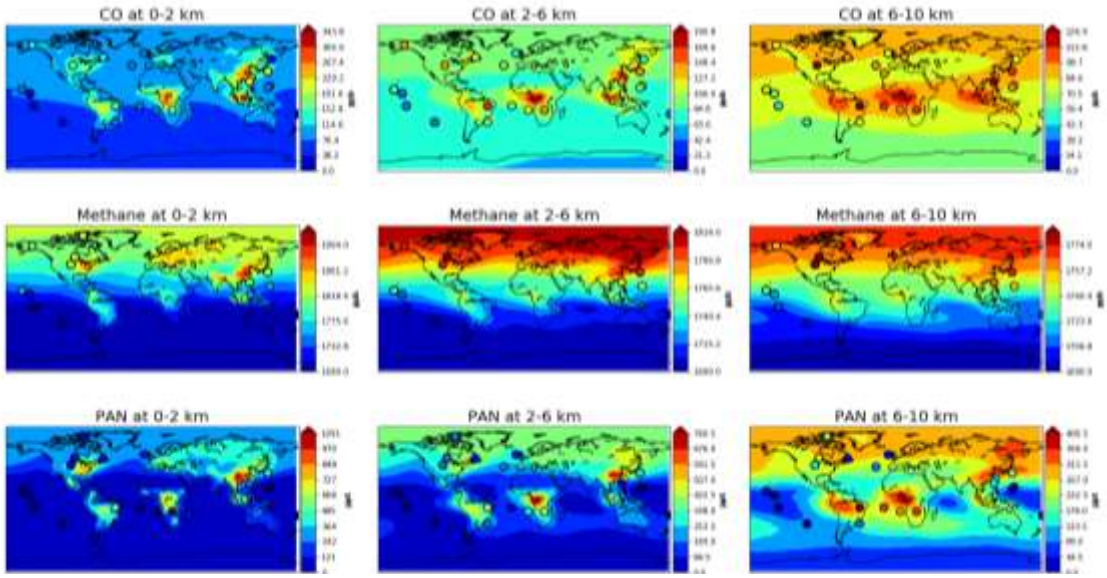

Figure 3.6 Global mean volume mixing ratios of CO (ppb), CH_4 (ppb) and PAN (ppt) from TOMCAT for the period 1993-2001 at 0-2 km (left panels), 2-6 km (middle panels) and 6-10 km (right panels). The filled circles show mean values from aircraft observation campaigns which took place between 1992 and 2001 (Appendix A.1) (Emmons et al., 2010).

CH_4 and PAN, with aircraft observations at 0–2, 2–6 and 6–10 km. Information relating to the aircraft measurement campaigns used is given in Appendix A.1.

The model captures broad characteristics of spatial distribution for all species, simulating higher concentrations in polluted urban or biomass burning regions, with lower concentrations over ocean and in the SH. CO concentrations decrease with altitude but the largest values still occur around urban areas and burning regions, which can be seen in both model and aircraft concentrations. The NMB between the model and aircraft observations has also been calculated and are shown in Figure 3.7. Consistent with the comparison with MOPITT satellite retrievals (Figure 3.1 and Figure 3.2), the model underestimates CO concentrations particularly near the surface, with a NMB of −11.1%, −9.93% and −0.25% at 0–2, 2–6 and 6–10 km, respectively. Absolute concentrations of CH_4 in TOMCAT simulations match aircraft data very well, although, given the global mean surface concentration scaling, it is expected that the magnitude of CH_4 will be well simulated. The latitudinal and vertical distributions are also well captured, giving confidence in the model transport and OH simulation. Aircraft observations show that CH_4 also decreases with altitude and the hemispheric disparity becomes more pronounced, with higher concentrations in the NH. For

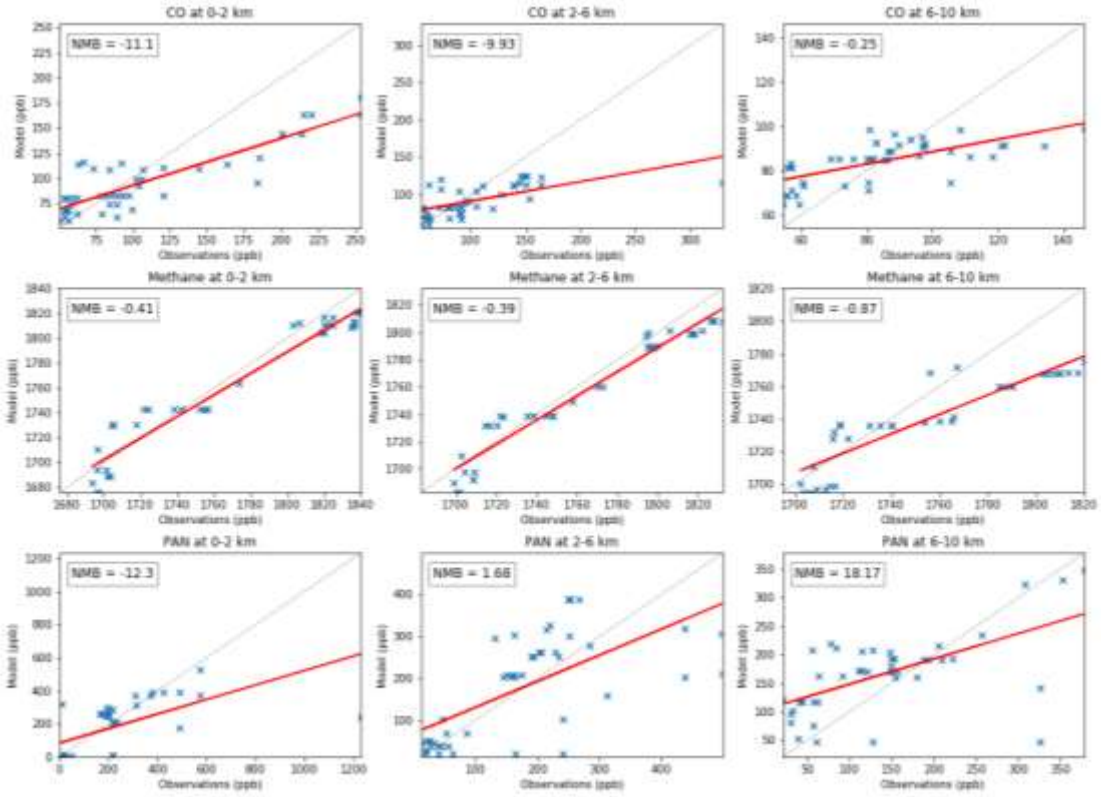

Figure 3.7 Comparison of annual global mean volume mixing ratios of CO (ppb), CH_4 (ppb) and PAN (ppt) from TOMCAT for the period 1993-2001 against aircraft observations that took place between 1992-2001, at 0-2 km (left panels), 2-6 km (middle panels) and 6-10 km (right panels). Normalised mean bias (NMB) values between the model and observations are shown in each panel.

PAN concentrations, the simulated spatial distribution is broadly well captured, as is the increased concentration with altitude. There is a general low bias in absolute concentrations near the surface (NMB = −12.3%), with a better comparison at 2–6 km (NMB = 1.68%) and overestimation at 6–10 km (NMB = 18.17%).

3.5.4. Evaluation of hydroxyl radical in TOMCAT-GLOMAP

Due to its very short lifetime, it is challenging to evaluate model-simulated OH over representative spatial and temporal scales. The evaluation methodology recommended by Lawrence et al. (2001) is used here, in which simulated tropospheric OH is divided into 12 subdomains, from the surface to a climatologically derived tropopause. This method was also used to evaluate TOMCAT in Monks et al. (2017), allowing for a direct comparison and assessment of the influence of the updated cloud scheme. The evaluation is performed for the year 2000. Figure 3.8 shows TOMCAT simulated OH compared to Monks et al. (2017) , the ACCMIP model mean (Naik et al., 2013) and the Spivakovsky et al. (2000) OH dataset estimated from methyl chloroform observations. The models and the observationally constrained distribution broadly agree in terms of the latitudinal spread of OH concentrations with a minimum in the SH and a maximum in the tropics; however, there is disagreement over the exact altitude of the maximum OH concentrations. In both

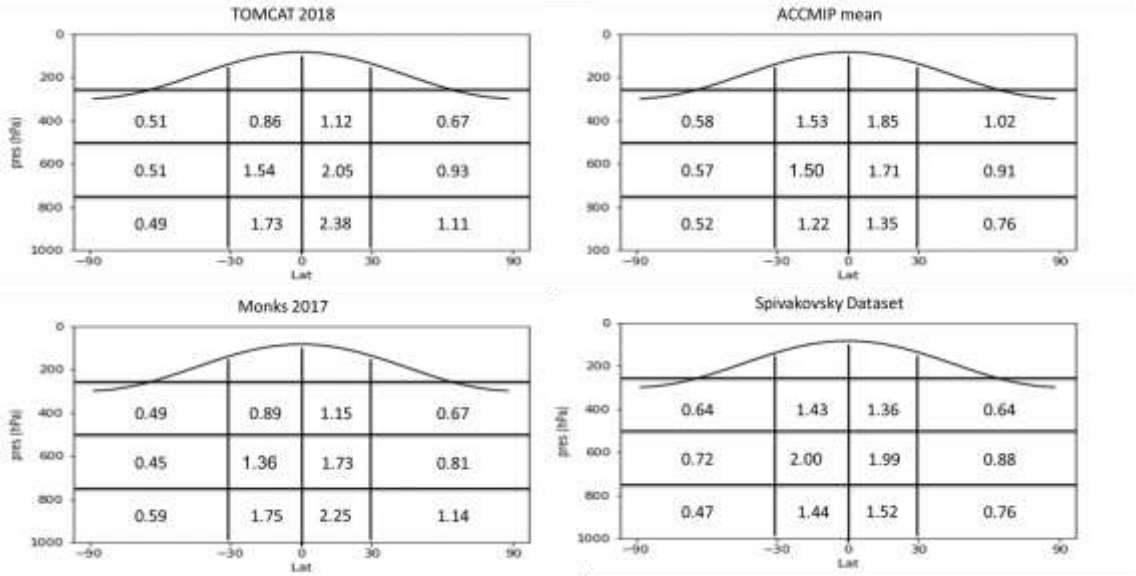

Figure 3.8 Annual zonal mean hydroxyl radical (OH) concentrations ($\times 10^6$ molecules cm^{-3}) divided into 12 sub-domains as recommended by Lawrence et al. (2001). The simulated OH from this study is compared to a dataset estimated from methyl chloroform observations (Spivakovsky et al., 2000) and the Atmospheric Chemistry and Climate Model Intercomparison Project (ACCMIP) multi-model mean (Naik et al., 2013). Results from a previous version of TOMCAT from Monks et al. (2017) are also shown. A climatological tropopause, indicated by the smooth black line near the top of each panel, has been used to remove stratospheric OH.

Table 3.1 Present-day (2000) TOMCAT model diagnostics compared to previous model version from Monks et al., (2017) and other published values.

Diagnostic	TOMCAT (this study)	Monks et al. (2017)	Other estimates
O_3 burden (Tg)	342	331	337 ± 23[a]
Tropospheric OH concentration ($\times 10^6$ molecules cm^{-3})	1.04	1.08	0.94-1.06[b]
CH_4 lifetime (years)	8.0	7.9	9.3 ± 0.9[c]

[a] Young et al. (2013)

[b] Prinn et al. (2001), Krol and Lelieveld (2003),Bousquet et al. (2005), Wang et al. (2008)

[c] Voulgarakis et al. (2013)

versions of TOMCAT the highest concentration is between the surface and 750 hPa, while ACCMIP and Spivakovsky et al. (2000) find peak OH in the upper and mid-level troposphere, respectively. The updated cloud fields used in the current TOMCAT-GLOMAP version have slightly increased OH concentrations in the mid-level and upper domains compared to Monks et al. (2017) but concentrations remain significantly higher in the NH and surface domains than in other studies. In addition, the simulated NH:SH ratio of 1.48 in the current TOMCAT version remains substantially higher than in the ACCMIP models (1.28 ± 0.1), indicating that TOMCAT photolysis rates and OH production in the NH are larger.

The total global tropospheric average OH in this version of TOMCAT is 1.04 × 10^6 molecules cm^{-3}, a decrease from Monks et al. (2017) and within the range of other published values (Table 3.1). This is primarily due to the updated treatment of clouds, (i.e. climatological cloud fields have been replaced with cloud fraction from ECMWF reanalyses data). The tropospheric O_3 burden of 342 Tg has increased relative to Monks et al. (2017) (331 Tg) and is within the range found in Wild (2007) (335 ± 10 Tg) and ACCMIP models (337 ± 23 Tg) (Young et al., 2013).

Due to the simplified treatment of CH_4, the scaling applied and its relatively long atmospheric lifetime, the total atmospheric lifetime cannot be determined from

TOMCAT simulations. Instead a chemical lifetime due to reaction with OH is calculated from CH_4 and OH burdens, disregarding stratospheric sinks and soil sinks (Fuglestvedt et al., 1999; Berntsen et al., 2005; Voulgarakis et al., 2013). The lifetime diagnosed from TOMCAT is 8.0 years, compared to the multi-model mean and range of 9.3 ± 0.9 years from (Voulgarakis et al., 2013). The shorter lifetime in TOMCAT is due to the overestimation of OH at the surface.

3.5.5. Evaluation of simulated aerosol fields

The simulated global annual sulphate burden is 0.45 Tg S in TOMCAT-GLOMAP, placing it at the lower end of the range of modelling estimates (i.e. 0.2 – 1.39 Tg S) (Spracklen et al., 2005; Mann et al., 2014; Sheng et al., 2015). The simulated annual global area weighted column mass of anthropogenic SO_4 in TOMCAT-GLOMAP is 1.38 mg m^{-2}. This is smaller than the Aerocom multi-model mean value of 2.15, but within the range of modelled values (1.19 – 3.64 mg m^{-2}) (Schulz et al., 2006).

Simulated sulphate aerosol from TOMCAT-GLOMAP is evaluated against an observational dataset from Heald et al. (2011), comprising of 17 aircraft campaigns which took place between 2001 and 2009. The locations of the aircraft campaigns is shown in Figure 3.9, with further details about the campaigns in Appendix A.2. The majority of the aircraft campaigns were conducted in the NH, with a mix of polluted regions (ACE, ADRIEX, TexAQS, ADIENT, EUCAARI), fire regions (DABEX, DODO, AMMA, ARCTAS spring and ARCTAS summer) and remote regions (ITOP, OP3, VOCALSUK). One campaign took place in a region with both fire and pollutant emissions (MILAGRO), while one was over a region considered remote but with aged particles (IMPEX). Due to data issues, the TROMPEX campaign dataset has been ignored here. All but two of the aircraft campaigns used the Aerodyne Aerosol Mass Spectrometer (AMS). The Aerodyne AMS measures particles with a dry diameter of less than 1µm (PM1), with an uncertainty of approximately 30-35% (Bahreini et al., 2009). The ACE campaign used Fourier Transform Infrared Spectroscopy (FTIR) filter measurements, while the ITCT used Particle-Into-

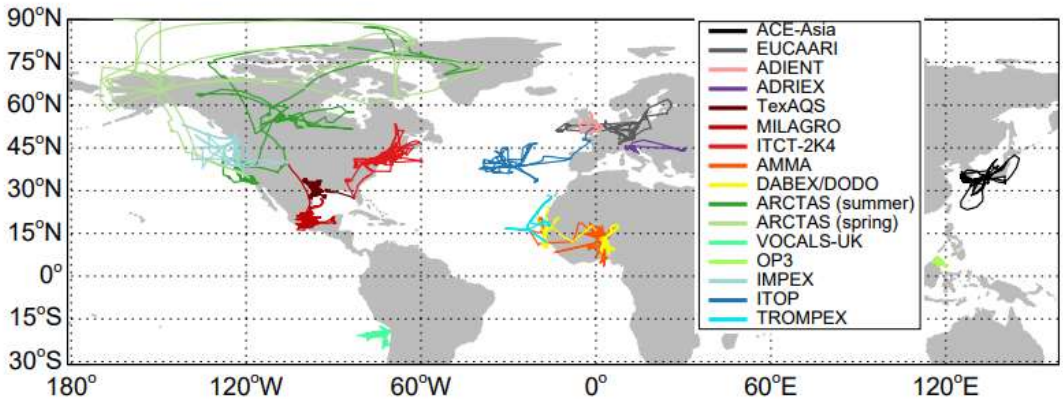

Figure 3.9 Flight tracks for the aircraft campaigns used in **Figure** 3.10. From Heald et al. (2011), Figure 1.

Liquid Sampler (PILS) measurements of water soluble organic carbon (Heald et al., 2011).

TOMCAT output for the year 2008 is used in the evaluation. The observational datasets from Heald et al. (2011) are given in mass concentrations (µg sm^{-3}) at standard temperature and pressure (STP, i.e. 298 K, 1atm). Therefore, in order to be equivalent all model data is converted into aerosol concentrations at STP following Kapadia (2015):

$$[Aerosol_x]_{STP_{i,j,k,m}} = [Aerosol_X]_{model_{i,j,k,m}} \cdot \frac{\rho air_{STP}}{\rho air_{model_{i,j,k,m}}} \cdot \frac{T_{model_{i,j,k,m}}}{T_{STP}} \quad (3.4)$$

where $[Aerosol_x]_{STP}$ = Concentration of aerosol component X at STP

$[Aerosol_x]_{model}$ = Concentration of aerosol component X from model

ρ_{airSTP} = Density of air at STP

$\rho_{airmodel}$ = Density of air from model

T_{model} = Temperature from model

T_{STP} = Temperature at STP (273 K)

Figure 3.10 displays the comparison of simulated and observed sulphate profiles. There is reasonable agreement between the model and observations from most aircraft campaigns, however there are several datasets with substantial discrepancies. Simulated sulphate concentrations are substantially larger than observations near the surface over the AMMA, ADRIEX and ACE

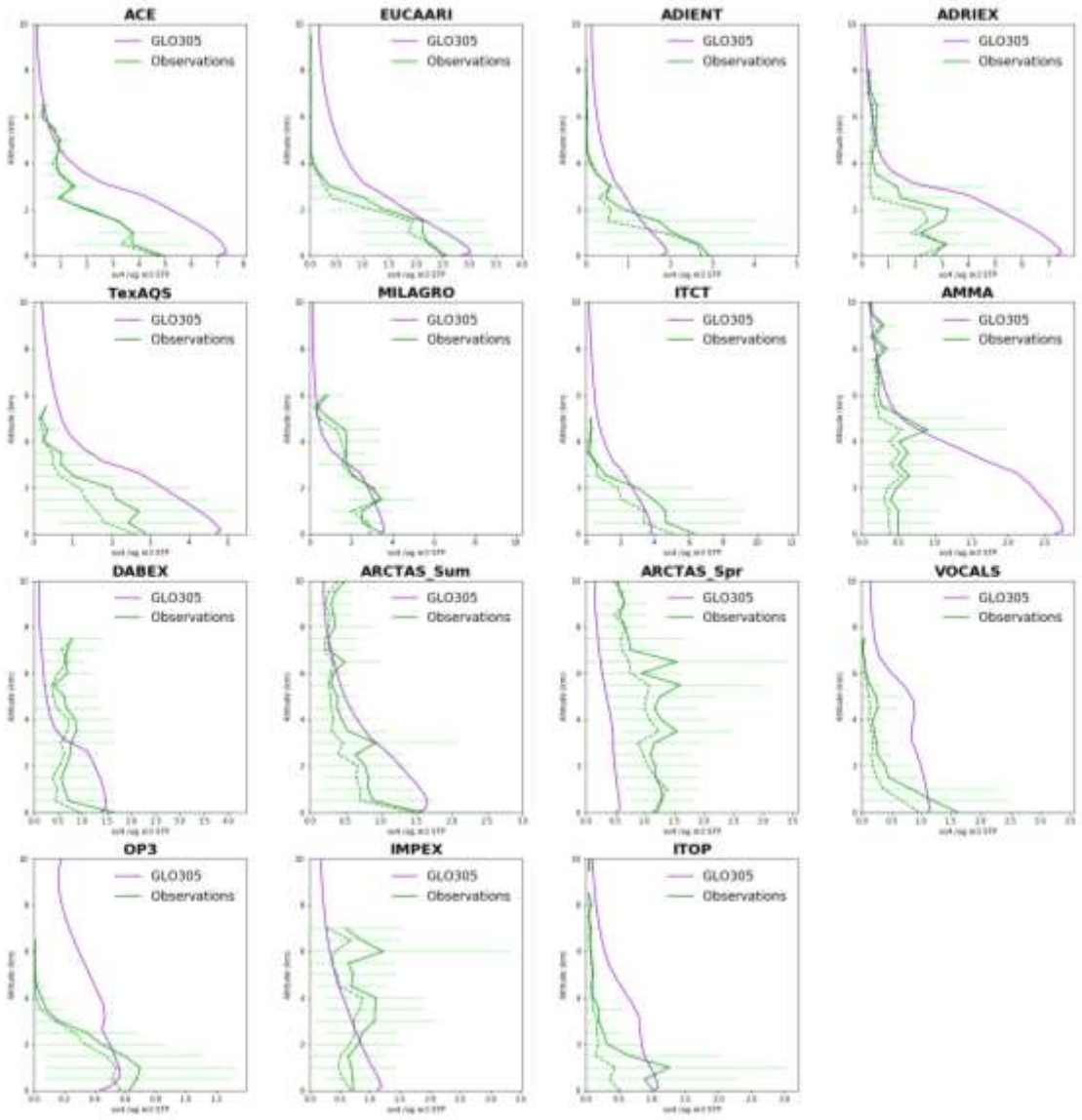

Figure 3.10 Monthly mean simulated sulphate aerosol concentrations (purple) compared against observed concentrations from aircraft campaigns Heald et al. (2011). Aircraft data is displayed as mean (solid green line), median (dashed line) and standard deviation (horizontal line).

campaign flight tracks. The ACE and ADRIEX campaigns were both over polluted regions (i.e. East Asia and Central Europe) while the AMMA campaign was over a fire region (West Africa), indicating that TOMCAT tends to overestimate sulphate concentrations in areas of higher aerosol concentrations. This may be a result of the emissions fields used in TOMCAT overestimating emissions sources, or simulated deposition and atmospheric loss of sulphate being too low. However, the simulated concentrations fall with one standard deviation of the observed concentrations for seven of the campaigns datasets.

Also, some of the difference is caused by the relatively coarse temporal and spatial resolution of TOMCAT simulated values compared to observed datasets. The global concentrations of simulated surface sulphate aerosol is shown in Figure 3.11b, showing the highest concentrations in or downwind of industrialised areas such as East Asia and India.

For BC aerosol, the global annual burden of 93.27 Tg is comparable to the range of estimates from other modelling studies (Reddy and Boucher, 2007; Vignati et al., 2010; Lee et al., 2013), however this value is poorly constrained (Lee et al., 2013). The simulated annual global area weighted column mass of anthropogenic SO_4 in TOMCAT-GLOMAP is 0.13 mg m^{-2}, which like sulphate is at the lower end of the estimated range in other studies (0.08-0.53 mg m^{-2}) (Bond et al., 2013). Global concentrations of surface BC aerosol is shown in Figure 3.11a, while the burden in important global regions has also been calculated and compared to Reddy and Boucher (2007) estimates in Table 3.2.

Table 3.2 Annual BC burden in geographical regions and globally in TOMCAT-GLOMAP and from Reddy and Boucher (2007).

Region	Annual BC burden (Gg yr^{-1})			
	TOMCAT-GLOMAP		LMD[a]	
S. America	6.09	(6.5%)[b]	4.52	(6.5%)
N. America	5.27	(5.7%)	6.97	(10.0%)
Africa	26.69	(28.6%)	9.47	(13.6%)
Europe	5.82	(6.2%)	8.23	(11.8%)
Middle East	1.40	(1.5%)	3.12	(4.5%)
South Asia	9.40	(10.1%)	10.86	(15.6%)
East Asia	32.57	(34.9%)	25.65	(36.8%)
Australia	0.36	(0.4%)	0.62	(0.7%)
Pacific Islands	0.21	(0.2%)	0.42	(0.6%)
Global	93.27		69.7	

[a] Laboratoire de Météorologie Dynamique General Circulation Model (Reddy and Boucher, 2007).

[b] Percentage contribution to global burden

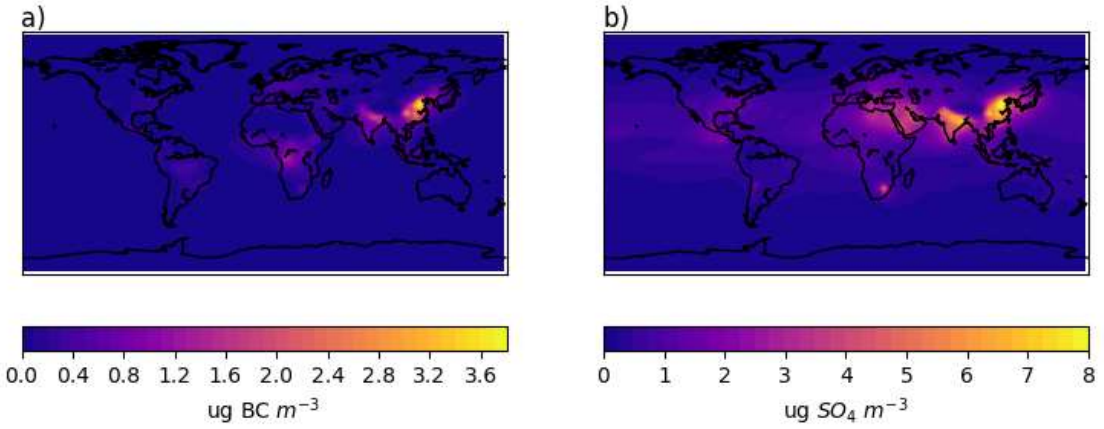

Figure 3.11 Simulated global surface concentrations of black carbon aerosol (a) and sulphate aerosol (b) in µg m^{-3}.

There is generally good agreement between the two models on the relative contribution of geographical regions to the global BC burden, with East Asia being the largest contributor. The greatest disagreement between the two is the relative contributions from Africa and South Asia, with TOMCAT simulating more than double the BC burden over Africa, at 28.6% of the global burden, compared to 13.6% in Reddy and Boucher (2007). This may be caused by larger estimates of fire emissions in TOMCAT emissions inventories, as biomass burning is a substantial source of BC emission in Africa. The Americas and Europe contribute similarly to the global burden in TOMCAT (~6%), while in Reddy and Boucher (2007) there is a slightly large contribution for North America and Europe, although the absolute simulated burden are comparable.

3.5.6. Model evaluation summary

The TOMCAT-GLOMAP model used has been updated from that described by Monks et al. (2017), with improved NPF, cloud and photolysis representation and the introduction of Mårtensson sea spray emissions (Gordon et al., 2017). Model simulations were evaluated for a number of gas-phase species (O_3, CH_4, NO_x, CO) and aerosol species (sulphate, BC), with observations from aircraft, satellites and ozonesondes.

In the gas-phase, the model broadly shows a good agreement with observed values, although with some regional biases. Compared to observations TOMCAT simulated O_3 and OH has improved relative to Monks et al. (2017), although there remains a slight low-bias in simulated sub-column O_3, and an overestimation of OH near the surface. For aerosol, TOMCAT is able to simulate global aerosol burdens in good agreement with other modelling estimates, with good regional representation of BC aerosol. Differences between the model and observations is likely due to a number of factors, such as the relatively coarse spatial and temporal model resolution, uncertainties in the emission inventories and errors in observations. However, good overall agreement of model simulations with different observations indicates that the model is suitable for simulating global changes to various SLCPs.

3.6. Offline radiative transfer model

Throughout this thesis the offline radiative transfer model SOCRATES is used to calculate the radiative effects of tropospheric O_3 and aerosol changes from the PI to PD. SOCRATES (Suite Of Community RAdiative Transfer codes based on Edwards and Slingo), is a model for calculating radiative fluxes, derived from the Edwards-Slingo offline radiative transfer model (Edwards and Slingo, 1996). SOCRATES has been used extensively in conjunction with TOMCAT-GLOMAP for calculating RF from simulated distributions of several SLCPs including BC, O_3 and CH_4 (Riese et al., 2012; Bekki et al., 2013; Rap et al., 2013; Richards et al., 2013; Rap et al., 2015). SOCRATES uses a delta-Eddington two-stream scattering solver at all wavelengths, splitting the radiation spectrum into six bands in the shortwave (SW) region and into nine bands in the longwave (LW). Monthly mean climatologies are used as input for gas-phase species, with temperature and water vapour taken from ECMWF reanalyses. Climatological clouds are provided by the International Satellite Cloud Climatology Project (ISCCP) dataset (Rossow and Schiffer, 1999). The SOCRATES code was run at the TOMCAT resolution (2.8° × 2.8° in the horizontal and 31 pressure levels).

3.6.1. Tropospheric ozone radiative forcing calculations

In this thesis, SOCRATES is used to calculate the RF of tropospheric O_3 changes simulated by TOMCAT-GLOMAP. Forster et al. (2011) found that Edwards-Slingo calculations of radiative changes due to tropospheric O_3 were in very good agreement with forcing estimates. In AR5, there was a move to the concept of effective RF (ERF) (Myhre et al., 2013b) to more completely capture the expected global energy budget change from a given driver. The ERF metric is a development of RF, accounting for all rapid adjustments including tropospheric temperature and cloud feedbacks (Myhre et al., 2013b). ERF is now commonly used as a more comprehensive indicator of the effect of a species on climate: however, previous studies suggest that the more traditional stratospherically adjusted RF is very similar to ERF for O_3 change (Myhre et al., 2013b; Shindell et al., 2013; Richardson et al., 2019). Here, the stratospherically adjusted RF is used due to the constraint of using a CTM rather than an online climate model. The fixed dynamical heating approximation from Fels et al. (1980) was used. The model calculates changes in the stratospheric heating rate due to the O_3 perturbation, which are then applied to the temperature field. SOCRATES is then run iteratively until stratospheric temperatures reach equilibrium (Forster and Shine, 1997; Rap et al., 2015). In Chapter 5, the Rap et al. (2015) radiative kernel is used, derived from SOCRATES, as a more efficient but still accurate approach to calculating O_3 radiative effects (Soden et al., 2008).

3.6.2. Aerosol radiative forcing calculations

SOCRATES was also used to calculate the radiative effect of changes to aerosols, with separate calculations for the forcing due to aerosol-radiation interactions (aerosol direct effect) and aerosol-cloud interactions (aerosol indirect effect). The radiative effects of changes to aerosol is computed by calculating the change in the top of atmosphere radiative flux between a control and perturbed simulation.

In order to calculate the direct aerosol radiative effect, the scattering and absorption coefficients (in m^2 kg^{-1}), for each aerosol mode and spectral band is calculated following the method of Bellouin et al. (2013). These optical properties determine the magnitude of scattering and absorption per unit mass of aerosol and are obtained for individual components from look up tables based on Table A1 in Bellouin et al. (2011).

The radiative effect of aerosol-cloud interaction calculated here considers only the first indirect effect, i.e. changes to reflective properties of clouds due to the availability of cloud condensation nuclei (CCN). To calculate this, cloud droplet number concentration (CDNC) are calculated from simulated aerosol fields. The Nenes and Seinfeld (2003) parameterisation of cloud drop formation is used here, a parameterisation used previously in conjunction with GLOMAP and shown to have good agreement with aircraft measurements of CDN (Pringle et al., 2009; Scott et al., 2015; Butt et al., 2016). The simulated monthly-mean aerosol size distribution is converted into a super-saturation distribution which is then used to calculate the number of activated particles for a given super-saturation. A constant updraft velocity is used of 0.3 m s^{-1} over land and 0.15 m s^{-1} over oceans. Once CDNC has been calculated, equation (6.5) is used to calculate the change to cloud droplet effective radius ($re_{perturbed}$) in each simulation. Radiative changes due to the first indirect effect are calculated relative to a control simulation, which has a fixed cloud droplet effective radius of 10 μm ($re_{control}$) due to constraints of the ISCCP approach to calculating liquid water path (Rossow and Schiffer, 1999).

The perturbed effective radius is calculated using the following equation:

$$re_{perturbed} = re_{control}[\frac{CDNC_{control}}{CDNC_{perturbed}}]^{\frac{1}{3}} \quad (6.5)$$

This calculation is performed for every grid point at 600 hPa and the surface, where clouds are assumed to be formed of liquid droplets. The perturbed effective radius is then used to calculate the change in perturbed TOA radiative flux relative to the control run.

4. Tropospheric ozone radiative forcing uncertainty due to pre-industrial natural emissions

4.1. Introduction

In this chapter, revised estimates of natural emissions in the pre-industrial atmosphere are utilised to examine uncertainty in tropospheric O_3 RF over the industrial era. As discussed in Section 2.2, tropospheric O_3 is the 3rd most important anthropogenic greenhouse gas after CO_2 and CH_4, however the estimated RF is highly uncertain. The Intergovernmental Panel on Climate Change (IPCC) current best estimate for tropospheric O_3 RF over the industrial era is 0.4 ± 0.2 Wm^{-2} (Myhre et al., 2013b). With the availability of satellite data and surface monitoring stations, present-day (PD) tropospheric O_3 radiative effect is relatively well constrained (Rap et al., 2015). The large uncertainty range (0.2-0.6 Wm^{-2}) is therefore primarily associated with the uncertainty in pre-industrial (PI) O_3 concentrations (Myhre et al., 2013b; Stevenson et al., 2013), caused by a lack of reliable quantitative measurements of tropospheric O_3 prior to the 1970s (Volz and Kley, 1988; Cooper et al., 2014). Checa-Garcia et al. (2018) found that differences in PI estimates between CMIP5 and CMIP6 cause an 8-12% variation in O_3 RF estimates. Recent analysis of oxygen isotopes in polar ice cores indicates that tropospheric O_3 increased by less than 40% between 1850 and 2005 and O_3 RF is likely lower than the 0.4 Wm^{-2} estimate (Yeung et al., 2019).

As well as anthropogenic sources, O_3 precursor gases such as CH_4, CO and NO_x have natural emission sources from wildfires, wetlands, lightning and biogenic emissions (see Section 2.2.2). Changes in the natural environment therefore also influence the concentration and distribution of tropospheric O_3 (Monks et al., 2015; Hollaway et al., 2017). However, the human impact on natural emissions over the industrial era is more uncertain than on anthropogenic emissions (Mickley et al., 2001; Arneth et al., 2010). For example, wildfires emit large quantities of CO, NO_x, CH_4 and non-methane volatile organic compounds (NMVOCs) (van der Werf et al., 2010; Voulgarakis and Field, 2015), which influence the chemical production of O_3 (Wild, 2007). Therefore, an accurate representation of PI fire occurrence is required for PI to PD tropospheric O_3 RF calculations.

Recent studies suggest that the relationship between humans and fire (Bowman et al., 2009) is more complex than previously assumed (Doerr and Santín, 2016). The expansion of agriculture and land segregation since PI has decreased the abundance and continuity of fuel, inhibiting fire spread (Marlon et al., 2008; Swetnam et al., 2016) and hence total emissions. Furthermore, at the global scale increased population density results in declining fire frequency (Knorr et al., 2014; Andela et al., 2017). Increased agricultural land coupled with active fire suppression and management policies mean that human activity has likely caused total fire emissions to decline since the PI (Daniau et al., 2012; Marlon et al., 2016; Hamilton et al., 2018). Paleoenvironmental archives of fire activity also reflect a decline of fire over the industrial era in many regions (Marlon et al., 2016; Rubino et al., 2016; Swetnam et al., 2016). This change in understanding of PI fire emissions has been shown to have a strong influence on aerosol RF: Hamilton et al. (2018) estimated a 35-91% decrease in global mean cloud albedo forcing over the industrial era when using revised PI fire emission inventories.

Emissions of biogenic VOCs (BVOCs), such as isoprene and monoterpenes, from vegetation also affect tropospheric O_3 formation. Isoprene contributes to the formation of peroxyacetylnitrate (PAN), which has a lifetime of several months in the upper atmosphere (Singh, 1987), allowing long-range transport of

reactive nitrogen and enhancing O_3 formation in remote regions. Previous studies of PI tropospheric O_3 frequently assumed that PI BVOC emissions were equivalent to those in PD (Stevenson et al., 2013). However, BVOC emissions are sensitive to climate, vegetation type and foliage density, each of which has changed since the PI (Laothawornkitkul et al., 2009; Hantson et al., 2017) and therefore need to be accounted for when calculating PI to PD O_3 RF.

The aim of this chapter is to examine the effect of revised PI fire and BVOC emission inventories on PI-PD tropospheric O_3 RF estimates. The global CTM TOMCAT is used in conjunction with the SOCRATES radiative transfer model to investigate the impact of these improved natural PI emission inventories on PI tropospheric O_3 and how changes in concentration subsequently alter O_3 RF.

4.2. Emission inventories

4.2.1. Fire emission inventories

Following the experimental setup of Hamilton et al. (2018), one PD fire emission inventory and three PI inventories are simulated in TOMCAT to investigate the sensitivity of tropospheric O_3 RF to PI fire uncertainty. The CMIP6 PI inventory is treated as a control, as this has been widely used in previous studies and was developed from a set of global fire models, with SIMFIRE-BLAZE and LMfire providing PI perturbation scenarios from this baseline.

4.2.1.1. Pre-industrial and present-day CMIP6

CMIP6 provides monthly mean emissions of CO, NO_x, CH_4 and VOCs from fires. In the PD, CMIP6 emissions are derived from satellite estimates of global burden area and active fire detections (Randerson et al., 2012; Giglio et al., 2013a). In the absence of satellite data, historical CMIP6 fire emissions are generated by merging PD satellite observations with fire proxy records, visibility records and analysis from six fire models (van Marle et al., 2017).

4.2.1.2. Pre-industrial SIMFIRE-BLAZE

The SIMFIRE-BLAZE PI fire emission inventory was developed using the LPJ-GUESS-SIMFIRE-BLAZE model. The PI emissions used in this study are the mean for the period 1750-1770 (Hamilton et al., 2018). The LPJ-GUESS dynamic vegetation model predicts ecosystem properties for given climate variables (Smith et al., 2014), which, combined with the HYDE 3.1 dataset of human land-use change, allows simulation of global PI land cover (Klein Goldewijk et al., 2011). The fire model SIMFIRE-BLAZE calculates total burned area (Knorr et al., 2014; Rabin et al., 2017). Akagi et al. (2011) emissions factors were used with separate treatment of herbaceous and non-herbaceous, tropical and extratropical vegetation to produce emission inventories. Total PI fire emissions of gas species in the SIMFIRE-BLAZE inventory are 28% larger than in the PI CMIP6 inventory (Figure 4.1).

4.2.1.3. Pre-industrial LMfire

The LPJ-LMfire model calculates dry matter consumed by fire and simulates natural wildfire ignition from lightning (Pfeiffer et al., 2013; Murray et al., 2014). Land use is prescribed for the year 1770 using the KK10 scenario from Kaplan et al. (2011). Emissions factors for herbaceous and non-herbaceous vegetation are used to calculate fire emissions from dry biomass burned in each grid cell (van der Werf et al., 2010; Li et al., 2012). Burned area is calculated based on fuel availability and an additional 10% of harvested agricultural crop material is assumed to be burned each year. Total PI fire emissions in LMfire are approximately double the SIMFIRE-BLAZE inventory, and thus four times larger than CMIP6 emissions (Figure 4.1).

4.2.1.4. Assessment of fire emissions inventories

Despite being significantly larger than CMIP6 and SIMFIRE-BLAZE, emissions from LMfire have been shown to be within the quantifiable uncertainty of fire emissions (Lee et al., 2013), and compare more favourably than the other two inventories with Northern Hemisphere (NH) ice core records in Greenland and Wyoming (Chellman et al., 2017; Hamilton et al., 2018). In addition to the

examination of paleoenvironmental archives with PI fire emissions datasets by Hamilton et al. (2018), simulated annual mean surface PI CO concentrations in Antarctica for each fire emissions inventory were compared to the Southern Hemisphere (SH) ice core CO record from Wang et al. (2010). Simulated Antarctic CO concentrations using PI CMIP6 emissions are 37 ppb, substantially lower than the value in Wang et al. (2010) of 45 ± 5 ppb in 1750. This CMIP6 value is closer to the 650-year minimum that occurred in the mid-17th century (38 ppb). When using SIMFIRE-BLAZE and LMfire emissions, Antarctic CO concentrations for 1750 are estimated at 48 ppb and 61 ppb, respectively. The overestimation when using LMfire suggest that SH CO emissions may be high for 1750; however, they are comparable to the peak CO concentration measured in the late 1800s (55 ± 5 ppb) when fire emissions also peaked (van der Werf et al., 2013). As 1850 is also often used as a PI baseline year when calculating RF, LMfire is proposes as a realistic upper bound to possible PI fire emissions.

The combined evaluation of these inventories in Hamilton et al. (2018) and here indicates that although the revised PI fire inventories differ considerably from each other and are larger than CMIP6, they are closer to proxy records than CMIP6 estimates and therefore their respective impacts on tropospheric O_3 RF need to be considered.

4.2.2. Biogenic emissions inventories

4.2.2.1. Present-day CCMI

The PD control biogenic emissions were provided from the CCMI biogenic emissions inventory. CCMI mean annual BVOC emissions, comprising of isoprene and monoterpenes, are derived using the Model of Emissions of Gases and Aerosols from Nature (MEGAN) model (Guenther et al., 2012) under the MACC project (Sindelarova et al., 2014). The CCMI inventory estimates global BVOC emissions at 623 Tg yr^{-1}, in reasonable agreement with surface flux measurements and other modelling studies (Arneth et al., 2008; Sindelarova et al., 2014; Rap et al., 2018).

4.2.2.2. Pre-industrial and present-day LPJ-GUESS

Alternative biogenic emissions were produced using the LPJ-GUESS dynamic vegetation model simulating isoprene and monoterpenes (Arneth et al., 2007; Schurgers et al., 2009). Total PD emissions and distribution in the LPJ-GUESS inventory (i.e. 607 Tg yr^{-1}) are similar to the PD CCMI inventory (Figure 4.2). The relative contributions from isoprene and monoterpenes differs between the inventories however, with substantially smaller monoterpene emissions in the LPG-GUESS inventory (Table 4.1). For the PI, the LPJ-GUESS biogenic emissions inventory is based on the mean for the period 1750-1770 and is estimated at 836 Tg yr^{-1}. The larger emissions in the PI estimates are primarily driven by larger isoprene emissions. There are large spatial differences between the PI LPJ-GUESS and PD CCMI inventories, with significantly higher emissions in South America and Central Africa, and lower emissions in South-East Asia in the PI LPJ-GUESS inventory (Figure 4.2).

Table 4.1 Annual emissions of isoprene and monoterpenes in each of the three inventories used in this study.

Inventory	Isoprene (Tg yr^{-1})	Monoterpenes (Tg yr^{-1})
CCMI (PD)	525	98
LPG-GUESS (PD)	568	39
LPJ-GUESS (PI)	788	47

4.3. Model specifications and simulations

In order to investigate the effect of natural PI emissions on PI to PD changes in tropospheric O_3 concentrations, a single PD and six PI simulations were performed with TOMCAT-GLOMAP. TOMCAT-GLOMAP was run for 1-year, using 2008 meteorological fields following a 1-year spin up period. The PD simulation used the Global Fire Emissions Database (GFED) version 4s (GFED v4s) fire emission inventory (as employed in the Coupled Model Intercomparison Project phase 6; CMIP6) (Randerson et al., 2017; van Marle et al., 2017), biogenic emissions from Chemistry-Climate Model Initiative (CCMI)

(Sindelarova et al., 2014) and anthropogenic emissions from the Monitoring Atmospheric Composition and Climate project (MACCity) (Lamarque et al., 2010).

Global mean surface CH_4 concentrations are scaled in TOMCAT to be 1789 ppb in PD and 722 ppb in the PI (Etheridge et al., 1998; Dlugokencky et al., 2005; Hartmann et al., 2013; McNorton et al., 2016a). In all PI simulations, anthropogenic emissions are zero except biofuel emissions taken from AeroCom for the year 1750 (Dentener et al., 2006). The first set of three simulations, namely CMIP6, SIMFIRE-BLAZE and LMfire, investigated the impact of fire emissions only by keeping PI BVOC emissions (i.e. isoprene and monoterpenes) at PD values (Table 4.2). The second set of three simulations, i.e. CMIP6-BIO, SIMFIRE-BLAZE-BIO and LMfire-BIO, investigated the additional impact of PI biogenic emissions, by combining each PI fire emission inventory with an estimate of PI BVOC emissions from the LPJ-GUESS model (Table 4.2).

4.4. Pre-industrial emissions

Figure 4.1a-d shows annual latitudinal fire emissions of CO, NO_x, CH_4 and VOCs for the CMIP6, SIMFIRE-BLAZE and LMfire PI inventories, compared to the total PD emissions from the CMIP6 inventory. BVOC emissions (i.e. isoprene and all

Table 4.2 Details of emissions used in each simulation. All simulations are run with present-day meteorology with a one-year spin-up.

Simulation	Fire emissions	Biogenic emissions
PD CMIP6	GFEDv4	CCMI
PI CMIP6	CMIP6	CCMI
PI SIMFIRE-BLAZE	SIMFIRE-BLAZE	CCMI
PI LMfire	LMfire	CCMI
PI CMIP6-BIO	CMIP6	LPJ-GUESS
PI SIMFIRE-BLAZE-BIO	SIMFIRE-BLAZE	LPJ-GUESS
PI LMfire-BIO	LMfire	LPJ-GUESS

monoterpenes) from the LPJ-GUESS inventory are compared with the PD CCMI inventory (Figure 4.1e). In the PI CMIP6 simulation, global CO emissions have increased by a factor of 2.5 between PI and PD from 381 Tg yr^{-1} to 970 Tg yr^{-1}. The main driver of this increase is industrial emissions, particularly in the NH mid-latitudes. There is large variation in simulated CO emissions between the three PI fire inventories: 644 Tg yr^{-1} in SIMFIRE-BLAZE (69% larger than CMIP6) and 1152 Tg yr^{-1} in LMfire (200% larger). Estimates of CO emissions using LMfire results in total global emissions which are larger than the PD estimate, which also includes anthropogenic sources.

Global NO_x emissions also vary considerably between PI inventories, with values in the SIMFIRE-BLAZE inventory increasing 13% compared to the CMIP6 inventory (36 Tg yr^{-1} compared to 32 Tg yr^{-1}). This difference is largely due to increased emission in NH mid-latitudes within SIMFIRE-BLAZE. NO_x emissions in LMfire are 112% larger than the CMIP6 total (68 Tg yr^{-1}), with the most significant increases in the extra-tropics (Figure 4.1b).

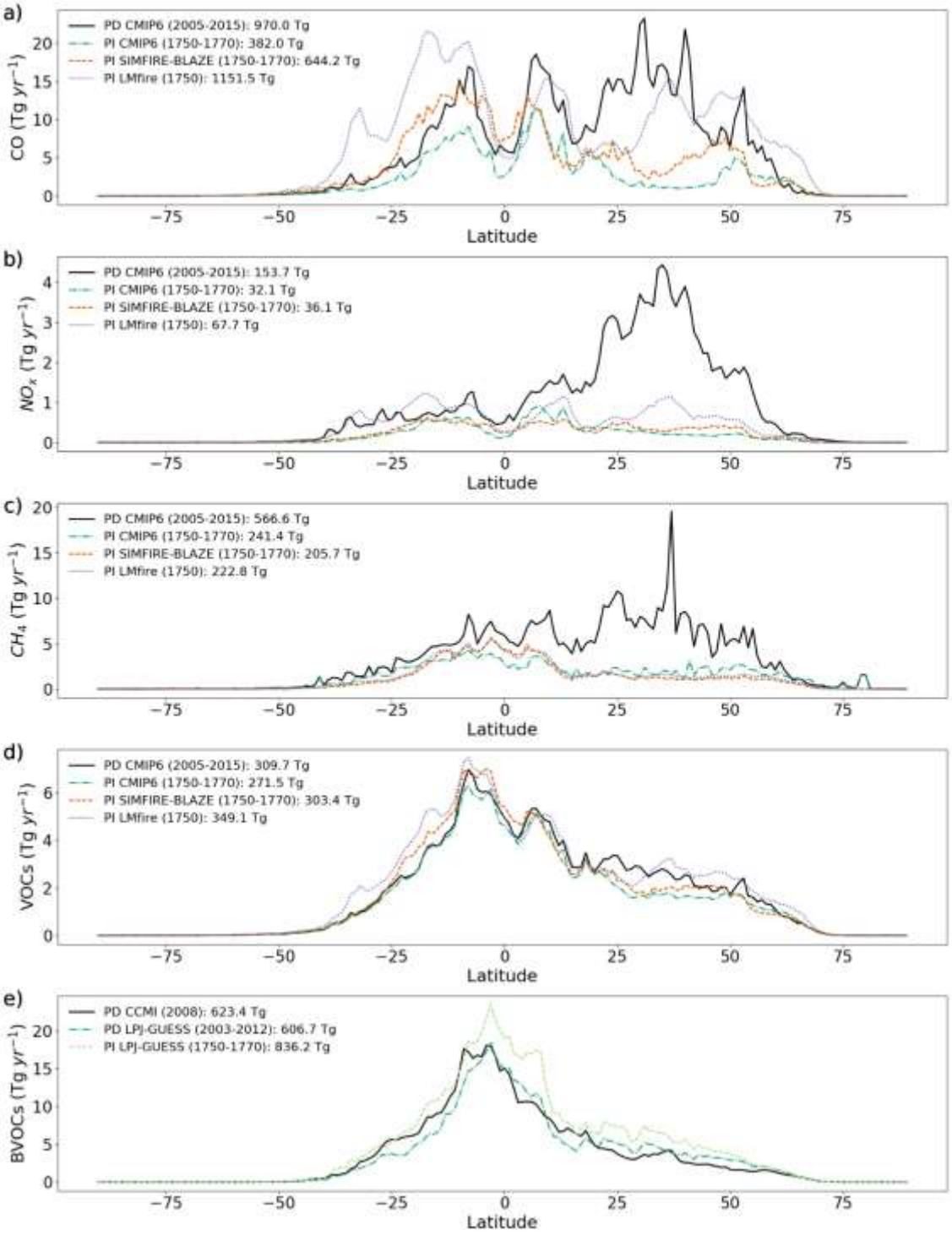

Figure 4.1 Annual latitudinal mean fire emissions (in Tg/yr) of (a) CO, (b) NO_x, (c) CH_4 and (d) VOCs and annual zonal mean BVOC emissions (e), for PD (solid black line), PI CMIP6 (dashed green), PI SIMFIRE-BLAZE (dotted orange), PI LMfire (dashed purple), PD LPJ-GUESS (dashed dark green) and PI LPJ-GUESS (dotted light green).

As CH_4 emissions from fires are significantly smaller than CO emissions (Voulgarakis and Field, 2015) increased PI fire estimates do not substantially alter total CH_4 emission. CH_4 emissions in SIMFIRE-BLAZE and LMfire are similar in amount and distribution, 15% and 9% lower than CMIP6, respectively. There is an increase in SH CH_4 emissions in both SIMFIRE-BLAZE and LMfire compared to CMIP6 but a decrease in the NH and SH mid-latitudes. Total PI CH_4 emissions are greatest in CMIP6 at 241 Tg yr^{-1}, approximately 43% of PD emissions (Figure 4.1c).

In terms of fire-emitted VOC species (i.e. sum of all VOC species with a significant source from wildfires), their size and distribution of emissions is fairly consistent between PD and PI inventories. Total global VOC emissions are largest in LMfire at 349 Tg yr^{-1}, 29% larger than PI CMIP6 (271 Tg yr^{-1}) and 13% larger than PD CMIP6 (310 Tg yr^{-1}). PI CMIP6 are 87% of PD CMIP6 values, with PI SIMFIRE-BLAZE at 97% (303 Tg yr^{-1}). The distribution of global VOC emissions is relatively uniform across all inventories, however, individual species do have larger variability between inventories. Formaldehyde and acetylene have substantially increased SH emissions in SIMFIRE-BLAZE and LMfire likely due to differences in emission factors (Figure 4.1d).

Figure 4.1e shows a comparison of the BVOC emission inventories from the PD CCMI, PD LPJ-GUESS and PI LPJ-GUESS. The BVOC emissions in the two PD inventories are similar although with larger NH and lower SH emissions in PD-LPG-GUESS compared to PD CCMI. The PI LPJ-GUESS estimate (836 Tg yr^{-1}) is 37% larger than its PD equivalent and 34% larger than PD CCMI, mainly due to decreased isoprene emissions in PD compared to PI, although with a very similar spatial distribution (Figure 4.2). The reduction of BVOC emissions between PI and PD is due to crop expansion, land cover changes and CO_2 inhibition (Hantson et al., 2017), and is consistent with previous studies reporting ~25% (Lathière et al., 2010; Pacifico et al., 2012; Hollaway et al., 2017) and ~35% (Unger, 2014) larger PI values than PD.

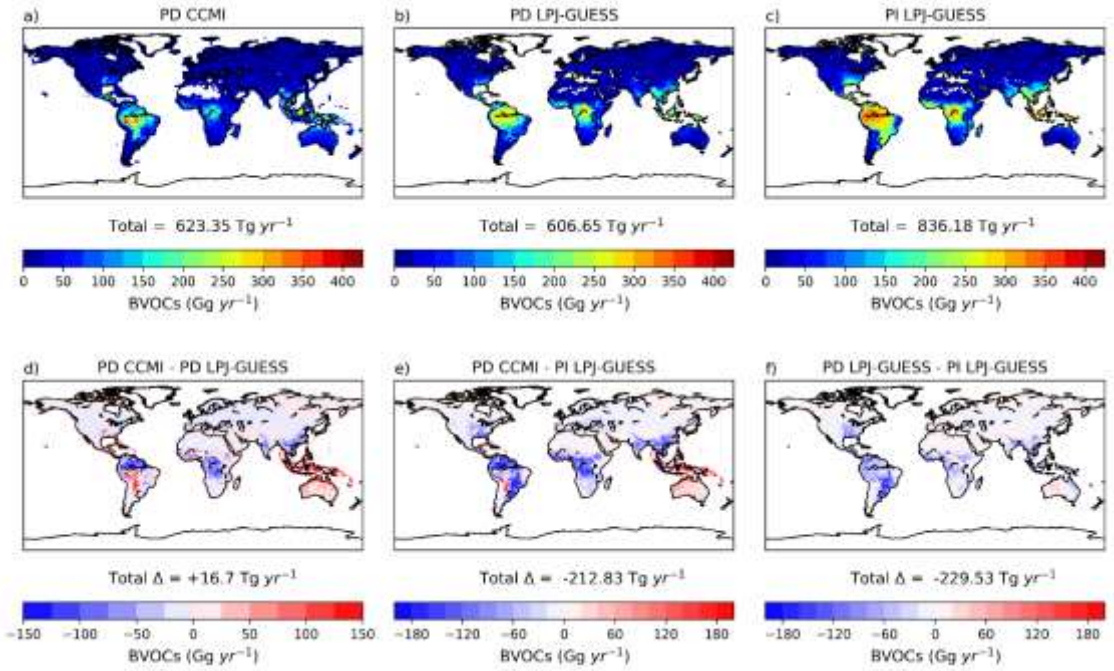

Figure 4.2 Annual BVOC (isoprene + monoterpenes) emissions in the two present-day biogenic emissions inventories (CCMI and LPJ-GUESS) and the pre-industrial LPJ-GUESS inventory. Top panels (a-c) show total emissions per year, while lower panels (d-f) show differences between the three inventories. Total annual emissions and difference in annual emissions are also shown.

4.5. Pre-industrial fire emissions effect on ozone

Annual emissions of O_3 precursors and their contribution to the formation of tropospheric O_3 are shown in Figure 4.3. The largest change between simulations is on the global tropospheric CO burden which varies by up to 100 Tg depending on the PI fire emission inventory employed: 195 Tg in the PI CMIP6 simulation, 232 Tg in PI SIMFIRE-BLAZE (18% higher than CMIP6) and 295 Tg in PI LMfire (50% higher) (Table 4.3).

The difference in global NO_x burden between PI simulations is less pronounced, with increases of 4% and 18% in PI SIMFIRE-BLAZE and PI LMfire respectively, relative to PI CMIP6. The annual mean NH/SH ratio of tropospheric NO_x burden in PI simulations is 1.09, 1.12 and 1.18 for CMIP6, SIMFIRE-BLAZE and LMfire, respectively. Simulated airmass-weighted global mean concentrations of tropospheric OH, which plays a key role in tropospheric O_3 precursor oxidation

and O_3 formation, are 1.06, 1.06 and 1.11 $\times 10^6$ mol cm^{-3} in CMIP6, SIMFIRE-BLAZE and LMfire, respectively. These values all fall within one standard deviation of the ACCMIP multi-model mean of 1.13 ± 0.17 (Naik et al., 2013). PI OH concentrations are lower than PD simulated values (1.12 $\times 10^6$ mol cm^{-3}), due to the higher concentrations of OH precursors NO_x and O_3 in PD outcompeting the effect of increased CH_4 and CO concentrations which deplete OH (Naik et al., 2013). The NH/SH OH ratio is 1.25 ± 0.02 in the PI simulations compared to 1.41 in PD, slightly larger than the corresponding ACCMIP multi-model mean values (1.13 ± 0.09 and 1.28 ± 10, respectively) but within the inter-model range and reflecting the expected PI to PD increase (Naik et al., 2013).

Changes to the atmospheric concentration and distribution of O_3 precursor species lead to changes in the tropospheric O_3 burden. The PI CMIP6 simulation produced the lowest tropospheric O_3 burden at 232 Tg. In PI SIMFIRE-BLAZE the burden is 242 Tg (4% higher than CMIP6) while in LMfire it is 273 Tg (18% higher). These represent a PI to PD tropospheric O_3 burden change of 55%, 49% and 32% for CMIP6, SIMFIRE-BLAZE and LMfire, respectively. Notably,

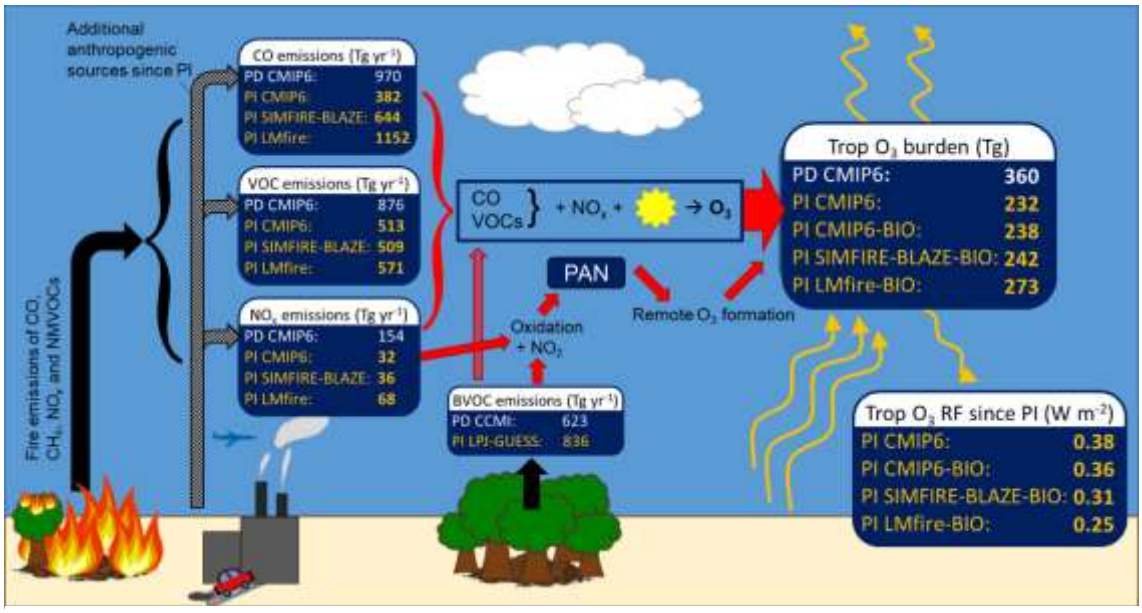

Figure 4.3 Summary schematic showing tropospheric O_3 precursor emissions from fire, biogenic and anthropogenic sources, the processes of photochemical O_3 formation, the tropospheric O_3 burden and the PI-PD RF. The magnitude of CO, NO_x, VOC and BVOC precursor emissions used in this study is shown for the PD (white text) and each PI inventory (yellow text). The resulting calculated tropospheric O_3 burden and RF when using each emission inventory are also shown.

the PI LMfire emissions inventory is the only inventory leading to a simulated PI to PD burden change of less than 40%, a value consistent with that recently indicated by isotope measurements in ice cores (Yeung et al., 2019). The differences from CMIP6 to SIMFIRE-BLAZE are primarily caused by an increase in tropospheric O_3 within the Amazon region (Figure 4.4a). The change in tropospheric O_3 vertical profile in the PI SIMFIRE-BLAZE simulation compared to PI CMIP6 (Figure 4.4c) shows increased annual mean concentrations throughout the troposphere, driven by changes at 30ºS and 50ºN. Changes between LMfire and CMIP6 tropospheric O_3 profiles are stronger, with increased O_3 at all latitudes. Compared to PI CMIP6, there is a mean global increase in O_3 column of 3.7 DU when using LMfire and 1.0 DU when using SIMFIRE-BLAZE. The largest changes occur over Central Asia, Australia and South America where tropospheric column O_3 can be as much as 9.0 DU higher in the PI LMfire simulation that the PI CMIP6 simulation (Figure 4.4). This is reflected in the changes to the vertical O_3 profile, with the largest increases in the subtropics. The difference between LMfire and CMIP6 is greatest between 600 and 800 hPa in the SH, and is roughly constant with respect to changes in altitude over the northern subtropics. The only regions where tropospheric O_3 is higher in the CMIP6 simulation are Central Africa and Indonesia, likely due to the PI CMIP6 emissions being anchored to PD fire observations and thus transferring these patterns to the PI (van Marle et al., 2017).

Table 4.3 Annual mean global tropospheric burdens of CO, NO_x and O_3, mean tropospheric OH concentration, tropospheric column O_3 in Dobson units (DU) and radiative forcing of tropospheric O_3 1750-2010 for present-day simulation and each PI fire and biogenic emission inventory.

	NO_x burden (Tg)	***CO burden (Tg)***	***Mean tropospheric OH ($x10^6$ mol cm^{-3})***	***Tropospheric column O_3 (DU)***	***O_3 burden (Tg)***	***O_3 RF 1750-2010 (Wm^{-2})***
PD CMIP6	73.2	342.6	1.12	31.0	359.9	-
PI CMIP6	44.8	195.5	1.06	19.9	231.7	0.38
PI SIMFIRE-BLAZE	46.7	231.5	1.06	20.9	241.6	0.35
PI LMfire	52.8	295.0	1.11	23.6	272.7	0.27
PI CMIP6-BIO	44.3	238.7	1.00	20.2	237.8	0.36
PI SIMFIRE-BLAZE-BIO	46.7	283.4	1.00	22.1	256.0	0.31
PI LMfire-BIO	53.4	337.1	1.08	24.4	282.8	0.25

The effect of different fire emission inventories on O_3 burden is significantly smaller than the impact on CO concentrations (Figure 4.4), as fire emissions are one of several sources of O_3 variability (Lelieveld and Dentener, 2000). O_3 production is reliant on a number of precursors which do not respond uniformly to the different estimates of fire occurrence in the inventories used here. The relatively minor response of NO_x concentrations across the three PI emissions estimates, and the prevailing NO_x-limited state across rural environments in PD (Duncan et al., 2010), suggests that increases in CO and VOCs have only a small impact on O_3 production because of NO_x availability limitations. Moreover, Stevenson et al. (2013) attributed the majority of the PI to PD shift in tropospheric O_3 to NO_x and CH_4 changes, with a relatively small contribution from CO and NMVOCs despite increasing emissions of both. However, the

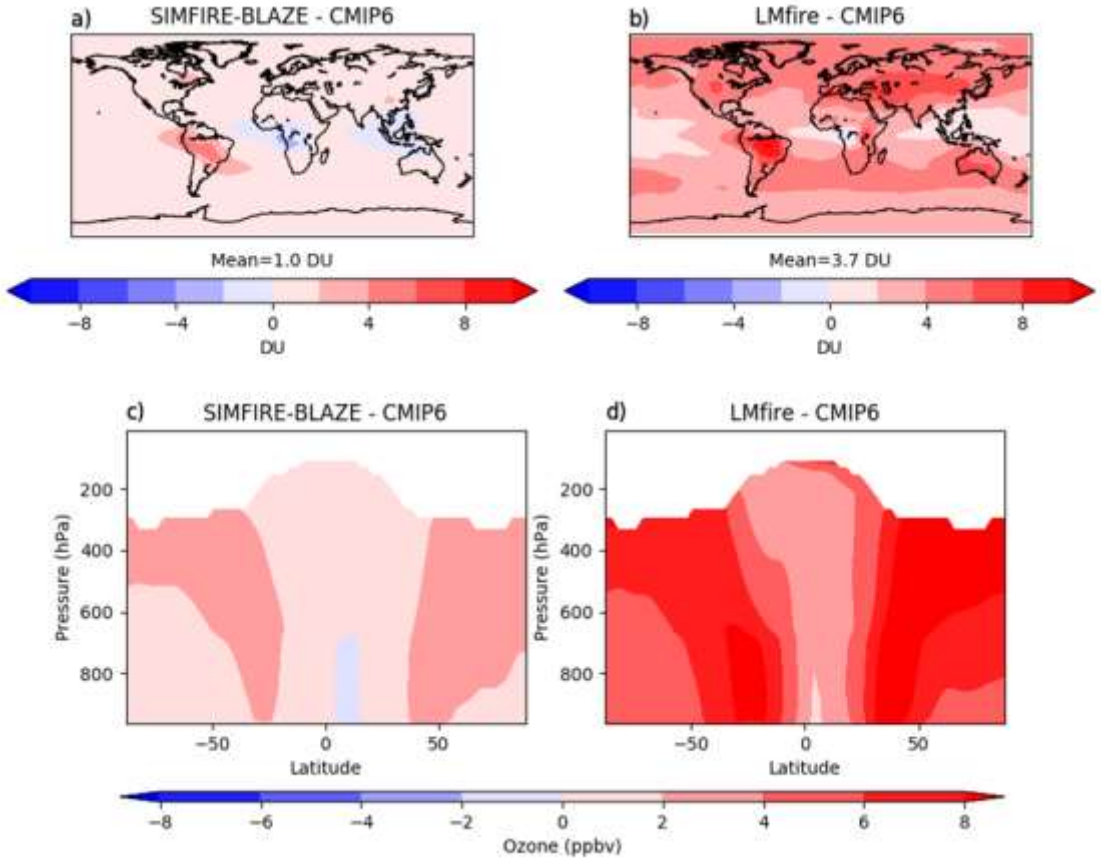

Figure 4.4 Difference in simulated PI O_3 between revised inventories SIMFIRE-BLAZE and LMfire and the CMIP6 control. Top panels (a, b) compare differences in tropospheric column O_3 in DU, lower panels (c, d) show differences in zonal mean vertical O_3 in ppb.

simulated changes still represent significant shifts in the abundance and distribution of tropospheric O_3 in the PI atmosphere.

4.6. Pre-industrial BVOC emissions effect on ozone

We repeated the three PI simulations, replacing the PD biogenic emissions with the PI LPJ-GUESS inventory. In general, the inclusion of PI BVOC emissions increases PI O_3 concentrations, due to an increased VOC source and PAN formation (Figure 4.3). For CMIP6 fire emissions, the inclusion of PI BVOCs increases the CO burden by 22% and tropospheric O_3 burden by 3%, while mean tropospheric OH concentration decreases by 6%. The decrease in OH is the most likely reason for the simulated increases in CO and O_3. The inclusion of PI BVOCs in the LMfire fire emission simulation causes a 3% decrease in tropospheric OH, and increases in tropospheric CO and O_3 of 14% and 4%, respectively.

For SIMFIRE-BLAZE, the inclusion of PI BVOCs decreases OH by 6% and increases CO and O_3 by 22% and 6%, respectively. In all simulations the inclusion of PI BVOCs has only a small effect on the NO_x burden (~1%). The effect on tropospheric O_3 of including PI BVOCs is notably larger in the simulation using SIMFIRE-BLAZE fire emissions compared to CMIP6 or LMfire. The SIMFIRE-BLAZE simulation combines fire and biogenic emissions produced using the same land-use model, with consistent vegetation distributions. The co-location of isoprene and NO_x emissions promotes PAN formation, enabling long-range transport of NO_x and enhancing O_3 production (Hollaway et al., 2017). This synergistic effect has been found to amplify the effect of biogenic emissions on tropospheric O_3 production (Bossioli et al., 2012). Therefore, if PI biogenic emissions inventories were specifically produced for each fire inventory, the corresponding impact on O_3 would likely be larger than presented here. With the inclusion of PI BVOC emissions, both the SIMFIRE-BLAZE and LMfire simulations result in a PI to PD tropospheric O_3 burden change of 40% or less, in line with estimates from ice core observations (Yeung et al., 2019).

4.7. Effect on ozone radiative forcing

The tropospheric O_3 RF was calculated using the SOCRATES radiative transfer model as described in Section 3.6.1.The estimated tropospheric O_3 RF, based on the CMIP6 PI and PD control simulations, is 0.38 Wm^{-2} (Figure 4.3 and Table 4.3), comparing well with the IPCC AR5 estimate of 0.4 ± 0.2 Wm^{-2} (Myhre et al., 2013b) and the ACCMIP multi-model mean of 0.41 ± 0.12 Wm^{-2} (Myhre et al., 2013b; Stevenson et al., 2013). When PI SIMFIRE-BLAZE and PI LMfire emissions are used instead of PI CMIP6 fire emissions, larger PI tropospheric O_3 concentrations lead to 8% (to 0.35 Wm^{-2}) and 29% (to 0.27 Wm^{-2}) decreases in O_3 RF, respectively. When the PI BVOC emission inventory is used in conjunction with each PI fires emission inventory, O_3 RF is further reduced compared to the control by 5% (to 0.36 Wm^{-2}), 18% (to 0.31 Wm^{-2}) and 34% (to 0.25 Wm^{-2}), for CMIP6, SIMFIRE-BLAZE and LMfire, respectively (Figure 4.3). While these reductions in O_3 RF are still within the IPCC uncertainty range, they are caused entirely by uncertainty in PI precursor emissions. Other key sources of uncertainty (e.g. inter-model spread, use of different radiative transfer schemes) are not accounted for here and could therefore lower estimates further. The majority of the effect on O_3 RF is caused by increased O_3 in the upper troposphere at subtropical latitudes (Figure 4.4d), where O_3 changes are up to 10 times more efficient at altering the radiative flux than in other regions (Rap et al., 2015). However, the lack of a vertical distribution to fire emissions in TOMCAT affects the simulated changes to the O_3 vertical profile. Previous studies which introduced an injection height scheme found small increases in O_3 production downwind of emission sources (Jian and Fu, 2014), although the change to total O_3 and precursors is relatively small (Bossioli et al., 2012; Zhu et al., 2018).

4.8. Summary

The revised inventories of PI fire and biogenic emissions used here substantially decrease estimates of PI to PD tropospheric O_3 RF. When using PI LMfire fire emissions, which represent a plausible upper emissions limit, O_3 RF is reduced

to 0.27 Wm^{-2}, 29% smaller than the CMIP6 simulation. Large increases in estimated PI fire occurrence drives increases in PI O_3 concentrations (3.7 DU global mean column O_3 increase for LMfire inventory) through larger emissions of CO, NO_x and VOCs. PI CO increases by up to 51% depending on the PI inventory, but the effect on O_3 production is limited by the relatively small increase in NO_x (~4%). Using PI biogenic emissions, rather than assuming PD values, further increases simulated PI tropospheric O_3, though the magnitude of this depends on the fire inventory. Thus, we find that the estimate of O_3 RF since PI decreases by up to 34% (to 0.25 Wm^{-2}) when accounting for uncertainty in PI emissions of both fires and BVOCs.

The impact of uncertainty in PI natural emissions on tropospheric O_3 RF shown here suggests that previous estimates of O_3 RF over the industrial era are likely too large. Our revised tropospheric O_3 RF estimates are at the lower end of the existing uncertainty range, without yet taking into account other sources of uncertainty. We therefore argue that the impact of uncertainty in PI natural emissions should be further investigated using more models, in order to reassess the current best-estimate and uncertainty range of O_3 RF.

5. Impact of El Niño-Southern Oscillation on the interannual variability of methane and tropospheric ozone

5.1. Introduction

In this chapter, the interannual variability (IAV) of climatically important greenhouse gases CH_4 and tropospheric O_3 is investigated. A comprehensive understanding of the processes controlling variability and trends of SLCPs in the past and present-day is essential to quantify the role of human activities in climate change. This enables the planning of effective strategies to reduce the anthropogenic impact on future climate, and improves projections of how SLCPs are likely to change in future and the impact of those changes.

Using the TOMCAT-GLOMAP CTM, different drivers of variability are isolated so that their relative importance for different species can be determined. The impact of these changes on RF is also calculated, particularly during large ENSO events such as the 1997 El Niño, which caused large changes to global emissions and atmospheric concentrations of SLCPs. ENSO is known to influence fire occurrence, wetland emission and atmospheric circulation, affecting sources and sinks of CH_4 and tropospheric O_3, but there are still important uncertainties associated with the exact mechanism and magnitude of this effect. Understanding the mechanisms driving IAV of SLCPs is important for accurate predictions of future CH_4 and O_3 concentrations, especially in the context of anthropogenic emission reductions.

While anthropogenic emissions have driven the long-term increase in CH_4 concentrations, CH_4 is also emitted from a range of natural sources (see Section 2.1.1), leading to strong IAV (Bousquet et al., 2006; Dlugokencky et al., 2011; Nisbet et al., 2016). Previous studies indicate that although anthropogenic sources may contribute to seasonal variations in atmospheric CH_4, natural sources are the primary drivers of IAV (Bousquet et al., 2006; Meng et al., 2015). Emissions from natural wetlands have been shown to be the dominant process, with emissions from fires and changes to the atmospheric sink also playing important roles (Bousquet et al., 2006; Chen and Prinn, 2006; Dlugokencky et al., 2011; Kirschke et al., 2013; McNorton et al., 2016b; Corbett et al., 2017; McNorton et al., 2018). These natural sources are climate sensitive, so interannual changes to temperature and precipitation affect the amount of CH_4 emitted into the atmosphere, as well as the spatial distribution (Zhu et al., 2017). A number of studies have found that biomass burning emissions are largely responsible for the IAV of CO and also affect O_3 concentrations (Granier et al., 2000; Monks et al., 2012; Voulgarakis et al., 2015); however, Szopa et al. (2007) suggested that meteorology is a more important driver of IAV for CO, explaining 50%–90% of IAV.

A major driver of climatic IAV is the El Niño–Southern Oscillation (ENSO) – a mode of climate variability originating in the Pacific Ocean with alternating warm (El Niño) and cold (La Niña) modes (McPhaden et al., 2006). Positive phase El Niño events lead to warmer and drier conditions in the Western Pacific and disrupts global circulation patterns, leading to widespread changes in fire occurrence, wetland emissions and atmospheric transport (Feely et al., 1987; Jones et al., 2001; McPhaden et al., 2006). These influences occur most strongly in the tropics but have global consequences (Jones et al., 2001). Global CH_4 concentrations have been observed to increase significantly during El Niño events, with an especially strong signal during the 1997– 1998 event when the CH_4 growth rate was 12 ppb yr^{-1}, almost triple the 1750–2018 mean annual growth rate (Rigby et al., 2008; Hodson et al., 2011). Due to the wide-ranging effects of El Niño and varied sources of CH_4, there are multiple factors which could trigger the increase in CH_4 growth rate. Chen and Prinn (2006) attributed the increase to anomalies in global wetland emissions; however, Zhu et al.

(2017) estimated that although 49% of the interannual variation in wetland emissions can be explained by ENSO, wetland emissions were significantly lower during El Niño, including the 1997–1998 event. Conversely, Schaefer et al. (2018) estimated that ENSO is responsible for up to 35% of global CH_4 variability, but the effect of wetland and biomass burning emission changes are dwarfed by processes affecting the OH sink. Bousquet et al. (2006) suggested that the increased CH_4 growth rate during the 1997–1998 El Niño was primarily caused by abnormally large peat fires in Indonesia emitting huge amounts of CH_4 while wetlands emissions remained stable (van der Werf et al., 2004; Butler et al., 2005; Bousquet et al., 2006).

In addition to direct emissions of CH_4 from fires, it has been proposed that anomalously large CO emissions during enhanced El Niño fire events could explain the changes to CH_4 growth rate (Butler et al., 2005; Bousquet et al., 2006). CO is emitted from biomass burning in much larger quantities than CH_4 (~ 20× larger) and its reaction with the hydroxyl radical (OH) is its primary atmospheric sink (Voulgarakis and Field, 2015). Abnormal increases in CO concentrations may suppress the availability of OH, thereby extending CH_4 lifetime and increasing its growth rate during and following large fire events (Butler et al., 2005; Manning et al., 2005). The reaction of CH_4 with OH is the largest term in the global CH_4 budget, accounting for ~ 90% of its sink (McNorton et al., 2016a); therefore, even minor changes to OH caused by the presence of other compounds or changes to atmospheric transport and photolysis rates could have a large impact on CH_4 growth rate (Dlugokencky et al., 2011). Butler et al. (2005) found that CO emissions suppressed OH concentrations by 2.2% in 1997–1998, which accounted for 75% of the observed change in CH_4 concentration. Bousquet et al. (2006) also reported a weakened OH sink during this El Niño event.

The aim of this chapter is to investigate how El Niño events affect global CH_4, CO and tropospheric O_3 concentrations through changes to fire occurrence and atmospheric transport. Using long-term simulations spanning multiple El Niño and La Niña events, the relative influence of changes to fire emissions and dynamical transport is quantified. This work also differentiates between the

effect of direct CH_4 emissions from fires and the indirect effect via CO emissions and atmospheric chemistry changes.

5.2. Model specifications

This study utilised the three-dimensional chemical transport model (TOMCAT) (Chipperfield, 2006) coupled to the GLOMAP global aerosol microphysics scheme (Mann et al., 2010) as described in Section 3.2. Annually varying emission inventories are included for all fire-emitted gas-species and aerosol emissions, such as black carbon (BC). The GFEDv4 biomass burning emissions inventory is used including CO, CH_4, nitrogen oxides (NO_x) and volatile organic compounds (VOC) (Randerson et al., 2017; Reddington et al., 2018). Monthly varying biogenic VOC emissions are from the MEGAN-MACC emissions inventory for reference year 2000, calculated from the Model of Emissions of Gases and Aerosols from Nature (MEGAN version 2) (Sindelarova et al., 2014). The CH_4 inventory was produced by (McNorton et al., 2016b), with wetland emissions derived from the Joint UK Land Environment Simulator (JULES) and biomass burning emissions from GFEDv4 (Randerson et al., 2017). These are then combined with anthropogenic emissions from EDGAR version 3.2, paddy field emissions from Yan et al. (2009) and termite, wild animal, mud volcano, hydrate and ocean emissions from Matthews and Fung (1987) (McNorton et al., 2016b). The global mean surface CH_4 mixing ratio is scaled in TOMCAT-GLOMAP to a best estimate based on observed global surface mean concentration (McNorton et al., 2016a; Dlugokencky, 2019).

5.3. Model evaluation for ENSO

In addition to the model evaluation in Chapter 3, an additional evaluation was performed to assess the capability of TOMCAT-GLOMAP to simulate observed responses to El Niño events. Ziemke et al. (2010) derived an Ozone ENSO index (OEI) using satellite observations of tropospheric O_3. The difference in monthly mean total O_3 column (TOC) over the eastern and western Pacific is indicative of the occurrence and strength of ENSO and can therefore be used as an ENSO index. Ziemke et al. (2010) relate their OEI to the commonly used

Niño 3.4 index, finding that for a +1 K change in the Niño 3.4, there was a 2.4 DU increase in the Ozone ENSO Index (OEI). The corresponding TOMCAT-GLOMAP calculated response is a 2.8 DU increase per +1 K in the Niño 3.4, indicating a slightly larger but comparable O_3 response to El Niño.

The regional response of tropospheric O_3 to El Niño was evaluated against an analysis using various observations and a chemistry–climate model in Zhang et al. (2015). That study observed enhanced TOC in the North Pacific, southern USA, north-eastern Africa and East Asia, with decreases over central Europe and the North Atlantic. All of these observed responses were present in TOMCAT-GLOMAP simulations, except with a slight increase in TOC in central Europe and a simulated decrease in Western Europe and the East Atlantic (Figure 5.1).

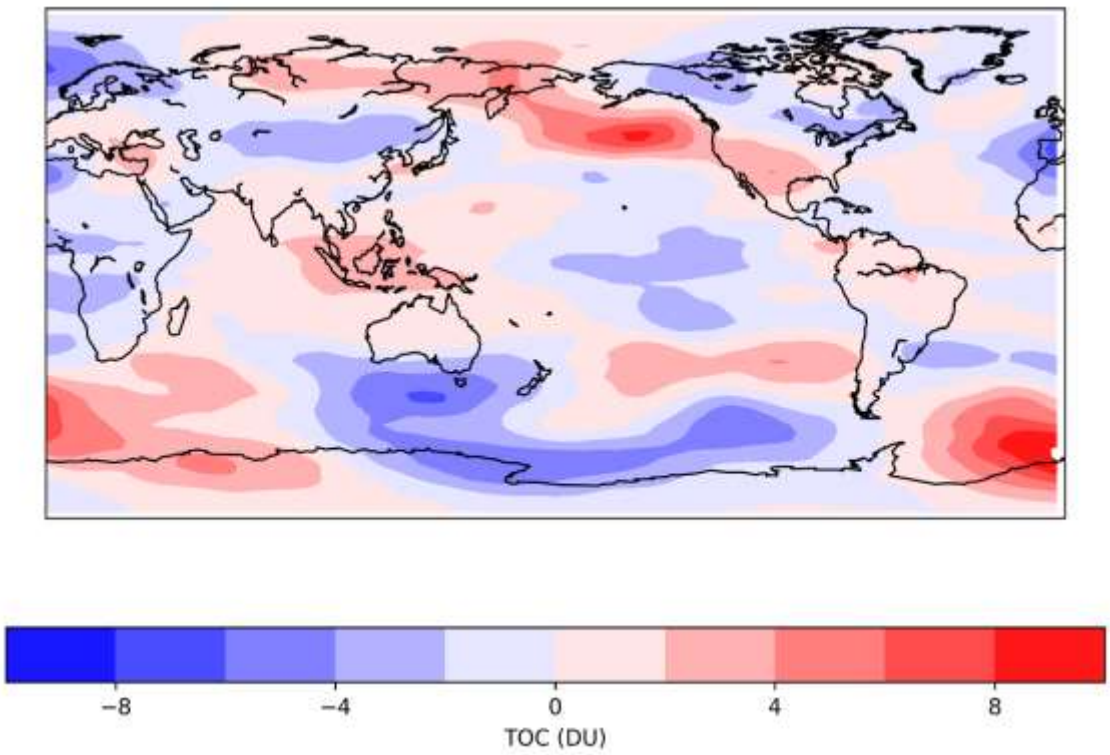

Figure 5.1 Difference in Total Ozone Column (TOC) during El Niño events (MEI > +1.0) from 1995-2014, compared to the TOC during the period mean.

5.4. CH_4 box model

The effect of changes to global OH concentrations on global mean surface CH_4 concentrations is calculated in a simple global box model using the following equation:

$$\frac{1}{\Delta t}(X_{t+\Delta t} - X_t) = E - L = E - k[OH][X] \text{ ,} \quad (4.1)$$

where, X = global mean CH_4 concentration in ppb

E = Annual emissions in Tg yr^{-1}

L = chemical loss to reaction with OH in Tg yr^{-1}

k = rate constant for reaction CH_4 + OH (k = 2.45×10^{-12} cm^3 $molecule^{-1}$ yr^{-1}) (Sander et al., 2011).

The box model uses equation (4.1) to integrate global mean CH_4 based on annual mean emissions and chemical loss in time steps of 1 month. This box model is similar to that described in McNorton et al. (2016a), which was found to compare well with other global and 12-box CH_4 models (Rigby et al., 2013; McNorton et al., 2016a). In this case, the box model used monthly mean tropospheric OH concentrations and CH_4 emissions for each simulation, while assuming constant temperature to calculate the effect of changing OH on global mean surface CH_4. The relevant CH_4 emissions and monthly mean tropospheric OH concentrations from each simulations were applied to the box model. McNorton et al. (2016a) found that using annually varying temperature had a very small effect on derived concentrations, therefore a constant temperature of 272.9 K was used.

5.5. Simulations

All simulations are performed for 1997–2014 with a 4-year spin-up through 1993–1996. The control run (CTRL) allows all emissions and meteorology to vary throughout the modelled period. GFED biomass burning emission inventories began in 1997; therefore, the 1993–1996 spin-up simulation uses

repeating 1999 emissions instead, as the closest year of “average” emissions, having excluded 1997 and 1998 due to the exceptionally high emissions in those years (Schultz et al., 2008). To test the impact of El Niño events on atmospheric chemistry, three perturbed simulations were performed (Table 5.1). Where model simulations used “fixed” parameters in Table 5.1, the year 2013 emissions or meteorology are specified as invariant throughout the simulation. This year is chosen as the ENSO-neutral case, due to it being the least active ENSO year during 1997–2014, with a maximum bimonthly multivariate ENSO index (MEI) magnitude of −0.4 and the only year without a single MEI value that could be considered an active El Niño or La Niña (Wolter and Timlin, 1993; Wolter and Timlin, 1998). Throughout this study, an El Niño event was considered as ongoing if its MEI was greater than +1. A factorial analysis was performed based on perturbed simulations in which global biomass burning emissions (FIREFIX) or global meteorology (METFIX) are fixed to the “ENSO-neutral” case. An additional perturbed simulation was performed in order to examine the secondary impact of CO on CH_4 via oxidation changes, where only CO emissions from biomass burning were fixed (COFIX).

5.6. Impact of meteorology and fire emissions on interannual variability of trace gases

First the mechanisms controlling interannual variability of simulated tropospheric CO, O_3 and mean OH are examined. The difference between the control (CTRL) and the perturbed simulations with fixed fires (FIREFIX) and fixed meteorology (METFIX) are used to determine the driving cause of IAV. Of particular interest is the effect of the 1997–1998 El Niño event (henceforth referred to as 1997 El Niño) and how the prevailing mechanisms controlling IAV change during such events. El Niño events are defined using the bimonthly multivariate ENSO index, calculated from six observed variables and standardized to accurately monitor ENSO occurrence (Wolter and Timlin, 1998; Wolter and Timlin, 2011).

Table 5.1 Details of TOMCAT model simulations. All simulations are run for 1997-2014.

Simulation name	Meteorology	CO biomass burning emissions	All other biomass burning emissions
CTRL	Varying	Varying	Varying
METFIX	Fixed	Varying	Varying
FIREFIX	Varying	Fixed	Fixed
COFIX	Varying	Fixed	Varying

Previous studies examining the dominant factor controlling global CO IAV have found contrasting results. Szopa et al. (2007) suggested that meteorology was the main driver, accounting for 50%–90% of IAV in the tropics. Conversely, a study by Monks et al. (2012) considered CO IAV in the Arctic, finding that biomass burning was the dominant driver with a strong correlation to El Niño. Voulgarakis et al. (2015) also suggested that biomass burning was the more important driver of IAV with only a small effect from meteorology. Some of these differences in results can be explained by the fact that Szopa et al. (2007) considered only surface CO, rather than the whole troposphere as in Voulgarakis et al. (2015). In this chapter, the whole tropospheric CO concentration is considered, and our results are in line with those from Voulgarakis et al. (2015). The dominant source of IAV across the entire period is emissions from biomass burning – indicated by the large difference between simulations CTRL and FIREFIX (Figure 5.2a), with a small effect from meteorological changes (CTRL – METFIX). This effect was largest during the 1997 El Niño, where an increase in fire events increased CO concentrations by more than 40%. Smaller increases of 5.8% and 7.6% occur during less extreme El Niño events of 2002/03 and 2006, respectively, with only a 1.8% increase during the 2009/10 El Niño, indicating that El Niño only significantly impacts CO concentrations when there is an associated increase in global fire events.

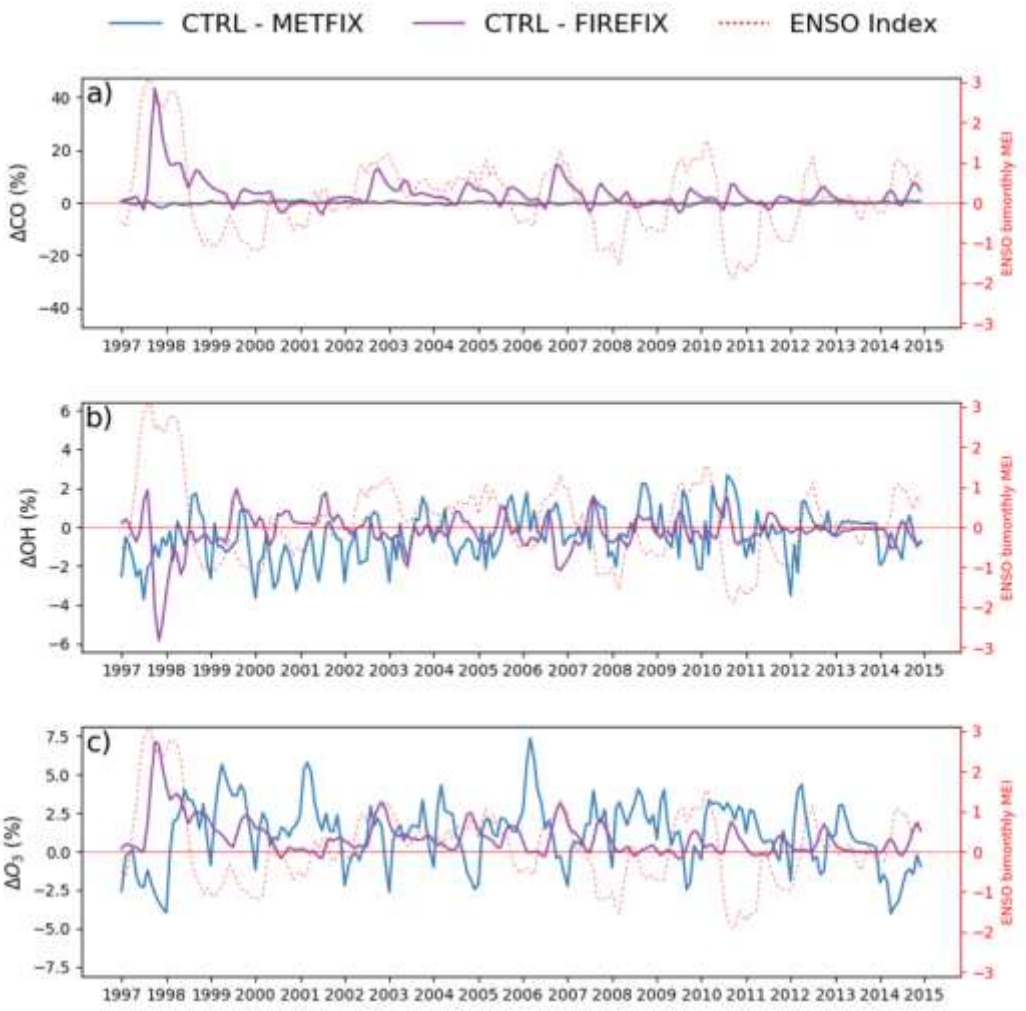

Figure 5.2 Time series of simulated differences (%) between the control and the fixed meteorology (CTRL - METFIX, blue line) and fixed fire emissions (CTRL – FIREFIX, purple line) simulations for the global tropospheric burden of (a) CO, (b) OH and (c) O_3. The ENSO bimonthly mean multivariate index is plotted in the dashed red line on the right-hand y axis in each panel.

Expanding on the work of Voulgarakis et al. (2015), the IAV is analysed using the coefficient of variation (CV), calculated as the multi-year standard deviation normalized by the mean (Figure 5.3). The global annual mean CO IAV over the whole period is 11.0% for the whole troposphere and 14.3% for surface concentrations. This is in very good agreement with Voulgarakis et al. (2015), who calculated 10% IAV; in fact, the comparison is even better when considering the same time period (2005–2009) with the corresponding IAV estimated at 9.7%. The slightly lower estimate here may be a result of the fixed-year biogenic

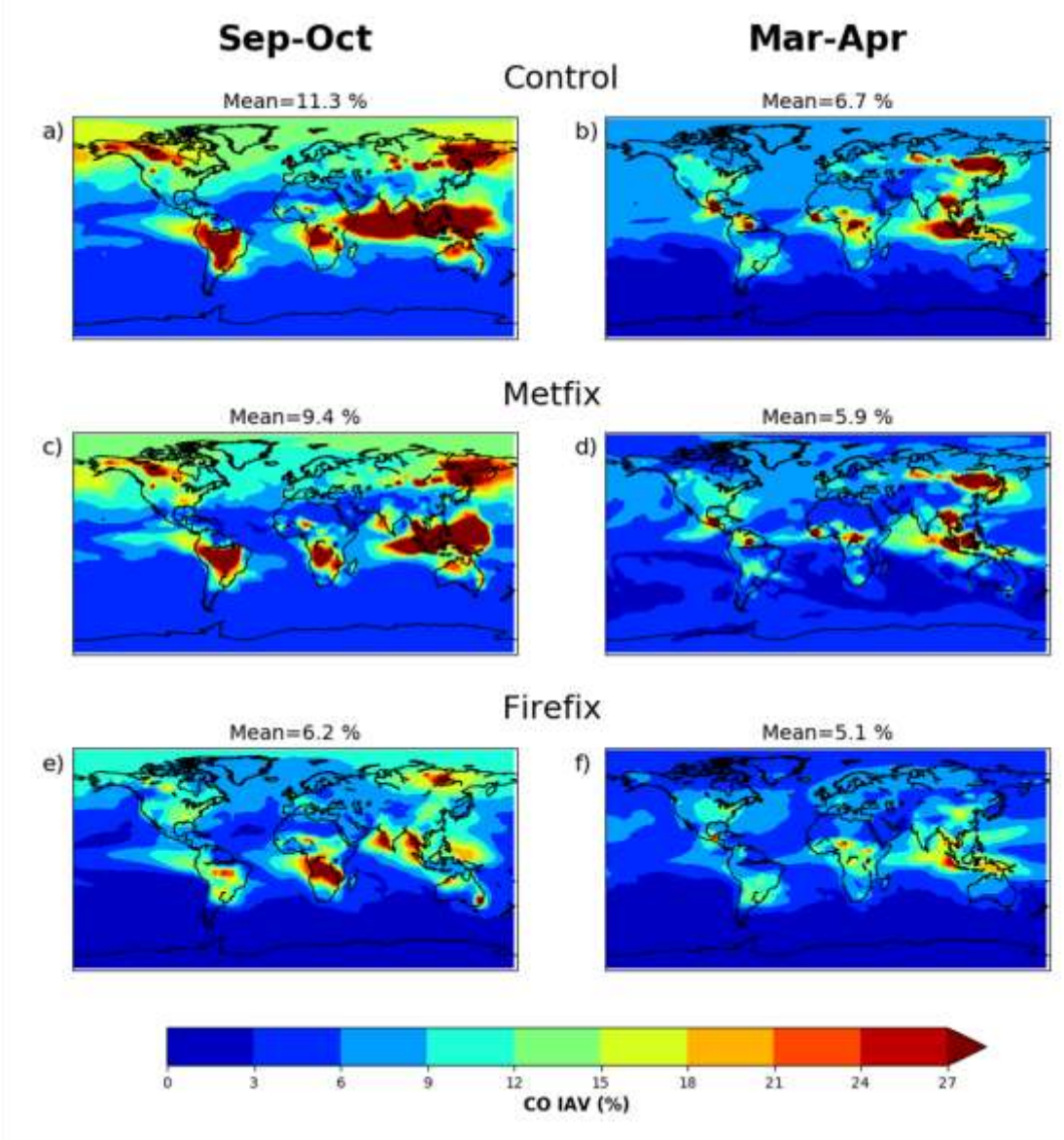

Figure 5.3 The calculated interannual variability (coefficient of variation) of CO over the period 1997-2014 for September – October (left panels) and March - April (right panels) from (a, b) control simulation (CTRL), (c, d) fixed meteorology (METFIX) and (e, f) fixed fire emissions (FIREFIX).

volatile organic compound (BVOC) emissions, removing the effect of the IAV of biogenic emissions on CO IAV. BVOC oxidation is estimated to contribute 15% of the total source of CO (Duncan et al., 2007b); however, the IAV of BVOC emissions has been found to be relatively small, ~2–4% (Naik et al., 2004; Lathière et al., 2005). Despite good global comparison with Voulgarakis et al. (2015), there are regional differences, e.g. CO IAV from TOMCAT is much larger in high-latitude boreal regions. This is likely due to the difference in the period studied, meaning this study includes additional extreme events including

unusually large Russia boreal wildfires in 2010 and 2012 (Gorchakov et al., 2014; Kozlov et al., 2014). Infrequent and extreme events such as these significantly increase IAV.

CO IAV is significantly greater in September–October, with peaks in known fire regions such as tropical South America, Africa, Southeast Asia and boreal forests. This indicates a strong contribution of fire emissions to IAV (Figure 5.2), especially from Indonesia, as also suggested by previous studies (Monks et al., 2012; Huang et al., 2014; Voulgarakis et al., 2015). In the FIREFIX simulation IAV is ~55% of the CTRL value, showing a large reduction in variability when interannual variability in fire emissions is removed. The IAV in March–April is significantly smaller than September–October as this period is outside the primary fire season for South America and Eurasia, although hotspots remain in Southeast Asia and Africa where fires commonly occur in March–April (van der Werf et al., 2017). Meteorology and atmospheric transport changes are most important in Africa in September–October and Indonesia in March–April (Fig. 5c,d). Fire emissions occur in these regions but the meteorological effects are important sources of IAV. This is in good agreement with Voulgarakis et al. (2015) who found that with fixed biomass burning emissions, high IAV remained over Africa during December–January, and Huang et al. (2014) who found CO over Central Africa correlated more closely with ice water content than CO emissions due to increased convective transport. However, the overall effect of meteorology on global IAV found here is much smaller than the 50–90% suggested by Szopa et al. (2007): when considering only surface CO over the same period, fixing meteorology decreases the mean CO IAV by just 5%.

The IAV of OH and O_3 have more complex contributions from fire emissions and meteorology (Figure 5.2b, Figure 5.2c). For both species, meteorology is the dominant cause of variability for the majority of the period, indicated by, on average, greater deviation from CTRL in METFIX simulation than FIREFIX, including during El Niño events other than the 1997 El Niño, such as in 2006. The results presented here compare well to Inness et al. (2015), who also found that changes to tropospheric O_3 during El Niño were driven by a combination of emissions and atmospheric dynamics. This is also in agreement with Doherty et

al. (2006), where a strong correlation was found between ENSO meteorology and global O_3 burden, albeit with a lag period of several months. Various meteorological variables are known to affect OH and O_3 variability, including humidity, clouds and temperature (Stevenson et al., 2005; Holmes et al., 2013; Nicely et al., 2018). OH variability is particularly sensitive to changes in lightning NO_x production which decreases during El Niño conditions (Turner et al., 2018). Murray et al. (2014) also examined factors affecting OH variability since the last glacial maximum, finding tropospheric water vapour, overhead stratospheric O_3 and lightning NO_x to be key controlling factors. Furthermore, circulation changes during El Niño events have been linked to lower stratospheric O_3 variability (Zhang et al., 2015; Manatsa and Mukwada, 2017), which in turn influences tropospheric OH and O_3 concentrations (Holmes et al., 2013; Murray et al., 2014). Despite the importance of meteorological drivers, fire emissions are the dominant cause of variation in both OH and O_3 during the 1997 El Niño, increasing global tropospheric O_3 burden by up to ~7% and decreasing tropospheric OH by up to ~6%. This result is supported by several other studies, which found that during large fire events such as that caused by the 1997 El Niño, fire emissions substantially decrease tropospheric OH and increase tropospheric O_3 (Hauglustaine et al., 1999; Sudo and Takahashi, 2001; Holmes et al., 2013). These results indicate that while meteorology is generally the most important driver of IAV in global tropospheric OH and O_3, fire emissions can also play a key role and become the dominant driver when there are particularly large fire emissions related to El Niño.

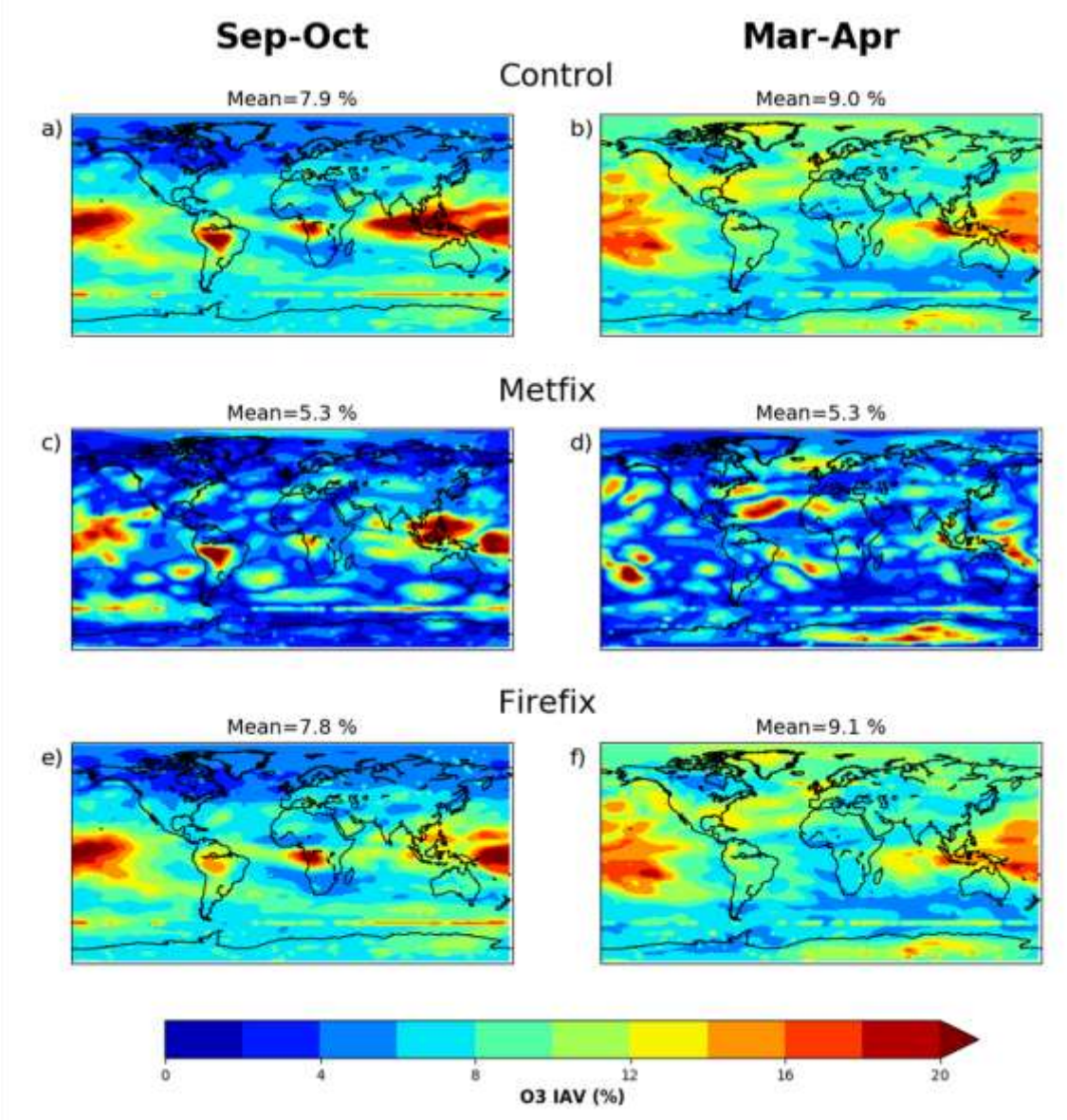

Figure 5.4 The calculated interannual variability (coefficient of variation) of tropospheric O_3 over the period 1997-2014 for September – October (left panels) and March - April (right panels) from (a, b) control simulation (CTRL), (c, d) fixed meteorology (METFIX) and (e, f) fixed fire emissions (FIREFIX).

Figure 5.4 shows the IAV of O_3, supporting the analysis of Figure 5.2 that also suggests meteorology is the dominant process in controlling IAV. METFIX-simulated IAV differs substantially from the CTRL, with much lower IAV in September–October (33% decrease) and in March–April (42% decrease) when meteorology is repeated. However, in the METFIX run there remain peaks in variability in close proximity to regions with large biomass burning emissions, demonstrating the significant contribution from fire emissions. In the FIREFIX simulation the distribution of IAV is broadly similar to the CTRL simulation and

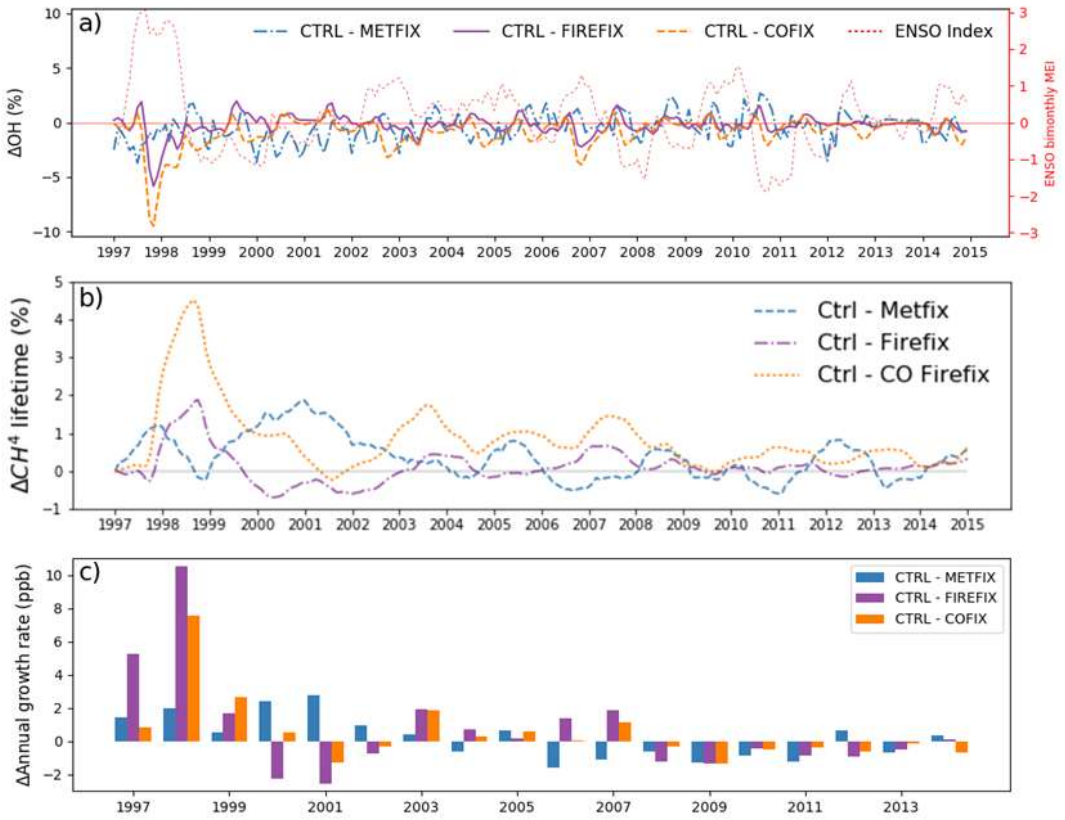

Figure 5.5 Time series of (a) the change (%) in mass-weighted tropospheric OH, (b) change (%) in CH_4 lifetime and (c) resultant change (ppb) in annual CH_4 growth rate calculated using an offline box model. The ENSO bimonthly mean multivariate index is plotted in the dashed red line on the right-hand y-axis in panel (a).

only shows a small change in global mean CV, indicating that fire emissions have less control on O_3 IAV. These results are again comparable to Voulgarakis et al. (2015) as the distribution of O_3 IAV in both CTRL and FIREFIX simulations is similar, despite slightly larger values of variation due to differing time period.

5.7. Indirect effect of CO on oxidation and lifetime of CH_4

The COFIX sensitivity experiment was conducted to determine the indirect influence of CO emissions on CH_4 variability through changes in tropospheric OH concentrations. Figure 5.5a shows the difference in COFIX monthly mean OH concentrations from the control experiment, compared to that from the METFIX and FIREFIX simulations. When CO emissions from biomass burning

are fixed, OH concentrations are consistently higher than in the CTRL simulation. This indicates that high CO emissions decrease global mean tropospheric OH. The greatest impact is during the 1997 El Niño, where CO emissions were abnormally large, suppressing mass weighted global monthly mean OH concentrations by up to 9%. The mean effect on OH over the 1997 El Niño of −3.6% is comparable to that simulated by Butler et al. (2005), who also found an increase in CO resulted in a change in OH of −2.2%. Duncan et al. (2003) found a similar magnitude response in OH to the Indonesian wildfires in 1997 of between −2.1% and −6.8%. The suppression of OH concentrations due to CO emission is also simulated to a lesser degree in the 2003 and 2006 El Niño events but is absent in the 2010 El Niño as this event had little impact on global fire occurrence (Randerson et al., 2017). The effect of fixing only CO from fires is greater than the effect of fixing all fire emissions due to co-emitted species such as NO_x, which act to increase OH concentrations.

As OH is also the primary sink of CH_4 (~90%) (McNorton et al., 2016a), another effect of the decrease in OH due to CO emissions is to weaken the sink of CH_4, increasing its atmospheric lifetime. The magnitude of this can be seen in Figure 5.5b; the COFIX simulation indicates that CO emissions from fires extended CH_4 atmospheric lifetime by more than 4% during the 1997 El Niño. Fixing all fire emissions also enhances CH_4 lifetime by around 2%. Increasing the lifetime of a species increases its concentration in steady-state equilibrium. Due to the scaling applied to CH_4 in TOMCAT it is not possible to directly calculate the response in CH_4 growth rate from TOMCAT, as simulated global mean surface CH_4 concentrations are nudged to the observed value. Therefore, to determine the impact of the change to OH on CH_4 concentrations, the simple global box model described in Section 5.4 was used. The estimated impact of fire emissions on the CH_4 growth rate is greatest in 1998, where all emissions from fires increased global CH_4 by 10.5 ppb (Figure 5.5c). Analysis of the COFIX simulation demonstrates that up to 7.5 ppb (72%) of that change could have been caused by the release of CO alone and its role as a sink for OH. The effect on growth rate in the FIREFIX simulation is larger than in the COFIX despite a greater effect on CH_4 lifetime from the COFIX, due to directly emitted CH_4 varying with El Niño conditions in the COFIX simulation and not in FIREFIX. The

influence of CO emissions on CH_4 growth rate calculated here is smaller than in Butler et al. (2005), despite a much larger effect on tropospheric OH. The estimated radiative effect of the change to CH_4 from CO emitted from biomass burning alone in 1998 is 0.004 W m^{-2}, calculated using updated expressions from Etminan et al. (2016).

5.8. Limiting factors of ozone production

In this section, the trends and the impact of El Niño on the production of tropospheric O_3 are evaluated. El Niño is known to have a large effect on tropospheric O_3 precursors such as CO and NO_x. Therefore, examining O_3 production regimes during El Niño can provide insights into the main mechanism responsible for the observed changes in tropospheric O_3. The ratio between formaldehyde (HCHO) and nitrogen dioxide (NO_2) concentrations can be used to indicate the limiting factor for tropospheric O_3 production (Duncan et al., 2010). HCHO is a good indicator of VOC concentrations as it is relatively abundant in the tropospheric and is formed in oxidation pathways of many

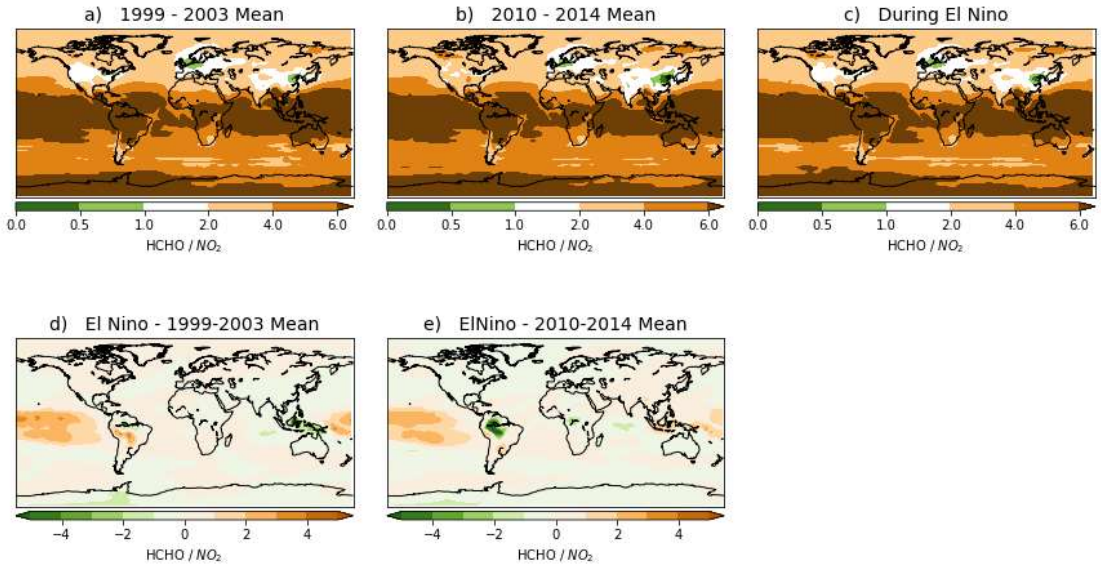

Figure 5.6 Mean ratio of simulated tropospheric column HCHO to NO_2 amounts for (a) the beginning of model period (1999-2003), (b) the end of model period (2010-2014) and (c) during all El Niño events. Panels (d) and (e) show difference during El Niño from the 5-year mean values in panels (a) and (b), respectively.

VOCs. Ratios smaller than 1 indicate that removing VOCs will decrease tropospheric O_3 formation (i.e. a VOC-limited regime), while ratios larger than 2 indicate that removing NO_x will reduce O_3 (i.e. a NO_x-limited regime). Ratios of 1–2 indicate that both NO_x and VOC reductions could decrease O_3 (i.e. a "both-limited" regime). This methodology is applied to determine the changes to this ratio from 1997 to 2014 and dependence of O_3 formation during the 1997 El Niño event. The early period mean (1999–2003) is compared to the end period mean (2010–2014) in order to determine whether significant changes have occurred over the 18-year period. Both periods are then also compared with mean El Niño conditions.

In general, the SH and tropical regions have very high $HCHO:NO_2$ ratios, meaning they are strongly NO_x-limited (Figure 5.6). The NH is also predominantly NO_x-limited, although less robustly, and polluted regions tend to be either VOC-limited or both-limited regimes. The ratio is largely constant across the modelled period; however, there are some significant shifts, such as in India, which was once solely NO_x-limited, becoming increasing VOC-limited due to increased NO_x pollution (Hilboll et al., 2017). This shift in the spatial distribution of O_3 precursor emissions to lower latitudes leads to increased tropospheric O_3 production proportional to total emissions (Zhang et al., 2016).

During El Niño there are large changes, increasing the ratio and therefore the NO_x limitation by more than 40% in the tropical Pacific. Significant changes to the ratio were also found in biomass burning regions of South America and Southeast Asia. This is due to the increase in NO_x emissions in larger fire seasons associated with El Niño. However, these regions are already very heavily NO_x-limited due to high VOC emissions in forest regions, meaning that although the shift in $HCHO:NO_2$ ratio during El Niño is large, it is not substantial enough to alter the limiting factor for formation of tropospheric O_3 from one regime to another. Over India, El Niño conditions inhibit the trend towards a both-limited regime, as the NO_x-limited regime continues to dominate throughout.

5.9. Impact on tropospheric ozone and radiative effects

The 1997 El Niño significantly altered the vertical distribution of O_3 in the troposphere, increasing O_3 concentrations in the NH while decreasing in the SH and tropics with an overall decrease in tropospheric O_3 of −0.82% compared to the 1997–2014 mean (Figure 5.7a). In the CTRL simulation there is decreased O_3 in the tropical upper troposphere, possibly related to increased convection over the eastern Pacific (Oman et al., 2013; Neu et al., 2014). There are also large simulated increases in the mid-latitude upper troposphere of both hemispheres in the CTRL and FIREFIX simulations but not in METFIX, implying that this is produced by El Niño-associated meteorological processes which promote intrusion of stratospheric air into the troposphere. These positive anomalies were also observed in Oman et al. (2013) and Zeng and Pyle (2005), attributed to El Niño influence on circulation patterns and enhanced stratosphere–troposphere exchange.

In general, the METFIX run simulates higher O_3 concentrations in the NH than the period mean and lower concentrations in the SH (Figure 5.7b). This hemispherical shift is also present in the CTRL and FIREFIX simulations but with greater negative O_3 anomalies in the SH. The simulated NH increases in the CTRL simulation agree with other studies of the 1997 El Niño (Koumoutsaris

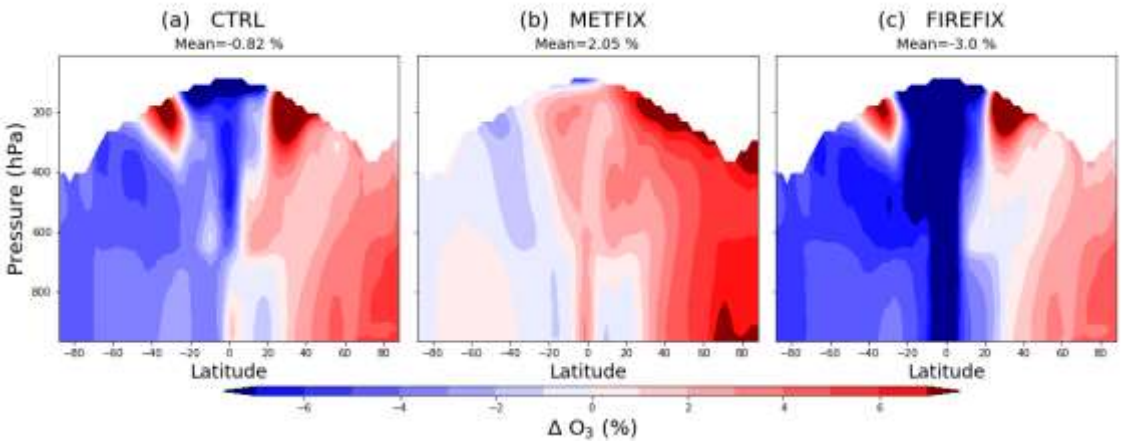

Figure 5.7 Latitude–pressure cross sections of the percentage difference in O_3 concentrations during the 1997 El Niño event compared to 1997–2014 period mean for the TOMCAT simulations: (a) CTRL, (b) METFIX and (c) FIREFIX simulations.

et al., 2008), while Oman et al. (2013) similarly reported negative O_3 anomalies in the SH during El Niño. Large increases in tropospheric O_3 in the western Pacific, Indian Ocean and Europe contribute to the increase in O_3 in the NH, despite decreased O_3 in the eastern Pacific (Chandra et al., 1998; Koumoutsaris et al., 2008; Oman et al., 2011).

There is an overall increase in O_3 (~ 2%) when meteorology was fixed to an ENSO-neutral year (i.e. 2013), meaning that meteorology during the 1997 El Niño caused a decrease in tropospheric O_3 concentrations despite large increases in O_3 in regions of the upper troposphere due to stratospheric intrusion. During the 1997 El Niño, there is a 0.4% increase in global tropospheric humidity compared to the period mean. This is likely partly

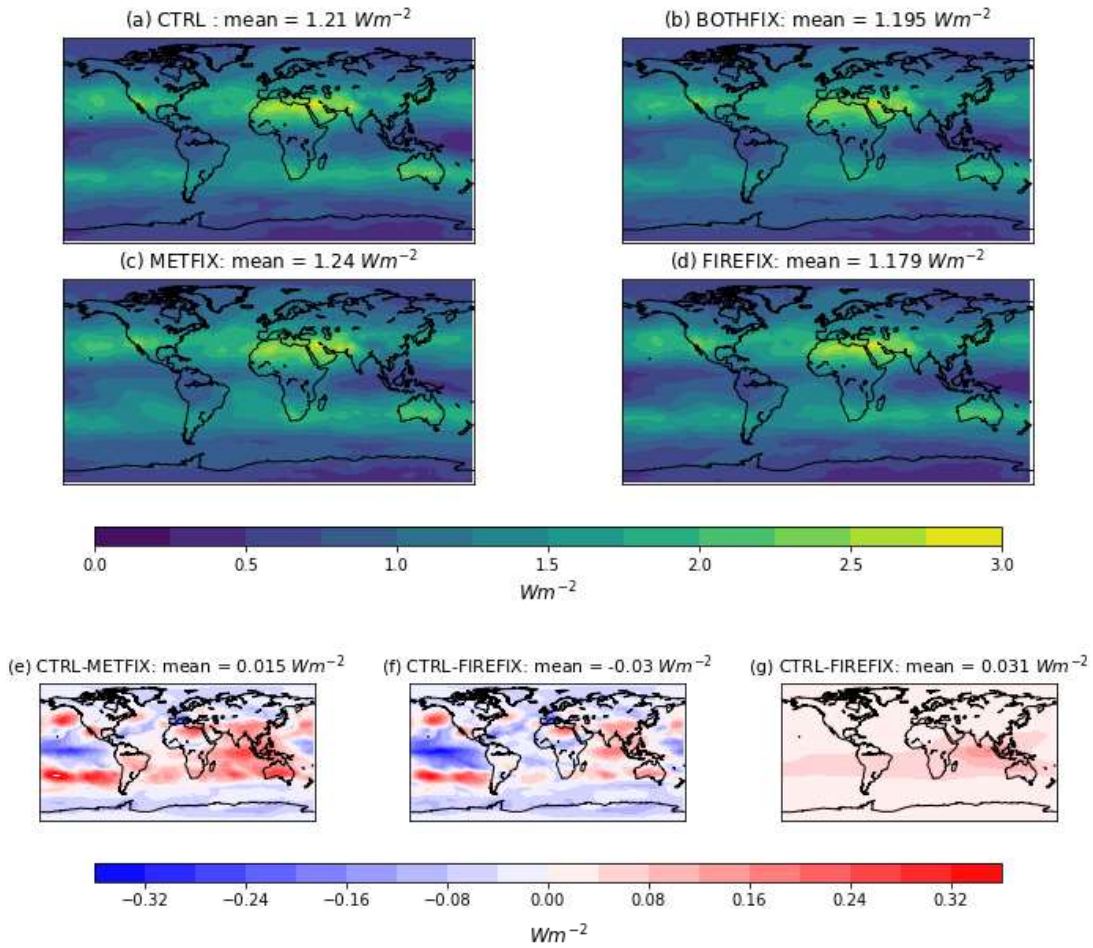

Figure 5.8 Tropospheric O_3 radiative effects (Wm^{-2}) from the TOMCAT simulations (a) control (CTRL), (b) fixed meteorology and fire emissions (BOTHFIX), (c) fixed meteorology only (METFIX) and (d) fixed fire emissions only (FIREFIX). Panels (e-g) show percentage differences between the control and the three perturbed simulations.

responsible for the general decrease in O_3 due to meteorology, as increased humidity enhances O_3 loss (Stevenson et al., 2000; Isaksen et al., 2009; Kawase et al., 2011). Changes to transport and distribution of O_3 will also impact how efficiently tropospheric O_3 is produced and lost.

The similarities between the tropospheric O_3 distribution in the CTRL and FIREFIX simulations show that fire emissions have a relatively small impact on the global distribution of O_3 but do affect absolute values, as concentrations in the FIREFIX run are significantly lower in the tropics. This is likely because of the removal of large emissions of O_3 precursors in that latitude band when fire emissions are fixed to a non-El Niño year, as several studies have found that enhanced fires in 1997 El Niño increased tropospheric O_3 in the region (Chandra et al., 1998; Thompson et al., 2001; Doherty et al., 2006; Oman et al., 2013).

Figure 5.8 shows the tropospheric O_3 radiative effect (RE) during the 1997 El Niño in each TOMCAT simulation, calculated by multiplying the Rap et al. (2015) tropospheric O_3 radiative kernel with simulated O_3 concentrations. Consistent with the relative changes in O_3 concentration, fire emissions and meteorology have contrasting effects on O_3 RE. When isolated, these effects are opposite and almost equal: fire emissions increase O_3 RE by 0.031 W m^{-2}, while meteorology decreases by −0.030 W m^{-2}. An additional simulation was performed to determine the effect of these factors occurring simultaneously (BOTHFIX) and found the increasing effect from fire emissions to be dominant over the decreasing effect from meteorology, leading to an overall increase in global mean O_3 RE of 0.015 W m^{-2}. The effect of fire emissions occurs almost entirely over Indonesia and the eastern Indian Ocean. This is due to the large influx of NO_x, CO and CH_4 from fire emissions during the 1997 El Niño, which causes large regional increases in tropospheric O_3. This increase, also observed in Chandra et al. (1998), causes a regional RE of up to 0.17 W m^{-2}. Meteorology has more varied impacts during El Niño, causing large decreases in O_3 RE over the central Pacific Ocean (~−0.36 Wm^{-2}) but increases at higher latitudes of the Pacific Ocean (~0.33 Wm^{-2}). Although the global mean change in RE is relatively small, there large regional changes have the potential to significantly alter regional atmospheric heating and dynamics.

5.10. Summary

Global model simulations using annually constant meteorology and fire emissions were performed for the period 1997–2014 in order to determine their relative impacts on the IAV of O_3 and CH_4, particularly during El Niño events. In general, the model showed good agreement with observed atmospheric responses to El Niño events competently simulating the distribution and magnitude of the tropospheric O_3 response (i.e. OEI change of 2.8 DU compared to 2.4 DU in Ziemke et al. (2010), providing confidence in model performance and results.

The results presented here indicate that the IAV of global CO concentrations is large and is primarily controlled by fire emissions over the modelled period. Exceptionally large CO emissions linked to El Niño in 1997 led to a decrease in OH concentrations of ~9%, which subsequently increased CH_4 lifetime by ~4%. The use of a simple box model quantifies the isolated impact of this change in atmospheric chemistry on global CH_4 growth rate to be 7.75 ppb, ~75% of the total effect of fires. This effect, combined with concurrent direct CH_4 emission from fires, explains the observed changes to CH_4 growth rate during the 1997 El Niño.

The variability of O_3 and OH is far more dependent on meteorology than fire emissions. Only during very large El Niño events, such as in 1997 and 1998, do fires become dominant in terms of total tropospheric burden, although meteorology still controls their distribution. The change to tropospheric O_3 concentrations during El Niño has increased O_3 RE by 0.17 W m^{-2} over Southeast Asia and decreased by 0.36 W m^{-2} over the central Pacific. The global mean O_3 RE change due to 1997 El Niño meteorology and fires is an increase of 0.015 W m^{-2}, as emissions of O_3 precursors from fires causes increased O_3. El Niño also causes significant shifts in the ratio of $HCHO:NO_2$ – an indicator of O_3 production regime – but most significantly in the tropics, which are heavily NO_x-limited, so this change does not cause a regime shift.

The work presented in this chapter highlights how El Niño events significantly affect the variability of two important drivers of anthropogenic climate change.

Further research into how El Niño events, with their associated effect on fire emissions, are likely to change in a warming climate is required to understand how these links between ENSO, CH_4 and O_3 may influence future climate change mitigation attempts.

6. The effect of SCLP emission scenarios on climate and air quality in 2050

6.1. Introduction

In this chapter, the potential for climate mitigation by decreasing anthropogenic emissions of SLCPs and their precursors is evaluated. Of particular interest is the opportunity for co-benefits for climate and air quality, as suggested by previous studies (Anenberg et al., 2012; Fiore et al., 2012; Shindell et al., 2012). Future emission inventories under several different scenarios are used within TOMCAT-GLOMAP to simulate atmospheric concentrations of SLCPs in 2050, investigating the suitability of emission reduction scenarios for optimum mitigation of climate and improved air quality.

Reductions of SLCPs have been proposed as possible pathways for short-term climate mitigation. The climate impact from short-lived forcers is composed of a positive forcing from greenhouse gases, black carbon and HFCs and a negative forcing from aerosol through the aerosol-radiation interaction and aerosol-cloud interaction. The negative RF due to aerosol, and the combined positive RF from warming SLCPs components make up RF terms that are estimated to be similar in magnitude to the RF associated with CO_2 (Myhre et al., 2013b). Unlike CO_2, their short atmospheric lifetimes mean that decreases in anthropogenic emissions would result in rapidly decreasing atmospheric concentrations. Hansen et al. (2000) was among the first studies to propose the importance of a non-CO_2 mitigation strategy, estimating that it has the potential to stall mean temperature warming completely until ~2050. Subsequent research indicated

that SLCP mitigation would not in fact stall the warming trend, at least not without substantial action on CO_2, however the consensus remains that measures to decrease emissions of SLCPs and their precursors would slow the rate of climate change by 2050 (Penner et al., 2010; Shindell et al., 2012; Bowerman et al., 2013; Carmichael et al., 2013; Hu et al., 2013; Smith and Mizrahi, 2013).

The degree of warming that can be avoided through SLCP reductions remains uncertain. Shindell et al. (2012) estimated 0.5°C of avoided warming by 2050 (Figure 1.2) through focused reductions in CH_4 and BC emissions. A UNEP (2011) report similarly estimated that 0.4-0.5°C of global mean surface temperature increase could be avoided by 2050 through implementation of 16 measures targeting SLCPs, with substantial simultaneous benefits for air quality. Shindell et al. (2017) found avoided warming of 0.59°C, with the largest contribution from CH_4 mitigation (Table 6.1). Furthermore, a study by Hu et al. (2013) found that SLCP mitigation could decrease global sea-level rise by up to 42% by 2100. However, Smith and Mizrahi (2013) estimated a smaller avoided warming of just 0.16°C (0.04-0.35°C), similar to what would be achieved in a comprehensive climate policy, eliminating the need for an SLCP focused policy.

It has been argued that the effect of mitigating SLCPs is often overestimated by failing to account for the reductions in SLCPs which would naturally follow from effective carbon reduction techniques (Rogelj et al., 2014). While Rogelj et al. (2014) acknowledge that SLCP mitigation may be capable of reducing the rate of warming, they also suggest that the natural co-benefits of traditional mitigation measures may negate the need for specialised SLCP measures. In addition, there have been a number of studies finding that although SLCP mitigation does indeed slow near-term warming rates, it will have no impact on peak temperature rise, hence failing to 'buy time' for CO_2 mitigation as has on occasion been suggested (Bowerman et al., 2013; Shoemaker and Schrag, 2013). This has led to concerns that such measures or shift in policy focus could delay effective CO_2 policy, locking the climate in higher peak temperature rise and being counter-productive (Shoemaker et al., 2013; Pierrehumbert, 2014).

Action on SLCPs could be of particular importance for the Arctic, where mean temperatures have risen at almost twice the global average rate (ACIA, 2004;

Table 6.1 Avoided warming by 2030 and 2050 relative to present-day, resulting from SLCP emission reductions **(Shindell et al., 2017)**.

SLCP mitigation	Change in temperature (°C)	
	2030	2050
All SLCPs (HFCs following Kigali Amendment)	0.22 ± 0.11	0.59 ± 0.27
Methane	0.09 ± 0.03	0.30 ± 0.12
HFCs following the Kigali Amendment	0.005 ± 0.002	0.07 ± 0.02
HFCs (Maximum Feasible Reduction)	0.02 ± 0.01	0.10 ± 0.03
Black carbon-rich sources	0.1 ± 0.1	0.2 ± 0.2

Hansen et al., 2007; Quinn et al., 2008). Zhang et al. (2018) found that SLCP mitigation could avoid up to 0.44°C of mean global surface temperature warming, with avoided warming of up to 0.8°C in the high northern latitudes. However, other studies have indicated that measures to decrease aerosol concentrations will further amplify Arctic warming and sea ice loss (Acosta Navarro et al., 2017; Wang et al., 2018), while Dobricic et al. (2019) found that the impact of aerosol emissions on Arctic warming is uncertain and will vary depending on CO_2 concentrations.

As both warming and cooling SLCP species tend to be produced from the same emission activity, it is important to consider the implications of co-emitted species when considering SLCP mitigation. Fiore et al. (2012) found that while targeting CH_4 emissions would effectively mitigate climate by decreasing CH_4 and tropospheric O_3 concentrations, a broader attempt to tackle SLCPs and air pollutants would temporarily enhance the rate of warming. Coincident emissions of sulphate and nitrate aerosol precursors would also be reduced, which coupled with the highly uncertain response of the aerosol indirect RF may result in increased near-term warming.

A number of studies have highlighted the issue of misleading metrics being used for long-term and short-term forcers, which may overstate the relative importance of SLCPs. GWP_{100} of CH_4 for example is 21, indicating a 21 times greater warming potential than CO_2 over 100 years. However in reality, a one-time pulse of CH_4 emission will have long been removed from the atmosphere

and have no effect on the climate 100 years later (Nelson and O'Rourke, 2018). Allen et al. (2016) showed that GWP_{100} effectively measured the relative impact of SLCPs on a timescale of 20-40 years, rather than 100 years. A new metric, denoted GWP*, which equates SLCP forcing to cumulative CO_2 equivalent forcings, has instead been proposed to accurately assess the impact of both long-lived and short-lived climate forcers (Allen et al., 2018). Global temperature potential (GTP) has also been suggested as a more robust metric than GWP, although Shindell et al. (2017) propose that for a mitigation policy perspective, long-lived and short-lived species should be considered entirely separately.

6.2. ECLIPSE project

The Evaluating the climate and air quality impacts of short-lived pollutants (ECLIPSE) project is an EU funded collaborative project set up in 2011, with the primary objective of providing sound scientific advice on the best ways to mitigate climate change, while simultaneously improving air quality. The ECLIPSE project developed recent historical SLCP emission inventories as well as several scenarios for future emissions. These were produced by emissions sector and tested for improvements to global air quality and climate change mitigation. In this chapter the ECLIPSE inventories are used with the TOMCAT-GLOMAP CTM to simulate future changes to SLCPs, with analysis of the impacts for climate mitigation and air pollution.

6.2.1. ECLIPSE emissions inventories

The first phase of the ECLIPSE project produced a new emission inventory to be used as a reference scenario. The inventory was created using the Greenhouse gas-Air pollution Interactions and Synergies (GAINS) model (Amann et al., 2011), for a range of aerosols and short-lived non-CO_2 gases, from the recent past (1990) to 2050. The GAINS model includes detailed information about environmental policy and emission sources for 160 countries and is based on projections of energy use, industrial production and agricultural activity distinguished by key sources and control measures. The International Energy Agency (IEA) and OECD Energy Technology Projections (ETP) were

the primary sources for this information (Stohl et al., 2015). Biomass burning emissions are not included in the GAINS model, therefore estimates were used from GFED version 3.1 for 2008 and 2009 and assumed constant in future simulations (van der Werf et al., 2010). The ECLIPSE inventory was the first to include emissions from gas-flaring in oil fields and emissions from wick lamps, which were particularly important for BC emissions (Stohl et al., 2015).

6.2.2. ECLIPSE emissions scenarios

In this chapter, version V5a of the ECLIPSE inventories have been used to examine changes in climate and air quality from present-day (considered here as 2010) to 2050 (Klimont et al., 2017; Klimont et al., 2019). Four scenarios have been used:

- The Current Legislation (CLE) baseline scenario
- Maximum Technically Feasible Reduction (MTFR)
- SLCP Mitigation (SLCPMIT)
- Two degree climate scenario (2deg)

In the CLE scenario inventory, all current and planned mitigation measures are assumed to take effect, but no new mitigation measures are introduced from 2015. The MTFR assumes that emission reductions that are technologically feasible for every emission species are implemented by 2050. The 2deg scenario introduces measures targeting CH_4 and air pollutant emissions, aimed to keep global mean surface temperature at below 2°C of warming by 2050. For the SLCP mitigation scenario, the forcings of all SLCP species, including regional and seasonal changes, were calculated along with estimates of GTP_{20} and regional temperature change potential (RTP) (Shindell and Faluvegi, 2009). These were then used to produce an emissions scenario of SLCPMIT mitigation, which would minimise climate impact through emissions reduction measures. All the measures introduced to create the SLCP mitigation scenario were projected to have benefits for both climate mitigation and air quality. For all

scenarios the emissions are provided as a total emissions per species, and split into the following emissions sectors:

1. AWB - agricultural waste burning on fields
2. DOM - Residential and commercial
3. ENE - power plants, energy conversion and extraction
4. IND – Industrial combustion and processing
5. TRA – surface transportation
6. WST – Waste emissions

The CLE inventory is given in 5-yearly steps from 1990 to 2030, then for 2040 and 2050. The MTFR scenario inventory was made for 2030-2050, while the SLCPMIT and 2deg scenarios run from 2020-2050. The simulations from the CLE inventory for 2010 were used as a PD control, from which changes by 2050 were calculated.

All ECLIPSE inventories are produced on a 0.5° × 0.5° grid and were regridded to the 1° × 1° TOMCAT grid before being used in these simulations. Figure 6.1a shows historical and future emissions of CH_4, SO_2, NO_x and CO in the ECLIPSE inventories used here, compared with emissions from the EDGAR inventory. For both CH_4 and SO_2, ECLIPSE and EDGAR total annual emissions compare very well. Each of the future emission reduction scenarios decrease CH_4 emissions relative to CLE, with MTFR and SLCPMIT scenarios resulting in the largest reduction in CH_4 emissions. For SO_2, under the CLE scenario future emissions are projected to decrease initially but then increase from ~2025 until 2050, due to increased emissions from developing countries. As expected, the MTFR scenario has the largest reduction in emissions, with a substantial decline also projected in the 2deg scenario emissions. The SLCPMIT scenario however decreases emissions slightly from 2010-2030 relative to CLE, but SO_2 emissions are very similar to the CLE scenario for the entire time period. For NO_x and CO, ECLIPSE and EDGAR emissions from 1990-2010 show some disagreement. In the future emissions scenarios, MTFR again has drastic reductions in emissions

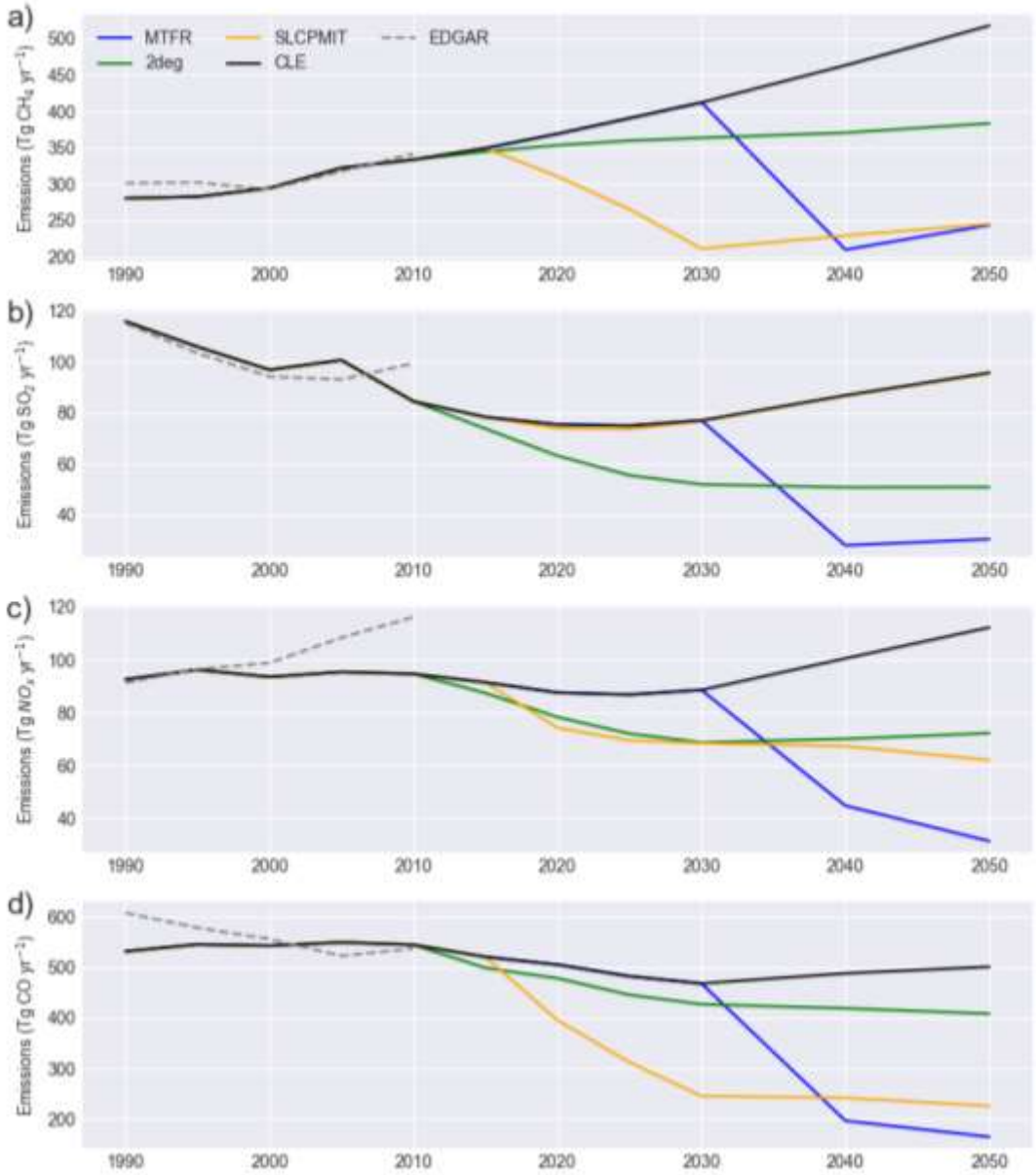

Figure 6.1 Historic and future ECLIPSE emissions from each scenario inventory for anthropogenic CH_4 (a), SO_2 (b), NO_x (c) and CO (d). Anthropogenic emissions from the EDGAR inventory (grey dashed line; Crippa et al. (2018)) from 1990-2010 are also shown for comparison.

from 2030. SLCPMIT and the 2deg scenario are very similar in terms of NOx emissions, but SLCPMIT has a larger drop in emissions of CO than 2deg from 2020 onwards.

6.3. FaIR climate model

The Finite Amplified Impulse Response (FaIR) climate model (version 1.3) is used here to estimate the effective RF (ERF) and temperature anomaly following implementation of the ECLIPSE emissions inventories. FaIR was used as it enables calculation of ERF due to SLCP changes in the context of simultaneous change to long-lived climate forcers such as CO_2 and N_2O. In addition, FaIR calculates the global mean temperature anomaly relative to a historic point such as 1750 (pre-industrial), allowing calculation of avoided warming in ECLIPSE scenarios.

FaIR was developed to calculate atmospheric concentrations and ERF of long-lived greenhouse gases and SLCPs, in a simple emulator model (Smith et al., 2018). In this section, a general description of the FaIR model is given, with detailed description of the calculation of ERF and temperature anomalies from SLCP emissions. A full description and evaluation of the FaIR model is given in Smith et al. (2018).

FaIR is driven by emissions of greenhouse gases and SLCPs, tuned by the historic ERF time series in AR5. The latest version of FaIR used here calculates ERFs from 13 different forcing agents (Table 6.2), including the SLCPs of most interest to this study: CH_4, tropospheric O_3 and aerosols. The uncertainty in the ERF of each forcing agent and the associated controlling factors are shown in Table 6.2.

ERFs of CO_2, N_2O and CH_4 are the updated estimates from Etminan et al. (2016). For CH_4, the ERF is assumed to be equal to RF with an increased uncertainty range, but has been revised upwards due to the inclusion of shortwave absorption (Myhre et al., 2013b; Etminan et al., 2016). Natural CH_4 emissions in future simulations are fixed at 191 Tg yr^{-1}, as a best-estimate of PD emissions (Prather et al., 2012). Due to the large spatial variability of tropospheric O_3, an ERF from global average concentrations cannot be reliably calculated. Instead FaIR calculates tropospheric O_3 forcing from CH_4 concentrations and emissions of precursors NO_x, CO and NMVOCs, based on coefficients from Stevenson et al. (2013). FaIR also includes a small climate feedback on tropospheric O_3, with a forcing of -0.02 to -0.03 Wm^{-2} (Stevenson et al., 2013).

For aerosols, a direct calculation is made from emissions to forcing, due to the short lifetime of aerosols in the atmosphere. The ERF from aerosol-radiation interaction is assumed to be a linear relationship between emissions and forcing (Myhre et al., 2013a). The rapid adjustments included in the aerosol-radiation interaction include the semi-direct effect. Biomass burning aerosol is assumed to have a net zero forcing and is therefore ignored along with mineral dust. Emissions of BC, OC and sulphur oxides (SO_x) corresponds directly to BC, OC

Table 6.2 The 13 separate forcing groups considered in FaIR v1.3 in the calculation of effective radiative forcing. The ERF uncertainty represents the 5–95% range and is used in the generation of the large ensemble. From Smith et al. (2018), Table 3.

Index	Forcing agent	Depends on	ERF uncertainty
0	CO_2	CO_2 emissions; CH_4 fossil fraction; cumulative C emissions; total temperature change	±20 %
1	CH_4	CH_4 emissions	±28 %
2	N_2O	N_2O emissions	±20 %
3	Other greenhouse gases	Emissions of other greenhouse gases	±20 %
4	Tropospheric ozone	Emissions of CH_4 and short-lived climate forcers	±50 %
5	Stratospheric ozone	Concentrations of ozone-depleting substances (subset of minor greenhouse gases)	±200 %
6	Stratospheric water vapour	CH_4 ERF	±72 %
7	Contrails	Aviation NO_x fraction; total NO_x emitted	−66 to +191 %
8	Aerosols	Emissions of short-lived climate forcers	−89 to +111 %
9	Black carbon on snow	Emissions of black carbon	−56 to +128 %
10	Land use change	Cumulative emissions of land-use-related CO_2	±167 %
11	Volcanic	Externally supplied forcing from volcanoes	±50 %
12	Solar	Externally supplied forcing from solar variability	±0.05 W m^{-2}

and sulphate aerosol forcings, respectively. For nitrate aerosol forcing, FaIR uses estimates from Shindell et al. (2009), with a contribution of 60% from NH_3 emissions and 40% from NO_x emissions. The semi-direct forcing is assumed to be from BC aerosol only (Boucher et al., 2013), with a forcing of -0.1 Wm^{-2}. For the ERF from aerosol-cloud interactions, the response is estimated to be non-linear. Therefore FaIR utilises an emulation of the Ghan et al. (2013) simple aerosol model, with a logarithmic dependence on emissions, scaled to the aerosol-cloud interaction ERF estimate -0.45 Wm^{-2} in AR5. For the effect of BC aerosol on snow, the best estimate of ERF from AR5 of 0.04 Wm^{-2} is scaled directly to emissions (Meinshausen et al., 2011) and assumed to be constant with time.

In this thesis, FaIR is run in the emissions-driven mode. All SLCP emissions are replaced by the relevant ECLIPSE inventory in each run. For emissions of long-lived forcers such as CO_2, representative concentration pathway 4.5 (RCP4.5) from IPCC AR5 is used.

6.4. Model specifications and simulations

We use the TOMCAT-GLOMAP model to simulate present-day and future SLCP concentrations using ECLIPSE emission inventories. The anthropogenic emission inventories for emissions of SO_2, BC, OC, NO_x, NMVOCs and NH_3 are replaced with the corresponding ECLIPSE inventory for each scenario. The anthropogenic portion of the CH_4 inventories is also replaced with the ECLIPSE emissions, keeping all other CH_4 sources as specified in Section 3.4. Otherwise TOMCAT-GLOMAP is run as described in Chapter 3, on 2.8° × 2.8° resolution. Natural emissions are kept constant in all simulations as described in Section 3.4, with biomass burning emissions from GFEDv4 for 2010. All simulations are run using 2010 meteorology with a one-year spin up period.

In the initial phase, five simulations were completed: a control using CLE emissions for 2010, and four sensitivity simulations, using 2050 total emissions of SLCPs for each of the four future emissions scenarios. In the second phase, the emission scenarios were examined by emissions sector (Table 6.3). For each scenario, six additional simulations were run altering the emissions from

Table 6.3 Details of the ECLIPSE emission sector inventories used in each TOMCAT-GLOMAP model simulation.

	Meteorology	AWB	DOM	ENE	IND	TRA	WST
CLE_2010	2010	CLE	CLE	CLE	CLE	CLE	CLE
CLE_2050	2050	CLE	CLE	CLE	CLE	CLE	CLE
MTFR	2050	MTFR	MTFR	MTFR	MTFR	MTFR	MTFR
SLCP	2050	SLCPMIT	SLCPMIT	SLCPMIT	SLCPMIT	SLCPMIT	SLCPMIT
2DEG	2050	2deg	2deg	2deg	2deg	2deg	2deg
MTFR_awb	2050	MTFR	CLE	CLE	CLE	CLE	CLE
MTFR_dom	2050	CLE	MTFR	CLE	CLE	CLE	CLE
MTFR_ene	2050	CLE	CLE	MTFR	CLE	CLE	CLE
MTFR_ind	2050	CLE	CLE	CLE	MTFR	CLE	CLE
MTFR_tra	2050	CLE	CLE	CLE	CLE	MTFR	CLE
MTFR_wst	2050	CLE	CLE	CLE	CLE	CLE	MTFR
SLCPMIT_awb	2050	SLCPMIT	CLE	CLE	CLE	CLE	CLE
SLCPMIT_dom	2050	CLE	SLCPMIT	CLE	CLE	CLE	CLE
SLCPMIT_ene	2050	CLE	CLE	SLCPMIT	CLE	CLE	CLE
SLCPMIT_ind	2050	CLE	CLE	CLE	SLCPMIT	CLE	CLE
SLCPMIT_tra	2050	CLE	CLE	CLE	CLE	SLCPMIT	CLE
SLCPMIT_wst	2050	CLE	CLE	CLE	CLE	CLE	SLCPMIT
2deg_awb	2050	2deg	CLE	CLE	CLE	CLE	CLE
2deg_dom	2050	CLE	2deg	CLE	CLE	CLE	CLE
2deg_ene	2050	CLE	CLE	2deg	CLE	CLE	CLE
2deg_ind	2050	CLE	CLE	CLE	2deg	CLE	CLE
2deg_tra	2050	CLE	CLE	CLE	CLE	2deg	CLE
2deg_wst	2050	CLE	CLE	CLE	CLE	CLE	2deg

just one sector at a time, leaving the remaining five sectors with CLE 2050 emissions (e.g. MTFR_awb, refers to a simulation driven by 2050 emissions under the CLE scenario for every sector except AWB, which is replaced by MTFR 2050 emissions).

Table 6.4 Global mean CH_4 concentrations in ppb for scaling in TOMCAT-GLOMAP simulations using each emissions scenario.

	2010	2050			
	CLE	CLE	MTFR	SLCP	2deg
Global mean surface CH_4 (ppb)	1780	2200	1450	1453	1841

In the 2050 simulations the scaling was applied depending on the projected emissions of CH_4. A global box model was used, assuming a fixed global mean tropospheric OH concentrations of 1.1×10^6 mol cm^{-3}, driven by the 2050 CH_4 emissions for each scenario, to estimate the resulting surface CH_4 concentration (Table 6.4). The resulting global mean CH_4 concentrations in 2050 in each scenario are comparable to estimates based on RCP scenarios (Meinshausen et al., 2011; Galmarini et al., 2017). In future work, a CH_4-OH feedback factor should be applied to account for changes in CH_4 which then influence OH concentrations, therefore feeding back on its own atmospheric lifetime. A multi-model median feedback factor of 1.28 was calculated by Stevenson et al. (2013), comparable to the estimate in Voulgarakis et al. (2013) of 1.24.

The SOCRATES radiative transfer model was then used to estimate the radiative effect of simulated changes to tropospheric O_3 and aerosol. For O_3, the stratospheric temperature adjusted RF was used (Section 3.6.1) while for aerosol, both the direct radiative forcing (DRF) and cloud albedo forcing (CAF, or first indirect effect) were calculated (Section 3.6.2).

6.5. 2050 surface ozone and PM concentrations

Figure 6.2 shows the simulated change in annual mean surface O_3 and PM2.5 concentrations in 2050 for each ECLIPSE scenario. Annual mean model values are used to indicate broad changes in average surface pollution over different regions in response to the changing emissions. In the simulations using emissions from the CLE scenario, there are substantial increases in tropospheric O_3 concentrations, most notably over India and South-East Asia.

The increase is simulated throughout the SH, with a maximum increase of 54% over India. O_3 concentrations decrease as expected over North America and Europe, continuing the present-day trend (Cooper et al., 2014). The global average change is an increase of 5.6%.

When using MTFR emissions, the change in simulated surface O_3 is much more homogeneous (Figure 6.2c). Comprehensive emissions reductions result in a global surface O_3 change of -20.5%. The change is substantially larger in the NH, where historically largest anthropogenic emissions of O_3 precursors are

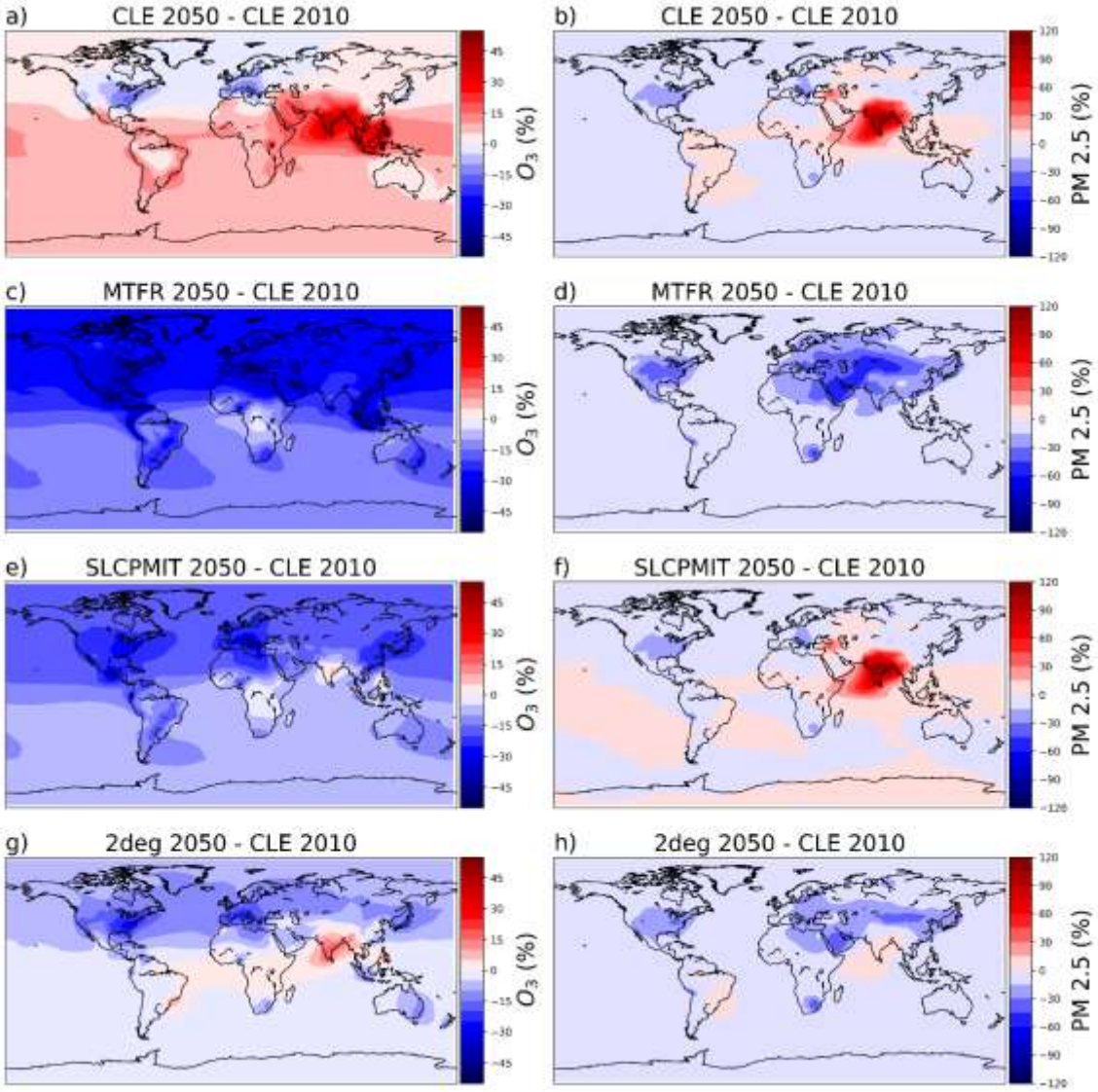

Figure 6.2 Simulated percentage change in annual mean 2050 global surface concentrations of O_3 (left panels) and PM2.5 (right panels), under the 4 ECLIPSE future emissions scenarios, relative to the 2010 reference emissions case (CLE).

located, leading to a larger relative change. A similar but smaller change is simulated when using the SLCPMIT emissions (Figure 6.2e), with the largest change in the NH, particularly over the USA, Western Europe and Eastern China. There is a 13.6% decrease in global mean surface tropospheric O_3 concentrations, with localised increases in India and parts of South East Asia of up to 21%. Figure 6.2g shows the simulated response of O_3 when using emissions for the 2deg scenario, with a smaller global mean drop in O_3 concentrations of 5%. The greatest difference in this scenario is a substantial increase in O_3 over India, and a much smaller decrease over China relative to the SLCPMIT or MTFR simulations.

For $PM_{2.5}$, the simulations with CLE and SLCPMIT emissions simulate very similar changes to surface concentrations, with global mean changes of less than 1%, but large regional changes (Figure 6.2b and Figure 6.2d). The most notable change is a large increase in $PM_{2.5}$ over India in both CLE and SLCPMIT, with concentrations increasing by 113% and 122%, respectively. North America and Europe have decreasing concentrations in both, with a slight decrease in background levels of surface O_3 also simulated. The difference in the simulated response of O_3 and $PM_{2.5}$ in the SLCPMIT runs indicates the focus on climate solutions in that emissions scenario, with an apparent lack of action on emissions that contribute only to air pollution and not to warming (e.g. sulphate aerosol). As expected, the MTFR simulation differs substantially, with falling O_3 concentrations globally, with a mean decrease of 6.5%. The most prominent decrease is a large drop in surface O_3 over central Eurasia of ~60%. The 2deg simulation exhibits a similar spatial pattern as the CLE and SLCPMIT simulations, but with a much smaller increase over India, and a stronger decline over the NH industrialised regions (Figure 6.2h), for a global mean decrease of 4.1%.

Table 6.5 Percentage change (%) in prescribed global mean CH_4 concentration and simulated 2050 global tropospheric burden of CO, NO_x and O_3, mean tropospheric OH concentrations and aerosol optical depth (AOD) under each ECLIPSE scenario, relative to 2010 CLE simulation.

	CH_4	CO	NO_x	O_3	Mean tropospheric OH	AOD (at 550 nm)
CLE	23.6	7.8	1.7	7.6	-2.9	10.7
MTFR	-18.5	-19.9	-21.2	-15.2	-3.9	-23.3
SLCPMIT	-18.4	-21.0	-9.0	-9.8	3.9	11.7
2deg	3.4	-2.0	-9.7	-2.1	-4.9	-12.6

Table 6.5 shows the percentage change in a number of relevant variables for each emission scenario, relative to the present-day control. Simulated tropospheric CO burdens in 2050 decrease in all scenarios apart from the CLE, with the largest decreases in the MTFR and SLCPMIT scenarios. Similarly for NO_x burden, all three emission reduction scenarios decrease the burden relative to the present-day, however there is a much smaller decrease from SLCPMIT compared to MTFR, with a larger drop in the 2deg scenario. The effect on tropospheric O_3 burden is as expected following the analysis of surface O_3 in Figure 6.2, with an increase from CLE emissions, a large reduction for MTFR and smaller reductions from SLCPMIT and 2deg scenarios. The large changes in global CH_4 and CO are likely the primary drivers of changes in simulated OH concentrations, with substantially increased CH_4 in the CLE 2050 simulation a probable driver of the decrease in OH (Holmes et al., 2013). The simulated change in precursor burdens indicates that the decrease in O_3 is driven by decreasing emissions of CH_4 and CO in the SLCPMIT scenario, reduced emission of NO_x in the 2deg scenario and a combination of these effects in the MTFR scenario. For the MTFR and 2deg experiments the decrease in O_3 and NO_x may have contributed to fall in OH concentrations despite decreased global CH_4 and CO concentrations. Whereas in the SLCPMIT scenario, the increase in simulated OH is a result of the sharp decrease in CH_4 emissions. Simulation of changes in future OH concentrations is limited by the use of present-day meteorology in TOMCAT-GLOMAP. In a warming climate, increased water vapour is likely to lead to an increase in OH concentrations through its reaction with $O(^1D)$ (Johnson et al., 2001).

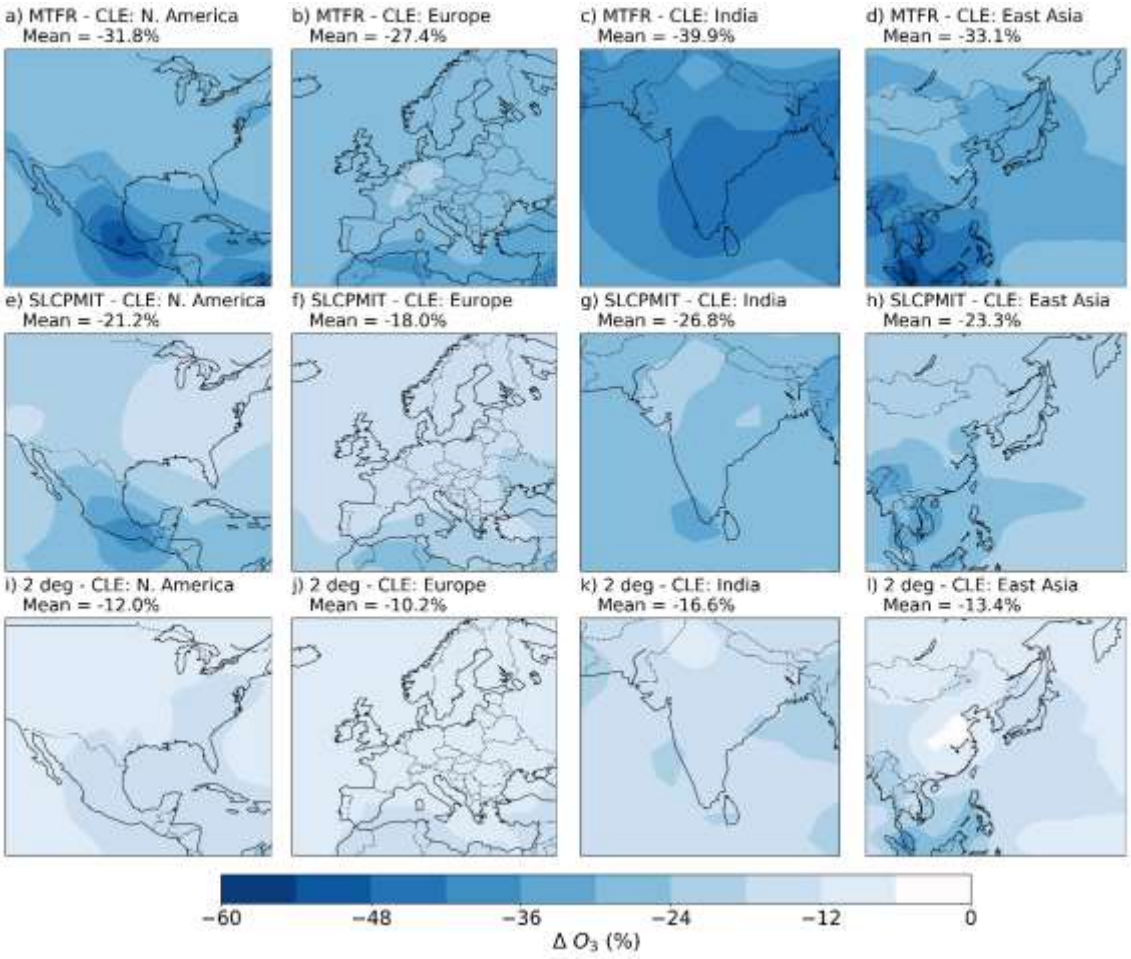

Figure 6.3 Regional changes (%) in 2050 surface O_3 concentrations for ECLIPSE scenarios MTFR (a-d), SLCPMIT (e-h) and 2deg (i-l), all relative to CLE 2050 scenario. The mean change over each region is also shown.

Figure 6.3 shows the difference in simulated surface O_3 between the CLE scenario and each of the emission reduction scenarios in 2050, over important regions for SLCP emission. The largest difference relative to CLE is in the simulation with MTFR emission reduction, with a global mean change of -24.6%. The simulated change is larger than the global mean over each of the four key regions examined here, with the largest reductions over India and South-East Asia. These two regions are the most important for each of the future emission scenarios. The simulated surface O_3 change in the SLCPMIT and 2deg scenarios is smaller than in MTFR, with a global change of -17.8 and -9.9%, respectively. However, the relative importance of each region is the same across all three scenarios, with the largest simulated decrease over India, followed by South-East Asia, North America and Europe. This suggests that each scenario targeted the same key regions for emission-driven reductions of O_3, but the

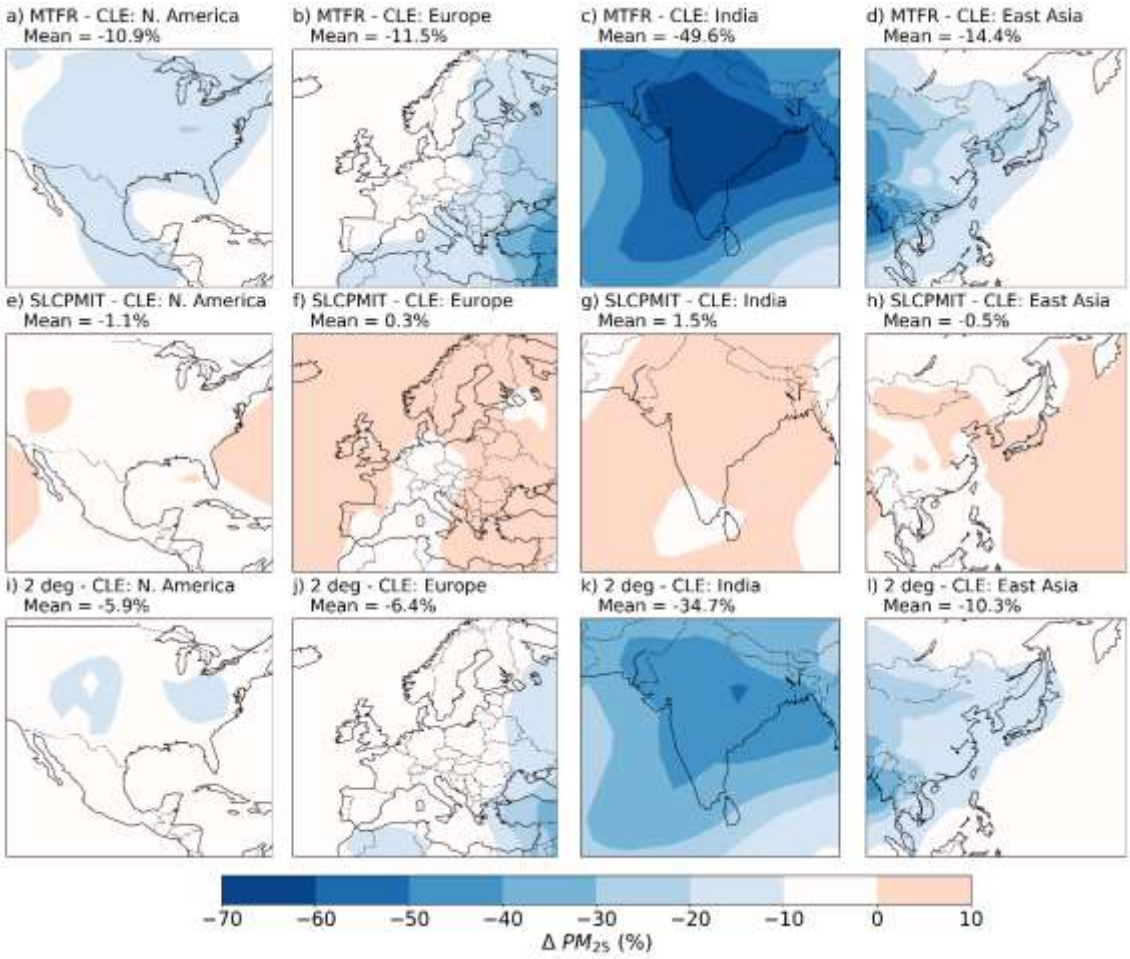

Figure 6.4 Regional changes (%) in 2050 surface $PM_{2.5}$ concentrations for ECLIPSE scenarios MTFR (a-d), SLCPMIT (e-h) and 2deg (i-l), all relative to CLE 2050 scenario. The mean change over each region is also shown.

extent to which emission reduction measures are implemented in the inventories differs considerably.

The regional difference in surface $PM_{2.5}$ concentrations between each scenario and the CLE reference scenario in 2050 is shown in Figure 6.4. By far the most substantial change in $PM_{2.5}$ concentration is simulated over India in the MTFR scenario, with a 50% reduction relative to CLE. There are also decreases in PM over the USA (-10.9%), Europe (-11.5%) and East Asia (-14.4%) which were larger than the global mean change (-5.8%). The simulated spatial change in O_3 is similar for the MTFR and 2deg scenarios, with the biggest reduction over India, and decreases in each key region more substantial than the global mean of -3.7%. Simulated $PM_{2.5}$ in the SLCPMIT scenario differs considerably from the other emission reduction scenarios, with very little change relative to the

reference scenario. The global mean surface $PM_{2.5}$ concentration increased by 0.3%. The most important regions were India with a 1.5% increase and the USA with a 1.1% decrease in surface $PM_{2.5}$. Together with Figure 6.2, this indicates the different priorities for emission reduction measures in the SLCPMIT scenario, with substantial effort to reduce tropospheric O_3, but a small increase in surface pollution relative to the CLE.

6.6. Radiative effect of emissions reduction scenarios

The radiative effects of the simulated changes to aerosol and O_3 concentrations were calculated using the SOCRATES offline radiative transfer model. Figure 6.5 shows the radiative effect of each component and the combined effect (aerosol DRF + aerosol CAF + O_3 RF) in Wm^{-2}, for simulations using 2050 emissions from each future emissions scenario, relative to the 2010 CLE simulation. In the CLE scenario, increasing total global emissions of aerosols

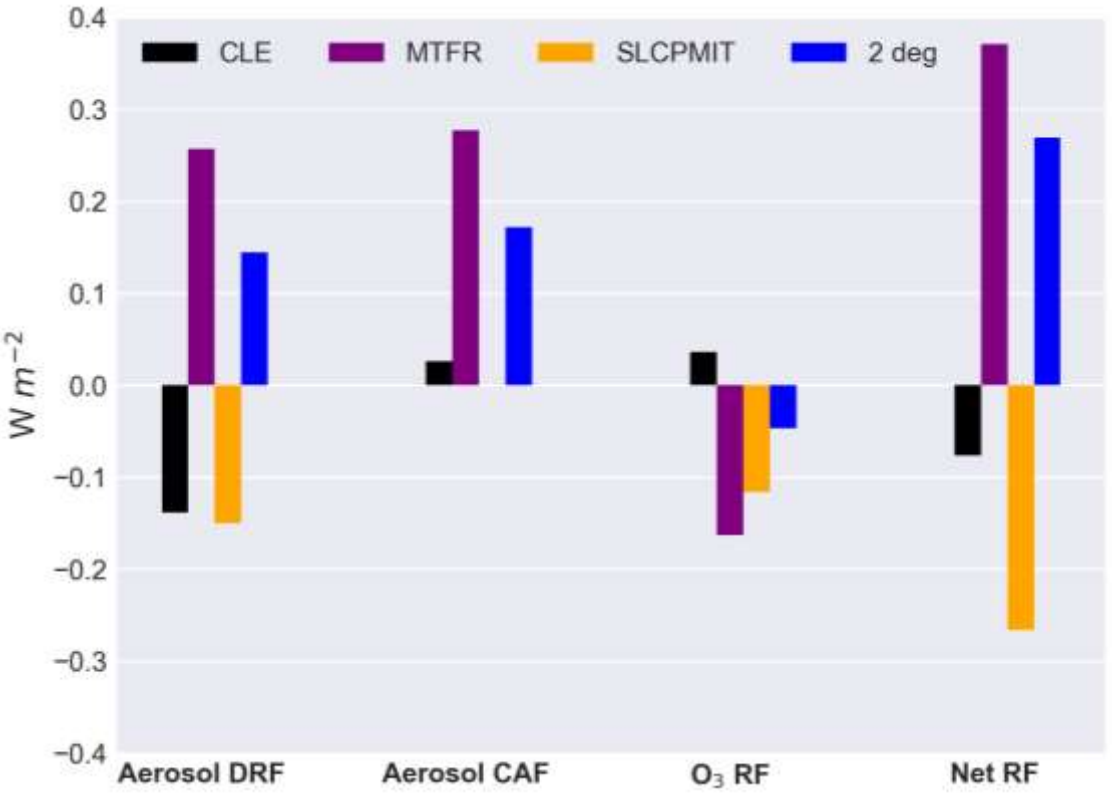

Figure 6.5 2010 – 2050 radiative effect (Wm^{-2}) for each ECLIPSE emissions scenario due to aerosol direct radiative forcing (DRF), aerosol cloud-albedo forcing (CAF), O_3 radiative forcing and the combined forcing.

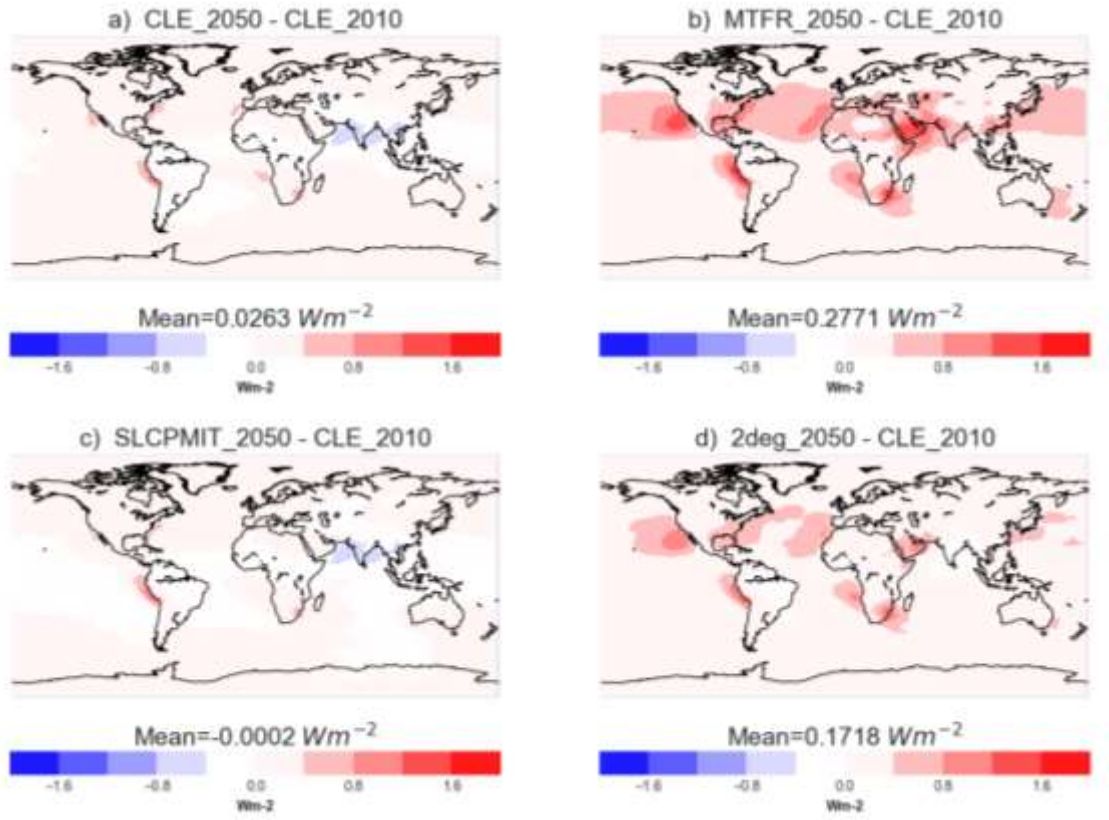

Figure 6.6 Global distribution of CAF for each ECLIPSE scenario in 2050, relative to the CLE 2010 simulation.

and O_3 precursors lead to increased atmospheric concentrations by 2050 (Figure 6.2). This results in continued negative forcing by aerosols, and a positive forcing by tropospheric O_3.

The negative DRF due to aerosol—radiation interaction in the CLE 2050 scenario is driven predominantly by large increases in simulated aerosol concentration over India, leading to increased scattering and a negative global mean radiative effect. Interestingly, despite the large increase in simulated aerosol over India, a slight positive CAF is calculated from the aerosol-cloud albedo effect. The negative forcing from the direct effect is due to increased emissions of SO_2, leading to increased sulphate concentrations in the 2050 CLE simulation. With increased atmospheric aerosol in 2050 relative to 2010 in the CLE scenario (Table 6.5), it would be expected that the cloud albedo effect would also be negative, as increased aerosol increases CDNC and cloud albedo. Anthropogenic emissions of SO_2, OC and BC have shifted towards the tropics in the 2050 inventory, due to increasing emissions over India and Africa,

while emissions from Europe and USA have continued to decrease. This results in increased aerosol loading at low-latitudes in the tropics, with decreasing aerosol and hence CDNC in much of the NH and high-latitudes of the SH. Therefore, a positive CAF is calculated for much of the globe, but with a negative effect over India and much of the tropics (Figure 6.6a). However, although the simulated global tropospheric aerosol burden is slightly larger in the CLE 2050 simulation than in 2010, there is an increase in simulated aerosol in the free troposphere in 2050, with a slight decrease in the boundary layer where the aerosol may interact with cloud processes. This effect is driven by the change in distribution of emissions, as in the tropics more efficient convective uplift results in greater transport of aerosols into higher altitudes. This effect results in a reduction in simulated global CDNC in the boundary layer where they have a climatic effect, and a positive CAF. In addition, aerosol components have different efficiencies as CCN, therefore the relative change in aerosol components may also have an effect. The 2050 simulation has increased emissions of precursors SO_2 and NO_x, but decreased emissions of BC and OC, changing the composition of atmospheric aerosol and their efficiency in affecting cloud processes.

The SLCPMIT simulation has a similar DRF as CLE, as the projected 2050 changes to aerosol emissions and their precursors are similar in both scenarios. SO_2 emissions for example, are just 0.25% smaller in the SLCPMIT scenario, although there is a slight change in distribution of emissions. The CAF differs between the two scenarios, with a negative forcing of 0.002 Wm^{-2} in the SLCPMIT experiment, due to a slight increase in aerosol burden and hence CDNC. Despite the minor decrease in SO_2 emissions, the sulphate aerosol burden is slightly higher in the SLCPMIT experiment, leading to an increase in CDNC and hence, cloud reflectively. This effect is caused by the substantial decrease in CH_4 emissions in the SLCPMIT simulation. The resulting decrease in global steady-state CH_4 concentration of ~34% (Table 6.4), leads to an increase in OH, which in turns increases oxidation rates of SO_2 and results in enhanced sulphate aerosol formation (Fiore et al., 2012).

The O_3 effect however differs considerably from CLE, as emissions of precursors CO, NO_x and VOCs (including CH_4) are decreased by 55%, 45% and 67%, respectively. This results in a substantial decrease in tropospheric O_3 and consequently a mean global RF of -0.12 Wm^{-2}. The combined negative RF from both aerosol forcing components and the O_3 forcing is estimated at -0.26 Wm^{-2}.

The MTFR scenario projects large decreases in emissions of aerosols, and therefore results in substantial simulated decreases in aerosol burden (Figure 6.2). This decrease in cooling aerosol results in a positive aerosol DRF of 0.26 Wm^{-2}. The decline in aerosol similarly results in a positive CAF of 0.27 Wm^{-2}, as a decrease in CDNC increases cloud effective radius and therefore reduces cloud albedo. The estimated combined aerosol forcing due to 2010 to 20150 aerosol emissions reductions is therefore 0.53 Wm^{-2}. This positive forcing is partially offset by a negative forcing of -0.16 Wm^{-2} due to decreases in tropospheric O_3. However, with the aerosol effect dominating, the combined forcing for the MTFR scenario is estimated at 0.37 Wm^{-2}. This represents a key challenge associated with the action needed to reduce air pollution, in that the side effect of removing harmful pollutants is the concurrent removal of their cooling effect on climate, exacerbating near-term warming.

The 2deg scenario emissions result in similar changes to the MTFR scenario but of smaller magnitude, which is reflected in the combined RF estimate of 0.27 Wm^{-2}. The removal of aerosol in the 2deg scenario results in a global positive forcing of 0.32 Wm^{-2}, with measures reducing O_3 precursor emissions resulting in a smaller forcing of – 0.047 Wm^{-2}.

6.7. Emissions sectors analysis

In this section, simulated SLCP concentrations from the second phase of model runs are used to examine the relative importance of the six emission sectors that make up the ECLIPSE emissions inventories.

6.7.1. Effect of sectors emissions changes on surface pollution

The impact of emission changes on simulated tropospheric burden and concentrations of pollutants at the surface is evaluated. The impact of emissions reduction measures in each sector in the four ECLIPSE scenarios on simulated tropospheric O_3 burden in 2050 is shown in Figure 6.7. The sector change with the largest effect in the MTFR scenario was agricultural waste burning (AWB), leading to a 12% decrease in global tropospheric O_3 relative to CLE. In the MTFR scenario, AWB and waste (WST) emissions are assumed to be zero for all species, leading to substantial decreases in O_3 precursors, particularly CO and VOCs which have a large sources from these sectors in present-day and the CLE scenario. The zero emissions in the MTFR scenario leads to substantial O_3 decreases from both the AWB and WST, however these sectors have only minor emissions change in the SLCPMIT and 2deg scenarios, leading to minor changes to O_3 burden.

The emission sector simulated to most efficiently decrease O_3 burden in the SLCPMIT and 2deg scenarios is surface transportation (TRA), with a global burden decrease of almost 4% in SLCPMIT and 2% in 2deg. The TRA sector emission reductions in MTFR also leads to a decrease in O_3 of ~4%. TRA emissions make up the largest proportion of anthropogenic emissions of the O_3 precursor NO_x (45%), and the second largest proportion of CO (29%) and VOCs (27%) (DOM was the largest contributing sector for both). Thus, changes to emission in these sectors is likely to have a major effect on tropospheric O_3 formation, particularly as NO_x is generally the limiting factor for production in all but the most polluted regions.

In the MTFR and SLCPMIT scenarios, NO_x emissions from TRA are reduced by 90%. The DOM sector is also a large emitter of O_3 precursors, and has similar magnitude precursor emission reductions in the MTFR scenario, of 79% and 64% for CO and NMVOCs, respectively. However, the result of the DOM emissions changes is less substantial for O_3, with a simulated global mean concentration decrease of ~1%, indicating that NO_x emissions reductions more efficiently mitigate tropospheric O_3 production. In the MTFR scenario, emission reductions in the ENE and IND sectors also lead to decreasing O_3 of 1-2%.

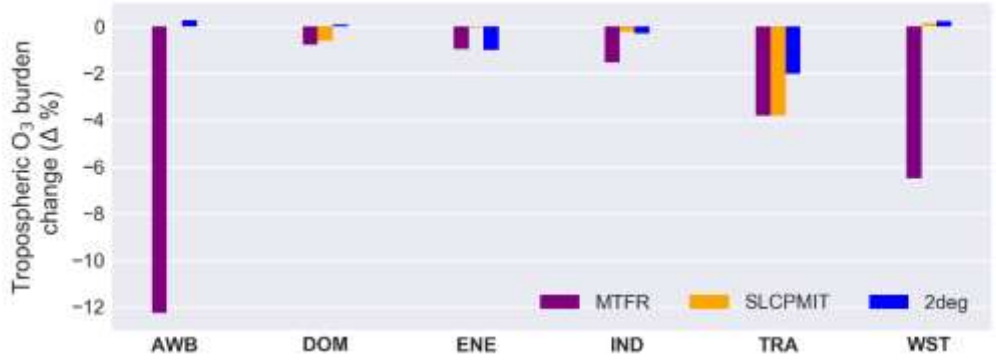

Figure 6.7 Percentage change in the 2050 simulated annual global tropospheric O_3 burden, from each sector simulation for scenarios MTFR (purple), SLCPMIT (orange) and 2deg (blue) ECLIPSE scenarios, relative to the 2050 CLE simulation.

These sectors contribute considerably to the total emissions of CO, NO_x, CH_4 and NMVOCS, however relative to the 100% emissions reduction in the AWB and WST sectors the projected emission change is small.

Individual sector emission changes in the SLCPMIT scenario lead to very little O_3 change in all but the TRA and DOM scenarios. An 80% CH_4 emission reduction in the AWB sector, compared to 100% reduction in the MTFR scenario, leads to only a minor effect on O_3, with a slight decrease by 2050 in the SLCPMIT AWB scenario. SLCPMIT changes in the ENE sector lead to only a 0.1% decrease in O_3, a smaller effect than the MTFR or 2deg scenarios. SLCP ENE emissions reductions of CH_4 and CO match the MTFR scenario, however, substantially smaller changes to NO_x and NMVOC ENE emissions resulted in the reduced effect on O_3, indicating again that NO_x emission changes have a large effect on O_3. Emission changes in the 2deg scenario are most efficient in the TRA sector, however there is also a large effect from ENE changes, almost equivalent to the MTFR scenario. The 2deg scenario is the only scenario in which WST emission reductions result in an increase in tropospheric O_3 burden.

The effect of emission sector changes in the MTFR scenario on simulated global surface O_3 concentrations is shown in Figure 6.8. As also reflected in Figure 6.7, the AWB and WST sectors have the largest impact, with a global mean surface

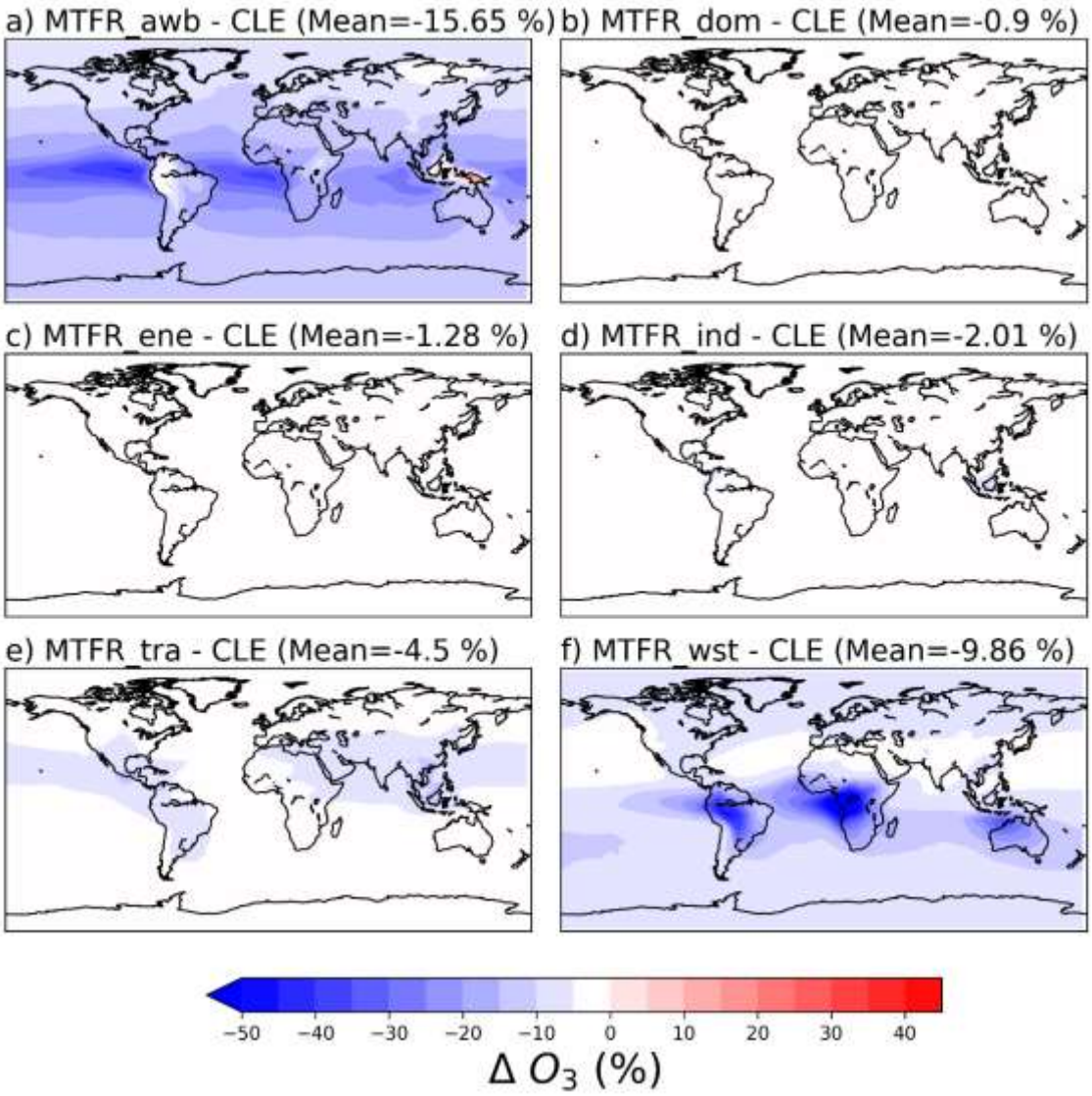

Figure 6.8 Percentage change in simulated global surface O_3 concentrations in 2050 due to MTFR scenario emission changes in each individual sector, relative to the CLE scenario.

O_3 concentration change of -15.7% and -9.9%, respectively. The largest impact from the simulation with MTFR AWB emissions is simulated over the tropics, particularly off the eastern coasts of South America and Africa. However, there is actually an increase in simulated surface O_3 over South-East Asia and parts of the Amazon. This is due to a large decrease in CO emissions from agricultural burning in these regions, resulting in a localised increase in OH concentrations of more than 10%. As AWB is only a minor source of NO_x, NO_x emissions remain high in this simulation and consequently the increase in OH slightly enhances tropospheric O_3 production. In addition, there is a large decrease in VOC

emissions in the MTFR_AWB scenario, resulting in decreases in simulated PAN concentrations of up to 70% over South East Asia. As a result, there is increased NO_x in areas with previously large VOC emission, promoting O_3 formation. The MTFR WST simulation simulates large changes over the Amazon basin, Central Africa and Northern Australia. The change is largely driven by the decrease in CH_4 emissions, which accounts for ~26% of all anthropogenic CH_4 emission in the 2050 CLE inventory. This results in a large decrease in O_3 formation, decreasing concentrations by up to 54% in Central Africa. Each of the other sectors simulate much smaller changes to surface O_3, with the TRA sector the next most effective at -4.7%, due to substantial NO_x emissions reductions, primarily over South East Asia.

Figure 6.9 shows the change in simulated surface $PM_{2.5}$ concentrations for emissions changes in each sector with the MTFR scenario. The ENE sector simulates the largest decrease in global surface PM, with a mean decrease of -3.2%. This decrease is largely driven by substantial reductions over India, where $PM_{2.5}$ concentrations fall by up to 44% relative to CLE 2050. Smaller changes are simulated over Central Asia, North Africa and the USA, with a slight decrease in $PM_{2.5}$ simulated globally. The IND sector results in a similar decrease in PM of -3.0%, with the largest change in this case occurring in Central Asia and the Middle East. A large decrease is also simulated over South Africa, lower concentrations of PM simulated globally, due to large decreases in SO_2, NO_x, BC and OC from all anthropogenic industrial sources. The next most effective sector for decreasing PM pollution is AWB, with a global mean change of -2.5%. The MTFR AWB run simulates large decreases in PM in South America, South East Asia and NH high-latitudes. However, TOMCAT-GLOMAP also simulates increases in PM over much of Asia and parts of Australia and South Africa. These changes are driven by the simultaneous emissions reductions of non-aerosol species. AWB is a relatively minor source of aerosols and precursors, whereas it is a major source sector of CO. Therefore relatively minor changes in SO_2 emissions coupled with a large reduction in CO emissions, results in a substantial increase in oxidation capacity of the troposphere, enhancing the rate at which SO_2 is oxidised into sulphate aerosol. Similarly, localised increases in PM are simulated in the simulation with DOM,

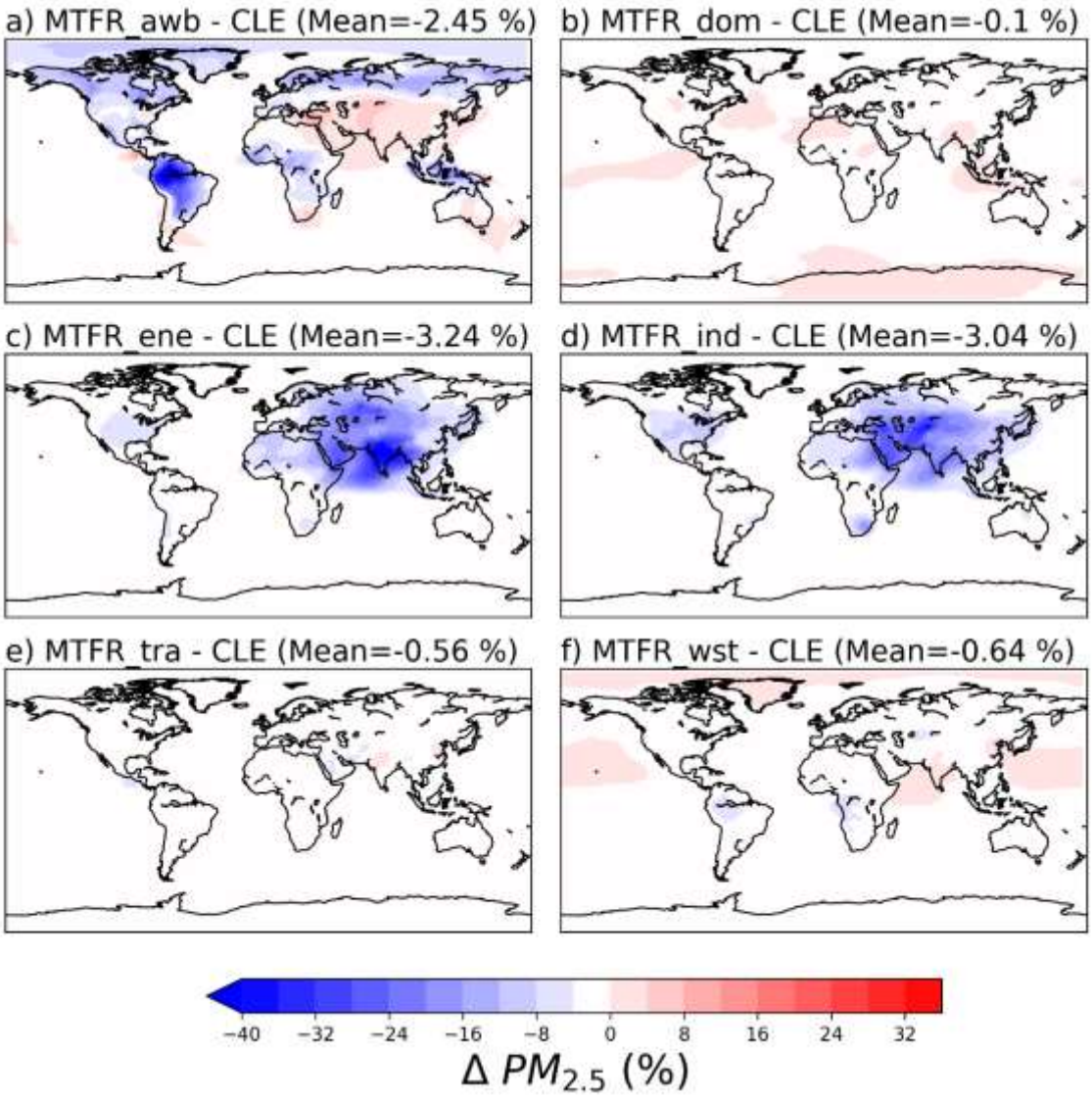

Figure 6.9 Percentage change in simulated global surface $PM_{2.5}$ concentrations in 2050 due to MTFR scenario emission changes in each individual sector, relative to the CLE scenario.

TRA and WST sector MTFR emissions, although all sectors result in a global mean decrease in surface O_3.

The emission sector simulations performed in this section demonstrate that different air pollutants are most effectively decreased by changes to different emissions sectors. For surface O_3, the AWB and WST sector emission changes lead to the largest decrease in simulated concentrations. This is the result of 100% emission decrease in these sectors under a MTFR scenario. The transport sector however most effectively reduced surface O_3 per unit of emission reduced, due to the higher proportion of NO_x emissions from the

transport sector, which most effectively mitigates tropospheric O_3 formation. Due to the likely difficulty in developing a globally circular economy, with zero waste or waste burning emission by 2050, the TRA sector is the likely the most effective emissions sector on which to focus emissions reduction efforts in order to decrease O_3 pollution. In terms of PM pollution, the ENE and IND sectors most efficiently improve global air quality in the MTFR scenario, with the largest improvement simulated over India and the Middle East.

6.7.2. Effect of sector emission changes on radiative forcing

In this section, the effect of emission sector changes on radiative forcing (RF) is evaluated, accounting for the aerosol direct radiative forcing (DRF), the aerosol cloud-albedo forcing (CAF) and tropospheric O_3 RF. Figure 6.10 displays the

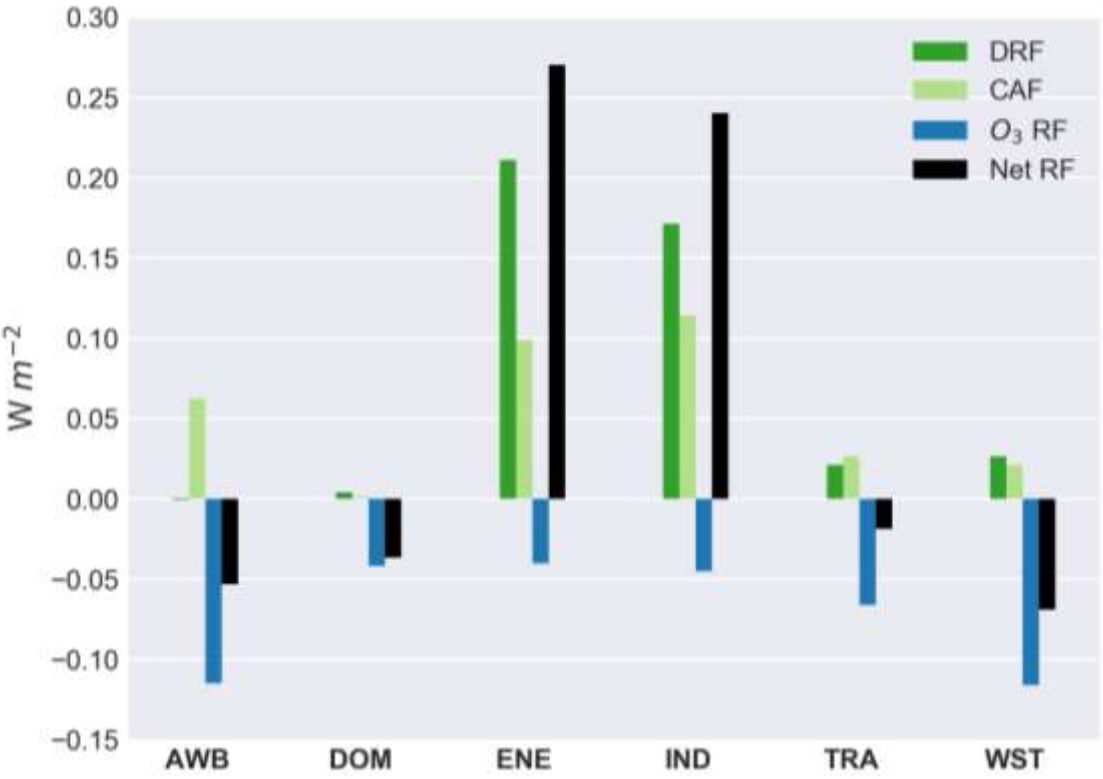

Figure 6.10 Global mean radiative forcing in 2050: aerosol direct effect (DRF, dark green), cloud-albedo forcing (CAF, light green) and tropospheric O_3 radiative forcing (blue) for each emissions sector change under the MTFR scenario, relative to the CLE scenario. The combined effect (aerosol DRF + aerosol CAF + O_3 RF) is shown in black.

estimated global mean radiative forcing of simulated changes to aerosol and O_3 due to emissions sector change in the MTFR scenario, relative to the CLE scenario, in 2050. The largest effect is caused by changes to the ENE and IND emission sectors, with a net positive forcing of 0.27 Wm^{-2} and 0.24 Wm^{-2}, respectively. The large reduction in simulated aerosol as seen in Figure 6.9 is the primary driver of the positive forcing, with an aerosol DRF of 0.21 Wm^{-2} in the ENE and 0.17 W m- in the IND sectors. The cloud-albedo effect is also considerable, contributing 0.10 Wm^{-2} and 0.12 Wm^{-2} for ENE and IND sectors, respectively. As a result, these sectors result in a net warming effect by 2050, despite a decrease in O_3 causing a negative RF of approximately -0.05 Wm^{-2} in both ENE and IND simulations. All MTFR emission sectors resulted in a negative RF due to tropospheric O_3 in 2050, due to decreases in precursor emissions and hence O_3 formation. The sectors causing the largest decrease in O_3 RF were AWB and WST, reflecting the changes to surface O_3 shown in Figure 6.8. With a negative O_3 RF of 0.12 in both sectors, the resulting net RF is a cooling effect of 0.05 Wm^{-2} for the AWB simulation, and 0.07 Wm^{-2} for the WST simulation. The more negative response in the WST simulation is caused by a smaller CAF than in the AWB simulation. Four of the six emissions sectors result in a negative RF relative to the CLE scenario. However the positive forcing resulting from the

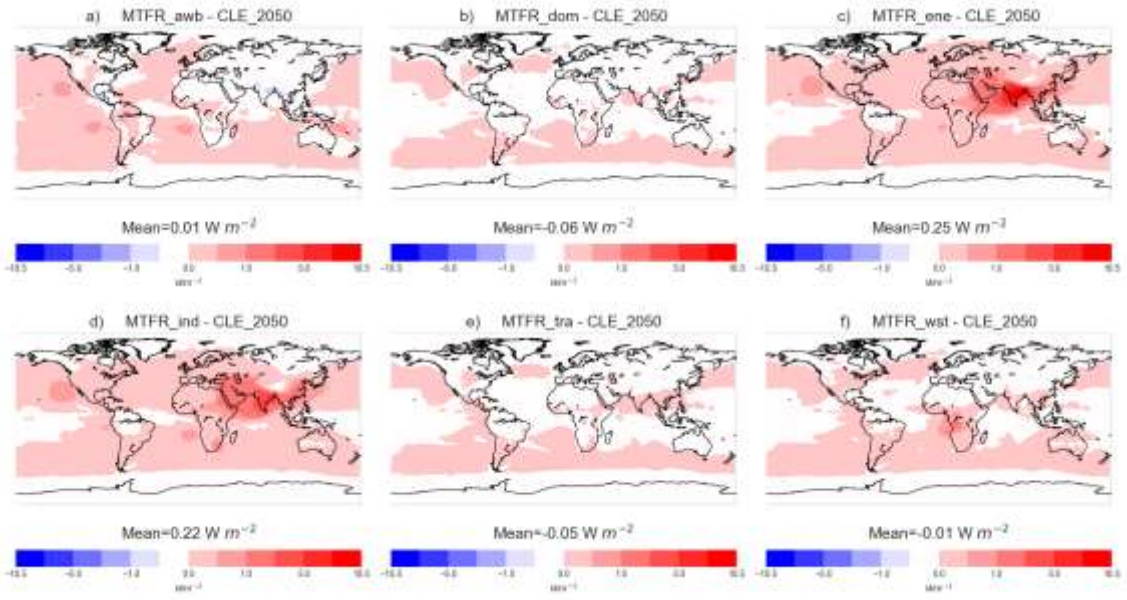

Figure 6.11 Combined (aerosol DRF + aerosol CAF + O_3 RF) RF for each emissions sector simulation in the MTFR scenario, relative to CLE, in 2050.

ENE and IND aerosol forcing response is substantially larger than the negative forcing in the other four sectors, indicating that overall the RF of the MTFR emission sectors is likely to be dominated by the positive forcing due to the decrease in global aerosol concentrations.

The global distribution of the calculated RF for each emission sector in the MTFR scenario is shown in Figure 6.11. The dominant feature is a warming effect over India in the ENE and IND emission sector simulations, caused by substantial decrease in aerosol concentration relative to the CLE simulation (see Figure 6.9). This leads to the net warming effect associated with the ENE and IND emission sector simulations, with a negative net RF in each of the other four sectors.

6.8. FaIR effective radiative forcing estimates

Here the FaIR model was employed to calculate the ERF from each SLCP component (Figure 6.12). Applying the ECLIPSE emission inventories in FaIR provides an estimate of RF due to SLCP emission changes which accounts for rapid adjustments to the climate system, and also estimates the simultaneous RF from changes in long-lived climate forcers such as CO_2 and N_2O. It should be noted that the SLCPMIT and 2deg scenarios were produced with more time steps, from 2020 to 2050, while the MTFR was provided only for 2030 and 2050. The poor time resolution of MTFR inventory emissions results in sharp changes to the simulated ERF of individual forcers, whereas in reality, there would be a more gradual change as emission reduction measures are introduced over several decades. For long-lived forcers, most notably CO_2, RCP4.5 emissions were used, leading to a growing CO_2 ERF between 1990 and 2050 in each simulation. Therefore in each ECLIPSE scenario simulated in FaIR, there was a persistently increasing ERF from CO_2 forcing (Figure 6.12a), contributing significantly to total ERF and temperature anomaly calculations, in order to estimates future ERF and temperature changes under realistic conditions.

For CH_4 ERF, implementing only emissions reduction from current legislation (CLE) leads to an increasing ERF, reaching 1.15 Wm^{-2} by 2050. Each of the ECLIPSE emission reduction scenarios result in a decrease in forcing by 2050 compared to the CLE scenario. The SLCPMIT and MTFR emissions cause a decrease in forcing almost immediately after implementation, and result in an almost equal ERF of 0.88 Wm^{-2}, a decrease in forcing of ~25%. The emission measures in the 2deg scenario are less effective at reducing CH_4 concentrations. CH_4 ERF continues to grow throughout the period, although at a slower rate than in CLE. This is partly due to the atmospheric lifetime of CH_4 of approximately one decade. The 2050 CH_4 ERF reaches 1.05 Wm^{-2}, a 9% decrease relative to CLE.

For tropospheric O_3 ERF (Figure 6.12c) the differences between the ECLIPSE scenarios are more drastic. Under CLE emissions, the ERF due to O_3 plateaus between 2010 and 2020, before increasing rapidly from 2030 to 2050. The resulting ERF of 1.10 Wm^{-2} in 2050 is almost as large as the CH_4 RF, indicating that tropospheric O_3 may become a more important climate forcer in the near-

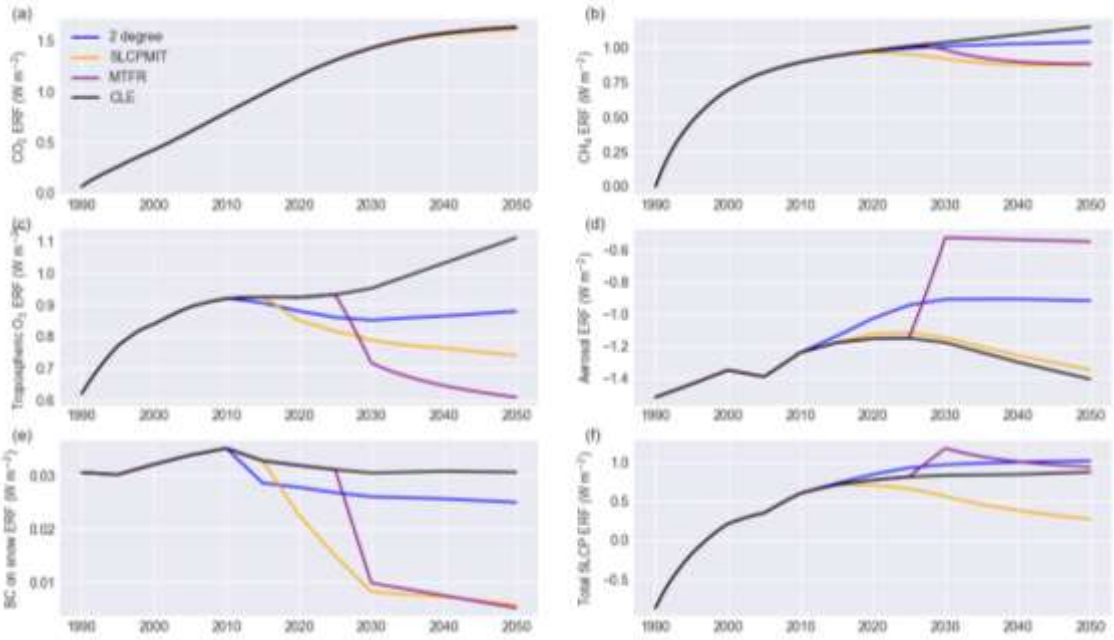

Figure 6.12 Effective radiative forcing of CO_2 (a), CH_4 (b), tropospheric O_3 (c), aerosol (d), BC on snow (e) and total ERF from SLCPs (f) from 1990-2050 for each ECLIPSE scenario, calculated by the FAIR model. All scenarios use RCP4.5 CO_2 emissions.

future without deliberate action to decrease emissions. Under the 2deg emissions scenario, O_3 ERF begin to decrease immediately following implementation, due to the short-atmospheric lifetime of O_3 compared to CH_4. Similarly to CLE, under the 2deg scenario there is a decrease in O_3 ERF from 2010 to 2030, but a small increase from 2030 onwards. This is most likely a result of projected population expansion and growth of developing economies having a strong effect from ~2030, limiting the effectiveness of current mitigation measures, as well as continued increases in global CH_4 concentrations. The 2050 CH_4 ERF under 2deg though is reduced to 0.88 Wm^{-2}, 20% lower than CLE. The SLCPMIT scenario simulates a larger decrease in O_3 ERF, falling to 0.74 Wm^{-2} in 2050 (a decrease of 33%). Under this scenario the simulated ERF decreases consistently from implementation until 2050. The MTFR scenario simulates an even larger decrease in O_3 ERF, falling to 0.61 Wm^{-2} by 2050, a drop of more than 55% compared to CLE.

The simulated aerosol ERF is shown in Figure 6.12d, with a negative forcing due to the predominantly cooling effect of atmospheric aerosols. Decreasing trends in aerosol emission in Europe and North America led to an increasing ERF (less cooling) from the late 20th century to 2010. The current legislation scenario projects a period of 1-2 decades of near constant forcing before a growing negative ERF from 2030 to 2050, due to increasing emissions from developing nations. This enhanced aerosol ERF results in a global cooling effect of -1.41 Wm^{-2} in 2050. This is the largest simulated cooling since 2005. Interestingly the simulated aerosol ERF in the SLCPMIT is very similar to the CLE scenario. There is a slight increase from 2020 onwards, leading to a 2050 aerosol ERF of -1.35 Wm^{-2}, just 0.06 Wm^{-2} larger than the scenario with no additional emission reduction measures from 2015. The 2deg scenario projects considerably lower aerosol emissions in coming decades, leading to a substantial decrease in the estimated global cooling effect. The 2050 aerosol ERF for 2deg is 0.92 Wm^{-2}, primarily due to reduced forcing from 2010 to 2030 which then remains almost constant until 2050. As expected the largest change in forcing is seen in the MTFR scenario, which significantly reduces anthropogenic aerosol emissions by 2050. This result in a substantial removal of the aerosol cooling effect, with an aerosol ERF -0.55 Wm^{-2} by 2050. Again,

this change in ERF was due to emissions changes implemented by 2030 when the aerosol ERF reaches a maximum of -0.52 Wm^{-2}, before a slight increase in aerosol from 2030 to 2050.

The effect of BC aerosol on snow (BC_{snow}) is also calculated in FaIR, as one of the primary mechanisms of aerosol causing a positive ERF and though to be a potentially important source of warming (Flanner et al., 2007; Myhre et al., 2013b). Similarly to the estimated ERF from CH_4, SLCPMIT and MTFR result in almost equal forcings by 2050, with BC_{snow} ERF of 5.7 mWm^{-2} and 5.2 mWm^{-2}, respectively. This is the largest reduction relative to the CLE scenario (30.6 mWm^{-2}) of any SLCP ERF, a decrease of more than 80%. However the ERF of BC_{snow} is considerably smaller than from other components, meaning the large relative change has little effect on the total ERF from the ECLIPSE scenarios. It does however illustrate again the targeted nature of the ECLIPSE emission scenarios, as estimates from the SLCPMIT emission scenario had very little change in the aerosol ERF, as reducing aerosol would lead to a warming effect, whereas there are significant changes for greenhouse gases and warming BC aerosol, which have a warming impact on climate. The 2deg scenario again has a more moderate response relative to CLE, with BC_{snow} ERF falling to 25 mW m^{-2}.

The total SLCP ERF (Figure 6.12f) is the net ERF of all SLCP forcing agents. The estimated ERF of all SLCPs was negative in the 20th century, before rising rapidly due to the decreasing aerosol and increasing CH_4 and O_3 ERF. The MTFR emissions scenario actually results in an increasing global ERF, larger than would be achieved from a CLE scenario with no additional action on SLCP emissions. This is the result of extensive measures to reduce aerosol emissions and improve air quality, removing the cooling impact of aerosols which cancels out the expected decreases in greenhouse gases CH_4 and O_3. The competing effects result in very little total ERF change in both the 2deg and MTFR scenarios relative to CLE, with 2050 SLCP ERFs of 1.02 Wm^{-2}, 0.95 Wm^{-2} and 0.88 Wm^{-2} for 2deg, MTFR and CLE scenarios, respectively. The peak SLCP ERF is actually estimated to be 2030 in the MTFR scenario (Wm^{-2}), due to the slowing rate of aerosol loss and increasing fall of O_3 and CH_4 between 2030 and

2050. The only scenario which decreases the ERF from all SLCPs is the SLCPMIT scenario, driven primarily a decrease in tropospheric O_3 precursors. However, in this context the absence of measures which reduce aerosol emissions in this scenario is perhaps a more important reason for the falling ERF. The 2050 SLCP ERF in SLCPMIT scenario is 69% lower than the CLE scenario at 0.27 Wm^{-2}.

6.9. Global temperature response

The FaIR climate model is also used to estimate the global mean surface temperature response to each emission scenario by 2050. Figure 6.13 shows the total ERF (including long-lived forcers) and global temperature response for each of the ECLIPSE future emission scenarios, coupled with RCP4.5 emissions. Historical temperature responses shows a steady increase since 1990 except for a sudden drop and recovery due the Mount Pinatubo eruption of 1991. The total ERF of the ECLIPSE inventories is larger than in RCP4.5 due to higher anthropogenic SLCP emissions in the historical ECLIPSE inventory than in RCP4.5, as CO_2 and other long-lived forcers are constant in each simulation. Each of the simulations estimates increasing total ERF from present-day to 2050, largely driven by the CO_2 forcing (Figure 6.12a). The estimated present-day total ERF is 2.96 Wm^{-2} using ECLIPSE emissions, an increase of 0.5 Wm^{-2} compared to the RCP4.5 estimates. Under the CLE scenario, this is estimated to increase by roughly 50% to 4.42 Wm^{-2} by 2050, with a projected temperature increase since PI of 2.09°C. This level of warming would exceed current targets to keep anthropogenic climate from reaching ‘dangerous’ levels as soon as 2050.

As a result of the increased total SLCP ERF (Figure 6.12), the 2deg scenario has a larger total ERF than the CLE scenario by 2050, reaching 4.56 Wm^{-2}. This is primarily caused by decreasing emissions of cooling aerosols and their precursors, which counteract efforts to decrease RF due to CH_4 and tropospheric O_3. SO_2 emissions for example are reduced by almost 50% in 2050 in the 2deg scenario inventory, leading to a substantial decrease in sulphate

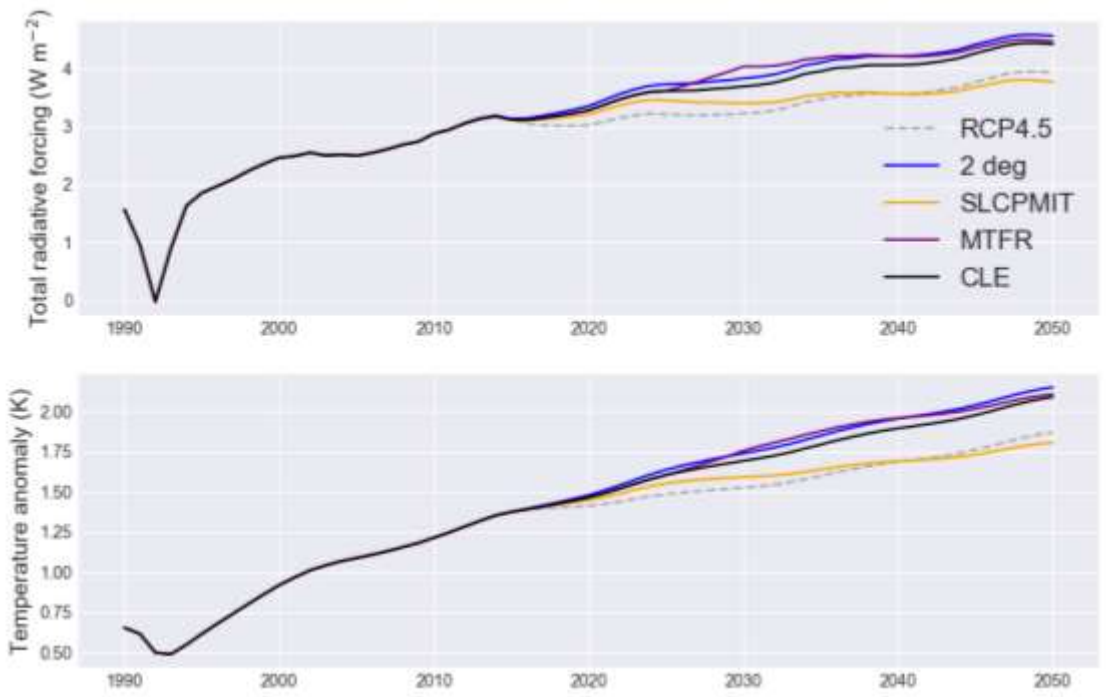

Figure 6.13 Total radiative forcing (upper panel) and temperature anomaly (lower panel) relative to the pre-industrial era (1750) from 1990-2050, for each ECLISPE emissions scenario and RCP4.5, as calculated by the FaIR model.

aerosol and consequently a decrease in the radiative cooling effect. The MTFR total ERF is slightly smaller than the 2deg scenario at 4.47 Wm^{-2}, due to the larger decreases in CH_4 and O_3 ERF. However, the MTFR and 2deg scenarios both surpasses the projected forcing from the CLE scenario, leading to global temperature anomalies of 2.11°C and 2.15°C, respectively. The possibility of enhanced warming through a comprehensive decrease in SLCPs is well known, due to the removal of aerosol and the corresponding cooling effect (Fiore et al., 2012). The 2deg emission scenario however was designed to limit global temperature change to 2 degrees of warming, whilst also pursuing air pollution management goals. The net ERF and resulting warming calculated here however indicates that in this scenario, insufficient action is taken to reduce warming components in order to offset removal of cooling aerosols.

The SLCPMIT scenario however results in a substantial decrease in the projected total ERF by 2050 and therefore also effectively reduces the expected global temperature change. Although the total SLCP forcing ERF decreases from 2030 onwards in the SLCPMIT scenario, the total ERF continues to rise

due to the influence of long-lived forcers CO_2 and N_2O. As a result, the 2050 total ERF is still 50% larger than the present-day ERF, estimated at 4.45 Wm^{-2}. This takes the projected ERF in the SLCPMIT scenario to below the RCP4.5 estimate, which has significantly smaller SLCP emissions relative to the ECLIPSE inventory. Notably, the decrease in total ERF leads to a global temperature change which does not surpass the 2°C target. The projected 2050 temperature anomaly of 1.81°C, indicates that mitigation of climate by tackling SLCP emissions has the potential to effectively reduce temperature change. However, when coupling the ECLIPSE SLCP emissions with the more extreme projected emission scenario of the RCP8.5 scenario, even the SLCPMIT scenario could not prevent the global temperature change from exceeding the 2°C target by 2050, with an estimated warming of 2.1°C. This is indicative of the importance of reducing emissions of long-lived forcers in climate mitigation strategies, with SLCP mitigation playing a supporting role to further mitigate global temperature change.

6.10. Summary

In this chapter, the effect of various future emission scenarios on surface air pollution and climate in 2050 has been analysed. The reference scenario was created to estimate historic SLCP emissions. Future emissions scenarios were then created to estimate the impact of changes to global SLCP emissions, ranging from the CLE with few measures to reduce emissions, to the MTFR scenario with widespread reductions to all anthropogenic emission sources. Each SLCP emissions from each scenario were employed in a modelling approach to estimate changes to atmospheric composition by 2050, with consequences for climate and air quality evaluated from a global, regional and sector-specific perspective.

As expected, the simulation driven by the MTFR scenario emissions for 2050 had the largest effect on surface concentrations of air pollutants. Both tropospheric O_3 and PM2.5 decreased globally compared to present-day and a 2050 scenario using CLE emission. The 2deg scenario also resulted in reduced

surface O_3 and PM2.5 but with a smaller decrease than MTFR, while the SLCPMIT and CLE scenarios resulted in a decrease in O_3, but increases in PM2.5 due to substantial increase over India. In all scenarios, the Indian subcontinent was the most important region for changes to surface pollution. Without measures to decrease anthropogenic emissions of SLCPs over India by 2050, surface concentrations of air pollutants could more than double. The transport sector is simulated to be the most important emission sector for SLCP mitigation of the six sectors included in ECLIPSE inventories, with the largest response in O_3 burden from changes to land transport emissions in all scenarios.

In terms of climate impacts, the MTFR scenario actually led to a net positive RF by 2050, despite large reductions in greenhouse gases CH_4 and tropospheric O_3 and BC aerosol. Substantial decreases in concentrations of cooling aerosol components resulted in a large decrease in the negative RF associated with aerosols, counteracting the change from greenhouse gases. This effect was smaller in the SLCPMIT scenario due to less stringent measures on emissions of cooling aerosols and their precursors. Year 2050 emissions of SO_2 in the SLCPMIT scenario were very similar to those in the CLE scenario, with the focus being on SLCP with a warming effect. Therefore the result of SLCPMIT emissions for climate was a considerable decrease in RF by 2050, relative to the CLE scenario. It is important to note that the ECLIPSE scenarios examined here are not necessarily realistic scenarios. In particular, the coupling of ECLIPSE emissions scenarios for short-lived forcers with RCP scenarios for long-lived emissions ignores the importance of co-varying long and short-lived emissions, creating scenarios which are not realistically viable. Rogelj et al. (2014) highlighted the importance of considering SLCP changes in the context of CO_2-led mitigation, while Shindell and Smith (2019) demonstrate that CO_2 mitigation can also affect near-term warming. It is therefore very important to consider SLCP changes in the context of likely changes to long-lived species (Rogelj et al., 2014; Rogelj et al., 2015). However, the scenarios applied here are intended as tools in understanding how climate and air quality will respond to hypothetical emission changes.

Of the emission reduction scenarios evaluated here, the SLCPMIT scenario is the only scenario with positives outcomes for both climate change mitigation and air quality by 2050. Measures to reduce CH_4, tropospheric O_3 precursors and BC effectively reduce global ERF by 2050, helping to decrease the rate of warming and demonstrating the possibility of keeping the global temperature anomaly below 2°C with accompanying action to reduce CO_2. The decrease in surface O_3 also has global benefits for human health and vegetation, preventing the premature loss of life and crop damage caused by O_3 pollution. However, the SLCPMIT scenario does not result in simultaneous advantages for aerosol air pollution. Other than stringent measures to reduce BC emission, SLCPMIT includes no emission reduction measures specifically targeting aerosols. As a result global air quality would worsen by 2050, costing the lives of many individuals and at a large economic cost. Therefore, while the SLCPMIT scenario may be very beneficial for climate outcomes and have some co-benefits through the action on O_3, it does not effectively tackle both climate change and air quality.

The findings presented in this chapter indicate that reducing air pollution and mitigating climate change simultaneously is difficult, due largely to the importance of aerosols in degrading air quality and their substantial negative climate forcing. However, decreasing tropospheric O_3 concentrations is effective at both mitigating climate change and improving air quality. Therefore policies which focus on decreasing emissions of precursors of tropospheric O_3 offer a clear, win-win outcome, and as such should be prioritised in coming decades. Some regions that are particularly affected by tropospheric O_3 such as India and South East Asia should be targeted more urgently, as decreases in these regions would present a substantial benefit in a relatively short period of time.

The confidence in the results presented here is limited by a number of factors, in particular the omission of CH_4 and long-lived species RF changes. Understanding the role of CH_4 RF in particular is relevant here as CH_4 also affects atmospheric oxidation and is a precursor of tropospheric O_3. Consideration of simultaneous changes in atmospheric concentrations will better inform estimates of net RF and will be necessary for policy making. Future

changes in climate and natural emissions are also ignored here in order to isolate the impact of anthropogenic actions through emission changes, however in order to put these changes into appropriate context these factors will need to be considered. Parameterisations and assumptions in both TOMCAT-GLOMAP and the FaIR model also limit certainty, as well as large uncertainties in emission inventories. Each of these has been evaluated extensively, therefore the results are useful to understand the likely impacts of specific changes and policies, although not for providing precise estimates or ranges without further ensembles or models being included.

Further research is required to determine the likely climate cost of improved air quality and whether this cost from aerosol forcing changes may be offset in part or in full by CO_2 and CH_4 mitigation. The urgency of air quality improvements for human health benefits means that pollution legislation will likely dominate climate mitigation in the short-term, but careful targeting of sources which co-emit absorbing BC aerosol and O_3 precursors, as well as cooling aerosol, is vital to limit the climate penalty.

7. Discussion

In this thesis, a suite of models and emission inventories have been used to investigate the sources of variability of major short-lived climate pollutants in the pre-industrial and present-day environment. SLCPs are a group of anthropogenic gases and aerosols which adversely impact air quality and contribute changes in global radiative balance. SLCPs may be crucial to future climate mitigation policies aimed at mitigating the worse impacts of climate change whilst also reducing global air pollution. However, this presents complex challenges as SLCP components vary greatly in their effect on climate, atmospheric lifetime, abundance, distribution and have numerous anthropogenic and natural sources. Therefore in order to understand the role of SLCPs in the mitigation of future climate change, it is vital to first have a comprehensive understanding of their role in the historic and present-day climate. This should include drivers of SLCP variability and trends, both natural and anthropogenic in origin. The results presented here improve understanding of the effect of SLCPs since the pre-industrial era and the causes of variations in global SLCP concentrations. Together with the results of Chapter 6, these findings highlight the importance of SLCPs in the future climate and are therefore assist in planning a strategy which aims to have co-benefits for climate and air quality. In this chapter, the major results of this thesis are discussed in the context of the original aims laid out in Chapter 1, as well as suggestions for further research.

7.1. Overview of main results

Thesis aim 1: Investigate the effect of uncertainty in pre-industrial natural emissions on tropospheric ozone radiative forcing.

The large uncertainty associated with the RF of tropospheric O_3 between the PI and PD is problematic when assessing the impact of SLCPs, especially when quantifying the relative contribution of SLCPs to observed climate change. Chapter 4 in this thesis utilised revised PI inventories of natural emissions, which have been recently developed to reflect the growing consensus that biomass burning and biogenic emissions were actually larger in the PI than in the present-day. These inventories were used in TOMCAT-GLOMAP to calculate new estimates of tropospheric O_3 concentrations and RF.

It was found that simulated tropospheric O_3 concentrations vary considerably depending on the PI inventories of natural emissions employed in the model. The simulated global tropospheric O_3 burden varied by up to 18%, with regional differences of more than 40%, highlighting the importance of using accurate PI inventories, anchored in estimates from proxy records of PI fire occurrence. Those inventories from which simulated values compare most favourably to estimates from proxy records should be employed preferentially in future studies. The different inventories resulted in much larger changes in concentrations of O_3 precursors such as CO, which contributed to the differences in O_3. However it was found that emissions of NO_x were the primary cause of changes to O_3, consistent with Stevenson et al. (2013). Emissions of NO_x were less varied across inventories than CO, moderating the effect on simulated tropospheric O_3.

Including a dedicated PI biogenic emission inventory, rather than simply assuming present-day emissions, was also found to affect simulated PI O_3 concentrations, increasing O_3 burden by between 3% and 6%. The effect of the biogenic emission inventory on simulated O_3 was largest when used in conjunction with biomass burning emissions produced from the same land-use model. This result supports the finding of Bossioli et al. (2012) that the

distribution of emissions and the coupling of appropriate inventories is important in modelling studies in order to accurately simulate tropospheric O_3.

Both simulations using revised PI emission inventories based on recent evidence of increased PI fire occurrence, result in an increase in simulated tropospheric O_3. In the case presented as a reasonable upper limit in this thesis (PI LMfire-BIO), tropospheric O_3 RF was 35% smaller than when using CMIP6 inventories. The estimated RF of 0.25 Wm^{-2} is at the lower end of the IPCC uncertainty range in Myhre et al. (2013b).

Although this study is limited by the use of just one CTM and one radiative transfer model, the results described in Chapter 1 demonstrate that uncertainty in PI emissions from natural sources has a large effect on simulated PI O_3, and therefore estimates of tropospheric O_3 RF. Given the favourable comparison of the revised inventories with proxy records of fire emissions, and recent evidence using a proxy for O_3 which suggests PI to present-day changes are smaller than previously estimated, it is reasonable to suggest that estimates using the revised inventories are more informative than those using previous assumptions. These findings indicate that previous multi-model studies of tropospheric O_3 RF such as Stevenson et al. (2013) may have overestimated O_3 RF since the PI by including models which assumed constant biogenic emissions across present-day and PI, and employing PI biomass burning inventories which were anchored in present-day emissions and are incompatible with estimates of fire emissions from proxy records.

Thesis aim 2: Evaluate the effect of the El Niño Southern Oscillation on the interannual variability of methane and tropospheric ozone.

In Chapter 5, the TOMCAT-GLOMAP CTM was used to investigate drivers of natural variability in SLCPs CH_4 and tropospheric O_3 in the present-day. It is particularly important to understand the exact mechanism driving observed changes in SLCPs, as El Niño events are expected to become more extreme with future climate change (Fasullo et al., 2018). Therefore, specific drivers in historic El Niño events need to be quantified, in order to improve understanding of the implications of future changes to El Niño events. The impact of ENSO on

the interannual variability of major SLCP species was evaluated for the period 1997-2014. The climate impacts of this variability were also estimated using SOCRATES, attributed to specific mechanisms.

The large IAV in simulated CO concentrations during the 1997 El Niño was driven primarily by variations in biomass burning emissions, which was relatively well-established in previous literature (Monks et al., 2012; Voulgarakis et al., 2015). In addition, Butler et al. (2005) estimated that this suppressed OH concentrations by 2.2%. The novelty of the results presented in this thesis lay in the investigation of the relative effect of meteorology, biomass burning emissions and indirect effect through atmospheric chemistry, which had not previously been quantified. This work quantified the prevalence of each driver during El Niño and La Niña events over an 18-year period. Using a number of sensitivity simulations it was determined that the indirect effect on CO emissions from biomass burning on oxidation chemistry increased the global mean CH_4 growth rate by up to 7.5 ppb yr^{-1} during the 1997 El Niño event. This is in reasonable agreement with Butler et al. (2005) and explains the large changes in global CH_4 growth rate during years of high fire occurrence, as direct emissions of CH_4 from biomass burning are small relative to the observed changes in CH_4 growth rate (Voulgarakis and Field, 2015). Although fire emissions are the primary driver of IAV of CH_4 during El Niño, emissions of CO are potentially more important than direct CH_4 emissions. The indirect atmospheric chemistry effect from biomass burning emissions of CO would be accounted for in future modelling studies which have fully interactive CH_4 simulation. However, understanding the precise drivers of CH_4 trends is important for assessing the likely impact of future changes to the distribution and emissions from biomass burning. Climate change is likely to alter not only the severity of El Niño events, but also the geographical distribution of the impacts, thereby changing the distribution of biomass burning and the relative composition of emissions.

The effect of El Niño on the IAV of O_3 was also estimated in Chapter 5, finding a relatively minor global mean RF during the 1997 El Niño but with large spatial variability. It was found that meteorology primarily controlled the IAV of both OH

and O_3 for the majority of the period studied, however, during large El Niño events which cause a substantial increase in global fire emissions, biomass burning emissions become dominant. During the 1997 El Niño, meteorological changes decreased tropospheric O_3 concentrations, while biomass burning emissions increased them, resulting in a simulated small net increase in global RF of 0.015 Wm^{-2}. Despite the relatively small global mean value, the contrasting effects causing it lead to a large regional variability, with RF changes of up to 0.36 Wm^{-2} over the Pacific Ocean. These large regional changes may have important consequences for atmospheric dynamics, causing increased in situ heating and regional changes in climate. The effects of El Niño on tropospheric O_3 had been examined in a number of previous studies, however, this was the first study to quantify the climate impact of meteorological and biomass burning driven changes collectively and individually. It is vital to understand the impact of the counter-acting effects on O_3 in order to estimate how future changes to meteorology or biomass burning under increasingly severe El Niño events may result in larger changes to global tropospheric O_3.

The limiting factor controlling production of tropospheric O_3 was also considered in Chapter 5, following the method of Duncan et al. (2010). It was found that El Niño substantially altered the HCHO:NO_2 ratio in TOMCAT-GLOMAP simulations, but these changes primarily occurred in regions already heavily NO_x-limited, therefore not altering the O_3 production regime. These results demonstrate the large changes in O_3 precursor concentrations which occur during El Niño events, however they also indicate that even under extreme El Niño conditions the NO_x-limited O_3 production regime seen over the majority of the globe is very stable.

Thesis aim 3: Assess the influence of future emissions scenarios on climate change and air quality in 2050

Chapter 6 of this thesis utilised future emission inventories of SLCPs and their precursors from the ECLIPSE project. The purpose of the study was to understand the effect of future emissions of SLCPs under various scenarios from both a climate change and air quality perspective. The results analyse the most effective approaches for simultaneously mitigating climate change and air

pollution by 2050, including improved understanding of the importance of individual emission sectors.

The Current Legislation scenario (CLE) emissions resulted in an increase in simulated global air pollution, as O_3 and $PM_{2.5}$ increased by up to 50% and 120%, respectively. This demonstrates the importance of further measures to decrease anthropogenic emissions if worsening global air quality is to be avoided. The CLE scenario however does result in decreased RF by 2050 compared to present-day, as the continued emission of aerosols and their precursors leads to a cooling effect, particularly over large emitters such as India. This slight decrease in SLCP RF does not substantially decrease the rate of global temperature change in the coming decades, with more than 2°C of warming estimated by 2050 when coupled to RCP4.5 long-lived emissions. The CLE scenario therefore does not meaningfully mitigate near-term anthropogenic climate change, and also results in substantially decreased air quality which will lead to an increase in the number of premature deaths due to air pollution exposure. The economic and human cost of this scenario is not estimated here, however, given the recent assessment of air pollution as the biggest environmental risk to human health in the present-day (WHO, 2016), and recent measures to combat pollution (Butt et al., 2017), it is unlikely that air pollution would be allowed to degrade to this extent by 2050.

The implications of the Maximum Technically Feasible Reductions (MTFR) scenario are in stark contrast to the CLE scenario. Under MTFR emissions simulated global O_3 and $PM_{2.5}$ surface concentrations were reduced by 20.5% and 6.5%, respectively, meaning considerable improvements in air quality. However this scenario results in an increase in RF by 2050, enhancing the rate near-term rate of global temperature change and resulting in higher temperatures than the CLE scenario. This is a result of the comprehensive measures decreasing emissions of cooling aerosol components. This scenario highlights the difficulty of seeking a win-win scenario which mitigates both climate change and air pollution, as the removal of particles damaging to human health also removes their cooling effect on climate which has counteracted the effect of increases in greenhouse gas concentrations (Myhre et al., 2013b). In a

more realistic scenario it is extremely unlikely that such large decreases to SLCP emissions could be made by 2050, but reductions in aerosols emissions over Europe and North America since the 1980s (Crippa et al., 2016; Butt et al., 2017) demonstrate the trend of removing cooling aerosols that is likely to continue in coming decades, making climate mitigation even more challenging. However, Shindell and Smith (2019) found that although gradual SO_2 emission reductions over the coming decades increase near-term warming, when coupled with action to decrease CO_2, the outcome is almost net-zero warming by around 2035, followed by a cooling trend as the CO_2 effect takes over.

The SLCP mitigation scenario (SLCPMIT) was the most effective scenario at reducing the rate of near-term climate change, keeping global temperature change below 2°C by 2050, a drop of 0.28°C relative to the CLE scenario. This is driven in part by measures decreasing tropospheric O_3 RF, but also through increased aerosol concentrations leading to a negative RF. As a result the SLCPMIT scenario results in higher air pollutants concentrations relative to present-day, with higher concentrations in many regions than the CLE 2050 scenario. Although simulated surface concentrations of tropospheric O_3 are decreased, PM concentrations increase, damaging human health and vegetation. Like the CLE scenario, the SLCPMIT scenario results in near-term mitigation of climate but at the cost of worsening air quality.

The 2 degree (2 deg) climate scenario was intended to target SLCP emissions with the intention of reducing air pollution whilst also keeping global temperature change at less than 2°C relative to the PI climate. However, despite causing a decrease in simulated O_3 in 2050, the 2 deg scenario actually increased the rate of near-term warming due to measures decreasing emissions of cooling aerosol. As a result, the global temperature anomaly was estimated to surpass 2°C by 2050 (when coupled with RCP 4.5 emissions), suggesting that the scenario was ineffective as a strategy for both air quality and climate benefits.

The only ECLIPSE scenario which effectively mitigates climates and improves air quality is the SLCPMIT scenario, as although $PM_{2.5}$ concentrations increase, surface O_3 does decline by 2050 bringing human health and economic benefits. However, the estimated rise in $PM_{2.5}$ negates much of the benefits from

tropospheric O_3 reductions, meaning that even this is not a genuine win-win scenario, tackling air pollution and climate change. The results presented in Chapter 6 demonstrates the complex factors to be considered when planning policy that will benefit both air pollution and climate. An important factor not considered here due to modelling and time constraints is the RF of decreases in CH_4 concentrations. The inclusion of this in net RF estimates will improve the mitigating potential of the MTFR, SLCPMIT and 2 deg scenarios as CH4 is a very important climate forcer while its influence on air quality through tropospheric O_3 production is less significant.

7.2. Discussion and conclusions of main results

Overall, the work presented in this thesis improves our understanding of the factors controlling SLCP variability from the perspective of their impact on today's climate and their role in mitigating future climate change. The results highlight the importance of considering natural processes and of disentangling contrasting impacts when setting out measures to combat climate change and improve air quality simultaneously. The potential of targeting SLCPs as a climate mitigation strategy has been demonstrated in Chapter 6, whilst also emphasising the complexities of achieving human health co-benefits. In Chapter 5, the role of natural cycles such as ENSO was quantified, a factor which needs to be accounted for when assessing the efficacy of climate mitigation scenarios. The significance of natural emissions was also shown in the findings of Chapter 4, underscoring the need to consider changes to the natural environment as well as human actions when planning a mitigation strategy.

The impact of future climate change on El-Niño events is highly uncertain, but a number of studies indicate that El Niño will become more frequent and severe in a warmer world (Timmermann et al., 1999; Collins, 2000; van Oldenborgh et al., 2005; Gergis and Fowler, 2009). This would likely result in biomass burning anomalies larger even than those observed during 1997-1998, including burning in regions not previously affected. The results set out in Chapter 5 not only explain observed trends in SLCPs, but the quantification of specific mechanisms

allows estimation of the impact of future El Niño events on SLCPs and hence climate, even if there are substantial changes to the manifestation of El Niño in the future climate.

Chapter 6 directly addresses the potential of reducing emissions of SLCPs and their precursors to alleviate near-term climate change. Although the findings presented here do not rule out the possibility of implementing an environmental co-benefit strategy, they do highlight the potential of dangerously exacerbating near-term climate change when addressing air pollution. The results detailed in Section 6.6 and 6.9, demonstrate that substantial reductions to air pollutants will result in a positive RF as the cooling aerosol effect is removed, but that this effect could be offset in part by simultaneously decreasing warming species. The contrasting RFs of changes to SLCP mean it is very difficult to put forward a comprehensive SLCP mitigation strategy that will not have negative outcomes for either climate or air quality. Taking long-lived forcing agents into account not only improves the outlook of climate mitigation, but also represents a more realistic scenario. SLCP changes will not occur in isolation but in the background of CO_2-led mitigation. As shown in Shindell and Smith (2019), the long-lifetime of CO_2 emissions does not preclude CO_2 mitigation from reducing the near-term rate of climate change, with an estimated decrease in short-term warming despite the concurrent removal of sulphate aerosol. Moreover, CO_2 mitigation will inevitably result in a decrease in co-emitted species (Rogelj et al., 2015), making an SLCP-only mitigation strategy unfeasible. It is therefore imperative that any SLCP mitigation strategy is designed in this context, endeavouring to complement the CO_2 mitigation measures which will necessarily dominate climate mitigation efforts.

7.3. Future work

The results presented in this thesis highlight a number of areas of remaining uncertainty and challenges which future research should address.

One area where improvements are likely to bring important benefits is incorporating dedicated pre-industrial emission inventories in O_3 modelling

studies. Ensuring that PI emissions are appropriate to a PI climate can have a large effect on estimated PI to PD O_3 change. There have been many studies in the past decade which have used proxy records to estimate PI fire occurrence and a number of studies designed to estimate PI biogenic emissions. These should be exploited in future studies to produce improved PI inventories and decreased tropospheric O_3 RF uncertainty. A dedicated study evaluating PI inventories through detailed comparison with proxy records to establish the most realistic and applicable PI inventory would allow more accurate estimation of PI O_3 concentrations. This could also be an opportunity to quantify the importance of emission co-location which cannot be established with certainty from a single modelling study.

A new multi-model tropospheric O_3 RF study, following Stevenson et al. (2013), using the recommended PI biomass burning and biogenic emissions from dedicated PI inventories would help to reduce uncertainty in tropospheric O_3 RF. Existing or future projects such as the Aerosol Chemistry Model Intercomparison Project (AerChemMIP) could feasibly be expanded upon to address the uncertainty in PI natural emissions, by incorporating alternative emission inventories such as those used in this study. In Collins et al. (2017), historical natural emission schemes varied by model. In future studies, an experiment in which PI natural emissions vary but are consistent across all models would improve our understanding of the impact of PI natural emissions, allowing analysis of the effect in a range of models. The results presented here indicate that this would likely result in a decreased estimate of tropospheric O_3 RF with implications for climate sensitivity, however the effect is likely to vary between models.

A number of studies have attempted to estimate how future climate change will affect the cycle and severity of ENSO events, often related to the change in frequency of extreme weather (Timmermann et al., 1999; Cai et al., 2015). Further research into the implications of future changes for biomass burning variability could then be used to estimate future variability in concentrations of key SLCP concentrations. This would inform on the impact of future changes to ENSO as well as being useful for proposing SLCP mitigation strategies.

In Chapter 5, the influence of El Niño on CH_4 was inferred from OH concentrations and an offline CH_4 box model. Fully interactive methane modelling would improve these estimates by accounting for all variability in CH_4 sources and sinks, while still allowing the examination of specific drivers.

A more detailed investigation into the impact of changing aerosol emissions would help disentangle the complex climate and air quality effects. In particular the role of nitrate aerosol (an aerosol component not included in TOMCAT-GLOMAP) should be considered, as nitrate is likely to become more important as sulphate aerosol concentrations fall (Bauer et al., 2007). Quantifying the likely impact of changes in nitrate aerosol under the ECLIPSE emissions scenarios would add to our understanding of the climate impact of emissions changes.

Furthermore, heterogeneous chemistry impacts following nitrate and sulphate aerosol changes should be examined on a global scale, to estimate the effect on climate forcers such as CH_4 and tropospheric O_3. A regional study by Matsui and Koike (2016) found that changes to aerosol precursor emissions had a large impact on OH concentrations and hence the formation of O_3. The global impact of this effect, as well as the implications for CH_4 lifetime and RF, need to be examined to fully understand the consequences of likely future emissions changes. Additionally, global OH concentrations are poorly constrained. Due to the difficulty of measuring OH on a large scale, direct validation of modelled OH concentrations with observations is very difficult (Patra et al., 2014) and OH abundance is generally derived from observations of methyl chloroform ($CH3CCl_3$) or CO (Montzka et al., 2011; Rigby et al., 2013; Patra et al., 2014). Reducing the uncertainty in global OH concentrations, variability and trends would greatly improve our understanding of changes in atmospheric chemistry affecting SLCPs and the resulting impact on climate. A study utilising the growing global network of long-term observations, coupled with sophisticated chemical transport models, could substantially improve estimates of global OH and subsequently its response to future climate change.

A recent study by Shindell and Smith (2019) modelled the impact of a realistic “phase-out” of emissions of SO_2 and CO_2, rather than abrupt, unrealistic changes. It was found that in this scenario, the combined effect actually

alleviated near-term warming whilst improving air quality. Using a realistic implementation representation in modelling and examining emissions scenarios of all SLCPs in the context of CO_2 mitigation is necessary before a coherent air quality and climate change environmental policy can be optimised.

Appendix A

Table A.1 Aircraft campaign information from Emmons et al. (2010) climatologies.

Campaign	Date collected	Species	Location
TRACE-A	Sep 21 – Oct 26, 1992	O_3, CO, NO_x	East Brazil Coast (-35- -25N, 310-320E) East Brazil (-15- -5N, 310-320E) South Africa (-25- -5N, 15-35E) South Atlantic (-20-0N, 340-350E) West Africa Coast (-25- -5N, 0-10E)
PEM-West-B	Feb 7 – Mar 14, 1994	CO, NO_x	China Coast (20-30N, 115-130E) Japan (25-40N, 135-150E) Philippine Sea (5-20N, 135-150E)
TOTE	Dec 6 – 22, 1995	O_3, CO, CH_4	Alaska (60-70N, 205-220E) Hawaii (15-25N, 195-210N)
VOTE	Jan 20 – Feb 19, 1996	O_3, CO, CH_4	Alaska (60-70N, 205-220E) Hawaii (15-25N, 195-210N)
SUCCESS	Apr 15 – May 15, 1996	O_3, CO	Central USA (35-40N, 260-265E)
PEM-Tropics-A	Aug 15-Oct 15, 1996	O_3, CO, CH_4, NO_x	Christmas Island (0-10N, 200-220E) Easter Island (−40- −20N, 240-260E) Hawaii (10-30N, 190- 210E) Tahiti (−20- 0N, 200-230E)
POLINAT-2	Sep 19 – Oct 25, 1997	O_3, CO, NO_x	Canary Islands (25-35N, 340-350E) Eastern Atlantic (35-45N, 330-340E) Europe (45-55N, 5-15E)

			Ireland (50-60N, 345-355E)
SONEX	Oct 7 – Nov 12, 1997	O_3, CO	East Atlantic (35-45N, 325-345E) Ireland (50-60N, 345-355E) Newfoundland (45-55N, 290-310E)
PEM-Tropics-B	Mar 6 – Apr 18, 1999	O_3, CO, CH_4, NO_x	Christmas Island (0-10N, 200-220E) Easter Island (−40- −20N, 240-260E) Fiji (-30- -10N, 170-190E) Hawaii (10-30N, 190- 210E) Tahiti (−20- 0N, 200-230E
TOPSE	Feb 5 – May 23, 2000	O_3, CH_4, NO_x	Boulder (37- 47N, 250-270E) Churchill (47-65N, 250-280E) Thule (65-90N, 250-300E)
TRACE-P	Feb 24 – Apr 10, 2001	O_3, CO, CH_4, NO_x	China (10-30N, 110-130E) Guam (10-20N, 140-150E) Hawaii (10-30N, 190-210E) Japan (20-40N, 130-150E)

Table A.2 Details of aircraft measurement campaigns to measure aerosol (chronological). From Heald et al. (2011).

Campaign (Aircraft)	Location	Date	Technique	Regional Class
ACE-Asia	North-West Pacific / Japan	30/03 – 40/05/01	Teflon filters + Fourier Transform Infrared Spectrometer (FTIR)	Pollution (mid-latitude)
ITCT-2K4	Eastern North America	05/07 – 15/08/04	Particle Into Liquid Sampler (PILS), Water Soluble Organic Carbon (WSOC)	Pollution/Fire (mid-latitude)
ITOP	Azores	12/07 – 03/08/04	Quadrupole Aerosol Mass Spectrometer (Q-AMS)	Remote (mid-latitude)
ADRIEX	North Italy, Adriatic and Black Sea	27/08 – 06/09/04	Q-AMS	Pollution (mid-latitude)
DABEX	West Africa	13/01 – 01/02/06	Q-AMS	Fire (tropics)
MILAGRO	Mexico City, Mexico	04/03 – 31/03/06	High Resolution Time-of-Flight (HR-ToF) AMS	Pollution/Fire (sub-tropics)
IMPEX	West North America and East Pacific	17/06 – 15/05/06	HR-ToF AMS	Remote (mid-latitude)
AMMA	West Africa	20/07 – 25/08/06	Q-AMS	Fire (tropics)
TexAQS	Texas, USA	11/09 – 13/10/06	Compact Time-of-Flight (C-ToF) AMS	Pollution (mid-latitude)
ADIENT	Europe / Atlantic	18/12/07 – 25/09/08	C-ToF AMS	Pollution (mid-latitude)
EUCAARI	North Europe	06/05 – 22/05/08	C-ToF AMS	Pollution (mid-latitude)
ARCTAS	Arctic / North Europe	01/04 – 20/04/08 18/06 – 13/07/08	HR-ToF AMS	Fire (high-latitude)
OP3	Borneo	10/07 – 20/07/08	C-ToF AMS	Remote (tropical)
VOCALS-UK	Eastern South Pacific	27/10 – 13/11/08	C-ToF AMS	Remote (tropical)

References

Aas, W., Mortier, A., Bowersox, V., Cherian, R., Faluvegi, G., Fagerli, H., Hand, J., Klimont, Z., Galy-Lacaux, C., Lehmann, C.M.B., Myhre, C.L., Myhre, G., Olivié, D., Sato, K., Quaas, J., Rao, P.S.P., Schulz, M., Shindell, D., Skeie, R.B., Stein, A., Takemura, T., Tsyro, S., Vet, R. and Xu, X. 2019. Global and regional trends of atmospheric sulfur. *Scientific reports.* **9**(1), pp.953-953.

ACIA. 2004. Impacts of a Warming Arctic: Arctic Climate Impact Assessment. *Cambridge University Press. http: //www.acia.uaf.edu/.*

Acosta Navarro, J.C., Ekman, A.M.L., Pausata, F.S.R., Lewinschal, A., Varma, V., Seland, Ø., Gauss, M., Iversen, T., Kirkevåg, A., Riipinen, I. and Hansson, H.C. 2017. Future Response of Temperature and Precipitation to Reduced Aerosol Emissions as Compared with Increased Greenhouse Gas Concentrations. **30**(3), pp.939-954.

Akagi, S.K., Yokelson, R.J., Wiedinmyer, C., Alvarado, M.J., Reid, J.S., Karl, T., Crounse, J.D. and Wennberg, P.O. 2011. Emission factors for open and domestic biomass burning for use in atmospheric models. *Atmos. Chem. Phys.* **11**(9), pp.4039-4072.

Albrecht, B.A. 1989. Aerosols, Cloud Microphysics, and Fractional Cloudiness. *Science.* **245**(4923), pp.1227-1230.

Allen, M.R., Fuglestvedt, J.S., Shine, K.P., Reisinger, A., Pierrehumbert, R.T. and Forster, P.M. 2016. New use of global warming potentials to compare cumulative and short-lived climate pollutants. *Nature Climate Change.* **6**, p.773.

Allen, M.R., Shine, K.P., Fuglestvedt, J.S., Millar, R.J., Cain, M., Frame, D.J. and Macey, A.H. 2018. A solution to the misrepresentations of CO2-equivalent emissions of short-lived climate pollutants under ambitious mitigation. *npj Climate and Atmospheric Science.* **1**(1), p.16.

Amann, M., Bertok, I., Borken-Kleefeld, J., Cofala, J., Heyes, C., Höglund-Isaksson, L., Klimont, Z., Nguyen, B., Posch, M., Rafaj, P., Sandler, R., Schöpp, W., Wagner, F. and Winiwarter, W. 2011. Cost-effective control of air quality and greenhouse gases in Europe: Modeling and policy applications. *Environmental Modelling & Software.* **26**(12), pp.1489-1501.

Anav, A., Menut, L., Khvorostyanov, D. and Viovy, N. 2011. Impact of tropospheric ozone on the Euro-Mediterranean vegetation. *Global Change Biology.* **17**(7), pp.2342-2359.

Andela, N., Morton, D.C., Giglio, L., Chen, Y., van der Werf, G.R., Kasibhatla, P.S., DeFries, R.S., Collatz, G.J., Hantson, S., Kloster, S., Bachelet, D., Forrest, M., Lasslop, G., Li, F., Mangeon, S., Melton, J.R., Yue, C. and Randerson, J.T. 2017. A human-driven decline in global burned area. *Science.* **356**(6345), pp.1356-1362.

Anenberg, S.C., Horowitz, L.W., Tong, D.Q. and West, J.J. 2010. An Estimate of the Global Burden of Anthropogenic Ozone and Fine Particulate Matter on Premature Human Mortality Using Atmospheric Modeling. *Environmental Health Perspectives.* **118**(9), pp.1189-1195.

Anenberg, S.C., Schwartz, J., Shindell, D., Amann, M., Faluvegi, G., Klimont, Z., Janssens-Maenhout, G., Pozzoli, L., Van Dingenen, R., Vignati, E., Emberson, L., Muller, N.Z., West, J.J., Williams, M., Demkine, V., Hicks, W.K., Kuylenstierna, J., Raes, F. and Ramanathan, V. 2012. Global air quality and health co-benefits of mitigating near-term climate change through methane and black carbon emission controls. *Environ Health Perspect.* **120**(6), pp.831-839.

Archer, D., Eby, M., Brovkin, V., Ridgwell, A., Cao, L., Mikolajewicz, U., Caldeira, K., Matsumoto, K., Munhoven, G., Montenegro, A. and Tokos, K. 2009. Atmospheric Lifetime of Fossil Fuel Carbon Dioxide. *Annual Review of Earth and Planetary Sciences.* **37**(1), pp.117-134.

Arneth, A., Monson, R.K., Schurgers, G., Niinemets, Ü. and Palmer, P.I. 2008. Why are estimates of global terrestrial isoprene emissions so similar (and why is this not so for monoterpenes)? *Atmos. Chem. Phys.* **8**(16), pp.4605-4620.

Arneth, A., Niinemets, Ü., Pressley, S., Bäck, J., Hari, P., Karl, T., Noe, S., Prentice, I.C., Serça, D., Hickler, T., Wolf, A. and Smith, B. 2007. Process-based estimates of terrestrial ecosystem isoprene emissions: incorporating the effects of a direct CO2-isoprene interaction. *Atmos. Chem. Phys.* **7**(1), pp.31-53.

Arneth, A., Sitch, S., Bondeau, A., Butterbach-Bahl, K., Foster, P., Gedney, N., de Noblet-Ducoudré, N., Prentice, I.C., Sanderson, M., Thonicke, K., Wania, R. and Zaehle, S. 2010. From biota to chemistry and climate: towards a comprehensive description of trace gas exchange between the biosphere and atmosphere. *Biogeosciences.* **7**(1), pp.121-149.

Arnold, S.R., Chipperfield, M.P. and Blitz, M.A. 2005. A three-dimensional model study of the effect of new temperature-dependent quantum yields for acetone photolysis. *Journal of Geophysical Research: Atmospheres (1984–2012).* **110**(D22), D22305.

Ashmore, M.R. 2005. Assessing the future global impacts of ozone on vegetation. *Plant, Cell & Environment.* **28**(8), pp.949-964.

Atkinson, R.W., Butland, B.K., Dimitroulopoulou, C., Heal, M.R., Stedman, J.R., Carslaw, N., Jarvis, D., Heaviside, C., Vardoulakis, S., Walton, H. and Anderson, H.R. 2016. Long-term exposure to ambient ozone and mortality: a quantitative systematic review and meta-analysis of evidence from cohort studies. *BMJ Open.* **6**(2), p.e009493.

Avnery, S., Mauzerall, D.L., Liu, J. and Horowitz, L.W. 2011a. Global crop yield reductions due to surface ozone exposure: 1. Year 2000 crop production losses and economic damage. *Atmospheric Environment.* **45**(13), pp.2284-2296.

Avnery, S., Mauzerall, D.L., Liu, J. and Horowitz, L.W. 2011b. Global crop yield reductions due to surface ozone exposure: 2. Year 2030 potential crop

production losses and economic damage under two scenarios of O3 pollution. *Atmospheric Environment.* **45**(13), pp.2297-2309.

Bahreini, R., Ervens, B., Middlebrook, A.M., Warneke, C., de Gouw, J.A., DeCarlo, P.F., Jimenez, J.L., Brock, C.A., Neuman, J.A., Ryerson, T.B., Stark, H., Atlas, E., Brioude, J., Fried, A., Holloway, J.S., Peischl, J., Richter, D., Walega, J., Weibring, P., Wollny, A.G. and Fehsenfeld, F.C. 2009. Organic aerosol formation in urban and industrial plumes near Houston and Dallas, Texas. *Journal of Geophysical Research: Atmospheres.* **114**(D7), D00F16.

Bândă, N., Krol, M., van Weele, M., van Noije, T., Le Sager, P. and Röckmann, T. 2016. Can we explain the observed methane variability after the Mount Pinatubo eruption? *Atmos. Chem. Phys.* **16**(1), pp.195-214.

Bauer, S.E., Koch, D., Unger, N., Metzger, S.M., Shindell, D.T. and Streets, D.G. 2007. Nitrate aerosols today and in 2030: a global simulation including aerosols and tropospheric ozone. *Atmos. Chem. Phys.* **7**(19), pp.5043-5059.

Bekki, S., Rap, A., Poulain, V., Dhomse, S., Marchand, M., Lefevre, F., Forster, P.M., Szopa, S. and Chipperfield, M.P. 2013. Climate impact of stratospheric ozone recovery. *Geophysical Research Letters.* **40**(11), pp.2796-2800.

Bellouin, N., Mann, G.W., Woodhouse, M.T., Johnson, C., Carslaw, K.S. and Dalvi, M. 2013. Impact of the modal aerosol scheme GLOMAP-mode on aerosol forcing in the Hadley Centre Global Environmental Model. *Atmos. Chem. Phys.* **13**(6), pp.3027-3044.

Bellouin, N., Rae, J., Jones, A., Johnson, C., Haywood, J. and Boucher, O. 2011. Aerosol forcing in the Climate Model Intercomparison Project (CMIP5) simulations by HadGEM2-ES and the role of ammonium nitrate. *Journal of Geophysical Research: Atmospheres (1984–2012).* **116**(D20), D20206.

Berntsen, T.K., Fuglestvedt, J.S., Joshi, M.M., Shine, K.P., Stuber, N., Ponater, M., Sausen, R., Hauglustaine, D.A. and Li, L. 2005. Response of climate to regional emissions of ozone precursors: sensitivities and warming potentials. *Tellus B: Chemical and Physical Meteorology.* **57**(4), pp.283-304.

Bond, T.C., Doherty, S.J., Fahey, D.W., Forster, P.M., Berntsen, T., DeAngelo, B.J., Flanner, M.G., Ghan, S., Kärcher, B., Koch, D., Kinne, S., Kondo, Y., Quinn, P.K., Sarofim, M.C., Schultz, M.G., Schulz, M., Venkataraman, C., Zhang, H., Zhang, S., Bellouin, N., Guttikunda, S.K., Hopke, P.K., Jacobson, M.Z., Kaiser, J.W., Klimont, Z., Lohmann, U., Schwarz, J.P., Shindell, D., Storelvmo, T., Warren, S.G. and Zender, C.S. 2013. Bounding the role of black carbon in the climate system: A scientific assessment. *Journal of Geophysical Research: Atmospheres.* **118**(11), pp.5380-5552.

Bond, T.C., Streets, D.G., Yarber, K.F., Nelson, S.M., Woo, J.-H. and Klimont, Z. 2004. A technology-based global inventory of black and organic

carbon emissions from combustion. *Journal of Geophysical Research: Atmospheres.* **109**(D14), D14203.

Bossioli, E., Tombrou, M., Karali, A., Dandou, A., Paronis, D. and Sofiev, M. 2012. Ozone production from the interaction of wildfire and biogenic emissions: a case study in Russia during spring 2006. *Atmos. Chem. Phys.* **12**(17), pp.7931-7953.

Boucher, O., Randall, D., Artaxo, P., Bretherton, C., Feingold, G., Forster, P., Kerminen, V.-M., Kondo, Y., Liao, H., Lohmann, U., Rasch, P., Satheesh, S.K., Sherwood, S., Stevens, B. and Zhang, X.Y. 2013. Clouds and Aerosols. In: Stocker, T.F., et al. eds. *Climate Change 2013: The Physical Science Basis. Contribution of Working Group I to the Fifth Assessment Report of the Intergovernmental Panel on Climate Change.* Cambridge, United Kingdom and New York, NY, USA: Cambridge University Press, pp.571–658.

Bousquet, P., Ciais, P., Miller, J.B., Dlugokencky, E.J., Hauglustaine, D.A., Prigent, C., Van der Werf, G.R., Peylin, P., Brunke, E.G., Carouge, C., Langenfelds, R.L., Lathière, J., Papa, F., Ramonet, M., Schmidt, M., Steele, L.P., Tyler, S.C. and White, J. 2006. Contribution of anthropogenic and natural sources to atmospheric methane variability. *Nature.* **443**, p.439.

Bousquet, P., Hauglustaine, D.A., Peylin, P., Carouge, C. and Ciais, P. 2005. Two decades of OH variability as inferred by an inversion of atmospheric transport and chemistry of methyl chloroform. *Atmos. Chem. Phys.* **5**(10), pp.2635-2656.

Bousquet, P., Ringeval, B., Pison, I., Dlugokencky, E.J., Brunke, E.G., Carouge, C., Chevallier, F., Fortems-Cheiney, A., Frankenberg, C., Hauglustaine, D.A., Krummel, P.B., Langenfelds, R.L., Ramonet, M., Schmidt, M., Steele, L.P., Szopa, S., Yver, C., Viovy, N. and Ciais, P. 2011. Source attribution of the changes in atmospheric methane for 2006–2008. *Atmos. Chem. Phys.* **11**(8), pp.3689-3700.

Bouwman, A.F., Lee, D.S., Asman, W.A.H., Dentener, F.J., Van Der Hoek, K.W. and Olivier, J.G.J. 1997. A global high-resolution emission inventory for ammonia. *Global Biogeochemical Cycles.* **11**(4), pp.561-587.

Bowerman, N.H.A., Frame, D.J., Huntingford, C., Lowe, J.A., Smith, S.M. and Allen, M.R. 2013. The role of short-lived climate pollutants in meeting temperature goals. *Nature Climate Change.* **3**, p.1021.

Bowman, D.M.J.S., Balch, J.K., Artaxo, P., Bond, W.J., Carlson, J.M., Cochrane, M.A., D'Antonio, C.M., DeFries, R.S., Doyle, J.C., Harrison, S.P., Johnston, F.H., Keeley, J.E., Krawchuk, M.A., Kull, C.A., Marston, J.B., Moritz, M.A., Prentice, I.C., Roos, C.I., Scott, A.C., Swetnam, T.W., van der Werf, G.R. and Pyne, S.J. 2009. Fire in the Earth System. *Science.* **324**(5926), pp.481-484.

Butler, T.M., Rayner, P.J., Simmonds, I. and Lawrence, M.G. 2005. Simultaneous mass balance inverse modeling of methane and carbon

monoxide. *Journal of Geophysical Research: Atmospheres.* **110**(D21), D21310.

Butt, E.W., Rap, A., Schmidt, A., Scott, C.E., Pringle, K.J., Reddington, C.L., Richards, N.A.D., Woodhouse, M.T., Ramirez-Villegas, J., Yang, H., Vakkari, V., Stone, E.A., Rupakheti, M., S. Praveen, P., G. van Zyl, P., P. Beukes, J., Josipovic, M., Mitchell, E.J.S., Sallu, S.M., Forster, P.M. and Spracklen, D.V. 2016. The impact of residential combustion emissions on atmospheric aerosol, human health, and climate. *Atmos. Chem. Phys.* **16**(2), pp.873-905.

Butt, E.W., Turnock, S.T., Rigby, R., Reddington, C.L., Yoshioka, M., Johnson, J.S., Regayre, L.A., Pringle, K.J., Mann, G.W. and Spracklen, D.V. 2017. Global and regional trends in particulate air pollution and attributable health burden over the past 50 years. *Environmental Research Letters.* **12**(10), p.104017.

Cai, W., Santoso, A., Wang, G., Yeh, S.-W., An, S.-I., Cobb, K.M., Collins, M., Guilyardi, E., Jin, F.-F., Kug, J.-S., Lengaigne, M., McPhaden, M.J., Takahashi, K., Timmermann, A., Vecchi, G., Watanabe, M. and Wu, L. 2015. ENSO and greenhouse warming. *Nature Climate Change.* **5**, p.849.

Carmichael, G.R., Kulkarni, S., Chen, Y., Ramanathan, V. and Spak, S. 2013. Short-Lived Climate Forcing Agents and Their Roles in Climate Change. *Procedia - Social and Behavioral Sciences.* **77**, pp.227-236.

Carslaw, K.S., Lee, L.A., Reddington, C.L., Pringle, K.J., Rap, A., Forster, P.M., Mann, G.W., Spracklen, D.V., Woodhouse, M.T., Regayre, L.A. and Pierce, J.R. 2013. Large contribution of natural aerosols to uncertainty in indirect forcing. *Nature.* **503**, p.67.

Chameides, W. and Walker, J.C.G. 1973. A photochemical theory of tropospheric ozone. *Journal of Geophysical Research (1896-1977).* **78**(36), pp.8751-8760.

Chandra, S., Ziemke, J.R., Min, W. and Read, W.G. 1998. Effects of 1997–1998 El Niño on tropospheric ozone and water vapor. *Geophysical Research Letters.* **25**(20), pp.3867-3870.

Checa-Garcia, R., Hegglin, M.I., Kinnison, D., Plummer, D.A. and Shine, K.P. 2018. Historical Tropospheric and Stratospheric Ozone Radiative Forcing Using the CMIP6 Database. *Geophysical Research Letters.* **45**(7), pp.3264-3273.

Chellman, N., McConnell, J.R., Arienzo, M., Pederson, G.T., Aarons, S.M. and Csank, A. 2017. Reassessment of the Upper Fremont Glacier Ice-Core Chronologies by Synchronizing of Ice-Core-Water Isotopes to a Nearby Tree-Ring Chronology. *Environmental Science & Technology.* **51**(8), pp.4230-4238.

Chen, Y.-H. and Prinn, R.G. 2006. Estimation of atmospheric methane emissions between 1996 and 2001 using a three-dimensional global chemical transport model. *Journal of Geophysical Research: Atmospheres.* **111**, D10307.

Chipperfield, M.P. 2006. New version of the TOMCAT/SLIMCAT off-line chemical transport model: Intercomparison of stratospheric tracer experiments. *Quarterly Journal of the Royal Meteorological Society.* **132**(617), pp.1179-1203.

Chipperfield, M.P., Cariolle, D., Simon, P., Ramaroson, R. and Lary, D.J. 1993. A three-dimensional modeling study of trace species in the Arctic lower stratosphere during winter 1989–1990. *Journal of Geophysical Research: Atmospheres.* **98**(D4), pp.7199-7218.

Ciais, P., Sabine, C., Bala, G., Bopp, L., Brovkin, V., Canadell, J., Chhabra, A., DeFries, R., Galloway, J., Heimann, M., Jones, C., Le Quéré, C., Myneni, R.B., Piao, S. and Thornton, P. 2013. Carbon and Other Biogeochemical Cycles. In: Stocker, T.F., et al. eds. *Climate Change 2013: The Physical Science Basis. Contribution of Working Group I to the Fifth Assessment Report of the Intergovernmental Panel on Climate Change.* Cambridge, United Kingdom and New York, NY, USA: Cambridge University Press, pp.465–570.

Collins, M. 2000. The El Niño–Southern Oscillation in the Second Hadley Centre Coupled Model and Its Response to Greenhouse Warming. **13**(7), pp.1299-1312.

Collins, W.J., Lamarque, J.F., Schulz, M., Boucher, O., Eyring, V., Hegglin, M.I., Maycock, A., Myhre, G., Prather, M., Shindell, D. and Smith, S.J. 2017. AerChemMIP: quantifying the effects of chemistry and aerosols in CMIP6. *Geosci. Model Dev.* **10**(2), pp.585-607.

Conibear, L., Butt, E.W., Knote, C., Spracklen, D.V. and Arnold, S.R. 2018. Current and Future Disease Burden From Ambient Ozone Exposure in India. *GeoHealth.* **2**(11), pp.334-355.

Cooper, O.R., Parrish, D., Ziemke, J., Balashov, N., Cupeiro, M., Galbally, I., Gilge, S., Horowitz, L., R. Jensen, N., Lamarque, J.-F., Naik, V., Oltmans, S., Schwab, J., T. Shindell, D., Thompson, A., Thouret, V., Wang, Y. and Zbinden, R. 2014. Global distribution and trends of tropospheric ozone: An observation-based review. *Elementa: Science of the Anthropocene.* **2**, p.000029.

Corbett, A., Jiang, X., Xiong, X., Kao, A. and Li, L. 2017. Modulation of midtropospheric methane by El Niño. *Earth and Space Science.* **4**(9), pp.590-596.

Crippa, M., Guizzardi, D., Muntean, M., Schaaf, E., Dentener, F., van Aardenne, J.A., Monni, S., Doering, U., Olivier, J.G.J., Pagliari, V. and Janssens-Maenhout, G. 2018. Gridded emissions of air pollutants for the period 1970–2012 within EDGAR v4.3.2. *Earth Syst. Sci. Data.* **10**(4), pp.1987-2013.

Crippa, M., Janssens-Maenhout, G., Dentener, F., Guizzardi, D., Sindelarova, K., Muntean, M., Van Dingenen, R. and Granier, C. 2016. Forty years of improvements in European air quality: regional policy-industry interactions with global impacts. *Atmos. Chem. Phys.* **16**(6), pp.3825-3841.

Daniau, A.L., Bartlein, P.J., Harrison, S.P., Prentice, I.C., Brewer, S., Friedlingstein, P., Harrison-Prentice, T.I., Inoue, J., Izumi, K., Marlon, J.R., Mooney, S., Power, M.J., Stevenson, J., Tinner, W., Andrič, M., Atanassova, J., Behling, H., Black, M., Blarquez, O., Brown, K.J., Carcaillet, C., Colhoun, E.A., Colombaroli, D., Davis, B.A.S., D'Costa, D., Dodson, J., Dupont, L., Eshetu, Z., Gavin, D.G., Genries, A., Haberle, S., Hallett, D.J., Hope, G., Horn, S.P., Kassa, T.G., Katamura, F., Kennedy, L.M., Kershaw, P., Krivonogov, S., Long, C., Magri, D., Marinova, E., McKenzie, G.M., Moreno, P.I., Moss, P., Neumann, F.H., Norström, E., Paitre, C., Rius, D., Roberts, N., Robinson, G.S., Sasaki, N., Scott, L., Takahara, H., Terwilliger, V., Thevenon, F., Turner, R., Valsecchi, V.G., Vannière, B., Walsh, M., Williams, N. and Zhang, Y. 2012. Predictability of biomass burning in response to climate changes. *Global Biogeochemical Cycles.* **26**(4), p.GB4007.

Dee, D.P., Uppala, S.M., Simmons, A.J., Berrisford, P., Poli, P., Kobayashi, S., Andrae, U., Balmaseda, M.A., Balsamo, G., Bauer, P., Bechtold, P., Beljaars, A.C.M., van de Berg, L., Bidlot, J., Bormann, N., Delsol, C., Dragani, R., Fuentes, M., Geer, A.J., Haimberger, L., Healy, S.B., Hersbach, H., Hólm, E.V., Isaksen, L., Kållberg, P., Köhler, M., Matricardi, M., McNally, A.P., Monge-Sanz, B.M., Morcrette, J.-J., Park, B.-K., Peubey, C., de Rosnay, P., Tavolato, C., Thépaut, J.-N. and Vitart, F. 2011. The ERA-Interim reanalysis: configuration and performance of the data assimilation system. **137**(656), pp.553-597.

Dentener, F., Kinne, S., Bond, T., Boucher, O., Cofala, J., Generoso, S., Ginoux, P., Gong, S., Hoelzemann, J.J., Ito, A., Marelli, L., Penner, J.E., Putaud, J.P., Textor, C., Schulz, M., van der Werf, G.R. and Wilson, J. 2006. Emissions of primary aerosol and precursor gases in the years 2000 and 1750 prescribed data-sets for AeroCom. *Atmos. Chem. Phys.* **6**(12), pp.4321-4344.

Diffey, B. 2003. Climate change, ozone depletion and the impact on ultraviolet exposure of human skin. *Physics in Medicine and Biology.* **49**(1), pp.R1-R11.

Dlugokencky, E. 2019. NOAA/ESRL. *(www. esrl.noaa.gov/gmd/ccgg/trends_ch4/).*

Dlugokencky, E.J., Houweling, S., Bruhwiler, L., Masarie, K.A., Lang, P.M., Miller, J.B. and Tans, P.P. 2003. Atmospheric methane levels off: Temporary pause or a new steady-state? *Geophysical Research Letters.* **30**(19).

Dlugokencky, E.J., Myers, R.C., Lang, P.M., Masarie, K.A., Crotwell, A.M., Thoning, K.W., Hall, B.D., Elkins, J.W. and Steele, L.P. 2005. Conversion of NOAA atmospheric dry air CH4 mole fractions to a gravimetrically prepared standard scale. *Journal of Geophysical Research: Atmospheres.* **110**, D18306.

Dlugokencky, E.J., Nisbet, E.G., Fisher, R. and Lowry, D. 2011. Global atmospheric methane: budget, changes and dangers. *Philosophical Transactions of the Royal Society A: Mathematical, Physical and Engineering Sciences.* **369**(1943), pp.2058-2072.

Dobricic, S., Pozzoli, L., Vignati, E., Van Dingenen, R., Wilson, J., Russo, S. and Klimont, Z. 2019. Nonlinear impacts of future anthropogenic aerosol emissions on Arctic warming. *Environmental Research Letters.* **14**(3), p.034009.

Doerr, S.H. and Santín, C. 2016. Global trends in wildfire and its impacts: perceptions versus realities in a changing world. **371**(1696), p.20150345.

Doherty, R.M., Stevenson, D.S., Johnson, C.E., Collins, W.J. and Sanderson, M.G. 2006. Tropospheric ozone and El Niño–Southern Oscillation: Influence of atmospheric dynamics, biomass burning emissions, and future climate change. **111**, p.D19304.

Duncan, B., Yoshida, Y., R. Olson, J., Sillman, S., Martin, R., Lamsal, L., Hu, Y., E. Pickering, K., Retscher, C. and J. Allen, D. 2010. Application of OMI observations to a space-based indicator of NOx and VOC controls on surface ozone formation. *Atmospheric Environment.* **44**, pp.2213-2223.

Duncan, B.N., Bey, I., Chin, M., Mickley, L.J., Fairlie, T.D., Martin, R.V. and Matsueda, H. 2003. Indonesian wildfires of 1997: Impact on tropospheric chemistry. **108**(D15), p.4458.

Duncan, B.N., Logan, J.A., Bey, I., Megretskaia, I.A., Yantosca, R.M., Novelli, P.C., Jones, N.B. and Rinsland, C.P. 2007a. Global budget of CO, 1988–1997: Source estimates and validation with a global model. *Geophysical Research Letters.* **112**, D22301.

Duncan, B.N., Logan, J.A., Bey, I., Megretskaia, I.A., Yantosca, R.M., Novelli, P.C., Jones, N.B. and Rinsland, C.P. 2007b. Global budget of CO, 1988–1997: Source estimates and validation with a global model. *Journal of Geophysical Research: Atmospheres.* **112**(D22).

Edwards, J.M. and Slingo, A. 1996. Studies with a flexible new radiation code. I: Choosing a configuration for a large-scale model. *Quarterly Journal of the Royal Meteorological Society.* **122**(531), pp.689-719.

Ehhalt, D., Prather, M., Dentener, F., Derwent, R., Dlugokencky, E.J., Holland, E., Isaksen, I., Katima, J., Kirchhoff, V., Matson, P., Midgley, P., Wang, M., Berntsen, T., Bey, I., Brasseur, G., Buja, L., Collins, W.J., Daniel, J.S., DeMore, W.B., Derek, N., Dickerson, R., Etheridge, D., Feichter, J., Fraser, P., Friedl, R., Fuglestvedt, J., Gauss, M., Grenfell, L., Grubler, A., Harris, N., Hauglustaine, D., Horowitz, L., Jackman, C., Jacob, D., Jaegle, L., Jain, A.K., Kanakidou, M., Karlsdottir, S., Ko, M., Kurylo, M., Lawrence, M., Logan, J.A., Manning, M., Mauzerall, D., McConnell, J., Mickley, L.J., Montzka, S., Muller, J.F., Olivier, J., Pickering, K., Pitari, G., Roelofs, G.-J., Rogers, H., Rognerud, B., Smith, S.J., Solomon, S., Staehelin, J., Steele, P., Stevenson, D.S., Sundet, J., Thompson, A., van Weele, M., von Kuhlmann, R., Wang, Y., Weisenstein, D.K., Wigley, T.M., Wild, O., Wuebbles, D.J., Yantosca, R., Joos, F. and McFarland, M. 2001. *Atmospheric Chemistry and Greenhouse Gases.* Houghton, J. T. et al; Cambridge University Press, Cambridge, United Kingdom.; Pacific Northwest National Lab. (PNNL), Richland, WA (United States).

Emmons, L.K., Deeter, M.N., Gille, J.C., Edwards, D.P., Attié, J.-L., Warner, J., Ziskin, D., Francis, G., Khattatov, B., Yudin, V., Lamarque, J.-F., Ho, S.-P., Mao, D., Chen, J.S., Drummond, J., Novelli, P., Sachse, G., Coffey, M.T., Hannigan, J.W., Gerbig, C., Kawakami, S., Kondo, Y., Takegawa, N., Schlager, H., Baehr, J. and Ziereis, H. 2004. Validation of Measurements of Pollution in the Troposphere (MOPITT) CO retrievals with aircraft in situ profiles. *Journal of Geophysical Research: Atmospheres.* **109**(D3).

Emmons, L.K., Walters, S., Hess, P.G., Lamarque, J.-F., Pfister, G.G., Fillmore, D., Granier, C., Guenther, A., Kinnison, D., Laepple, T., Orlando, J., Tie, X., Tyndall, G., Wiedinmyer, C., Baughcum, S.L. and Kloster, S. 2010. Description and evaluation of the Model for Ozone and Related chemical Tracers, version 4 (MOZART-4). *Geoscientific Model Development.* **3**(1), pp.43-67.

Etheridge, D.M., Steele, L.P., Francey, R.J. and Langenfelds, R.L. 1998. Atmospheric methane between 1000 A.D. and present: Evidence of anthropogenic emissions and climatic variability. *Journal of Geophysical Research: Atmospheres.* **103**(D13), pp.15979-15993.

Etminan, M., Myhre, G., Highwood, E.J. and Shine, K.P. 2016. Radiative forcing of carbon dioxide, methane, and nitrous oxide: A significant revision of the methane radiative forcing. *Geophysical Research Letters.* **43**(24), pp.12,614-612,623.

Evans, M.J. and Jacob, D.J. 2005. Impact of new laboratory studies of N2O5 hydrolysis on global model budgets of tropospheric nitrogen oxides, ozone, and OH. *Geophysical Research Letters.* **32**, L09813.

Fasullo, J.T., Otto-Bliesner, B.L. and Stevenson, S. 2018. ENSO's Changing Influence on Temperature, Precipitation, and Wildfire in a Warming Climate. *Geophysical Research Letters.* **45**(17), pp.9216-9225.

Feely, R.A., Gammon, R.H., Taft, B.A., Pullen, P.E., Waterman, L.S., Conway, T.J., Gendron, J.F. and Wisegarver, D.P. 1987. Distribution of chemical tracers in the eastern equatorial Pacific during and after the 1982–1983 El Niño/Southern Oscillation event. *Journal of Geophysical Research: Oceans.* **92**(C6), pp.6545-6558.

Fels, S.B., Mahlman, J.D., Schwarzkopf, M.D. and Sinclair, R.W. 1980. Stratospheric Sensitivity to Perturbations in Ozone and Carbon Dioxide: Radiative and Dynamical Response. *Journal of Atmospheric Sciences.* **37**(10), pp.2265-2297.

Finney, D.L., Doherty, R.M., Wild, O. and Abraham, N.L. 2016. The impact of lightning on tropospheric ozone chemistry using a new global lightning parametrisation. *Atmos. Chem. Phys.* **16**(12), pp.7507-7522.

Finney, D.L., Doherty, R.M., Wild, O., Stevenson, D.S., MacKenzie, I.A. and Blyth, A.M. 2018. A projected decrease in lightning under climate change. *Nature Climate Change.* **8**(3), pp.210-213.

Fiore, A.M., Naik, V., Spracklen, D.V., Steiner, A., Unger, N., Prather, M., Bergmann, D., Cameron-Smith, P.J., Cionni, I., Collins, W.J., Dalsøren, S., Eyring, V., Folberth, G.A., Ginoux, P., Horowitz, L.W., Josse, B.,

Lamarque, J.-F., MacKenzie, I.A., Nagashima, T., O'Connor, F.M., Righi, M., Rumbold, S.T., Shindell, D.T., Skeie, R.B., Sudo, K., Szopa, S., Takemura, T. and Zeng, G. 2012. Global air quality and climate. *Chemical Society Reviews.* **41**(19), pp.6663-6683.

Flanner, M.G., Zender, C.S., Randerson, J.T. and Rasch, P.J. 2007. Present-day climate forcing and response from black carbon in snow. *Journal of Geophysical Research: Atmospheres.* **112**, D11202.

Folberth, G.A., Hauglustaine, D.A., Lathière, J. and Brocheton, F. 2006. Interactive chemistry in the Laboratoire de Météorologie Dynamique general circulation model: model description and impact analysis of biogenic hydrocarbons on tropospheric chemistry. *Atmos. Chem. Phys.* **6**(8), pp.2273-2319.

Forster, P., Ramaswamy, V., Artaxo, P., Berntsen, T., Betts, R., Fahey, D.W., Haywood, J., Lean, J., Lowe, D.C., Myhre, G., Nganga, J., Prinn, R., Raga, G., Schulz, M. and Van Dorland, R. 2007. Changes in Atmospheric Constituents and in Radiative Forcing. In: Climate Change 2007: The Physical Science Basis. Contribution of Working Group I to the Fourth Assessment Report of the Intergovernmental Panel on Climate Change [Solomon, S., D. Qin, M. Manning, Z. Chen, M. Marquis, K.B. Averyt, M.Tignor and H.L. Miller (eds.)]. . *Cambridge University Press, Cambridge, United Kingdom and New York, NY, USA.*

Forster, P. and Shine, K.P. 1997. Radiative forcing and temperature trends from stratospheric ozone changes. *Geophysical Research Letters.* **102**(D9), pp.10841-10855.

Forster, P.M., Fomichev, V.I., Rozanov, E., Cagnazzo, C., Jonsson, A.I., Langematz, U., Fomin, B., Iacono, M.J., Mayer, B., Mlawer, E., Myhre, G., Portmann, R.W., Akiyoshi, H., Falaleeva, V., Gillett, N., Karpechko, A., Li, J., Lemennais, P., Morgenstern, O., Oberländer, S., Sigmond, M. and Shibata, K. 2011. Evaluation of radiation scheme performance within chemistry climate models. *Journal of Geophysical Research: Atmospheres (1984–2012).* **116**, D10302.

Fuglestvedt, J.S., Berntsen, T.K., Isaksen, I.S.A., Mao, H., Liang, X.-Z. and Wang, W.-C. 1999. Climatic forcing of nitrogen oxides through changes in tropospheric ozone and methane; global 3D model studies. *Atmospheric Environment.* **33**(6), pp.961-977.

Fuhrer, J. and Booker, F. 2003. Ecological issues related to ozone: agricultural issues. *Environment International.* **29**(2), pp.141-154.

Gakidou, E. et al. 2017. Global, regional, and national comparative risk assessment of 84 behavioural, environmental and occupational, and metabolic risks or clusters of risks, 1990-2016: a systematic analysis for the Global Burden of Disease Study 2016. *The Lancet.* **390**(10100), pp.1345-1422.

Galmarini, S., Koffi, B., Solazzo, E., Keating, T., Hogrefe, C., Schulz, M., Benedictow, A., Griesfeller, J.J., Janssens-Maenhout, G., Carmichael, G., Fu, J. and Dentener, F. 2017. Technical note: Coordination and harmonization of the multi-scale, multi-model activities HTAP2,

AQMEII3, and MICS-Asia3: simulations, emission inventories, boundary conditions, and model output formats. *Atmos. Chem. Phys.* **17**(2), pp.1543-1555.

Gaudel, A., R. Cooper, O., Ancellet, G., Brice, B., Boynard, A., P. Burrows, J., Clerbaux, C., F. Coheur, P., Cuesta, J., Cuevas, E., Doniki, S., Dufour, G., Ebojie, F., Foret, G., García, O., J. Granados Muños, M., Hannigan, J., Hase, F., Huang, G. and Ziemke, J. 2018. Tropospheric Ozone Assessment Report: Present-day distribution and trends of tropospheric ozone relevant to climate and global atmospheric chemistry model evaluation. *Elem Sci Anth.* **6**, p.39.

Gergis, J.L. and Fowler, A.M.J.C.C. 2009. A history of ENSO events since A.D. 1525: implications for future climate change. **92**(3), pp.343-387, Gergis2009.

Ghan, S.J., Smith, S.J., Wang, M., Zhang, K., Pringle, K., Carslaw, K., Pierce, J., Bauer, S. and Adams, P. 2013. A simple model of global aerosol indirect effects. *Journal of Geophysical Research: Atmospheres.* **118**(12), pp.6688-6707.

Giglio, L., Randerson, J.T. and van der Werf, G.R. 2013a. Analysis of daily, monthly, and annual burned area using the fourth-generation global fire emissions database (GFED4). **118**(1), pp.317-328.

Giglio, L., Randerson, J.T. and van der Werf, G.R. 2013b. Analysis of daily, monthly, and annual burned area using the fourth-generation global fire emissions database (GFED4). *Journal of Geophysical Research.* **118**(1), pp.317-328.

Glass, T.A., Goodman, S.N., Hernan, M.A. and Samet, J.M. 2013. Causal inference in public health. *Annu Rev Public Health.* **34**, pp.61-75.

Gondwe, M., Krol, M., Gieskes, W., Klaassen, W. and de Baar, H. 2003. The contribution of ocean-leaving DMS to the global atmospheric burdens of DMS, MSA, SO2, and NSS SO4=. *Global Biogeochemical Cycles.* **17**, p.1056.

Gorchakov, G.I., Sitnov, S.A., Sviridenkov, M.A., Semoutnikova, E.G., Emilenko, A.S., Isakov, A.A., Kopeikin, V.M., Karpov, A.V., Gorchakova, I.A., Verichev, K.S., Kurbatov, G.A. and Ponomareva, T.Y. 2014. Satellite and ground-based monitoring of smoke in the atmosphere during the summer wildfires in European Russia in 2010 and Siberia in 2012. *International Journal of Remote Sensing.* **35**(15), pp.5698-5721.

Gordon, H., Kirkby, J., Baltensperger, U., Bianchi, F., Breitenlechner, M., Curtius, J., Dias, A., Dommen, J., Donahue, N.M., Dunne, E.M., Duplissy, J., Ehrhart, S., Flagan, R.C., Frege, C., Fuchs, C., Hansel, A., Hoyle, C.R., Kulmala, M., Kürten, A., Lehtipalo, K., Makhmutov, V., Molteni, U., Rissanen, M.P., Stozkhov, Y., Tröstl, J., Tsagkogeorgas, G., Wagner, R., Williamson, C., Wimmer, D., Winkler, P.M., Yan, C. and Carslaw, K.S. 2017. Causes and importance of new particle formation in the present-day and preindustrial atmospheres. *Journal of Geophysical Research: Atmospheres.* **122**(16), pp.8739-8760.

Granier, C., Müller, J.-F. and Brasseur, G. 2000. The Impact of Biomass Burning on the Global Budget of Ozone and Ozone Precursors. In: Innes J.L., B.M., Verstraete M.M. ed. *Biomass Burning and Its Inter-Relationships with the Climate System.* Dordrecht: Springer.

Granier, C., S. Darras, H. Denier van der Gon, J. Doubalova, N. Elguindi, B. Galle, M.G., M. Guevara, J.-P. Jalkanen, J. Kuenen, C. Liousse, B. Quack, D. Simpson and Sindelarova, K. 2019. Copernicus Atmosphere Monitoring Service global and regional emissions (April 2019 version). Copernicus Atmosphere Monitoring Service (CAMS) report.

Guenther, A.B., Jiang, X., Heald, C.L., Sakulyanontvittaya, T., Duhl, T., Emmons, L.K. and Wang, X. 2012. The Model of Emissions of Gases and Aerosols from Nature version 2.1 (MEGAN2.1): an extended and updated framework for modeling biogenic emissions. *Geosci. Model Dev.* **5**(6), pp.1471-1492.

Hamilton, D.S., Hantson, S., Scott, C.E., Kaplan, J.O., Pringle, K.J., Nieradzik, L.P., Rap, A., Folberth, G.A., Spracklen, D.V. and Carslaw, K.S. 2018. Reassessment of pre-industrial fire emissions strongly affects anthropogenic aerosol forcing. *Nature Communications.* **9**(1), p.3182.

Hansen, J., Sato, M. and Ruedy, R. 1997. Radiative forcing and climate response. **102**(D6), pp.6831-6864.

Hansen, J., Sato, M., Ruedy, R., Kharecha, P., Lacis, A., Miller, R., Nazarenko, L., Lo, K., Schmidt, G.A., Russell, G., Aleinov, I., Bauer, S., Baum, E., Cairns, B., Canuto, V., Chandler, M., Cheng, Y., Cohen, A., Del Genio, A., Faluvegi, G., Fleming, E., Friend, A., Hall, T., Jackman, C., Jonas, J., Kelley, M., Kiang, N.Y., Koch, D., Labow, G., Lerner, J., Menon, S., Novakov, T., Oinas, V., Perlwitz, J., Perlwitz, J., Rind, D., Romanou, A., Schmunk, R., Shindell, D., Stone, P., Sun, S., Streets, D., Tausnev, N., Thresher, D., Unger, N., Yao, M. and Zhang, S. 2007. Dangerous human-made interference with climate: a GISS modelE study. *Atmos. Chem. Phys.* **7**(9), pp.2287-2312.

Hansen, J., Sato, M., Ruedy, R., Lacis, A. and Oinas, V. 2000. Global warming in the twenty-first century: An alternative scenario. *Proceedings of the National Academy of Sciences.* **97**(18), pp.9875-9880.

Hantson, S., Knorr, W., Schurgers, G., Pugh, T.A.M. and Arneth, A. 2017. Global isoprene and monoterpene emissions under changing climate, vegetation, CO2 and land use. *Atmospheric Environment.* **155**, pp.35-45.

Hartmann, D.L., Klein Tank, A.M.G., Rusticucci, M., Alexander, L.V., Brönnimann, S., Charabi, Y., Dentener, F.J., Dlugokencky, E.J., Easterling, D.R., Kaplan, A., Soden, B.J., Thorne, P.W., Wild, M. and Zhai, P.M. 2013. Observations: Atmosphere and Surface. In: Stocker, T.F., et al. eds. *Climate Change 2013: The Physical Science Basis. Contribution of Working Group I to the Fifth Assessment Report of the Intergovernmental Panel on Climate Change.* Cambridge, United Kingdom and New York, NY, USA: Cambridge University Press, pp.159–254.

Hauglustaine, D.A., Brasseur, G.P. and Levine, J.S. 1999. A sensitivity simulation of tropospheric ozone changes due to the 1997 Indonesian fire emissions. **26**(21), pp.3305-3308.

Hauglustaine, D.A., Brasseur, G.P., Walters, S., Rasch, P.J., Müller, J.-F., Emmons, L.K. and Carroll, M.A. 1998. MOZART, a global chemical transport model for ozone and related chemical tracers: 2. Model results and evaluation. *Journal of Geophysical Research.* **103**(D21), pp.28291-28335.

Hausmann, P., Sussmann, R. and Smale, D. 2016. Contribution of oil and natural gas production to renewed increase in atmospheric methane (2007–2014): top–down estimate from ethane and methane column observations. *Atmos. Chem. Phys.* **16**(5), pp.3227-3244.

Haustein, K., Allen, M.R., Forster, P.M., Otto, F.E.L., Mitchell, D.M., Matthews, H.D. and Frame, D.J. 2017. A real-time Global Warming Index. *Scientific Reports.* **7**(1), p.15417.

Heald, C.L., Coe, H., Jimenez, J.L., Weber, R.J., Bahreini, R., Middlebrook, A.M., Russell, L.M., Jolleys, M., Fu, T.M., Allan, J.D., Bower, K.N., Capes, G., Crosier, J., Morgan, W.T., Robinson, N.H., Williams, P.I., Cubison, M.J., DeCarlo, P.F. and Dunlea, E.J. 2011. Exploring the vertical profile of atmospheric organic aerosol: comparing 17 aircraft field campaigns with a global model. *Atmos. Chem. Phys.* **11**(24), pp.12673-12696.

HEI. 2018. State of Global Air. Health Effects Institute Special Report, Boston, MA.

Helmig, D., Rossabi, S., Hueber, J., Tans, P., Montzka, S.A., Masarie, K., Thoning, K., Plass-Duelmer, C., Claude, A., Carpenter, L.J., Lewis, A.C., Punjabi, S., Reimann, S., Vollmer, M.K., Steinbrecher, R., Hannigan, J.W., Emmons, L.K., Mahieu, E., Franco, B., Smale, D. and Pozzer, A. 2016. Reversal of global atmospheric ethane and propane trends largely due to US oil and natural gas production. *Nature Geoscience.* **9**, p.490.

Hilboll, A., Richter, A. and Burrows, J.P. 2017. NO2 pollution over India observed from space — the impact of rapid economic growth, and a recent decline. *Atmos. Chem. Phys.* **2017**, pp.1-18.

Hinds, W.C. 1999. *Aerosol Technology: Properties, Behavior, and Measurement of Airborne Particles, 2nd Edition.* New York, USA: John Wiley and Sons.

Hodson, E.L., Poulter, B., Zimmermann, N.E., Prigent, C. and Kaplan, J.O. 2011. The El Niño–Southern Oscillation and wetland methane interannual variability. *Geophysical Research Letters.* **38**, L08810.

Hoesly, R.M., Smith, S.J., Feng, L., Klimont, Z., Janssens-Maenhout, G., Pitkanen, T., Seibert, J.J., Vu, L., Andres, R.J., Bolt, R.M., Bond, T.C., Dawidowski, L., Kholod, N., Kurokawa, J.I., Li, M., Liu, L., Lu, Z., Moura, M.C.P., O'Rourke, P.R. and Zhang, Q. 2018. Historical (1750–2014) anthropogenic emissions of reactive gases and aerosols from the

Community Emissions Data System (CEDS). *Geosci. Model Dev.* **11**(1), pp.369-408.

Hollaway, M.J., Arnold, S.R., Collins, W.J., Folberth, G. and Rap, A. 2017. Sensitivity of midnineteenth century tropospheric ozone to atmospheric chemistry-vegetation interactions. *Journal of Geophysical Research.* **122**(4), pp.2452-2473.

Holmes, C.D., Prather, M.J., Søvde, O.A. and Myhre, G. 2013. Future methane, hydroxyl, and their uncertainties: key climate and emission parameters for future predictions. *Atmos. Chem. Phys.* **13**(1), pp.285-302.

Holtslag, A.A.M. and Boville, B.A. 1993. Local Versus Nonlocal Boundary-Layer Diffusion in a Global Climate Model. *Journal of Climate.* **6**(10), pp.1825-1842.

Hossaini, R., Chipperfield, M.P., Saiz-Lopez, A., Fernandez, R., Monks, S., Feng, W., Brauer, P. and Glasow, R.v. 2016. A global model of tropospheric chlorine chemistry: Organic versus inorganic sources and impact on methane oxidation. *Journal of Geophysical Research: Atmospheres.* **121**(23), pp.14,271-214,297.

Hu, A., Xu, Y., Tebaldi, C., Washington, W.M. and Ramanathan, V. 2013. Mitigation of short-lived climate pollutants slows sea-level rise. *Nature Climate Change.* **3**, p.730.

Hu, L., Jacob, D.J., Liu, X., Zhang, Y., Zhang, L., Kim, P.S., Sulprizio, M.P. and Yantosca, R.M. 2017. Global budget of tropospheric ozone: Evaluating recent model advances with satellite (OMI), aircraft (IAGOS), and ozonesonde observations. *Atmospheric Environment.* **167**, pp.323-334.

Huang, G., Brook, R., Crippa, M., Janssens-Maenhout, G., Schieberle, C., Dore, C., Guizzardi, D., Muntean, M., Schaaf, E. and Friedrich, R. 2017. Speciation of anthropogenic emissions of non-methane volatile organic compounds: a global gridded data set for 1970–2012. *Atmos. Chem. Phys.* **17**(12), pp.7683-7701.

Huang, L., Fu, R. and Jiang, J.H. 2014. Impacts of fire emissions and transport pathways on the interannual variation of CO in the tropical upper troposphere. *Atmos. Chem. Phys.* **14**(8), pp.4087-4099.

Hudman, R.C., Moore, N.E., Mebust, A.K., Martin, R.V., Russell, A.R., Valin, L.C. and Cohen, R.C. 2012. Steps towards a mechanistic model of global soil nitric oxide emissions: implementation and space based-constraints. *Atmos. Chem. Phys.* **12**(16), pp.7779-7795.

Inness, A., Benedetti, A., Flemming, J., Huijnen, V., Kaiser, J.W., Parrington, M. and Remy, S. 2015. The ENSO signal in atmospheric composition fields: emission-driven versus dynamically induced changes. *Atmos. Chem. Phys.* **15**(15), pp.9083-9097.

IPCC. 1990. Climate Change: The IPCC scientific assessment. Intergovernmental Panel on Climate Change. Cambridge, UK.

Isaksen, I.S.A., Granier, C., Myhre, G., Berntsen, T.K., Dalsøren, S.B., Gauss, M., Klimont, Z., Benestad, R., Bousquet, P., Collins, W., Cox, T., Eyring, V., Fowler, D., Fuzzi, S., Jöckel, P., Laj, P., Lohmann, U., Maione, M., Monks, P., Prevot, A.S.H., Raes, F., Richter, A., Rognerud, B., Schulz, M., Shindell, D., Stevenson, D.S., Storelvmo, T., Wang, W.C., van Weele, M., Wild, M. and Wuebbles, D. 2009. Atmospheric composition change: Climate–Chemistry interactions. *Atmospheric Environment.* **43**(33), pp.5138-5192.

Jerrett, M., Burnett, R.T., Pope, C.A., Ito, K., Thurston, G., Krewski, D., Shi, Y., Calle, E. and Thun, M. 2009. Long-Term Ozone Exposure and Mortality. *New England Journal of Medicine.* **360**(11), pp.1085-1095.

Jian, Y. and Fu, T.M. 2014. Injection heights of springtime biomass-burning plumes over peninsular Southeast Asia and their impacts on long-range pollutant transport. *Atmos. Chem. Phys.* **14**(8), pp.3977-3989.

Jin, X. and Holloway, T. 2015. Spatial and temporal variability of ozone sensitivity over China observed from the Ozone Monitoring Instrument. *Journal of Geophysical Research: Atmospheres.* **120**(14), pp.7229-7246.

Johnson, B.T., Shine, K.P. and Forster, P.M. 2004. The semi-direct aerosol effect: Impact of absorbing aerosols on marine stratocumulus. *Quarterly Journal of the Royal Meteorological Society.* **130**(599), pp.1407-1422.

Johnson, C.E., Stevenson, D.S., Collins, W.J. and Derwent, R.G. 2001. Role of climate feedback on methane and ozone studied with a Coupled Ocean-Atmosphere-Chemistry Model. *Geophysical Research Letters.* **28**(9), pp.1723-1726.

Jones, C.D., Collins, M., Cox, P.M. and Spall, S.A. 2001. The Carbon Cycle Response to ENSO: A Coupled Climate–Carbon Cycle Model Study. *Journal of Climate.* **14**(21), pp.4113-4129.

Junge, C.E. 1962. Global ozone budget and exchange between stratosphere and troposphere. **14**(4), pp.363-377.

Kang, Y., Liu, M., Song, Y., Huang, X., Yao, H., Cai, X., Zhang, H., Kang, L., Liu, X., Yan, X., He, H., Zhang, Q., Shao, M. and Zhu, T. 2016. High-resolution ammonia emissions inventories in China from 1980 to 2012. *Atmos. Chem. Phys.* **16**(4), pp.2043-2058.

Kapadia, Z.Z. 2015. *Quantifying the climate and air quality impacts of nonCO2 species from the combustion of standard and alternative fuels in aviation*. PhD thesis, University of Leeds.

Kaplan, J.O., Krumhardt, K.M., Ellis, E.C., Ruddiman, W.F., Lemmen, C. and Goldewijk, K.K. 2011. Holocene carbon emissions as a result of anthropogenic land cover change. *The Holocene.* **21**(5), pp.775-791.

Kawase, H., Nagashima, T., Sudo, K. and Nozawa, T. 2011. Future changes in tropospheric ozone under Representative Concentration Pathways (RCPs). **38**(5).

Kettle, A.J. and Andreae, M. 2000. Flux of dimethylsulfide from the oceans: A comparison of updated data sets and flux models. *Journal of*

Geophysical Research, v.105, 26,793-26,808 (2000). **105**, pp.26793–26808.

Kirschke, S., Bousquet, P., Ciais, P., Saunois, M., Canadell, J.G., Dlugokencky, E.J., Bergamaschi, P., Bergmann, D., Blake, D.R., Bruhwiler, L., Cameron-Smith, P., Castaldi, S., Chevallier, F., Feng, L., Fraser, A., Heimann, M., Hodson, E.L., Houweling, S., Josse, B., Fraser, P.J., Krummel, P.B., Lamarque, J.-F., Langenfelds, R.L., Le Quéré, C., Naik, V., O'Doherty, S., Palmer, P.I., Pison, I., Plummer, D., Poulter, B., Prinn, R.G., Rigby, M., Ringeval, B., Santini, M., Schmidt, M., Shindell, D.T., Simpson, I.J., Spahni, R., Steele, L.P., Strode, S.A., Sudo, K., Szopa, S., van der Werf, G.R., Voulgarakis, A., van Weele, M., Weiss, R.F., Williams, J.E. and Zeng, G. 2013. Three decades of global methane sources and sinks. *Nature Geoscience.* **6**, p.813.

Klein Goldewijk, K., Beusen, A., van Drecht, G. and de Vos, M. 2011. The HYDE 3.1 spatially explicit database of human-induced global land-use change over the past 12,000 years. *Global Ecology and Biogeography.* **20**(1), pp.73-86.

Klimont, Z., Hoglund-Isaksson, L., Heyes, C., Rafaj, P., Schopp, W., Cofala, J., Purohit, P., Borken-Kleefeld, J., Kupiainen, K., Kiesewetter, G., Winiwarter, W., Amann, M., Zhao, B., Bertok, I. and Sander, R. 2019. Global scenarios of air pollutants and methane: 1990–2050. *in prep.*

Klimont, Z., Kupiainen, K., Heyes, C., Purohit, P., Cofala, J., Rafaj, P., Borken-Kleefeld, J. and Schöpp, W. 2017. Global anthropogenic emissions of particulate matter including black carbon. *Atmos. Chem. Phys.* **17**(14), pp.8681-8723.

Knorr, W., Kaminski, T., Arneth, A. and Weber, U. 2014. Impact of human population density on fire frequency at the global scale. *Biogeosciences.* **11**(4), pp.1085-1102.

Koumoutsaris, S., Bey, I., Generoso, S. and Thouret, V. 2008. Influence of El Niño–Southern Oscillation on the interannual variability of tropospheric ozone in the northern midlatitudes. *Journal of Geophysical Research: Atmospheres (1984–2012).* **113**, D19301.

Kozlov, V.S., Yausheva, E.P., Terpugova, S.A., Panchenko, M.V., Chernov, D.G. and Shmargunov, V.P. 2014. Optical–microphysical properties of smoke haze from Siberian forest fires in summer 2012. *International Journal of Remote Sensing.* **35**(15), pp.5722-5741.

Krol, M. and Lelieveld, J. 2003. Can the variability in tropospheric OH be deduced from measurements of 1,1,1-trichloroethane (methyl chloroform)? *Journal of Geophysical Research: Atmospheres.* **108**(D3), p.4125.

Krupa, S.V. and Manning, W.J. 1988. Atmospheric ozone: Formation and effects on vegetation. *Environmental Pollution.* **50**(1), pp.101-137.

Lamarque, J.F., Bond, T.C., Eyring, V., Granier, C., Heil, A., Klimont, Z., Lee, D., Liousse, C., Mieville, A., Owen, B., Schultz, M.G., Shindell, D., Smith, S.J., Stehfest, E., Van Aardenne, J., Cooper, O.R., Kainuma, M., Mahowald, N., McConnell, J.R., Naik, V., Riahi, K. and van Vuuren,

D.P. 2010. Historical (1850–2000) gridded anthropogenic and biomass burning emissions of reactive gases and aerosols: methodology and application. *Atmos. Chem. Phys.* **10**(15), pp.7017-7039.

Laothawornkitkul, J., Taylor, J.E., Paul, N.D. and Hewitt, C.N. 2009. Biogenic volatile organic compounds in the Earth system. **183**(1), pp.27-51.

Lathière, J., Hauglustaine, D.A., De Noblet-Ducoudré, N., Krinner, G. and Folberth, G.A. 2005. Past and future changes in biogenic volatile organic compound emissions simulated with a global dynamic vegetation model. *Geophysical Research Letters.* **32**(20).

Lathière, J., Hewitt, C.N. and Beerling, D.J. 2010. Sensitivity of isoprene emissions from the terrestrial biosphere to 20th century changes in atmospheric CO2 concentration, climate, and land use. *Global Biogeochemical Cycles.* **24**(1).

Lawrence, M., Jöckel, P. and Kuhlmann, R. 2001. What does the global mean OH concentration tell us? *Atmos. Chem. Phys.* **1**, pp.37-49.

Le Mer, J. and Roger, P. 2001. Production, oxidation, emission and consumption of methane by soils: A review. *European Journal of Soil Biology.* **37**(1), pp.25-50.

Lee, L.A., Pringle, K.J., Reddington, C.L., Mann, G.W., Stier, P., Spracklen, D.V., Pierce, J.R. and Carslaw, K.S. 2013. The magnitude and causes of uncertainty in global model simulations of cloud condensation nuclei. *Atmos. Chem. Phys.* **13**(17), pp.8879-8914.

Lee, L.A., Reddington, C.L. and Carslaw, K.S. 2016. On the relationship between aerosol model uncertainty and radiative forcing uncertainty. *Proceedings of the National Academy of Sciences.* **113**(21), pp.5820-5827.

Lelieveld, J. and Crutzen, P.J. 1990. Influences of cloud photochemical processes on tropospheric ozone. *Nature.* **343**(6255), pp.227-233.

Lelieveld, J. and Dentener, F.J. 2000. What controls tropospheric ozone? *Journal of Geophysical Research.* **105**(D3), pp.3531-3551.

Lelieveld, J., Evans, J.S., Fnais, M., Giannadaki, D. and Pozzer, A. 2015. The contribution of outdoor air pollution sources to premature mortality on a global scale. *Nature.* **525**, p.367.

Li, F., Zeng, X.D. and Levis, S. 2012. A process-based fire parameterization of intermediate complexity in a Dynamic Global Vegetation Model. *Biogeosciences.* **9**(7), pp.2761-2780.

Maasakkers, J.D., Jacob, D.J., Sulprizio, M.P., Scarpelli, T.R., Nesser, H., Sheng, J.X., Zhang, Y., Hersher, M., Bloom, A.A., Bowman, K.W., Worden, J.R., Janssens-Maenhout, G. and Parker, R.J. 2019. Global distribution of methane emissions, emission trends, and OH concentrations and trends inferred from an inversion of GOSAT satellite data for 2010–2015. *Atmos. Chem. Phys.* **19**(11), pp.7859-7881.

Malavelle, F.F., Haywood, J.M., Jones, A., Gettelman, A., Clarisse, L., Bauduin, S., Allan, R.P., Karset, I.H.H., Kristjánsson, J.E., Oreopoulos,

L., Cho, N., Lee, D., Bellouin, N., Boucher, O., Grosvenor, D.P., Carslaw, K.S., Dhomse, S., Mann, G.W., Schmidt, A., Coe, H., Hartley, M.E., Dalvi, M., Hill, A.A., Johnson, B.T., Johnson, C.E., Knight, J.R., O'Connor, F.M., Partridge, D.G., Stier, P., Myhre, G., Platnick, S., Stephens, G.L., Takahashi, H. and Thordarson, T. 2017. Strong constraints on aerosol–cloud interactions from volcanic eruptions. *Nature.* **546**, p.485.

Manatsa, D. and Mukwada, G. 2017. A connection from stratospheric ozone to El Niño-Southern Oscillation. *Scientific Reports.* **7**(1), p.5558.

Mann, G., S. Carslaw, K., Spracklen, D., A. Ridley, D., T. Manktelow, P., Chipperfield, M., Pickering, S. and E. Johnson, C. 2010. Description and evaluation of GLOMAP-mode: A modal global aerosol microphysics model for the UKCA composition-climate model. *Geosci. Model Dev.* **3**(2), pp.519-551.

Mann, G.W., Carslaw, K.S., Reddington, C.L., Pringle, K.J., Schulz, M., Asmi, A., Spracklen, D.V., Ridley, D.A., Woodhouse, M.T., Lee, L.A., Zhang, K., Ghan, S.J., Easter, R.C., Liu, X., Stier, P., Lee, Y.H., Adams, P.J., Tost, H., Lelieveld, J., Bauer, S.E., Tsigaridis, K., van Noije, T.P.C., Strunk, A., Vignati, E., Bellouin, N., Dalvi, M., Johnson, C.E., Bergman, T., Kokkola, H., von Salzen, K., Yu, F., Luo, G., Petzold, A., Heintzenberg, J., Clarke, A., Ogren, J.A., Gras, J., Baltensperger, U., Kaminski, U., Jennings, S.G., O'Dowd, C.D., Harrison, R.M., Beddows, D.C.S., Kulmala, M., Viisanen, Y., Ulevicius, V., Mihalopoulos, N., Zdimal, V., Fiebig, M., Hansson, H.C., Swietlicki, E. and Henzing, J.S. 2014. Intercomparison and evaluation of global aerosol microphysical properties among AeroCom models of a range of complexity. *Atmos. Chem. Phys.* **14**(9), pp.4679-4713.

Manning, M.R., Lowe, D.C., Moss, R.C., Bodeker, G.E. and Allan, W. 2005. Short-term variations in the oxidizing power of the atmosphere. *Nature.* **436**, p.1001.

Marlon, J.R., Bartlein, P.J., Carcaillet, C., Gavin, D.G., Harrison, S.P., Higuera, P.E., Joos, F., Power, M.J. and Prentice, I.C. 2008. Climate and human influences on global biomass burning over the past two millennia. *Nature Geoscience.* **1**, p.697.

Marlon, J.R., Kelly, R., Daniau, A.L., Vannière, B., Power, M.J., Bartlein, P., Higuera, P., Blarquez, O., Brewer, S., Brücher, T., Feurdean, A., Romera, G.G., Iglesias, V., Maezumi, S.Y., Magi, B., Courtney Mustaphi, C.J. and Zhihai, T. 2016. Reconstructions of biomass burning from sediment-charcoal records to improve data–model comparisons. *Biogeosciences.* **13**(11), pp.3225-3244.

Mårtensson, E.M., Nilsson, E.D., de Leeuw, G., Cohen, L.H. and Hansson, H.-C. 2003. Laboratory simulations and parameterization of the primary marine aerosol production. *Journal of Geophysical Research: Atmospheres.* **108**(D9), p.4297.

Matsui, H. and Koike, M. 2016. Enhancement of aerosol responses to changes in emissions over East Asia by gas-oxidant-aerosol coupling and

detailed aerosol processes. *Journal of Geophysical Research: Atmospheres.* **121**(12), pp.7161-7171.

Matthews, E. and Fung, I. 1987. Methane emission from natural wetlands: Global distribution, area, and environmental characteristics of sources. **1**(1), pp.61-86.

McNeill, V.F. 2017. Atmospheric Aerosols: Clouds, Chemistry, and Climate. *Annual Review of Chemical and Biomolecular Engineering.* **8**(1), pp.427-444.

McNorton, J., Chipperfield, M., Gloor, M., Wilson, C., Wuhu, F., Hayman, G., Rigby, M., B. Krummel, P., O'Doherty, S., Prinn, R., Weiss, R., Young, D., Dlugokencky, E. and Montzka, S.A. 2016a. Role of OH variability in the stalling of the global atmospheric CH4 growth rate from 1999 to 2006. *Geophysical Research Letters.* **2016**, pp.1-24.

McNorton, J., Gloor, E., Wilson, C., Hayman, G.D., Gedney, N., Comyn-Platt, E., Marthews, T., Parker, R.J., Boesch, H. and Chipperfield, M.P. 2016b. Role of regional wetland emissions in atmospheric methane variability. **43**(21), pp.11,433-411,444.

McNorton, J., Wilson, C., Gloor, M., Parker, R.J., Boesch, H., Feng, W., Hossaini, R. and Chipperfield, M.P. 2018. Attribution of recent increases in atmospheric methane through 3-D inverse modelling. *Atmos. Chem. Phys.* **18**(24), pp.18149-18168.

McPhaden, M.J., Zebiak, S.E. and Glantz, M.H. 2006. ENSO as an Integrating Concept in Earth Science. *Science.* **314**(5806), pp.1740-1745.

Meinshausen, M., Smith, S.J., Calvin, K., Daniel, J.S., Kainuma, M.L.T., Lamarque, J.-F., Matsumoto, K., Montzka, S.A., Raper, S.C.B., Riahi, K., Thomson, A., Velders, G.J.M. and van Vuuren, D.P.P. 2011. The RCP greenhouse gas concentrations and their extensions from 1765 to 2300. *Climatic Change.* **109**(1), p.213, Meinshausen2011.

Meng, L., Paudel, R., G. M. Hess, P. and Mahowald, N. 2015. Seasonal and inter-annual variability in wetland methane emissions simulated by CLM4Me' and CAM-chem and comparisons to observations of concentrations. *Biogeosciences Discussions.* **12**, pp.4029--4049.

Merikanto, J., Spracklen, D.V., Mann, G.W., Pickering, S.J. and Carslaw, K.S. 2009. Impact of nucleation on global CCN. *Atmos. Chem. Phys.* **9**(21), pp.8601-8616.

Messina, P., Lathière, J., Sindelarova, K., Vuichard, N., Granier, C., Ghattas, J., Cozic, A. and Hauglustaine, D.A. 2016. Global biogenic volatile organic compound emissions in the ORCHIDEE and MEGAN models and sensitivity to key parameters. *Atmos. Chem. Phys.* **16**(22), pp.14169-14202.

Mickley, L.J., Jacob, D.J. and Rind, D. 2001. Uncertainty in preindustrial abundance of tropospheric ozone: Implications for radiative forcing calculations. *Journal of Geophysical Research.* **106**(D4), pp.3389-3399.

Miles, G.M., Siddans, R., Kerridge, B.J., Latter, B.G. and Richards, N.A.D. 2015. Tropospheric ozone and ozone profiles retrieved from GOME-2 and their validation. *Atmos. Meas. Tech.* **8**(1), pp.385-398.

Miyazaki, K., Eskes, H., Sudo, K., Boersma, K.F., Bowman, K. and Kanaya, Y. 2017. Decadal changes in global surface NOx emissions from multi-constituent satellite data assimilation. *Atmos. Chem. Phys.* **17**(2), pp.807-837.

Molina, M., Zaelke, D., Sarma, K.M., Andersen, S.O., Ramanathan, V. and Kaniaru, D. 2009. Reducing abrupt climate change risk using the Montreal Protocol and other regulatory actions to complement cuts in CO2 emissions. *Proceedings of the National Academy of Sciences.* **106**(49), pp.20616-20621.

Monks, P.S., Archibald, A.T., Colette, A., Cooper, O., Coyle, M., Derwent, R., Fowler, D., Granier, C., Law, K.S., Mills, G.E., Stevenson, D.S., Tarasova, O., Thouret, V., von Schneidemesser, E., Sommariva, R., Wild, O. and Williams, M.L. 2015. Tropospheric ozone and its precursors from the urban to the global scale from air quality to short-lived climate forcer. *Atmos. Chem. Phys.* **15**(15), pp.8889-8973.

Monks, S., R. Arnold, S., Hollaway, M., Pope, R., Wilson, C., Wuhu, F., Emmerson, K., J. Kerridge, B., Latter, B., M. Miles, G., Siddans, R. and P. Chipperfield, M. 2017. The TOMCAT global chemical transport model v1.6: Description of chemical mechanism and model evaluation. *Geosci. Model Dev.* **10**, pp.3025-3057.

Monks, S.A., Arnold, S.R. and Chipperfield, M.P. 2012. Evidence for El Niño–Southern Oscillation (ENSO) influence on Arctic CO interannual variability through biomass burning emissions. *Geophysical Research Letters.* **39**, L14804.

Montzka, S.A., Krol, M., Dlugokencky, E., Hall, B., Jöckel, P. and Lelieveld, J. 2011. Small Interannual Variability of Global Atmospheric Hydroxyl. **331**(6013), pp.67-69.

Moxim, W.J., Levy II, H. and Kasibhatla, P.S. 1996. Simulated global tropospheric PAN: Its transport and impact on NO x. *Journal of Geophysical Research: Atmospheres.* **101**(D7), pp.12621-12638.

Müller, W.A. and Roeckner, E.J.C.D. 2008. ENSO teleconnections in projections of future climate in ECHAM5/MPI-OM. **31**(5), pp.533-549, Müller2008.

Murray, L.T., Mickley, L.J., Kaplan, J.O., Sofen, E.D., Pfeiffer, M. and Alexander, B. 2014. Factors controlling variability in the oxidative capacity of the troposphere since the Last Glacial Maximum. *Atmos. Chem. Phys.* **14**(7), pp.3589-3622.

Myhre, G., Samset, B.H., Schulz, M., Balkanski, Y., Bauer, S., Berntsen, T.K., Bian, H., Bellouin, N., Chin, M., Diehl, T., Easter, R.C., Feichter, J., Ghan, S.J., Hauglustaine, D., Iversen, T., Kinne, S., Kirkevåg, A., Lamarque, J.F., Lin, G., Liu, X., Lund, M.T., Luo, G., Ma, X., van Noije, T., Penner, J.E., Rasch, P.J., Ruiz, A., Seland, Ø., Skeie, R.B., Stier, P., Takemura, T., Tsigaridis, K., Wang, P., Wang, Z., Xu, L., Yu, H., Yu, F.,

Yoon, J.H., Zhang, K., Zhang, H. and Zhou, C. 2013a. Radiative forcing of the direct aerosol effect from AeroCom Phase II simulations. *Atmos. Chem. Phys.* **13**(4), pp.1853-1877.

Myhre, G., Shindell, D., Bréon, F.-M., Collins, W., Fuglestvedt, J., Huang, J., Koch, D., Lamarque, J.-F., Lee, D., Mendoza, B., Nakajima, T., Robock, A., Stephens, G., Takemura, T. and Zhang, H. 2013b. Anthropogenic and Natural Radiative Forcing. In: Stocker, T.F., et al. eds. *Climate Change 2013: The Physical Science Basis. Contribution of Working Group I to the Fifth Assessment Report of the Intergovernmental Panel on Climate Change.* Cambridge, United Kingdom and New York, NY, USA: Cambridge University Press, pp.659–740.

Naik, V., Delire, C. and Wuebbles, D.J. 2004. Sensitivity of global biogenic isoprenoid emissions to climate variability and atmospheric CO2. *Journal of Geophysical Research: Atmospheres.* **109**(D6).

Naik, V., Voulgarakis, A., Fiore, A.M., Horowitz, L.W., Lamarque, J.F., Lin, M., Prather, M.J., Young, P.J., Bergmann, D., Cameron-Smith, P.J., Cionni, I., Collins, W.J., Dalsøren, S.B., Doherty, R., Eyring, V., Faluvegi, G., Folberth, G.A., Josse, B., Lee, Y.H., MacKenzie, I.A., Nagashima, T., van Noije, T.P.C., Plummer, D.A., Righi, M., Rumbold, S.T., Skeie, R., Shindell, D.T., Stevenson, D.S., Strode, S., Sudo, K., Szopa, S. and Zeng, G. 2013. Preindustrial to present-day changes in tropospheric hydroxyl radical and methane lifetime from the Atmospheric Chemistry and Climate Model Intercomparison Project (ACCMIP). *Atmos. Chem. Phys.* **13**(10), pp.5277-5298.

Nelson, R. and O'Rourke, P. 2018. Black Carbon and Other Short-Lived Climate Pollutants (SLCPs): How SLCPs are Altering Our Understanding of the Global Climate System - And How This Will Require the Abandonment of the Standard Climate Metric CO2e. *SSRN Electronic Journal.* p.10.2139/ssrn.3202394.

Nenes, A. and Seinfeld, J.H. 2003. Parameterization of cloud droplet formation in global climate models. *Journal of Geophysical Research: Atmospheres (1984–2012).* **108**(D14), p.4415.

Neu, J.L., Flury, T., Manney, G.L., Santee, M.L., Livesey, N.J. and Worden, J. 2014. Tropospheric ozone variations governed by changes in stratospheric circulation. *Nature Geoscience.* **7**, p.340.

Nicely, J., Canty, T., Manyin, M., D. Oman, L., Salawitch, R., Steenrod, S., E. Strahan, S. and A. Strode, S. 2018. *Changes in Global Tropospheric OH Expected as a Result of Climate Change Over the Last Several Decades.*

Nisbet, E.G., Dlugokencky, E.J., Manning, M.R., Lowry, D., Fisher, R.E., France, J.L., Michel, S.E., Miller, J.B., White, J.W.C., Vaughn, B., Bousquet, P., Pyle, J.A., Warwick, N.J., Cain, M., Brownlow, R., Zazzeri, G., Lanoisellé, M., Manning, A.C., Gloor, E., Worthy, D.E.J., Brunke, E.-G., Labuschagne, C., Wolff, E.W. and Ganesan, A.L. 2016. Rising atmospheric methane: 2007–2014 growth and isotopic shift. *Global Biogeochemical Cycles.* **30**(9), pp.1356-1370.

Nisbet, E.G., Manning, M.R., Dlugokencky, E.J., Fisher, R.E., Lowry, D., Michel, S.E., Myhre, C.L., Platt, S.M., Allen, G., Bousquet, P., Brownlow, R., Cain, M., France, J.L., Hermansen, O., Hossaini, R., Jones, A.E., Levin, I., Manning, A.C., Myhre, G., Pyle, J.A., Vaughn, B.H., Warwick, N.J. and White, J.W.C. 2019. Very Strong Atmospheric Methane Growth in the 4 Years 2014–2017: Implications for the Paris Agreement. *Global Biogeochemical Cycles.* **33**(3), pp.318-342.

OECD. 2016. *The Economic Consequences of Outdoor Air Pollution.* Paris: OECD Publishing.

Olivier, J.G.J., Bloos, J.P.J., Berdowski, J.J.M., Visschedijk, A.J.H. and Bouwman, A.F. 1999. A 1990 global emission inventory of anthropogenic sources of carbon monoxide on 1°×1° developed in the framework of EDGAR/GEIA. *Chemosphere - Global Change Science.* **1**(1), pp.1-17.

Olivier, J.G.J., Van Aardenne, J.A., Dentener, F.J., Pagliari, V., Ganzeveld, L.N. and Peters, J.A.H.W. 2005. Recent trends in global greenhouse gas emissions:regional trends 1970–2000 and spatial distributionof key sources in 2000. *Environmental Sciences.* **2**(2-3), pp.81-99.

Oman, L.D., Douglass, A.R., Ziemke, J.R., Rodriguez, J.M., Waugh, D.W. and Nielsen, J.E. 2013. The ozone response to ENSO in Aura satellite measurements and a chemistry-climate simulation. **118**(2), pp.965-976.

Oman, L.D., Ziemke, J.R., Douglass, A.R., Waugh, D.W., Lang, C., Rodriguez, J.M. and Nielsen, J.E. 2011. The response of tropical tropospheric ozone to ENSO. **38**, p.L13706.

Orel, A.E. and Seinfeld, J.H. 1977. Nitrate formation in atmospheric aerosols. *Environmental Science & Technology.* **11**(10), pp.1000-1007.

Pacifico, F., Folberth, G.A., Jones, C.D., Harrison, S.P. and Collins, W.J. 2012. Sensitivity of biogenic isoprene emissions to past, present, and future environmental conditions and implications for atmospheric chemistry. *Journal of Geophysical Research.* **117**(D22), D22302.

Patra, P.K., Krol, M.C., Montzka, S.A., Arnold, T., Atlas, E.L., Lintner, B.R., Stephens, B.B., Xiang, B., Elkins, J.W., Fraser, P.J., Ghosh, A., Hintsa, E.J., Hurst, D.F., Ishijima, K., Krummel, P.B., Miller, B.R., Miyazaki, K., Moore, F.L., Mühle, J., O'Doherty, S., Prinn, R.G., Steele, L.P., Takigawa, M., Wang, H.J., Weiss, R.F., Wofsy, S.C. and Young, D. 2014. Observational evidence for interhemispheric hydroxyl-radical parity. *Nature.* **513**, p.219.

Paulot, F., J. Jacob, D., Johnson, M., Bell, T., R. Baker, A., C. Keene, W., D. Lima, I., Doney, S. and A. Stock, C. 2015. Global oceanic emission of ammonia: Constraints from seawater and atmospheric observations. *Global Biogeochemical Cycles.* **29**, pp.1165– 1178.

Penner, J.E., Prather, M.J., Isaksen, I.S.A., Fuglestvedt, J.S., Klimont, Z. and Stevenson, D.S. 2010. Short-lived uncertainty? *Nature Geoscience.* **3**, p.587.

Pfeiffer, M., Spessa, A. and Kaplan, J.O. 2013. A model for global biomass burning in preindustrial time: LPJ-LMfire (v1.0). *Geosci. Model Dev.* **6**(3), pp.643-685.

Pham, M., Müller, J.F., Brasseur, G.P., Granier, C. and Mégie, G. 1995. A three-dimensional study of the tropospheric sulfur cycle. *Journal of Geophysical Research: Atmospheres.* **100**(D12), pp.26061-26092.

Pierrehumbert, R.T. 2014. Short-Lived Climate Pollution. *Annual Review of Earth and Planetary Sciences.* **42**(1), pp.341-379.

Pison, I., Ringeval, B., Bousquet, P., Prigent, C. and Papa, F. 2013. Stable atmospheric methane in the 2000s: key-role of emissions from natural wetlands. *Atmos. Chem. Phys.* **13**(23), pp.11609-11623.

Pöschl, U., von Kuhlmann, R., Poisson, N. and Crutzen, P.J. 2000. Development and Intercomparison of Condensed Isoprene Oxidation Mechanisms for Global Atmospheric Modeling. *Journal of Atmospheric Chemistry.* **37**(1), pp.29-52, Pöschl2000.

Poulter, B., Bousquet, P., Canadell, J.G., Ciais, P., Peregon, A., Saunois, M., Arora, V.K., Beerling, D.J., Brovkin, V., Jones, C.D., Joos, F., Gedney, N., Ito, A., Kleinen, T., Koven, C.D., McDonald, K., Melton, J.R., Peng, C., Peng, S., Prigent, C., Schroeder, R., Riley, W.J., Saito, M., Spahni, R., Tian, H., Taylor, L., Viovy, N., Wilton, D., Wiltshire, A., Xu, X., Zhang, B., Zhang, Z. and Zhu, Q. 2017. Global wetland contribution to 2000–2012 atmospheric methane growth rate dynamics. *Environmental Research Letters.* **12**(9), p.094013.

Prather, M.J., Holmes, C.D. and Hsu, J. 2012. Reactive greenhouse gas scenarios: Systematic exploration of uncertainties and the role of atmospheric chemistry. *Geophysical Research Letters.* **39**, L09803.

Pringle, K.J., Carslaw, K.S., Spracklen, D.V., Mann, G.M. and Chipperfield, M.P. 2009. The relationship between aerosol and cloud drop number concentrations in a global aerosol microphysics model. *Atmos. Chem. Phys.* **9**(12), pp.4131-4144.

Prinn, R.G., Huang, J., Weiss, R.F., Cunnold, D.M., Fraser, P.J., Simmonds, P.G., McCulloch, A., Harth, C., Salameh, P., O'Doherty, S., Wang, R.H.J., Porter, L. and Miller, B.R. 2001. Evidence for Substantial Variations of Atmospheric Hydroxyl Radicals in the Past Two Decades. *Science.* **292**(5523), pp.1882-1888.

Proietti, C., Anav, A., De Marco, A., Sicard, P. and Vitale, M. 2016. A multi-sites analysis on the ozone effects on Gross Primary Production of European forests. *Sci Total Environ.* **556**, pp.1-11.

Quinn, P.K., Bates, T.S., Baum, E., Doubleday, N., Fiore, A.M., Flanner, M., Fridlind, A., Garrett, T.J., Koch, D., Menon, S., Shindell, D., Stohl, A. and Warren, S.G. 2008. Short-lived pollutants in the Arctic: their climate impact and possible mitigation strategies. *Atmos. Chem. Phys.* **8**(6), pp.1723-1735.

Rabin, S.S., Melton, J.R., Lasslop, G., Bachelet, D., Forrest, M., Hantson, S., Kaplan, J.O., Li, F., Mangeon, S., Ward, D.S., Yue, C., Arora, V.K.,

Hickler, T., Kloster, S., Knorr, W., Nieradzik, L., Spessa, A., Folberth, G.A., Sheehan, T., Voulgarakis, A., Kelley, D.I., Prentice, I.C., Sitch, S., Harrison, S. and Arneth, A. 2017. The Fire Modeling Intercomparison Project (FireMIP), phase 1: experimental and analytical protocols with detailed model descriptions. *Geosci. Model Dev.* **10**(3), pp.1175-1197.

Ramanathan, V. and Carmichael, G. 2008. Global and regional climate changes due to black carbon. *Nature Geoscience.* **1**, pp.221–227.

Ramanathan, V. and Xu, Y. 2010. The Copenhagen Accord for limiting global warming: Criteria, constraints, and available avenues. *Proceedings of the National Academy of Sciences.* **107**(18), pp.8055-8062.

Randerson, J.T., Chen, Y., van der Werf, G.R., Rogers, B.M. and Morton, D.C. 2012. Global burned area and biomass burning emissions from small fires. *Journal of Geophysical Research.* **117**, G04012.

Randerson, J.T., Van Der Werf, G.R., Giglio, L., Collatz, G.J. and Kasibhatla, P.S. 2017. *Global Fire Emissions Database, Version 4.1 (GFEDv4)*. ORNL Distributed Active Archive Center.

Rap, A., Richards, N.A.D., Forster, P.M., Monks, S.A., Arnold, S.R. and Chipperfield, M.P. 2015. Satellite constraint on the tropospheric ozone radiative effect. *Geophysical Research Letters.* **42**(12), pp.5074-5081.

Rap, A., Scott, C.E., Reddington, C.L., Mercado, L., Ellis, R.J., Garraway, S., Evans, M.J., Beerling, D.J., MacKenzie, A.R., Hewitt, C.N. and Spracklen, D.V. 2018. Enhanced global primary production by biogenic aerosol via diffuse radiation fertilization. *Nature Geoscience.* **11**(9), pp.640-644.

Rap, A., Scott, C.E., Spracklen, D.V., Bellouin, N., Forster, P.M., Carslaw, K.S., Schmidt, A. and Mann, G. 2013. Natural aerosol direct and indirect radiative effects. *Geophysical Research Letters.* **40**(12), pp.3297-3301.

Reay, D.S., Smith, P., Christensen, T.R., James, R.H. and Clark, H. 2018. Methane and Global Environmental Change. *Annual Review of Environment and Resources.* **43**(1), pp.165-192.

Reddington, C.L., Morgan, W.T., Darbyshire, E., Brito, J., Coe, H., Artaxo, P., Marsham, J. and Spracklen, D.V. 2018. Biomass burning aerosol over the Amazon: analysis of aircraft, surface and satellite observations using a global aerosol model. *Atmos. Chem. Phys. Discuss.* **2018**, pp.1-32.

Reddy, M.S. and Boucher, O. 2007. Climate impact of black carbon emitted from energy consumption in the world's regions. *Geophysical Research Letters.* **34**(11), L11802.

Richards, N.A.D., Arnold, S.R., Chipperfield, M.P., Miles, G., Rap, A., Siddans, R., Monks, S.A. and Hollaway, M.J. 2013. The Mediterranean summertime ozone maximum: global emission sensitivities and radiative impacts. *Atmos. Chem. Phys.* **13**(5), pp.2331-2345.

Richardson, T., Forster, P.M., Smith, C.J., Maycock, A., C,, Wood, T., Andrews, T., Boucher, O., Faluvegi, G., Fläschner, D., Hodnebrog, Ø., Kasoar, M., Kirkevåg, A., Lamarque, J.-F., Mülmenstädt, J., Myhre, G.,

Olivié, D., Portmann, R.W., Samset, B.H., Shawki, D., Shindell, D., Stier, P., Takemura, T., Voulgarakis, A. and Watson-Parris, D. 2019. Efficacy of climate forcings in PDRMIP models. *Journal of Geophysical Research: Atmospheres.* **124**, pp.12824-12844.

Riese, M., Ploeger, F., Rap, A., Vogel, B., Konopka, P., Dameris, M. and Forster, P. 2012. Impact of uncertainties in atmospheric mixing on simulated UTLS composition and related radiative effects. *Journal of Geophysical Research: Atmospheres.* **117**, D16305.

Rigby, M., Montzka, S.A., Prinn, R.G., White, J.W.C., Young, D., O'Doherty, S., Lunt, M.F., Ganesan, A.L., Manning, A.J., Simmonds, P.G., Salameh, P.K., Harth, C.M., Mühle, J., Weiss, R.F., Fraser, P.J., Steele, L.P., Krummel, P.B., McCulloch, A. and Park, S. 2017. Role of atmospheric oxidation in recent methane growth. *Proceedings of the National Academy of Sciences.* **114**(21), pp.5373-5377.

Rigby, M., Prinn, R.G., Fraser, P.J., Simmonds, P.G., Langenfelds, R.L., Huang, J., Cunnold, D.M., Steele, L.P., Krummel, P.B., Weiss, R.F., O'Doherty, S., Salameh, P.K., Wang, H.J., Harth, C.M., Mühle, J. and Porter, L.W. 2008. Renewed growth of atmospheric methane. *Geophysical Research Letters.* **35**, L22805.

Rigby, M., Prinn, R.G., O'Doherty, S., Montzka, S.A., McCulloch, A., Harth, C.M., Mühle, J., Salameh, P.K., Weiss, R.F., Young, D., Simmonds, P.G., Hall, B.D., Dutton, G.S., Nance, D., Mondeel, D.J., Elkins, J.W., Krummel, P.B., Steele, L.P. and Fraser, P.J. 2013. Re-evaluation of the lifetimes of the major CFCs and CH3CCl3 using atmospheric trends. *Atmos. Chem. Phys.* **13**(5), pp.2691-2702.

Rodhe, H., Crutzen, P. and Vanderpol, A. 1981. Formation of sulfuric and nitric acid in the atmosphere during long-range transport. *Tellus.* **33**(2), pp.132-141.

Rogelj, J., Meinshausen, M., Schaeffer, M., Knutti, R. and Riahi, K. 2015. Impact of short-lived non-CO2mitigation on carbon budgets for stabilizing global warming. *Environmental Research Letters.* **10**(7), p.075001.

Rogelj, J., Schaeffer, M., Meinshausen, M., Shindell, D.T., Hare, W., Klimont, Z., Velders, G.J.M., Amann, M. and Schellnhuber, H.J. 2014. Disentangling the effects of CO2 and short-lived climate forcer mitigation. *Proceedings of the National Academy of Sciences.* **111**(46), pp.16325-16330.

Rossow, W.B. and Schiffer, R.A. 1999. Advances in Understanding Clouds from ISCCP. *Bulletin of the American Meteorological Society.* **80**(11), pp.2261-2288.

Rubino, M., D'Onofrio, A., Seki, O. and Bendle, J.A. 2016. Ice-core records of biomass burning. *The Anthropocene Review.* **3**(2), pp.140-162.

Sander, S.P., Abbatt, J., Barker, J., Burkholder, J.B., Friedl, R.R., Golden, D.M., Huie, R., Kurylo, M., Moortgat, G., Orkin, V. and Wine, P. 2011. Chemical Kinetics and Photochemical Data for Use in Atmospheric

Studies, Evaluation No. 17. *JPL Publication.* **06-2**(Jet Propulsion Laboratory), p.523.

Saunois, M., Bousquet, P., Poulter, B., Peregon, A., Ciais, P., Canadell, J.G., Dlugokencky, E.J., Etiope, G., Bastviken, D., Houweling, S., Janssens-Maenhout, G., Tubiello, F.N., Castaldi, S., Jackson, R.B., Alexe, M., Arora, V.K., Beerling, D.J., Bergamaschi, P., Blake, D.R., Brailsford, G., Brovkin, V., Bruhwiler, L., Crevoisier, C., Crill, P., Covey, K., Curry, C., Frankenberg, C., Gedney, N., Höglund-Isaksson, L., Ishizawa, M., Ito, A., Joos, F., Kim, H.S., Kleinen, T., Krummel, P., Lamarque, J.F., Langenfelds, R., Locatelli, R., Machida, T., Maksyutov, S., McDonald, K.C., Marshall, J., Melton, J.R., Morino, I., Naik, V., O'Doherty, S., Parmentier, F.J.W., Patra, P.K., Peng, C., Peng, S., Peters, G.P., Pison, I., Prigent, C., Prinn, R., Ramonet, M., Riley, W.J., Saito, M., Santini, M., Schroeder, R., Simpson, I.J., Spahni, R., Steele, P., Takizawa, A., Thornton, B.F., Tian, H., Tohjima, Y., Viovy, N., Voulgarakis, A., van Weele, M., van der Werf, G.R., Weiss, R., Wiedinmyer, C., Wilton, D.J., Wiltshire, A., Worthy, D., Wunch, D., Xu, X., Yoshida, Y., Zhang, B., Zhang, Z. and Zhu, Q. 2016. The global methane budget 2000–2012. *Earth Syst. Sci. Data.* **8**(2), pp.697-751.

Schaefer, H., Fletcher, S.E.M., Veidt, C., Lassey, K.R., Brailsford, G.W., Bromley, T.M., Dlugokencky, E.J., Michel, S.E., Miller, J.B., Levin, I., Lowe, D.C., Martin, R.J., Vaughn, B.H. and White, J.W.C. 2016. A 21st-century shift from fossil-fuel to biogenic methane emissions indicated by 13CH4. *Science.* **352**(6281), pp.80-84.

Schaefer, H., Smale, D., Nichol, S.E., Bromley, T.M., Brailsford, G.W., Martin, R.J., Moss, R., Englund Michel, S. and White, J.W.C. 2018. Limited impact of El Niño–Southern Oscillation on variability and growth rate of atmospheric methane. *Biogeosciences.* **15**(21), pp.6371-6386.

Schultz, M.G., Heil, A., Hoelzemann, J.J., Spessa, A., Thonicke, K., Goldammer, J.G., Held, A.C., Pereira, J.M.C. and van het Bolscher, M. 2008. Global wildland fire emissions from 1960 to 2000. *Global Biogeochemical Cycles.* **22**, p.GB2002.

Schultz, M.G., Schröder, S., Lyapina, O., Cooper, O., Galbally, I., Petropavlovskikh, I., Von Schneidemesser, E., Tanimoto, H., Elshorbany, Y., Naja, M., Seguel, R., Dauert, U., Eckhardt, P., Feigenspahn, S., Fiebig, M., Hjellbrekke, A.-G., Hong, Y.-D., Christian Kjeld, P., Koide, H. and Ma, Z. 2017. Tropospheric Ozone Assessment Report: Database and Metrics Data of Global Surface Ozone Observations. *Elem Sci Anth.* **5**, p.58.

Schulz, M., Textor, C., Kinne, S., Balkanski, Y., Bauer, S., Berntsen, T., Berglen, T., Boucher, O., Dentener, F., Guibert, S., Isaksen, I.S.A., Iversen, T., Koch, D., Kirkevåg, A., Liu, X., Montanaro, V., Myhre, G., Penner, J.E., Pitari, G., Reddy, S., Seland, Ø., Stier, P. and Takemura, T. 2006. Radiative forcing by aerosols as derived from the AeroCom present-day and pre-industrial simulations. *Atmos. Chem. Phys.* **6**(12), pp.5225-5246.

Schumann, U. and Huntrieser, H. 2007. The global lightning-induced nitrogen oxides source. *Atmos. Chem. Phys.* **7**(14), pp.3823-3907.

Schurgers, G., Arneth, A., Holzinger, R. and Goldstein, A.H. 2009. Process-based modelling of biogenic monoterpene emissions combining production and release from storage. *Atmos. Chem. Phys.* **9**(10), pp.3409-3423.

Scott, C.E., Arnold, S.R., Monks, S.A., Asmi, A., Paasonen, P. and Spracklen, D.V. 2018. Substantial large-scale feedbacks between natural aerosols and climate. *Nature Geoscience.* **11**(1), pp.44-48.

Scott, C.E., Spracklen, D.V., Pierce, J.R., Riipinen, I., D'Andrea, S.D., Rap, A., Carslaw, K.S., Forster, P.M., Artaxo, P., Kulmala, M., Rizzo, L.V., Swietlicki, E., Mann, G.W. and Pringle, K.J. 2015. Impact of gas-to-particle partitioning approaches on the simulated radiative effects of biogenic secondary organic aerosol. *Atmos. Chem. Phys.* **15**(22), pp.12989-13001.

Selin, N.E., Wu, S., Nam, K.M., Reilly, J.M., Paltsev, S., Prinn, R.G. and Webster, M.D. 2009. Global health and economic impacts of future ozone pollution. *Environmental Research Letters.* **4**(4), p.044014.

Sheng, J.X., Weisenstein, D.K., Luo, B.P., Rozanov, E., Stenke, A., Anet, J., Bingemer, H. and Peter, T. 2015. Global atmospheric sulfur budget under volcanically quiescent conditions: Aerosol-chemistry-climate model predictions and validation. *Journal of Geophysical Research: Atmospheres.* **120**(1), pp.256-276.

Shindell, D. and Faluvegi, G. 2009. Climate response to regional radiative forcing during the twentieth century. *Nature Geoscience.* **2**, p.294.

Shindell, D., Kuylenstierna, J.C.I., Vignati, E., van Dingenen, R., Amann, M., Klimont, Z., Anenberg, S.C., Muller, N., Janssens-Maenhout, G., Raes, F., Schwartz, J., Faluvegi, G., Pozzoli, L., Kupiainen, K., Höglund-Isaksson, L., Emberson, L., Streets, D., Ramanathan, V., Hicks, K., Oanh, N.T.K., Milly, G., Williams, M., Demkine, V. and Fowler, D. 2012. Simultaneously Mitigating Near-Term Climate Change and Improving Human Health and Food Security. *Science.* **335**(6065), pp.183-189.

Shindell, D. and Smith, C.J. 2019. Climate and air-quality benefits of a realistic phase-out of fossil fuels. *Nature.* **573**(7774), pp.408-411.

Shindell, D.T., Faluvegi, G., Bell, N. and Schmidt, G.A. 2005. An emissions-based view of climate forcing by methane and tropospheric ozone. *Geophysical Research Letters.* **32**, L04803.

Shindell, D.T., Faluvegi, G., Koch, D.M., Schmidt, G.A., Unger, N. and Bauer, S.E. 2009. Improved Attribution of Climate Forcing to Emissions. *Science.* **326**(5953), pp.716-718.

Shindell, D.T., Klimont, Z., Borgford-Parnell, N., Höglund-Isaksson, L., Kallbekken, S., Kuylenstierna, J., Molina, L., Srivastava, L., Tao, S. and Venkataraman, C. 2017. Bridging the Gap: The Role of Short-Lived Climate Pollutants. Chapter 6 of United Nations Environmental

Program, The Emissions Gap Report 2017: A UN Environmental Synthesis Report, (UNEP). Nairobi, Kenya.

Shindell, D.T., Pechony, O., Voulgarakis, A., Faluvegi, G., Nazarenko, L., Lamarque, J.F., Bowman, K., Milly, G., Kovari, B., Ruedy, R. and Schmidt, G.A. 2013. Interactive ozone and methane chemistry in GISS-E2 historical and future climate simulations. *Atmos. Chem. Phys.* **13**(5), pp.2653-2689.

Shoemaker, J.K. and Schrag, D.P. 2013. The danger of overvaluing methane's influence on future climate change. *Climatic Change.* **120**(4), pp.903-914, Shoemaker2013.

Shoemaker, J.K., Schrag, D.P., Molina, M.J. and Ramanathan, V. 2013. What Role for Short-Lived Climate Pollutants in Mitigation Policy? *Science.* **342**(6164), pp.1323-1324.

Sillman, S., Logan, J.A. and Wofsy, S.C. 1990. The sensitivity of ozone to nitrogen oxides and hydrocarbons in regional ozone episodes. *Journal of Geophysical Research.* **95**(D2), pp.1837-1851.

Silver, B., Reddington, C.L., Arnold, S.R. and Spracklen, D.V. 2018. Substantial changes in air pollution across China during 2015–2017. *Environmental Research Letters.* **13**(11), p.114012.

Sindelarova, K., Granier, C., Bouarar, I., Guenther, A., Tilmes, S., Stavrakou, T., Müller, J.F., Kuhn, U., Stefani, P. and Knorr, W. 2014. Global data set of biogenic VOC emissions calculated by the MEGAN model over the last 30 years. *Atmos. Chem. Phys.* **14**(17), pp.9317-9341.

Singh, H.B. 1987. Reactive nitrogen in the troposphere. *Environmental Science & Technology.* **21**(4), pp.320-327.

Sitch, S., Cox, P.M., Collins, W.J. and Huntingford, C. 2007. Indirect radiative forcing of climate change through ozone effects on the land-carbon sink. *Nature.* **448**, p.791.

Smith, B., Wårlind, D., Arneth, A., Hickler, T., Leadley, P., Siltberg, J. and Zaehle, S. 2014. Implications of incorporating N cycling and N limitations on primary production in an individual-based dynamic vegetation model. *Biogeosciences.* **11**(7), pp.2027-2054.

Smith, C.J., Forster, P.M., Allen, M., Leach, N., Millar, R.J., Passerello, G.A. and Regayre, L.A. 2018. FAIR v1.3: a simple emissions-based impulse response and carbon cycle model. *Geosci. Model Dev.* **11**(6), pp.2273-2297.

Smith, S.J. and Mizrahi, A. 2013. Near-term climate mitigation by short-lived forcers. *Proceedings of the National Academy of Sciences.* **110**(35), pp.14202-14206.

Soden, B.J., Held, I.M., Colman, R., Shell, K.M., Kiehl, J.T. and Shields, C.A. 2008. Quantifying Climate Feedbacks Using Radiative Kernels. *Journal of Climate.* **21**(14), pp.3504-3520.

Spivakovsky, C.M., Logan, J.A., Montzka, S.A., Balkanski, Y.J., Foreman-Fowler, M., Jones, D.B.A., Horowitz, L.W., Fusco, A.C., Brenninkmeijer,

C.A.M., Prather, M.J., Wofsy, S.C. and McElroy, M.B. 2000. Three-dimensional climatological distribution of tropospheric OH: Update and evaluation. *Journal of Geophysical Research: Atmospheres.* **105**(D7), pp.8931-8980.

Spracklen, D.V., Pringle, K.J., Carslaw, K.S., Chipperfield, M.P. and Mann, G.W. 2005. A global off-line model of size-resolved aerosol microphysics: I. Model development and prediction of aerosol properties. *Atmos. Chem. Phys.* **5**(8), pp.2227-2252.

Stavrakou, T., Müller, J.F., De Smedt, I., Van Roozendael, M., van der Werf, G.R., Giglio, L. and Guenther, A. 2009. Global emissions of non-methane hydrocarbons deduced from SCIAMACHY formaldehyde columns through 2003–2006. *Atmos. Chem. Phys.* **9**(11), pp.3663-3679.

Stevenson, D., Doherty, R., Sanderson, M., Johnson, C., Collins, B. and Derwent, D. 2005. Impacts of climate change and variability on tropospheric ozone and its precursors. *Faraday Discuss.* **130**, pp.41-57; discussion 125-151, 519-124.

Stevenson, D.S., Johnson, C.E., Collins, W.J., Derwent, R.G. and Edwards, J.M. 2000. Future estimates of tropospheric ozone radiative forcing and methane turnover — The impact of climate change. *Geophysical Research Letters.* **27**(14), pp.2073-2076.

Stevenson, D.S., Young, P.J., Naik, V., Lamarque, J.F., Shindell, D.T., Voulgarakis, A., Skeie, R.B., Dalsoren, S.B., Myhre, G., Berntsen, T.K., Folberth, G.A., Rumbold, S.T., Collins, W.J., MacKenzie, I.A., Doherty, R.M., Zeng, G., van Noije, T.P.C., Strunk, A., Bergmann, D., Cameron-Smith, P., Plummer, D.A., Strode, S.A., Horowitz, L., Lee, Y.H., Szopa, S., Sudo, K., Nagashima, T., Josse, B., Cionni, I., Righi, M., Eyring, V., Conley, A., Bowman, K.W., Wild, O. and Archibald, A. 2013. Tropospheric ozone changes, radiative forcing and attribution to emissions in the Atmospheric Chemistry and Climate Model Intercomparison Project (ACCMIP). *Atmos. Chem. Phys.* **13**(6), pp.3063-3085.

Stewart, G.A. and Hursthouse, S.A. 2018. Environment and Human Health: The Challenge of Uncertainty in Risk Assessment. *Geosciences.* **8**(1), p.24.

Stocker, T.F., Qin, D., Plattner, G.-K., Alexander, L.V., Allen, S.K., Bindoff, N.L., Bréon, F.-M., Church, J.A., Cubasch, U., Emori, S., Forster, P., Friedlingstein, P., Gillett, N., Gregory, J.M., Hartmann, D.L., Jansen, E., Kirtman, B., Knutti, R., Krishna Kumar, K., Lemke, P., Marotzke, J., Masson-Delmotte, V., Meehl, G.A., Mokhov, I.I., Piao, S., Ramaswamy, V., Randall, D., Rhein, M., Rojas, M., Sabine, C., Shindell, D., Talley, L.D., Vaughan, D.G. and Xie, S.-P. 2013. Technical Summary. In: Stocker, T.F., et al. eds. *Climate Change 2013: The Physical Science Basis. Contribution of Working Group I to the Fifth Assessment Report of the Intergovernmental Panel on Climate Change.* Cambridge, United Kingdom and New York, NY, USA: Cambridge University Press, pp.33–115.

Stockwell, D.Z., Giannakopoulos, C., Plantevin, P.H., Carver, G., Chipperfield, M., Law, K.S., Shallcross, D. and Wang, K.Y. 1999. Modelling NOx from lightning and its impact on global chemical fields. *Atmospheric Environment.* **33**, pp.4477-4493.

Stohl, A., Aamaas, B., Amann, M., Baker, L.H., Bellouin, N., Berntsen, T.K., Boucher, O., Cherian, R., Collins, W., Daskalakis, N., Dusinska, M., Eckhardt, S., Fuglestvedt, J.S., Harju, M., Heyes, C., Hodnebrog, Ø., Hao, J., Im, U., Kanakidou, M., Klimont, Z., Kupiainen, K., Law, K.S., Lund, M.T., Maas, R., MacIntosh, C.R., Myhre, G., Myriokefalitakis, S., Olivié, D., Quaas, J., Quennehen, B., Raut, J.C., Rumbold, S.T., Samset, B.H., Schulz, M., Seland, Ø., Shine, K.P., Skeie, R.B., Wang, S., Yttri, K.E. and Zhu, T. 2015. Evaluating the climate and air quality impacts of short-lived pollutants. *Atmos. Chem. Phys.* **15**(18), pp.10529-10566.

Storelvmo, T. 2017. Aerosol Effects on Climate via Mixed-Phase and Ice Clouds. *Annual Review of Earth and Planetary Sciences.* **45**(1), pp.199-222.

Sudo, K. and Takahashi, M. 2001. Simulation of tropospheric ozone changes during 1997–1998 El Niño: Meteorological impact on tropospheric photochemistry. **28**(21), pp.4091-4094.

Sun, L., Xue, L., Wang, T., Gao, J., Ding, A., Cooper, O.R., Lin, M., Xu, P., Wang, Z., Wang, X., Wen, L., Zhu, Y., Chen, T., Yang, L., Wang, Y., Chen, J. and Wang, W. 2016. Significant increase of summertime ozone at Mount Tai in Central Eastern China. *Atmos. Chem. Phys.* **16**(16), pp.10637-10650.

Swetnam, T.W., Farella, J., Roos, C.I., Liebmann, M.J., Falk, D.A. and Allen, C.D. 2016. Multiscale perspectives of fire, climate and humans in western North America and the Jemez Mountains, USA. *Philosophical Transactions of the Royal Society B: Biological Sciences.* **371**(1696), p.20150168.

Szopa, S., Hauglustaine, D.A. and Ciais, P. 2007. Relative contributions of biomass burning emissions and atmospheric transport to carbon monoxide interannual variability. *Geophysical Research Letters.* **34**, p.L18810.

Tereszchuk, K.A., Moore, D.P., Harrison, J.J., Boone, C.D., Park, M., Remedios, J.J., Randel, W.J. and Bernath, P.F. 2013. Observations of peroxyacetyl nitrate (PAN) in the upper troposphere by the Atmospheric Chemistry Experiment-Fourier Transform Spectrometer (ACE-FTS). *Atmos. Chem. Phys.* **13**(11), pp.5601-5613.

Tevini, M. and Teramura, A.H. 1989. UV-B Effects On Terrestrial Plants. *Photochemistry and Photobiology.* **50**(4), pp.479-487.

Thompson, A.M., Witte, J.C., Hudson, R.D., Guo, H., Herman, J.R. and Fujiwara, M. 2001. Tropical Tropospheric Ozone and Biomass Burning. *Science.* **291**(5511), pp.2128-2132.

Tiedtke, M. 1989. A Comprehensive Mass Flux Scheme for Cumulus Parameterization in Large-Scale Models. *Monthly Weather Review.* **117**(8), pp.1779-1800.

Tilmes, S., Lamarque, J.-F., Emmons, L., Conley, A., G. Schultz, M., Saunois, M., Thouret, V., Thompson, A., Oltmans, S., Johnson, B. and Tarasick, D. 2012. Technical Note: Ozonesonde climatology between 1995 and 2009: Description, evaluation and applications. *Atmos. Chem. Phys.* **12**, pp.7475-7497.

Timmermann, A., Oberhuber, J., Bacher, A., Esch, M., Latif, M. and Roeckner, E. 1999. Increased El Niño frequency in a climate model forced by future greenhouse warming. *Nature.* **398**(6729), pp.694-697.

Toll, V., Christensen, M., Quaas, J. and Bellouin, N. 2019. Weak average liquid-cloud-water response to anthropogenic aerosols. *Nature.* **572**(7767), pp.51-55.

Torres, O., Bhartia, P.K., Jethva, H. and Ahn, C. 2018. Impact of the ozone monitoring instrument row anomaly on the long-term record of aerosol products. *Atmos. Meas. Tech.* **11**(5), pp.2701-2715.

Turner, A.J., Frankenberg, C. and Kort, E.A. 2019. Interpreting contemporary trends in atmospheric methane. *Proceedings of the National Academy of Sciences.* **116**(8), pp.2805-2813.

Turner, A.J., Frankenberg, C., Wennberg, P.O. and Jacob, D.J. 2017. Ambiguity in the causes for decadal trends in atmospheric methane and hydroxyl. *Proceedings of the National Academy of Sciences.* **114**(21), pp.5367-5372.

Turner, A.J., Fung, I., Naik, V., Horowitz, L.W. and Cohen, R.C. 2018. Modulation of hydroxyl variability by ENSO in the absence of external forcing. *Proceedings of the National Academy of Sciences.* **115**(36), pp.8931-8936.

Turner, M.C., Jerrett, M., Pope, C.A., 3rd, Krewski, D., Gapstur, S.M., Diver, W.R., Beckerman, B.S., Marshall, J.D., Su, J., Crouse, D.L. and Burnett, R.T. 2016. Long-Term Ozone Exposure and Mortality in a Large Prospective Study. *American journal of respiratory and critical care medicine.* **193**(10), pp.1134-1142.

Twomey, S. 1977. The Influence of Pollution on the Shortwave Albedo of Clouds. *Journal of the Atmospheric Sciences.* **34**(7), pp.1149-1152.

UNEP. 2011. Near-term Climate Protection and Clean Air Benefits: Actions for Controlling Short-Lived Climate Forcers. United Nations Environment Programme (UNEP). Nairobi, Kenya.78pp.

UNEP and WMO. 2011. (United Nations Environment Programme and World Meteorological Organisation): Integrated Assessment of Black Carbon and Tropospheric Ozone. Nairobi, Kenya, 285 pp.

Unger, N. 2012. Global Climate Forcing by Criteria Air Pollutants. *Annual Review of Environment and Resources.* **37**(1), pp.1-24.

Unger, N. 2014. Human land-use-driven reduction of forest volatiles cools global climate. *Nature Climate Change.* **4**, p.907.

Van Amstel, A. 2012. Methane. A review. *Journal of Integrative Environmental Sciences.* **9**(sup1), pp.5-30.

van der Werf, G.R., Peters, W., van Leeuwen, T.T. and Giglio, L. 2013. What could have caused pre-industrial biomass burning emissions to exceed current rates? *Clim. Past.* **9**(1), pp.289-306.

van der Werf, G.R., Randerson, J.T., Collatz, G.J., Giglio, L., Kasibhatla, P.S., Arellano, A.F., Olsen, S.C. and Kasischke, E.S. 2004. Continental-Scale Partitioning of Fire Emissions During the 1997 to 2001 El Niño/La Niña Period. *Science.* **303**(5654), pp.73-76.

van der Werf, G.R., Randerson, J.T., Giglio, L., Collatz, G.J., Mu, M., Kasibhatla, P.S., Morton, D.C., DeFries, R.S., Jin, Y. and van Leeuwen, T.T. 2010. Global fire emissions and the contribution of deforestation, savanna, forest, agricultural, and peat fires (1997–2009). *Atmos. Chem. Phys.* **10**(23), pp.11707-11735.

van der Werf, G.R., Randerson, J.T., Giglio, L., van Leeuwen, T.T., Chen, Y., Rogers, B.M., Mu, M., van Marle, M.J.E., Morton, D.C., Collatz, G.J., Yokelson, R.J. and Kasibhatla, P.S. 2017. Global fire emissions estimates during 1997–2016. *Earth Syst. Sci. Data.* **9**(2), pp.697-720.

van Marle, M.J.E., Kloster, S., Magi, B.I., Marlon, J.R., Daniau, A.L., Field, R.D., Arneth, A., Forrest, M., Hantson, S., Kehrwald, N.M., Knorr, W., Lasslop, G., Li, F., Mangeon, S., Yue, C., Kaiser, J.W. and van der Werf, G.R. 2017. Historic global biomass burning emissions for CMIP6 (BB4CMIP) based on merging satellite observations with proxies and fire models (1750–2015). *Geosci. Model Dev.* **10**(9), pp.3329-3357.

van Oldenborgh, G.J., Philip, S.Y. and Collins, M. 2005. El Niño in a changing climate: a multi-model study. *Ocean Sci.* **1**(2), pp.81-95.

Verstraeten, W.W., Neu, J.L., Williams, J.E., Bowman, K.W., Worden, J.R. and Boersma, K.F. 2015. Rapid increases in tropospheric ozone production and export from China. *Nature Geoscience.* **8**, p.690.

Vignati, E., Karl, M., Krol, M., Wilson, J. and Cavalli, F. 2010. Sources of uncertainties in modelling Black Carbon at the global scale. *Atmospheric Chemistry and Physics.* **10**, pp.2595-2611.

Vinken, G.C.M., Boersma, K.F., Maasakkers, J.D., Adon, M. and Martin, R.V. 2014. Worldwide biogenic soil NOx emissions inferred from OMI NO2 observations. *Atmos. Chem. Phys.* **14**(18), pp.10363-10381.

Volz, A. and Kley, D. 1988. Evaluation of the Montsouris series of ozone measurements made in the nineteenth century. *Nature.* **332**(6161), pp.240-242.

Voulgarakis, A. and Field, R.D. 2015. Fire Influences on Atmospheric Composition, Air Quality and Climate. *Current Pollution Reports.* **1**(2), pp.70-81, Voulgarakis2015.

Voulgarakis, A., Marlier, M.E., Faluvegi, G., Shindell, D.T., Tsigaridis, K. and Mangeon, S. 2015. Interannual variability of tropospheric trace gases and aerosols: The role of biomass burning emissions. *Journal of Geophysical Research: Atmospheres.* **120**(14), pp.7157-7173.

Voulgarakis, A., Naik, V., Lamarque, J.F., Shindell, D.T., Young, P.J., Prather, M.J., Wild, O., Field, R.D., Bergmann, D., Cameron-Smith, P., Cionni, I., Collins, W.J., Dalsøren, S.B., Doherty, R.M., Eyring, V., Faluvegi, G., Folberth, G.A., Horowitz, L.W., Josse, B., MacKenzie, I.A., Nagashima, T., Plummer, D.A., Righi, M., Rumbold, S.T., Stevenson, D.S., Strode, S.A., Sudo, K., Szopa, S. and Zeng, G. 2013. Analysis of present day and future OH and methane lifetime in the ACCMIP simulations. *Atmos. Chem. Phys.* **13**(5), pp.2563-2587.

Wang, J.S., McElroy, M.B., Logan, J.A., Palmer, P.I., Chameides, W.L., Wang, Y. and Megretskaia, I.A. 2008. A quantitative assessment of uncertainties affecting estimates of global mean OH derived from methyl chloroform observations. *Journal of Geophysical Research: Atmospheres.* **113**, D12302.

Wang, Y., Jiang, J.H., Su, H., Choi, Y.-S., Huang, L., Guo, J. and Yung, Y.L. 2018. Elucidating the Role of Anthropogenic Aerosols in Arctic Sea Ice Variations. *Journal of Climate.* **31**(1), pp.99-114.

Wang, Z., Chappellaz, J., Park, K. and Mak, J.E. 2010. Large Variations in Southern Hemisphere Biomass Burning During the Last 650 Years. *Science.* **330**(6011), pp.1663-1666.

Warner, J.X., Wei, Z., Strow, L.L., Dickerson, R.R. and Nowak, J.B. 2016. The global tropospheric ammonia distribution as seen in the 13-year AIRS measurement record. *Atmos. Chem. Phys.* **16**(8), pp.5467-5479.

West, J.J., Smith, S.J., Silva, R.A., Naik, V., Zhang, Y., Adelman, Z., Fry, M.M., Anenberg, S., Horowitz, L.W. and Lamarque, J.-F. 2013. Co-benefits of mitigating global greenhouse gas emissions for future air quality and human health. *Nature Climate Change.* **3**, p.885.

WHO. 2016. Ambient air pollution: A global assessment of exposure and burden of disease. World Health Organisation. Geneva, Switzerland.

Wild, O. 2007. Modelling the global tropospheric ozone budget: exploring the variability in current models. *Atmos. Chem. Phys.* **7**(10), pp.2643-2660.

Wild, O. and Akimoto, H. 2001. Intercontinental transport of ozone and its precursors in a three-dimensional global CTM. *Journal of Geophysical Research: Atmospheres.* **106**(D21), pp.27729-27744.

Wittig, V.E., Ainsworth, E.A., Naidu, S.L., Karnosky, D.F. and Long, S.P. 2009. Quantifying the impact of current and future tropospheric ozone on tree biomass, growth, physiology and biochemistry: a quantitative meta-analysis. *Global Change Biology.* **15**(2), pp.396-424.

WMO. 1999. Scientific Assessment of Ozone Depletion: 1998. World Meteorological Organisation. Geneva, Switzerland.

Wolter, K. and Timlin, M. 1993. Monitoring ENSO in COADS with a seasonally adjusted principal component index. In: *17th Climate Diagnostics*

Workshop, 01/1993, Norman, OK. NOAA/NMC/CAC, NSSL, Oklahoma Clim. Survey, CIMMS and the School of Meteor., Univ. of Oklahoma, pp.52-57.

Wolter, K. and Timlin, M.S. 1998. Measuring the strength of ENSO events: How does 1997/98 rank? *Weather.* **53**(9), pp.315-324.

Wolter, K. and Timlin, M.S. 2011. El Niño/Southern Oscillation behaviour since 1871 as diagnosed in an extended multivariate ENSO index (MEI.ext). *International Journal of Climatology.* **31**(7), pp.1074-1087.

Woodhouse, M.T., Carslaw, K.S., Mann, G.W., Vallina, S.M., Vogt, M., Halloran, P.R. and Boucher, O. 2010. Low sensitivity of cloud condensation nuclei to changes in the sea-air flux of dimethyl-sulphide. *Atmos. Chem. Phys.* **10**(16), pp.7545-7559.

Worden, J.R., Bloom, A.A., Pandey, S., Jiang, Z., Worden, H.M., Walker, T.W., Houweling, S. and Röckmann, T. 2017. Reduced biomass burning emissions reconcile conflicting estimates of the post-2006 atmospheric methane budget. *Nature Communications.* **8**(1), p.2227.

Xu, R., Tian, H., Pan, S., Prior, S.A., Feng, Y., Batchelor, W.D., Chen, J. and Yang, J. 2019. Global ammonia emissions from synthetic nitrogen fertilizer applications in agricultural systems: Empirical and process-based estimates and uncertainty. *Global Change Biology.* **25**(1), pp.314-326.

Yan, X., Akiyama, H., Yagi, K. and Akimoto, H. 2009. Global estimations of the inventory and mitigation potential of methane emissions from rice cultivation conducted using the 2006 Intergovernmental Panel on Climate Change Guidelines. *Global Biogeochemical Cycles.* **23**, p.GB2002.

Yang, H., Chen, G., Tang, Q. and Hess, P. 2016. Quantifying isentropic stratosphere-troposphere exchange of ozone. *Journal of Geophysical Research: Atmospheres.* **121**(7), pp.3372-3387.

Yeung, L.Y., Murray, L.T., Martinerie, P., Witrant, E., Hu, H., Banerjee, A., Orsi, A. and Chappellaz, J. 2019. Isotopic constraint on the twentieth-century increase in tropospheric ozone. *Nature.* **570**(7760), pp.224-227.

Yienger, J.J. and Levy, H. 1995. Empirical model of global soil-biogenic NO_χ emissions. *Journal of Geophysical Research: Atmospheres.* **100**(D6), pp.11447-11464.

Yin, Y., Chevallier, F., Ciais, P., Broquet, G., Fortems-Cheiney, A., Pison, I. and Saunois, M. 2015. Decadal trends in global CO emissions as seen by MOPITT. *Atmospheric Chemistry and Physics Discussions.* **15**, pp.14505-14547.

Young, P., Naik, V., M. Fiore, A., Gaudel, A., Guo, J., Lin, M., L. Neu, J., Parrish, D., E. Rieder, H., Schnell, J., Tilmes, S., Wild, O., Zhang, L., Ziemke, J., Brandt, J., Delcloo, A., Doherty, R., Geels, C., Hegglin, M. and Lewis, A. 2018. Tropospheric Ozone Assessment Report: Assessment of global-scale model performance for global and regional ozone distributions, variability, and trends. *Elem Sci Anth.* **6**, p.10.

Young, P.J., Archibald, A.T., Bowman, K.W., Lamarque, J.F., Naik, V., Stevenson, D.S., Tilmes, S., Voulgarakis, A., Wild, O., Bergmann, D., Cameron-Smith, P., Cionni, I., Collins, W.J., Dalsøren, S.B., Doherty, R.M., Eyring, V., Faluvegi, G., Horowitz, L.W., Josse, B., Lee, Y.H., MacKenzie, I.A., Nagashima, T., Plummer, D.A., Righi, M., Rumbold, S.T., Skeie, R.B., Shindell, D.T., Strode, S.A., Sudo, K., Szopa, S. and Zeng, G. 2013. Pre-industrial to end 21st century projections of tropospheric ozone from the Atmospheric Chemistry and Climate Model Intercomparison Project (ACCMIP). *Atmos. Chem. Phys.* **13**(4), pp.2063-2090.

Zeng, G. and Pyle, J.A. 2005. Influence of El Niño Southern Oscillation on stratosphere/troposphere exchange and the global tropospheric ozone budget. *Geophysical Research Letters.* **32**(1), p.L01814.

Zhang, H., Xie, B. and Wang, Z. 2018. Effective Radiative Forcing and Climate Response to Short-Lived Climate Pollutants Under Different Scenarios. *Earth's Future.* **6**(6), pp.857-866.

Zhang, J., Tian, W., Wang, Z., Xie, F. and Wang, F. 2015. The Influence of ENSO on Northern Midlatitude Ozone during the Winter to Spring Transition. *Journal of Climate.* **28**(12), pp.4774-4793.

Zhang, Y., Cooper, O.R., Gaudel, A., Thompson, A.M., Nédélec, P., Ogino, S.-Y. and West, J.J. 2016. Tropospheric ozone change from 1980 to 2010 dominated by equatorward redistribution of emissions. *Nature Geoscience.* **9**, p.875.

Zhang, Y., Dore, A.J., Ma, L., Liu, X.J., Ma, W.Q., Cape, J.N. and Zhang, F.S. 2010. Agricultural ammonia emissions inventory and spatial distribution in the North China Plain. *Environ Pollut.* **158**(2), pp.490-501.

Zhong, Q., Huang, Y., Shen, H., Chen, Y., Chen, H., Huang, T., Zeng, E.Y. and Tao, S. 2017. Global estimates of carbon monoxide emissions from 1960 to 2013. *Environmental Science and Pollution Research.* **24**(1), pp.864-873, Zhong2017.

Zhu, L., Val Martin, M., Gatti, L.V., Kahn, R., Hecobian, A. and Fischer, E.V. 2018. Development and implementation of a new biomass burning emissions injection height scheme (BBEIH v1.0) for the GEOS-Chem model (v9-01-01). *Geosci. Model Dev.* **11**(10), pp.4103-4116.

Zhu, Q., Peng, C., Ciais, P., Jiang, H., Liu, J., Bousquet, P., Li, S., Chang, J., Fang, X., Zhou, X., Chen, H., Liu, S., Lin, G., Gong, P., Wang, M., Wang, H., Xiang, W. and Chen, J. 2017. Interannual variation in methane emissions from tropical wetlands triggered by repeated El Niño Southern Oscillation. *Global Change Biology.* **23**(11), pp.4706-4716.

Ziemke, J.R., Chandra, S., Oman, L.D. and Bhartia, P.K. 2010. A new ENSO index derived from satellite measurements of column ozone. *Atmos. Chem. Phys.* **10**(8), pp.3711-3721.

Zigler, C.M. and Dominici, F. 2014. Uncertainty in Propensity Score Estimation: Bayesian Methods for Variable Selection and Model Averaged Causal Effects. *J Am Stat Assoc.* **109**(505), pp.95-107.